

**Studies on Macroscale Structuralization  
of Porous Coordination Polymers**

**Kenji Hirai**

**2013**



## Preface

The study in this thesis has been carried out under the direction of Professor Susumu Kitagawa at during April 2007 - March 2013 at Department of Synthetic Chemistry and Biological Chemistry, Graduate School of Engineering, Kyoto University.

The author is greatly indebted to Professor Susumu Kitagawa for his significant guidance, valuable suggestions and continuous encouragement. The author wishes to express his heartfelt gratitude to Professor Masaaki Ohba (Kyushu University), Dr. Ho-Chol Chang (Hokkaido University), Dr. Takashi Uemura, Dr. Satoshi Horike, Dr. Masakazu Higuchi, Professor Takafumi Ueno (Tokyo Institute of Technology), Dr. Ryotaro Matsuda and Dr. Hiroshi Kajiro (Nippon Steel & Sumitomo Metal Corporation), for their helpful suggestions and hearty encouragements.

The author is grateful to Dr. Shuhei Furukawa for his continuous guidance and helpful discussions. The author expresses his gratitude to Dr. Osami Sakata (National Institute for Materials Science) for his collaborative work on the synchrotron X-ray diffraction experiments and valuable discussions. The author is grateful to Professor Christof Wöll (The Karlsruhe Institute of Technology), Dr. Osama Shekah (King Abdullah University of Science and Technology), Dr. Hui Wang and Professor Roland Fischer (Ruhr-Universität Bochum) for their collaborative work and kind hospitality during my short stay in Germany.

The author expresses his extreme gratitude to his colleges, Dr. Yohei Takashima (University of Glasgow), Dr. Ingmar Piglosiewicz (Wacker Chemie AG), Dr. Mio Kondo (Institute for Molecular Science), Dr. Takaaki Tsuruoka (Konan University), Dr. Hiromitsu Uehara (Hokkaido University), Dr. Stéphane Diring, Dr. Julien Reboul, Mr. Masashi Nakahama, Dr. Nicolas Louvain (Blaise Pascal University), Dr. Ayako Umemura (Futaba Project), Dr. Yoko Sakata (Kobe University), Mr. Kebi Chen (Daikin Industries, Ltd.), Ms. Nao Horike, Dr. Mikhail Meilikhov (SCOPION Management Consultants), Dr. Manuel Tsotsalas (The Karlsruhe Institute of Technology), Ms. Kira Khaletskaya (Ruhr-Universität Bochum), Mr. Chiwon Kim, Dr. Kenji Sumida, Mr. Kenji Yoshida for their valuable suggestions and kind technical supports.

The author expresses his gratitude to Dr. Hiroshi Sato, Dr. Daisuke Tanaka (Osaka University), Dr. Hirotohi Sakamoto (Shinshu University), Dr. Maw Lin Foo, Dr.

Munehiro Inukai, Dr. Satoru Shimomura, Dr. Yu Hijikata, Mr. Keiji Nakagawa, Mr. Keisuke Kishida, Mr. Kohei Nakamura, Mr. Ryo Ohtani, Mr. Tomohiro Fukushima, Mr. Daiki Umeyama, for their valuable discussions. The author wishes to express his heartfelt gratitude to all the members of Kitagawa group.

The author is much indebted for the financial support of Research Fellowship of the Japan Society for the Promotion of Science for Young Scientists. Finally, the author wishes to offer special thanks to his parents, Yoshiyuki Hirai and Machiko Hirai, and his brother Shin-ichiro Hirai for constant financial supports and warm-hearted encouragements.

Kenji Hirai

Department of Synthetic Chemistry and Biological Chemistry  
Graduate School of Engineering, Kyoto University

March, 2013

# Contents

<b>General Introduction</b>	<b>1</b>
<b>Chapter 1.</b> Heterogeneously Hybridized Porous Coordination Polymer Crystals: Fabrication of Heterometallic Core–Shell Single Crystals with an In-Plane Rotational Epitaxial Relationship	<b>19</b>
<b>Chapter 2.</b> A Block PCP Crystal: Anisotropic Hybridization of Porous Coordination Polymers by Face-selective Epitaxial Growth	<b>33</b>
<b>Chapter 3.</b> Sequential Functionalization of Porous Coordination Polymer Crystals	<b>45</b>
<b>Chapter 4.</b> Targeted Functionalisation of a Hierarchically-Structured Porous Coordination Polymer Crystal Enhances Its Entire Function	<b>65</b>
<b>Chapter 5.</b> Programmed Crystallization via Epitaxial Growth and Ligand Replacement towards a Hybridized Porous Coordination Polymer	<b>79</b>
<b>Chapter 6.</b> Multilength-scales structuralization emerged from one reaction	<b>93</b>
<b>Chapter 7.</b> Redox Reaction in Two-Dimensional Porous Coordination Polymers Based on Ferrocenedicarboxylate	<b>115</b>
<b>Chapter 8.</b> Crystal Orientation Controls Analyte Detection Kinetics of Porous	

Coordination Polymer Hybrid Sensor with Quartz Oscillator 135

**List of Publications** 157

# General Introduction

## 1. Structuralization of Materials

Chemistry is the art of manipulating bonds, interactions, and arrangements of atoms in a controlled and reproducible fashion. A wide variety of chemical reactions allows us to precisely design the molecular structures. In contrast, chemistry is now evolving away from the manipulation of individual molecules and toward the control of complex systems like living cells or materials. This evolution toward complexity bridges molecular chemistry and macroscopic science, thus opening a way for further development of molecular-based materials.

The properties of solid-state materials are determined by two structures across different length scales, chemical and macroscale structures. The chemical structures (individual molecular structures or arrangement of molecules) determine their inherent properties. In addition to the properties originating from chemical structures, the macroscale structures (size, morphology and structural hierarchy) often endow further properties with the materials. In particular, nanomaterials and photonic crystals are representative examples, in which macroscale structures significantly contribute to their properties. Downsizing the metallic compounds into nanometer-scale produces a band gap energy, so-called quantum effect,<sup>1</sup> and leads to characteristic optical<sup>2</sup> and electronic properties.<sup>3</sup> In another case, the periodic nanostructures affect the propagation of electromagnetic waves and result in the characteristic optical properties.<sup>4-5</sup> These phenomena are strongly depends on the macroscale structures of materials rather than the chemical structures. As seen in the examples provided above, control of macroscale structures of materials expands the range of practical applications and opens a way for new scientific areas.

Considerable effort has been devoted to the development of method to design the macroscale structures of a variety of materials. The solid-state materials can be remodeled in two main ways through bottom-up chemistry and top-down engineering

strategies. The bottom-up approaches involve ordinary chemical synthesis, template synthesis and assembly of the materials. On the other hand, laser, heating or mechanical processing methods are categorized into the top-down approaches. Both approaches can be applied to materials, if the materials are strong enough to endure harsh conditions of top-down approaches. In general, molecular materials comprising of weak chemical bonds, are often not stable under such harsh conditions of top-down approaches. In that sense, chemical approaches are the promising way to design both of chemical and macroscale structures of molecular materials.

## 2. Porous Coordination Polymers

The discovery of new solid-state materials has been considered as one of most critical factors in developing science and technology. In recent years, inorganic-organic hybrid materials, which composed of metal ions as connectors and organic ligands as linkers, have been emerged as a new class of porous solids, so-called porous coordination polymers (PCPs) or metal organic frameworks (MOFs). PCPs have been extensively studied not only for the scientific interest but also for the commercial interest in their applications for molecular storage,<sup>6-8</sup> separation,<sup>9-10</sup> catalysis,<sup>11-13</sup> polymerization,<sup>14</sup> and chemical sensing<sup>15-16</sup>. The remarkable progress of PCPs as functional materials is mainly due to the fact that compared to other conventional microporous materials (zeolites and activated carbons), PCPs are rationally designed based on the modifications of organic ligands and variation of coordination geometries. Therefore, these prominent features enables to precisely design the channel structures, pore sizes, and pore surface functionalities (Figure 1).

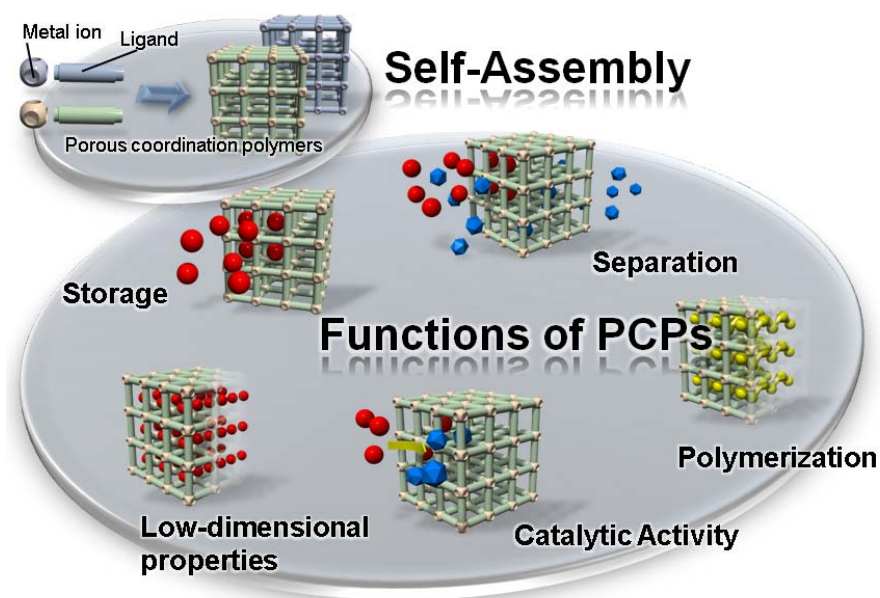


**Figure 1.** Porous coordination polymers (PCPs)

The inherent properties of PCPs are basically dominated by the chemical structures: pore size, pore surface functionality and framework topology. In that context, considerable effort has been devoted to synthesis of new compounds and evaluate these molecular-based properties at the early stage of this research field. In contrast, the macroscale structure is also one of crucial factors to sophisticate the properties, especially for separation efficiency, catalytic activity, and adsorption kinetics.<sup>17-18</sup> Furthermore, the morphology and size of PCPs strongly influenced on the cooperative phenomena such as magnetic transition<sup>19</sup> and structural transformation.<sup>20</sup> (Figure 2)

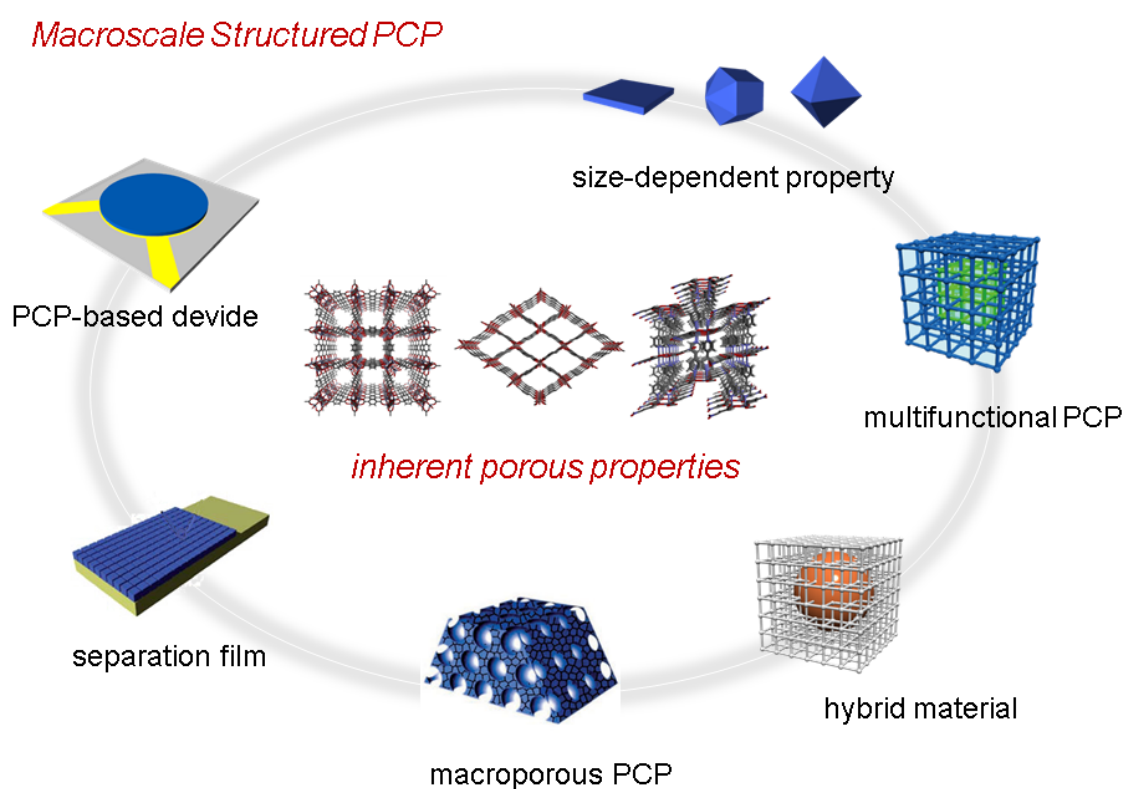


**Figure 2.** Macroscale structured PCP

The well-designed macroscale architectures of PCPs are generated from the assembly of individual components (metal ions and organic ligands). Firstly, the molecular structures of individual organic ligands are designed and the proper metal ions are chosen. Secondly, the organization of metal centers by connecting them with organic linkers leads to the construction of crystalline microporous frameworks. Thirdly, the spatial control of this crystallization process results in the macroscale architectures of PCPs. This structural hierarchy from individual components to the macroscale architectures can be divided into three structural classifications (Figure 3).

**Primary structure:** metal ions and molecular structures of organic ligands

The molecular structures of organic ligands can be precisely designed. The pore surface functionality, pore size and framework geometry are manipulated by chemical modification on organic ligands and careful choice of metal ions.

**Secondary structure:** crystalline microporous framework composed of metal ions and organic ligands

The self-assembly of metal ions and organic ligands results in construction of crystalline coordination frameworks. The coordination number of metal ions and molecular structures of organic ligands potentially determine the framework structures.

**Ternary structure:** Macroscale architectures of PCP crystals

The control of the crystal morphology, spatial position or assembly of crystals enable to construct macroscale structures such as membranes,<sup>21-22</sup> hollow particles,<sup>23</sup> three-dimensional superstructures<sup>24</sup> and hybrid particles.<sup>25-27</sup>

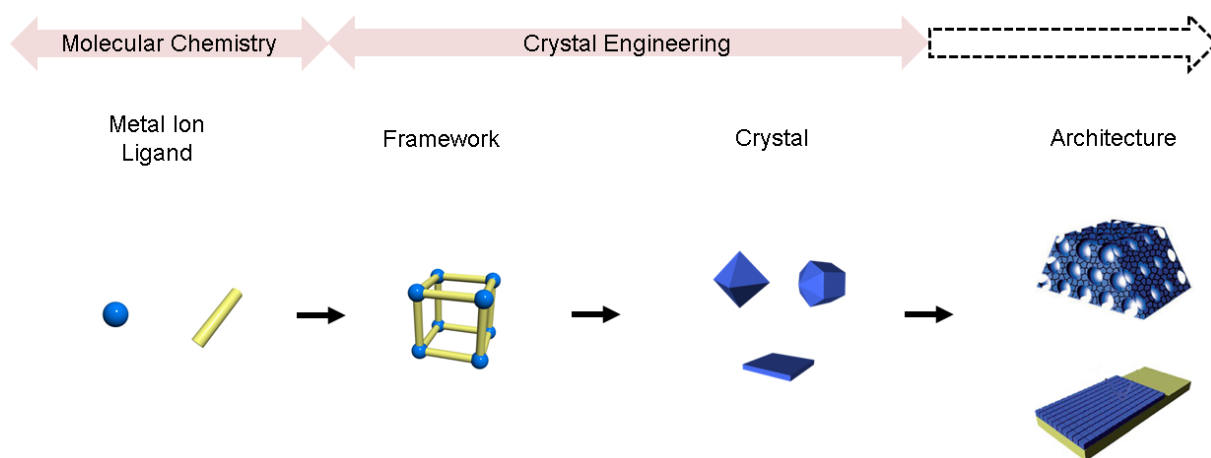


**Figure 3.** Structural hierarchy from individual components to macroscale structures of PCPs

The huge amount of accumulated knowledge in molecular chemistry and crystal engineering allows for designing the individual framework structures and crystalline particles; however, the development of methods to control the macroscale structures of PCPs are required in order to further sophisticate this material. Since PCPs are comprising of weak coordination bonds, top-down approaches including laser, heating and mechanical processing methods are often not suitable for fabricating the macroscale structures of PCPs. To control the macroscale structures of PCPs, three bottom-up approaches could be employed; chemical synthesis, templating and crystal assembly (Figure 4).

### 3. Macroscale structuralization of PCPs

Since PCPs are comprising of weak coordination bonds, top-down approaches including laser, heating and mechanical processing methods are not versatile method to fabricate the macroscale structures. Thus, three kinds of bottom-up approaches can be employed to design the macroscale structures of PCPs, chemical synthesis, templating and crystal assembly (Figure 3)

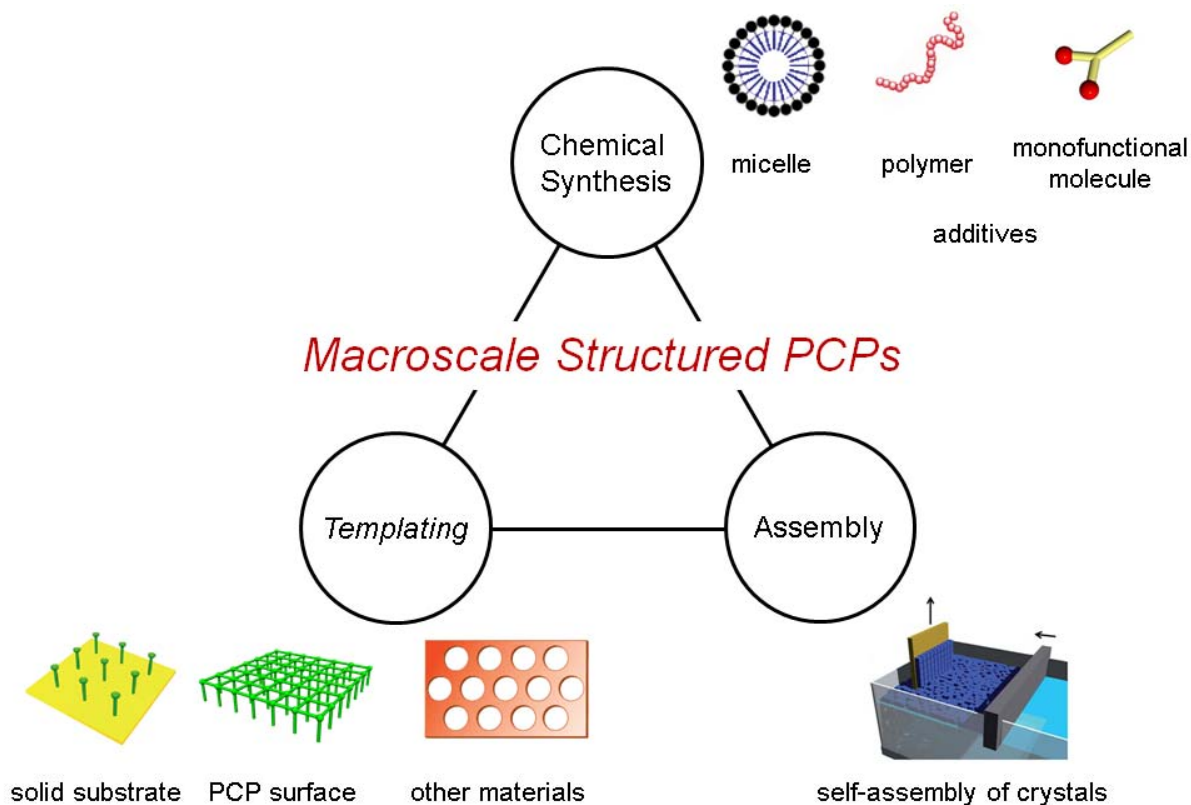


**Figure 4.** Three bottom-up approaches for macroscale structured PCPs

#### 3.1 Chemical Synthesis

Controlling the size or morphology of PCP crystals have attracted much attention due to the size-dependent characteristics for a variety of applications, including catalysis, spin-crossover, biomedical imaging, and drug-delivery. Several distinct approaches have recently been undertaken by exploring the possibility of controlling the shape and size of PCP crystals.

##### • Additives

One way to control the crystal size is adding functional molecules,<sup>28-29</sup> which

influence on the coordination equilibrium. Such additives like polymers and monofunctional molecules coordinate to metal ions or stabilize the precursors during nucleation or growth processes, consequently, the crystal size and morphology of PCPs are well controlled. For instances, uniform-sized PCP nanocrystals are fabricated; so-called coordination modulation method,<sup>29</sup> by altering the coordination equilibrium at the crystal surface during the growth process, through competitive interactions originating from a capping additive (modulator) with the same chemical functionality as the framework linker.

#### • **Confined crystallization**

Another technique for the preparation of nanocrystals is to spatially confine the crystallization. Water-in-oil,<sup>30</sup> or reverse microemulsions<sup>31</sup> are highly tailorable systems that consist of nanometer-sized water droplets stabilized by a surfactant in a predominantly organic phase. The micelles in the microemulsion essentially serve as “nanoreactors” that spatially restrict the particle formation. Thanks to the confinement of crystallization, the uniform-sized particles are obtained.

#### • **Instrument-assisted reaction**

Furthermore, some apparatus such as microwave and ultrasonicator are utilized for controlling the crystallization. The microwave-<sup>32</sup> and ultrasound-assisted methods<sup>33</sup> allow for the synthesis of nanocrystals. However, the size, shape and dimensionality of the nanocrystals are often not precisely controlled by using these methods. Hence, ultrasound-assisted methods combining with microemulsion has been developed to prevent the formation of amorphous coordination polymer particles.<sup>34</sup> The microwave-assisted conditions with coordination modulation method<sup>35</sup> is also a promising way to prepare the uniform-sized crystals with keeping the crystallinity.

### **3.2 Templating**

One of key principles to fabricate macroscale architectures is to control the spatial positions of the materials. Thus, spatial control of PCP crystals is traditionally performed by using templates, which induce the crystallization or support the architectures of deposited crystals. The increasing number of reports that focus on the processing of PCPs into thin films, two-dimensional patterns and spheres accounts for the significance of their integration into directly applicable materials.

#### • **Solid substrate**

The methods to prepare well-defined crystalline layers on a given substrate enable to integrate the PCPs into functional devices. Roland Fischer and his co-workers firstly reported the immobilization of MOF-5 thin film on a gold substrate.<sup>36</sup> Nowadays, the methodologies to synthesize PCP films on substrates are well developed<sup>37-38</sup> and the film thickness and channel orientations can be precisely controlled.<sup>39</sup> This development enabled fabrication of PCPs on electronic devices such as microcantilever,<sup>40</sup> Fabry-Pérot interference<sup>41</sup> and quartz crystal microbalance,<sup>42</sup> leading to PCP-based sensors. In addition to the device applications, the gas separation efficiency of PCP thin film is intensively studied.<sup>43-44</sup>

#### • **PCP surface**

PCPs also offer the opportunity of being utilized as molecular-based crystalline substrates for the assembly of functional molecules on their surfaces. By employing this features, second PCPs can be grown on the crystal surface of core PCPs through epitaxial growth, forming core-shell type PCPs.<sup>25-27</sup> Such heterogeneous structured PCPs enable multifunctionality even when two contradictory properties are combined, such as small and large pore sizes providing a simultaneous size selectivity and storage.<sup>45</sup>

#### • **Other materials**

Other templates, polymer particles<sup>46</sup> microdroplet,<sup>23</sup> or metaloxide can be also utilized to create the macroscale structures. The formation of PCPs on the sphere templates and the elimination of the templates resulted in hollow PCPs. More complicated 3D templates enable the 3D structures of PCPs. In particular, 3D ordered macroporous structures endows the resulting materials with an additional optical element or improve the separation efficiency.<sup>47-48</sup> Furthermore, the formation of PCPs on the surface of other materials often gives core-shell type hybrid particles, for instances, metallic nanoparticles as a core and PCP as a shell.

### **3.3 Assembly**

A wide variety of methods to design the crystal shapes and morphologies are developed. Challenges related to making the complex structures using PCP crystals as building blocks emerged. PCP superstructures offer even greater variety of nano/microscale systems than individual PCPs and enable investigations of collective behavior/properties. Some pioneering researches on PCP crystals assemblies came out

recently.<sup>49-50</sup> The assembled structures of PCP crystals will likely facilitate integration with microscale technologies such as sensor devices or stimuli-responsive optoelectronic materials.

## 4. Survey of this Thesis

The purpose of this thesis is to establish methods to fabricate the macroscale structures of PCPs. The templating methods were employed to create the core-shell, hollow and membrane structures of PCPs.

**Chapter 1** describes the fabrication of a core-shell PCP by epitaxial growth. All crystal surfaces of the core crystal,  $[\text{Zn}_2(\text{bdc})_2(\text{dabco})]_n$ , was covered by the shell crystal,  $[\text{Cu}_2(\text{bdc})_2(\text{dabco})]_n$  (bdc = 1,4-benzenedicarboxylate, dabco = 1,4-diazabicyclo[2,2,2]octane). Synchrotron X-ray diffraction measurements unveiled the structural relationship between the shell and core crystal, where in-plane rotational epitaxial growth compensates the difference in lattice constant (Figure 4).

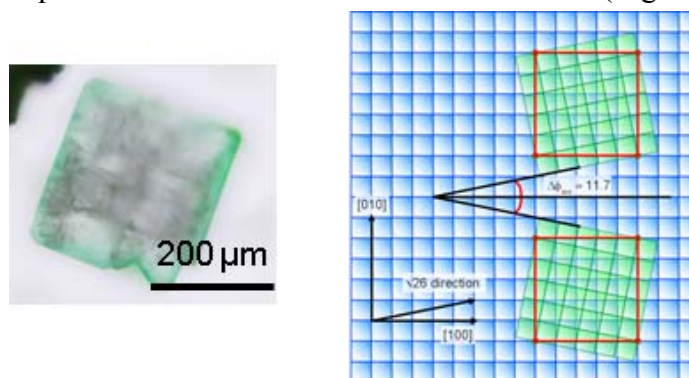


**Figure 4.** Heterometallic core-shell type PCP

**Chapter 2** describes the fabrication of sandwich type crystal;  $[\text{Zn}_2(\text{ndc})_2(\text{dabco})]_n$  as the core crystal and  $[\text{Zn}_2(\text{ndc})_2(\text{dpndi})]_n$  as the second crystal, (ndc = 1,4-naphthalenedicarboxylate, dabco = 1,4-diazabicyclo[2,2,2]octane, dpndi = *N,N'*-di(4-pyridyl)-1,4,5,8-naphthalenetetracarboxydiimide). The secondary crystal growth at the {100} surfaces of the core crystal was prohibited because of the mismatch of molecular lengths between dabco and dpndi. The second crystal,  $[\text{Zn}_2(\text{ndc})_2(\text{dpndi})]_n$  is grown only at the {001} surfaces that consists of the common component, ndc (Figure 5).

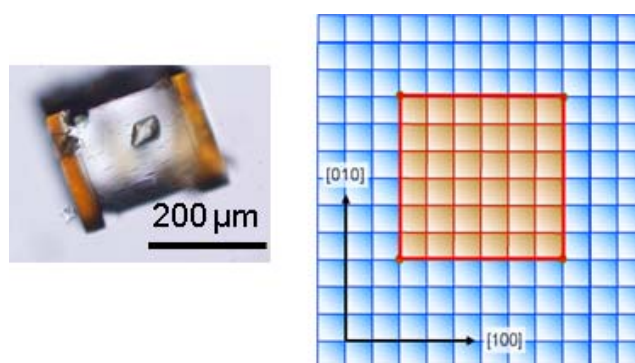


**Figure 5.** Heteroligand sandwich type PCP

**Chapter 3** describes the heterostructured PCP crystal fabricated using epitaxial growth simultaneously process two contradictory porous functions, size selectivity and high storage. The framework is grown using small pores as a shell around the isorecticular core framework, which has large pores on the micrometre scale for a single crystal. The core/shell crystal not only perfectly extracted the linear petroleum molecule of hexadecane (cetane) from a mixture with its branched isomer isocetane, even when the cetane was present at a very low concentration (1 wt %), but also showed improved accumulation of the molecules in its pores (Figure 6).

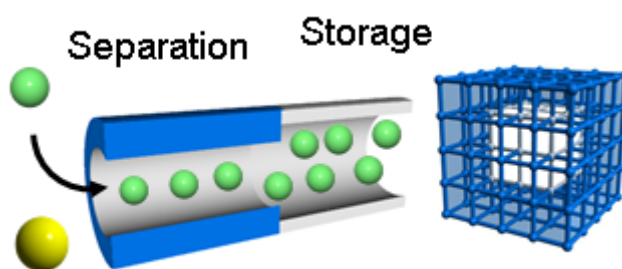


**Figure 6.** Selective storage of alkane isomers based on core-shell PCP

**Chapter 4** describes the synthesis of a core-shell type PCP:  $[\text{Zn}_2(\text{adc})_2(\text{dabco})]_n$  as the core crystal and  $[\text{Zn}_2(\text{abdc})_2(\text{dabco})]_n$  as the shell crystal (adc = 9,10-anthracene dicarboxylate, dabco = diazabicyclo[2.2.2]octane, abdc = 2-amino-1,4-benzene dicarboxylate). After the formation of the core-shell structure, a free carboxyl group was embedded in the shell crystal via heterogeneous acylation of amino groups with succinic anhydride to enhance the selectivity for *N,N*-dimethylaniline (DMA). The shell crystal allowed the core crystal to selectively accommodate DMA, thus leading to turning on intense exciplex emission by the formation of excited state between anthracene moiety and DMA (Figure 7).

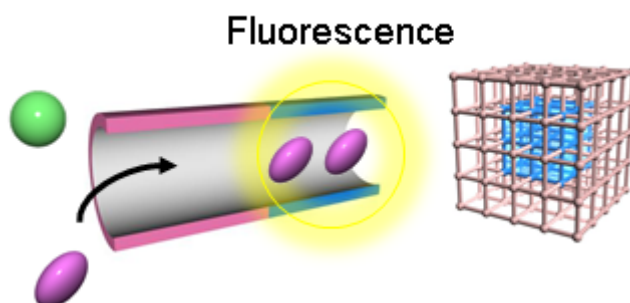


**Figure 7.** Guest-responsive fluorescence based of core-shell PCP

**Chapter 5** describes hybridization of two-dimensional (2D) PCP:  $[\text{Zn}_2(\text{NO}_2\text{-ip})_2(\text{dpndi})]_n$  as the core crystal and  $[\text{Zn}_2(\text{NO}_2\text{-ip})_2(\text{bpy})]_n$  as the shell crystal ( $\text{NO}_2\text{-ip}$  = 5-nitroisophthalate,  $\text{dpndi}$  =  $N,N'$ -di(4-pyridyl)-1,4,5,8-naphthalenetetracarboxydiimide,  $\text{bpy}$  = 4,4'-bipyridyl). Whereas the epitaxial growth on the core crystal leads to a sandwich type PCP, the ligand replacement nearby surface of the core crystal results in a core-shell type PCP (Figure 8).

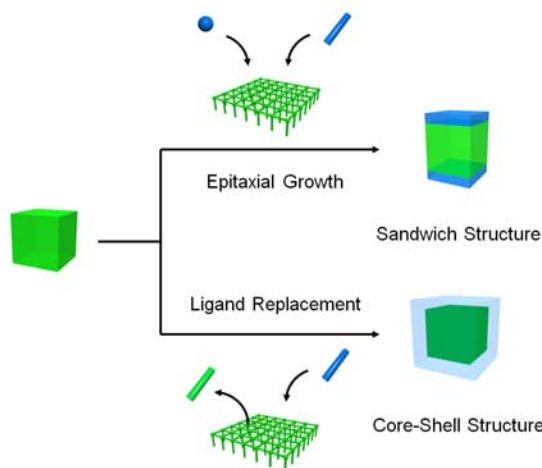


**Figure 8.** Hybridized 2D PCPs for modulating gate-opening pressure

**Chapter 6** describes a new phenomenon, in which the macropore is formed inside the crystal synchronized with the generation of solid-solution type PCPs. As a result, a box-shaped architecture consisting of solid-solution type PCP is synthesized. The ligand exchange results in the conversion of framework topology from not-interpenetrated to interpenetrated structures. The interpenetration stabilizes the framework and improve the uptake amount of  $\text{CO}_2$ , furthermore, the hollow structure enhances the diffusion kinetics of  $\text{CO}_2$ . This phenomenon is derived from the differences in the transported amounts of two organic ligands during dissolution of pre-existing PCP and crystallization of a new solid-solution PCP (Figure 9).

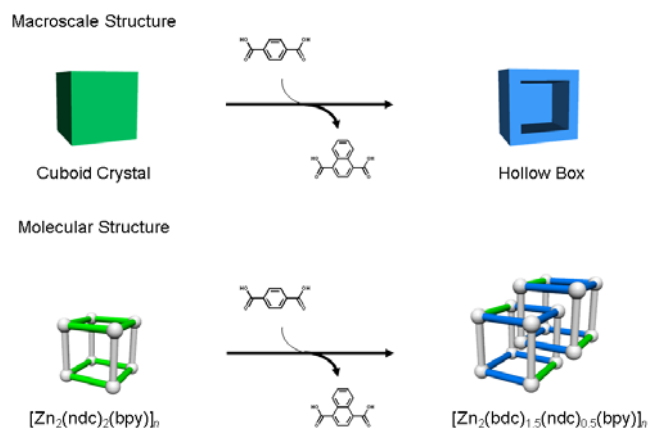


**Figure 9.** Synchronic transformation across chemical and macroscale structures

**Chapter 7** describes the synthesis of a series of 1,1'-ferrocenedicarboxylate(Fcdc)-based 2D PCPs by incorporating different diamine coligands,  $[\text{Zn}(\text{Fcdc})(\text{bpy})]_n$ ,  $[\text{Zn}(\text{Fcdc})(\text{bpb})]_n$  and  $[\text{Zn}(\text{Fcdc})(\text{bpy})]_n$ , (dpb = 1,4-di(pyridin-4-yl)benzene, dpndi =  $N,N'$ -di(4-pyridyl)-1,4,5,8-naphthalenetetracarboxydiimide),. The compounds immobilized on electrodes, exhibited reversible redox reactions, arising from ferrocenyl moiety (Figure 10).

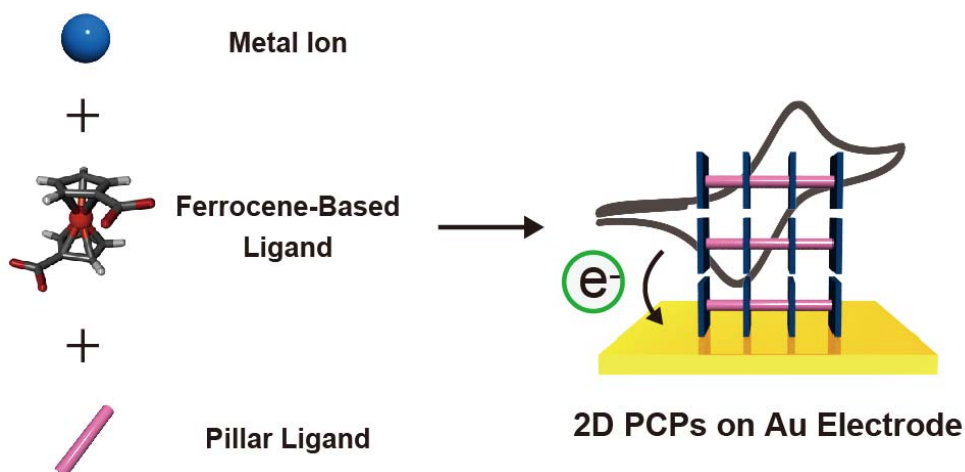


**Figure 10.** Redox reaction of PCP membranes

**Chapter 8** describes the integration of flexible PCPs with quartz crystal microbalance (QCM), creating hybrid gas sensor. Since the guest uptake leads to weight gain of the PCPs, depositing flexible PCPs onto QCM, in which the mass change is converted to a change of oscillation frequency, enables the quantitatively detect specific molecules. The crystal orientation was controlled and the diffusion of organic vapor was clearly enhanced, thus leading to quick response to the organic vapor by the change of oscillation frequency of QCM (Figure 11).

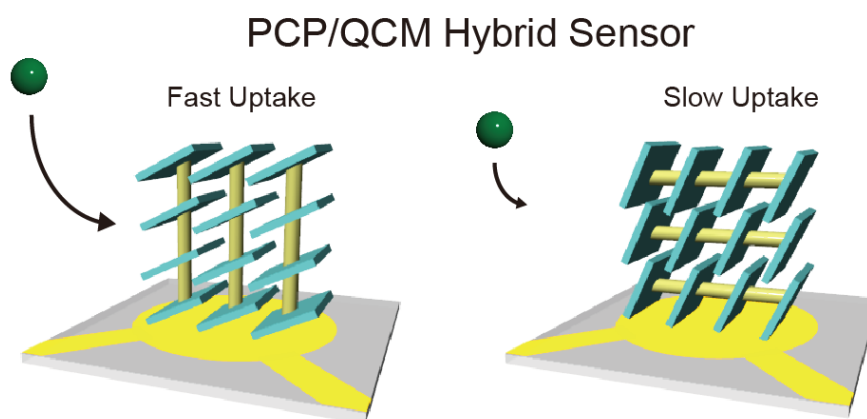


**Figure 11.** PCP/QCM hybrid sensor

## References

- (1) P. A. Alivisatos, *Science* **1996**, *271*, 933-937.
- (2) R. Yan, D. Gargas, P. Yang, *Nature Photon.* **2009**, *3*, 569-576.
- (3) Y. Wu, J. Xiang, C. Yang, W. Lu, C. M. Lieber, *Nature* **2004**, *430*, 61-65.
- (4) H. Matsubara, S. Yoshimoto, H. Saito, Y. Jianglin, Y. Tanaka, S. Noda, *Science* **2008**, *319*, 445-447.
- (5) S. Noda, K. Tomoda, N. Yamamoto, A. Chutinan, *Science* **2000**, *289*, 604-606.
- (6) R. Matsuda, R. Kitaura, S. Kitagawa, Y. Kubota, R. V. Belosludov, T. C. Kobayashi, H. Sakamoto, T. Chiba, M. Takata, Y. Kawazoe, Y. Mita, *Nature* **2005**, *436*, 238-241.
- (7) M. Dincă, A. Dailly, Y. Liu, C. M. Brown, D. A. Neumann, J. R. Long, *J. Am. Chem. Soc.* **2006**, *128*, 16876-16883.
- (8) S. Ma, D. Sun, M. Ambrogio, J. A. Fillinger, S. Parkin, H.-C. Zhou, *J. Am. Chem. Soc.* **2007**, *129*, 1858-1859.
- (9) L. Alaerts, C. E. A. Kirschhock, M. Maes M. A. van der Veen, V. Finsy, A. Depla, J. A. Martens, G. V. Baron, P. A. Jacobs, J. F. M. Denayer, D. E. De Vos, *Angew. Chem. Int. Ed.* **2007**, *46*, 4293-4297.
- (10) K. Nakagawa, D. Tanaka, S. Horike, S. Shimomura, M. Higuchi, S. Kitagawa, *Chem. Commun.* **2010**, *46*, 4258-4260.
- (11) J. S. Seo, D. Whang, H. Lee, S. I. Jun, J. Oh, Y. J. Jeon, K. Kim, *Nature* **2000**, *404*, 982-986.
- (12) C.-D. Wu, A. Hu, L. Zhang, W. Lin, *J. Am. Chem. Soc.* **2005**, *127*, 8940-8941.
- (13) S. Hasegawa, S. Horike, R. Matsuda, S. Furukawa, K. Mochizuki, Y. Kinoshita, S. Kitagawa, *J. Am. Chem. Soc.* **2007**, *129*, 2607-2614.
- (14) T. Uemura, S. Horike, S. Kitagawa, *Chem. Asian. J.* **2006**, *1*, 36-44.
- (15) M. D. Allendorf, C. A. Bauer, R. K. Bhakta and R. J. T. Houk, *Chem. Soc. Rev.*, **2009**, *38*, 1330-1352.
- (16) Y. Takashima, V. M. Martinez, S. Furukawa, M. Kondo, S. Shimomura, H. Uehara, M. Nakahama, K. Sugimoto, S. Kitagawa, *Nature Commun.*, **2011**, *2*, 168.
- (17) S. H. Jhung, J. H. Lee, J. W. Yoon, C. Serre, G. Férey, J. S. Chang, *Adv. Mater.* **2007**, *19*, 121-124.
- (18) D. Tanaka, A. Henke, K. Albrecht, M. Moeller, K. Nakagawa, S. Kitagawa, J. Groll, *Nature Chem.* **2010**, *2*, 410-416.
- (19) I. Boldog, A. B. Gaspar, V. Martínez, P. Pardo-Ibañez, V. Ksenofontov, A. Bhattacharjee, P. Gülich, J. A. Real, *Angew. Chem. Int. Ed.* **2008**, *47*, 6433-6437.

- (20) Y. Sakata, S. Furukawa, M. Kondo, K. Hirai, N. Horike, Y. Takashima, H. Uehara, N. Louvain, M. Meilikhov, T. Tsuruoka, S. Isoda, W. Kosaka, O. Sakata, S. Kitagawa, *Science* **2012**, *in press*
- (21) D. Zacher, O. Shekhah, C. Wöll, R. A. Fischer, *Chem. Soc. Rev.* **2009**, *38*, 1418-1429.
- (22) L. Yang, S. Kinoshita, T. Yamada, S. Kanda, H. Kitagawa, M. Tokunaga, T. Ishimoto, T. Ogura, R. Nagumo, A. Miyamoto, M. Koyama, *Angew. Chem. Int. Ed.* **2010**, *49*, 5348-5531.
- (23) R. Ameloot, F. Vermoortele, W. Vanhove, M. B. J. Roeffaers, B. F. Sels, D. E. De Vos., *Nature Chem.* **2011**, *3*, 382-387.
- (24) Y. Wu, F. Li, W. Zhu, J. Cui, C. Tao, C. Lin, P. M. Hannam, G. Li, *Angew. Chem. Int. Ed.* **2011**, *50*, 12518-12522
- (25) S. Furukawa, K. Hirai, K. Nakagawa, Y. Takashima, R. Matsuda, T. Tsuruoka, M. Kondo, R. Haruki, D. Tanaka, H. Sakamoto, S. Shimomura, O. Sakata, S. Kitagawa, *Angew. Chem. Int. Ed.* **2009**, *48*, 1766-1770.
- (26) S. Furukawa, K. Hirai, Y. Takashima, K. Nakagawa, M. Kondo, T. Tsuruoka, O. Sakata, S. Kitagawa, *Chem. Commun.* **2009**, 5077-5079.
- (27) K. Koh, A. G. Wong-Foy, A. J. Matzger, *Chem. Commun.* **2009**, 6162-6164.
- (28) T. Uemura, S. Kitagawa, *J. Am. Chem. Soc.* **2003**, *125*, 7814-7815.
- (29) T. Tsuruoka, S. Furukawa, Y. Takashima, K. Yoshida, S. Isoda, S. Kitagawa, *Angew. Chem. Int. Ed.* **2009**, *48*, 4739-4743.
- (30) S. Vaucher, J. Fielden, M. Li, E. Dujardin, S. Mann, *Nano Lett.* **2002**, *2*, 225-229.
- (31) S. Vaucher, M. Li, S. Mann, *Angew. Chem. Int. Ed.* **2000**, *39*, 1793-1796.
- (32) Z. Ni, R. I. Masel, *J. Am. Chem. Soc.* **2006**, *128*, 12394-12395.
- (33) Z. Q. Li, L. G. Qiu, T. Xu, Y. Wu, W. Wang, Z. Y. Wu, X. Jiang, *Mater. Lett.* **2009**, *63*, 78-80.
- (34) K. M. L. Taylor, A. Jin, W. Lin, *Angew. Chem. Int. Ed.* **2008**, *47*, 7722-7725.
- (35) S. Diring, S. Furukawa, Y. Takashima, T. Tsuruoka, S. Kitagawa, *Chem. Mater.* **2010**, *22*, 4531-4538.
- (36) S. Hermes, F. Schröder, R. Chelmowski, C. Wöll, R. A. Fischer, *J. Am. Chem. Soc.* **2005**, *127*, 13744-13745.
- (37) P. Horcajada, C. Serre, D. Grosso, C. Boissière, S. Perruchas, C. Sanchez, G. Férey, *Adv. Mater.* **2009**, *21*, 1931-1935.
- (38) E. Biemmi, C. Scherb, T. Bein, *J. Am. Chem. Soc.* **2007**, *129*, 8054-8055.
- (39) O. Shekhah, H. Wang, T. Strunskus, P. Cyganik, D. Zacher, R. Fischer, C. Wöll, *Langmuir* **2007**, *23*, 7440-7442.

- (40) M. D. Allendorf, R. J. T. Houk, L. Andruszkiewicz, A. A. Talin, J. Pikarsky, A. Choudhury, K. A. Gall, P. J. Hesketh, *J. Am. Chem. Soc.* **2008**, *130*, 14404-14405.
- (41) L. E. Kreno, J. T. Hupp, R. P. Van Duyne, *Anal. Chem.* **2010**, *82*, 8042-8046.
- (42) E. Biemmi, A. Darga, N. Stock, T. Bein, *Micropor. Mesopor. Mater.* **2008**, *114*, 380-386.
- (43) H. Bux, F. Liang, Y. Li, J. Cravillon, M. Wiebcke, J. Caro, *J. Am. Chem. Soc.* **2009**, *131*, 16000-16001.
- (44) S. R. Venna, M. A. Carreon, *J. Am. Chem. Soc.* **2010**, *132*, 76-78.
- (45) K. Hirai, S. Furukawa, M. Kondo, H. Uehara, O. Sakata, S. Kitagawa, *Angew. Chem. Int. Ed.* **2011**, *50*, 8057-8061.
- (46) H. J. Lee, W. Cho, M. Oh, *Chem. Commun.* **2012**, *48*, 221-223.
- (47) Y. Wu, F. Li, W. Zhu, J. Cui, C. Tao, C. Lin, P. M. Hannam, G. Li, *Angew. Chem. Int. Ed.* **2011**, *50*, 12518-12522.
- (48) J. Reboul, S. Furukawa, N. Horike, M. Tsotsalas, K. Hirai, H. Uehara, M. Kondo, N. Louvain, O. Sakata, S. Kitagawa, *Nature Mater.* **2012**, *11*, 717-723.
- (49) M. Tsotsalas, A. Umemura, F. Kim, Y. Sakata, J. Reboul, S. Kitagawa, S. Furukawa, *J. Mater. Chem.* **2012**, *22*, 10519-10165.
- (50) N. Yanai, S. Granick, *Angew. Chem. Int. Ed.* **2012**, *51*, 5638-5641.



## Chapter 1

# Heterogeneously Hybridized Porous Coordination Polymer Crystals: Fabrication of Heterometallic Core–Shell Single Crystals with an In-Plane Rotational Epitaxial Relationship

### Abstract

Porous coordination polymers (PCPs) or metal–organic frameworks (MOFs) have attracted considerable attention due to their wide variety of scientific and technological applications, such as adsorption, separation, and catalysis. Over the past decade, the chemical functionalization of PCP framework scaffold has been intensively studied to improve their properties. The promising strategy to develop the PCP property is to integrate several framework structures, thus several functions, into one crystal – so called, hybridized PCP crystals. This class of hybridized PCP crystals allows for systematically tuning the framework composition of both metal ions and designed organic ligands, which especially influences the spatial configuration of crystals and their structural relationship, leading to the novel porous property that single PCP framework never achieves. Here we demonstrate fabrication of a core-shell porous coordination polymer crystal at the single-crystal level by epitaxial growth in solution. All crystal surfaces of the core crystal,  $[\text{Zn}_2(\text{bdc})_2(\text{dabco})]_n$  (**1**), was covered by the shell crystal,  $[\text{Cu}_2(\text{bdc})_2(\text{dabco})]_n$  (**2**) (bdc = 1,4-benzenedicarboxylate, dabco = 1,4-diazabicyclo[2,2,2]octane). Synchrotron X-ray diffraction measurements unveiled the structural relationship between the shell crystal and the core crystal, where in-plane rotational epitaxial growth compensates the difference in lattice constant.

## Introduction

The formation of interfaces between two solid phases is of great significance in the development of new materials, because mechanical and electronic properties of materials are strongly influenced by distorted interfacial structures, leading to properties that differ from those of the individual phases. Moreover, properties of porous materials, such as gas sorption and guest-molecule accommodation, should also correlate with the interfacial structure of such materials, because guest molecules (adsorbates) first encounter the surface of the porous materials. Hence, the affinity of porous materials for guest molecules can be tuned by modifying the surface structure.<sup>1</sup> Porous coordination polymers (PCPs), or metal–organic frameworks (MOFs), are an interesting class of crystalline porous materials, as it is possible to design their framework topologies and pore sizes and the functionality of the pore surfaces.<sup>2-6</sup> Recent progress of the “post-synthetic approach” allows for the pore-surface functionalities (on the inner surfaces of materials) to be altered after the lattice is constructed.<sup>7-16</sup> On the other hand, functionalization of PCP outer surfaces is a great challenge, but it is a promising methodology not only for modification of the porous properties but also for the addition of a new function to the PCP without changing the characteristic features of the PCP crystal itself,<sup>17</sup> resulting in the fabrication of multifunctional PCPs. One way to decorate the crystal surfaces of a PCP is to hybridize the core PCP crystal with a different shell crystal by epitaxial growth at the single-crystal level, thus creating core-shell PCP heteroepitaxial crystals. Such a lattice match promises pore connections at the interface between crystals, where the modified crystal structure should influence the mobility and diffusion of adsorbates. Such fabrication of hybridized PCP single crystals in the nanometer or micrometer regime also allows for utilization of these materials in biological systems and as sensors in electronic devices.<sup>17-23</sup> Although a few pioneering synthetic studies on the hybridization of extended coordination structures have been reported,<sup>24-27</sup> structural determination at the interfaces is not yet known, most likely because of the lack of a methodology, despite its significance for the design of new materials. Herein, we demonstrate the first synthesis of core–shell PCP single crystals by epitaxial growth; the structural relationship between the shell and the core was determined using surface X-ray diffraction analysis. The key to success is to choose excellent candidates for epitaxial growth, such as the  $[M_2(\text{dicarboxylate})_2(\text{N-ligand})]_n$  series of PCP frameworks, wherein three components, namely the metal ions, dicarboxylate layer ligands, and bidentate nitrogen pillar ligands, can be varied without changing the original tetragonal topology (Figure 1).<sup>24-36</sup> A variety of isorecticular

tetragonal frameworks with similar unit cell parameters are available. The heterometallic system chosen for hybridization consists of different metal ions with the same organic ligands:  $[\text{Zn}_2(\text{ndc})_2(\text{dabco})]_n$ <sup>32</sup> (**1**) as the core crystal and  $[\text{Cu}_2(\text{ndc})_2(\text{dabco})]_n$ <sup>35</sup> (**2**) as the shell crystal (ndc = 1,4-naphthalene dicarboxylate, dabco = 1,4-diazabicyclo[2.2.2]octane). Note that **1** can be grown as a single crystal with cubic morphology at a scale of hundreds of micrometers, but **2** gives only microcrystalline powder. Therefore, synthesis of the reverse composition is essentially impossible. To elucidate the growth process of the core crystal **1**, faceindex analysis was carried out using single-crystal X-ray diffraction. The tetragonal framework appears as a right rectangular prism crystal with (100), (100), (010), (010), (001), and (001) faces. The four (*h*00) and (0*k*0) surfaces can be end-capped by the layer carboxylic acid groups, whereas the two remaining (00*l*) surfaces are terminated by the nitrogen pillar ligands. These ligands can be used as coordination sites to grow the shell crystal.

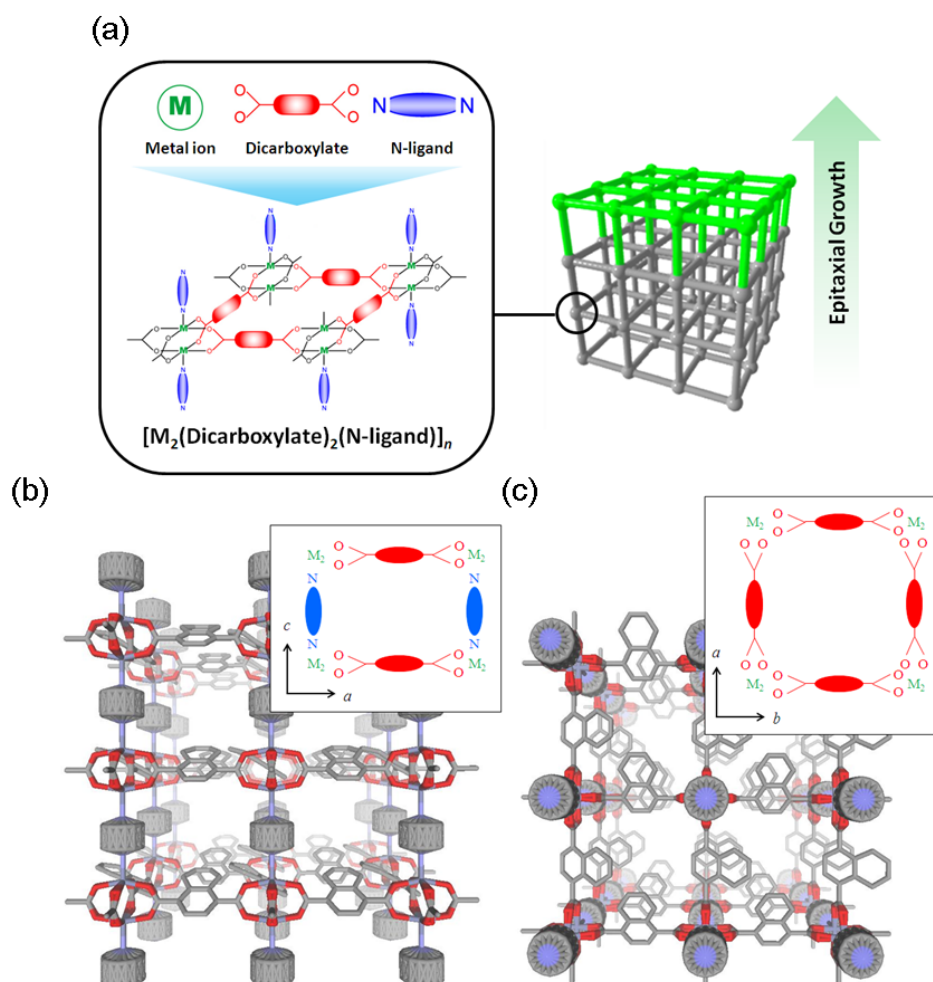


**Figure 1.** (a) The schematic illustration of the series of frameworks,  $[\text{M}_2(\text{dicarboxylate})_2(\text{N-ligand})]_n$ . The crystal structure of **1**; (b) the view from *a* axis, and (c) the view from *c* axis. The naphthalene moieties are disordered due to the symmetry.

## Results and Discussion

The hybridization of two frameworks into one single crystal has been successfully achieved by a simple solvothermal synthesis; pieces of single crystals of **1** were put into a solution of  $\text{CuSO}_4 \cdot 5\text{H}_2\text{O}$ , 1,4-naphthalene dicarboxylic acid, and dabco in toluene/methanol (1:1), and the solution was heated to 393 K. The core-shell crystals (**1/2**) were obtained as light greenish cubic crystals in 93% yield. Figure 2a shows an optical microscopy image of the sliced single crystal of **1/2**. The colorless core crystal is surrounded by the greenish shell crystal. Each part of the core-shell crystal was analyzed by microscopic attenuated total reflectance (ATR) IR spectroscopy. The characteristic carboxylate asymmetric stretching frequencies of **1/2** (core:  $1633\text{ cm}^{-1}$ , shell:  $1621\text{ cm}^{-1}$ ) resemble those of **1** ( $1629\text{ cm}^{-1}$ ) and **2** ( $1621\text{ cm}^{-1}$ ), respectively. The lower absorption energy of zinc-coordinated carboxylate relative to copper-coordinated carboxylate can be explained by the strength of carboxylate coordination; copper is coordinated more strongly than zinc.<sup>37-38</sup> Note that the multiple absorption bands around  $800\text{ cm}^{-1}$ , which can be assigned to the out-of-plane CH bending vibration modes and the ring bending mode of the naphthalene moieties of ndc,<sup>39</sup> exhibit a trend similar to the carboxylate stretching (Figure 2b–d): quadruple bands for the core and **1**; triplet bands for the shell and **2**. Both the core crystal (**1**) and the shell crystal (**2**) have the same tetragonal space group ( $P4/mmm$ ) and similar unit cell parameters ( $a = 10.921(1)$ ,  $c = 9.611(1)$  for **1**, and  $a = 10.8190(3)$ ,  $c = 9.6348(6)$  for **2**), which differ enough, especially along the  $a$  axis, to distinguish the shell crystal from the core crystal and to allow investigation of the structural correlation between them. Synchrotron X-ray measurements for film structural analysis were, therefore, performed using a four-circle diffractometer at beamline BL13XU for surface and interface structures, SPring-8.

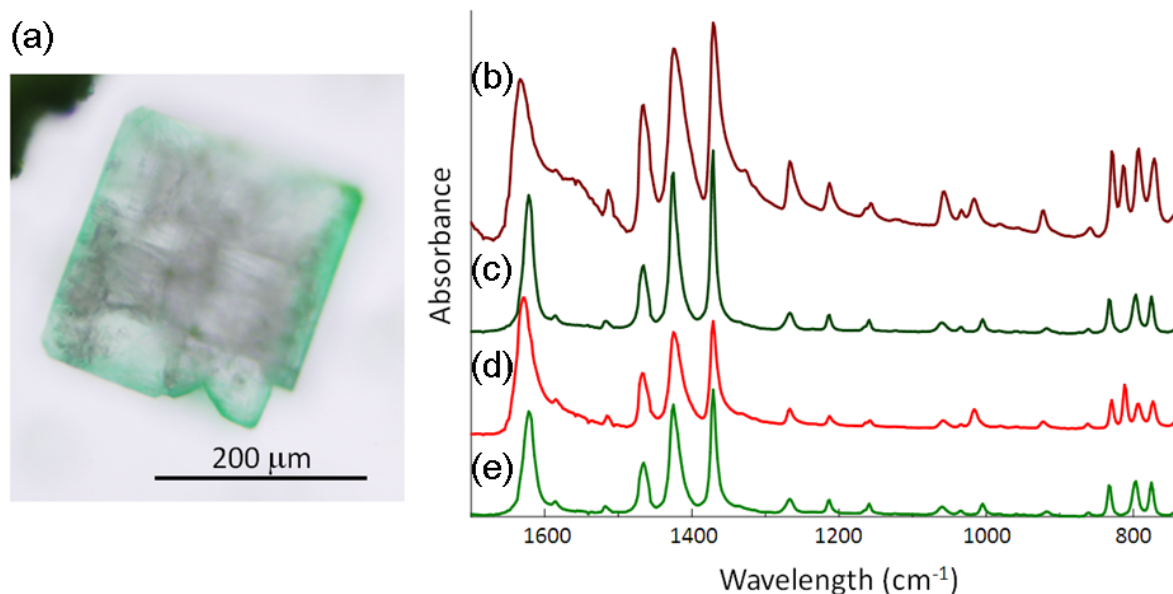


**Figure 2.** a) The optical microscopic image of the sliced core/shell crystal, **1/2**. b) The infrared spectrum by microscopic attenuated total reflection (ATR) measurement of the colorless part of **1/2**, c) the greenish part of **1/2**, d) the powder sample of **1**, and e) the powder sample of **2**.

A hybridized core–shell crystal of **1/2** with a size greater than 200  $\mu\text{m}$  and a shell crystal thickness greater than 20  $\mu\text{m}$  was fixed on a glass surface with the *a* axis normal to the glass surface, and diffractions were recorded using an X-ray beam with a size of 15  $\times$  30  $\text{mm}^2$ . The  $\theta$ – $2\theta$  scan of **1/2** from the initial position ( $\chi = 90^\circ$ ) provided two sharp peaks assigned to *h*00 Bragg peaks, and a scan of the rotation angle around the [100] direction (the  $\phi$  scan) at the 110 Bragg position gave two sharp peaks assigned to the 110 and  $\bar{1}\bar{1}0$  Bragg peaks (Figure 3a–c). These diffraction peaks indicate that the shell crystal of **1/2** is a single crystal. This finding indicates, surprisingly, that growth of the copper shell crystal (**2**) as a single crystal on the surface of the zinc core crystal (**1**) was supported despite the fact that the copper shell crystal had only been obtained previously as a powder.

The structural relationship between the core crystal and the shell crystal at the interface is more evident at the (001) surface, because the diffractions from the two crystals are observed simultaneously. Note that the (001) surface of the tetragonal space group can be recognized as the quadratic lattice shown in Figure 1 c, because the *a* and *b* lattice constants are the same. The hybridized crystal (**1/2**) was mounted with the *c* axis normal to the glass surface. While the  $\theta$ – $2\theta$  scan gave the 00*l* Bragg peaks, characteristic triplet peaks were observed periodically every  $90^\circ$  in the scan of rotation angle around [001] (the  $\phi$  scan) at the 101 position (Figure 3d–f). Corresponding to the model in the

reciprocal lattice space (Figure 4a), the  $k$  scan at the 101 position and the  $h$  scan at the 011 position also gave triplet peaks (Figure 4b–c). Each central peak of the triplet can be assigned to the 101 and 011 Bragg peaks of the core crystal (**1**), whereas the two side peaks are assigned to diffraction from the shell crystal (**2**). This situation arises because the refined  $2\theta$  angles of the side peaks ( $2\theta_{\text{side}} = 8.1864\text{--}8.1997$ ) are significantly larger than those of the central peaks ( $2\theta_{\text{central}} = 8.1136\text{--}8.1170$ ), which coincides with the fact that the lattice constant  $a$  of **2** is smaller than that of **1**.

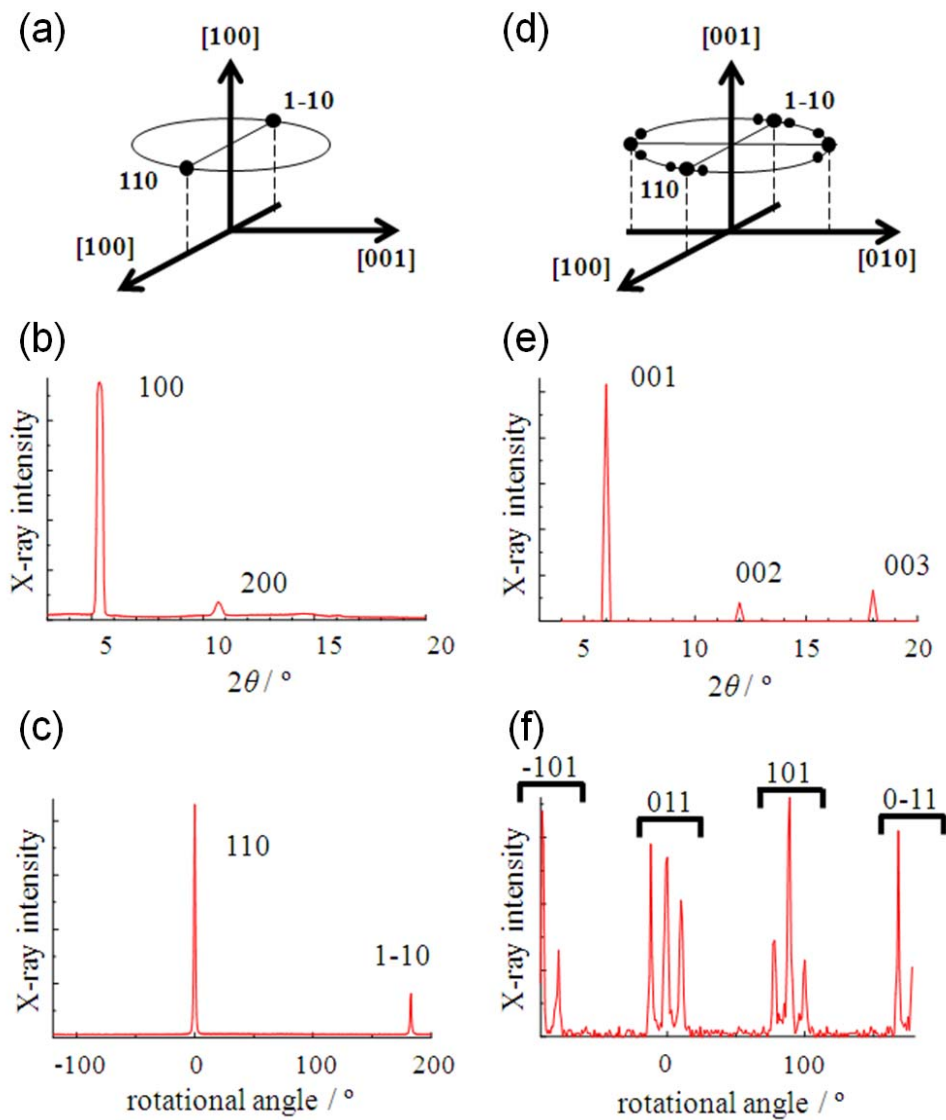


**Figure 3.** The reciprocal lattice space corresponding to the rotational scan, (a) around the [100] direction, and (d) around the [001] direction. The  $\theta$ - $2\theta$  scan of the core/shell crystal (**1/2**) immobilized on the glass substrate at the initial position ( $\chi = 90^\circ$ ), (b) with the  $a$  axis orientation, and (e) with the  $c$  axis orientation. The scan of the rotation angle, (c) around the [100] direction (the  $\phi$  scan), and (f) around the [001] direction.

**Table 1.** The refined angles of  $2\theta$ ,  $\chi$ , and  $\phi$  at the 100, and 110 Bragg positions of the core crystal, **1**, and the core/shell crystal, **1/2** for the a axis orientation, and at the 001, 101, and 011 Bragg position of **1/2** for the c axis orientation.

Crystal	Bragg position	$2\theta$	$\chi$	$\phi$ ( $\Delta\phi$ ) <sup>[a]</sup>
<b>1</b> (a oriented)	100	5.2733	90.286	—
	110	7.4616	44.914	0
<b>1/2</b> (a oriented)	100	5.3140	87.957	—
	110	7.5181	45.656	-0.117
<b>1/2</b> (c oriented)	001	6.0194	89.753	—
	101 <sub>central</sub>	8.117	47.634	0.8620
	101 <sub>side1</sub>	8.1989	47.1202	12.5533 (11.6913)
	101 <sub>side2</sub>	8.1902	46.9784	-10.6010 (11.4630)
	011 <sub>central</sub>	8.1136	47.5630	-87.9900
	011 <sub>side1</sub>	8.1997	47.0458	-100.2938 (12.3038)
	011 <sub>side2</sub>	8.1864	46.8704	-76.8410 (11.1490)

[a] The difference of the  $\phi$  angle of the side peak from the central peak,  $\Delta\phi = |\phi_{\text{side}} - \phi_{\text{central}}|$ .

The difference in  $\phi$  angle of the side peak and the central peak ( $\Delta\phi$ ) is interpreted as rotation of the shell crystal lattice by  $\Delta\phi$  with respect to the [100] direction of the core crystal lattice (Figure 4d). The result that two side peaks emerge with the central peaks, separated by similar values of  $\Delta\phi$  in the  $k$  and  $h$  scans ( $\Delta\phi = 11.5 \pm 0.1$  at the 101 position and  $\Delta\phi = 11.7 \pm 0.6$  at the 011 position), implies that two Miller domains of the shell crystal (**2**) are grown epitaxially on the (001) surface of the core crystal (**1**) while maintaining the in-plane rotational angle  $\Delta\phi$ .<sup>40,41</sup> Interestingly, the average of the rotational angles ( $\Delta\phi_{\text{av}}=11.7$ ) reflects the angle between the [100] direction and the  $\sqrt{26}$  direction of the quadratic lattice ( $\Delta\phi = 11.3$ ). Because the lattice constant of the shell crystal is significantly smaller than that of the core crystal, the ( $\sqrt{26} \times \sqrt{26}$ ) structure of the shell (001) surface matches the ( $5 \times 5$ ) structure of the core crystal. Hence, in-plane rotational epitaxial growth can compensate for the difference in the lattice constants. Such rotational crystal growth evidently does not occur at the (100) surface, because the lattice constant for the [001] direction of the shell crystal is not very different from that of the core crystal, which is also evident from the lack of peak separation observed in the crystal oriented along the a axis. Thus, the lattice of the shell crystal matches that of the core crystal along the [100] direction by near-matched epitaxy.

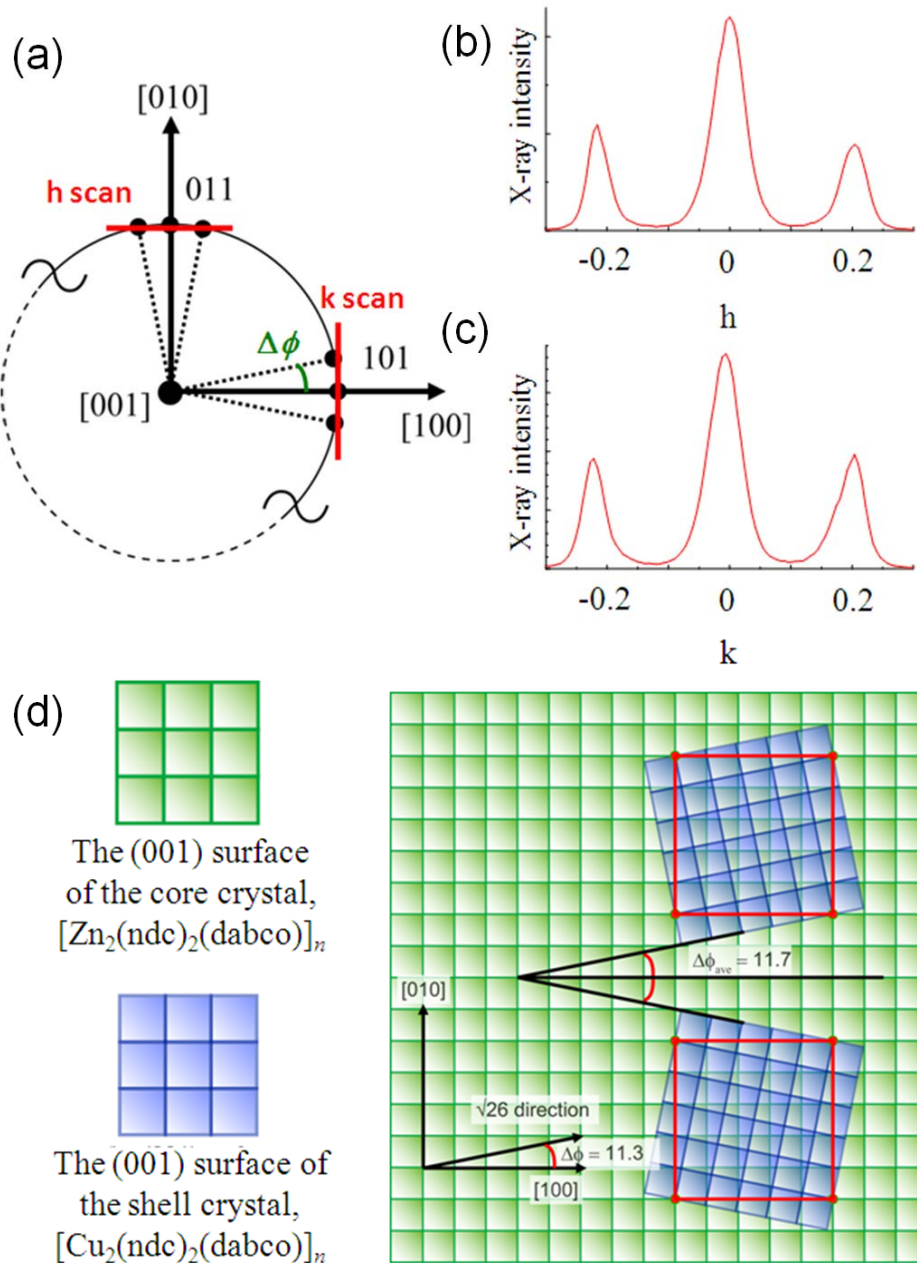


**Figure 4.** (a) The view from the [001] direction of the reciprocal lattice space. The  $k$  scan at the 101 position and the  $h$  scan at the 011 position are indicated as red lines. (b) The  $k$  scan at the 101 position. (c) The  $h$  scan at the 011 position. (d) The schematic model of the structural relationship between the core lattice and the shell lattice on the (001) surface. The green circles indicate the commensurate lattice points between the core lattice and the shell lattice. Two miller domains of the shell crystal are grown on the (001) surface of the core crystal with keeping the relative angle ( $\Delta\phi_{\text{ave}} = 11.6518$ ), which is corresponding to the  $\sqrt{26}$  direction of the (001) surface. The offset shows the chemical structure of the (001) surface.

## Conclusion

These results open the way for the fabrication of hybridized PCP crystals by epitaxial growth in solution and, moreover, for the determination of the structural relationship between the shell crystal and the core crystal by surface X-ray diffraction. The surfaces of the core PCP crystal support the growth of a single-shell crystal, which was otherwise obtained only as a microcrystalline powder in the bulk. Two other layer and pillar ligands are exchangeable in this hybridization system, and functional organic ligands can be introduced. Careful choice of components should allow us to control and design the in-plane rotational angles. The next stage of progress is to correlate the interfacial structure and the function, especially the adsorption properties, which can be strongly influenced by the interfacial structure. Such rotational domain growth of a PCP crystal on the surface of the PCP core crystal apparently can work as a filter or a sieve for separation of guest molecules. Moreover, these properties originate from the formation of the interface between two PCP crystals so that the PCP framework itself can be still modified to fabricate multifunctional PCPs.

## Experimental Section

The syntheses of individual compounds **1**<sup>31</sup> and **2**<sup>35</sup> were prepared according to literature procedures.

### Synthesis of the hybridized crystal, **1/2**

The stocked reaction solution of **2** was prepared as CuSO<sub>4</sub>·5H<sub>2</sub>O (21.0 mg, 8.41 × 10<sup>-2</sup> mmol), ndc (18.2 mg, 8.42 × 10<sup>-2</sup> mmol), and dabco (4.67 mg, 4.16 × 10<sup>-2</sup> mmol) in the mixed solvent (2.5 mL of toluene and 2.5 mL of methanol). Dozens of the core crystals (the sizes about 200 × 200 × 100 μm<sup>3</sup>) of **1**, were put into 4 mL of the stocked reaction solution, then, the reaction mixture was heated up to 393 K for 48 hours. After cooling, the greenish hybridized crystals (**1/2**) were harvested.

### Microscopic infrared spectroscopy

The spectra were measured both by a Nicolet 6700 (Thermo Fisher Scientific Inc.) with a infrared microscope, Nicolet Continuum, and by a FT/IR 6200 (JASCO) with a infrared microscope, IRT-3000. The attenuated total reflection attachment (ATR) was used for the measurement. Whereas the powder samples of **1** and **2** were measured to obtain their individual spectra, the sliced single crystal sample of **1/2** was investigated for hybridization. The prism of ATR attachment was separately put on the core part and the shell part, and then each spectrum was observed.

### Synchrotron X-ray measurements for film-structural analysis

The measurements were performed with a four-circle diffractometer having  $\phi$ ,  $\chi$ ,  $\theta$ , and  $2\theta$  circles at beamline BL13XU for surface and interface structures, SPring-8. The desired crystal in DMF solvent was picked up just before the measurement, and then fixed on the glass substrate with double-faced adhesive. The measurement was carried out under Helium gas condition. In such a condition, guest DMF molecules were most likely accommodated in pores of the PCP crystal.

### Powder X-ray diffraction measurement

The powder sample of compound **2** was sealed in a silica glass capillary (0.4 mm inside diameter). Diffraction pattern with good counting statistics was measured by the synchrotron radiation powder X-ray diffraction experiment with the large Debye-Scherrer camera and imaging plate as detectors on the BL02B2 beam line at SPring-8.<sup>42</sup> The diffraction pattern was obtained with a 0.01° step.

## Structure Determination

The structure determination was performed using a high brilliance synchrotron powder diffraction data. The pattern was indexed by using the indexing program DICVOL91.<sup>43</sup> A good quality unit cell refinement was obtained by using the structure-less Le Bail fitting method.<sup>44</sup> The peak shape was modeled by a Split-Pearson function. The structure refinement was performed by Rietveld method with RIETAN software.<sup>45,46</sup> Soft constraints about bond angles and bond distances was adapted throughout the refinement. Hydrogen atoms were placed at calculated position and their parameters were not refined. Crystallographic data for **1**: C<sub>15</sub>H<sub>12</sub>CuNO<sub>4</sub>,  $M = 333.81$ ,  $\lambda = 0.80081$  Å, tetragonal, space group  $P4/mmm$  (no. 123),  $a = 10.8190(3)$ ,  $c = 9.6348(6)$  Å,  $V = 1127.76(9)$  Å<sup>3</sup>,  $Z = 4$ ,  $T = 298$  K,  $2\theta_{\min} = 2.50$  °,  $2\theta_{\max} = 30.0$  °, step size  $0.01$  °, number of reflections = 125,  $R_{\text{wp}} = 0.0367$ ,  $R_1 = 0.0105$ . CCDC-260861 contains the supplementary crystallographic data for this paper. These data can be obtained free of charge from The Cambridge Crystallographic Data Centre via [www.ccdc.cam.ac.uk/data\\_request/cif](http://www.ccdc.cam.ac.uk/data_request/cif).

## References

- (1) N. K. Mal, M. Fujiwara, Y. Tanaka, *Nature* **2003**, *421*, 350-353.
- (2) M. Yaghi, M. O'Keeffe, N. W. Ockwig, H. K. Chae, M. Eddaoudi, J. Kim, *Nature* **2003**, *423*, 705-714.
- (3) S. Kitagawa, R. Kitaura, S. -i. Noro, *Angew. Chem. Int. Ed.* **2004**, *43*, 2334-2375.
- (4) G. Férey, C. Mellot-Draznieks, C. Serre, F. Millange, *Acc. Chem. Res.* **2005**, *38*, 217-225.
- (5) U. Mueller, M. Schubert, F. Teich, H. Puetter, K. Schierle-Arndt, J. Pastré, *J. Mater. Chem.* **2006**, *16*, 626-636.
- (6) R. E. Morris, P. S. Wheatley, *Angew. Chem. Int. Ed.* **2008**, *47*, 4966-4981.
- (7) M. Dincă, J. R. Long, *Angew. Chem. Int. Ed.* **2008**, *47*, 6766-6779.
- (8) Z. Wang, S. M. Cohen, *J. Am. Chem. Soc.* **2007**, *129*, 12368-12369.
- (9) Z. Q. Wang, S. M. Cohen, *Angew. Chem. Int. Ed.* **2008**, *47*, 4699-4702.
- (10) K. K. Tanabe, Z. Wang, S. M. Cohen, *J. Am. Chem. Soc.* **2008**, *130*, 8508-8517.
- (11) E. Dugan, Z. Wang, M. Okamura, A. Medina, S. M. Cohen, *Chem. Commun.* **2008**, 3366-3368.
- (12) T. Haneda, M. Kawano, T. Kawamichi, M. Fujita, *J. Am. Chem. Soc.* **2008**, *130*, 1578-1579.
- (13) Y. F. Song, L. Cronin, *Angew. Chem. Int. Ed.* **2008**, *47*, 4635-4637.
- (14) J. S. Costa, P. Gamez, C. A. Black, O. Roubeau, S. J. Teat, J. Reedijk, *Eur. J. Inorg. Chem.* **2008**, 1551-1554.
- (15) M. J. Ingleson, J. Perez Barrio, J. B. Guilbaud, Y. Z. Khimyak, M. J. Rosseinsky, *Chem. Commun.* **2008**, 2680-2682.
- (16) J. S. Costa, P. Gamez, C. A. Black, O. Roubeau, S. J. Teat, J. Reedijk, *Eur. J. Inorg. Chem.* **2008**, 1551-1554.
- (17) W. J. Rieter, K. M. Taylor, W. Lin, *J. Am. Chem. Soc.* **2007**, *129*, 9852-9853.
- (18) P. Horcajada, C. Serre, M. Vallet-Regí, M. Sebban, F. Taulelle, G. Férey, *Angew. Chem. Int. Ed.* **2006**, *45*, 5974-5978.
- (19) W. J. Rieter, K. M. Taylor, H. An, W. Lin, W. Lin, *J. Am. Chem. Soc.* **2006**, *128*, 9024-9025.
- (20) B. Xiao, P. S. Wheatley, X. Zhao, A. J. Fletcher, S. Fox, A. G. Rossi, I. L. Megson, L. Regli, K. M. Thomas, R. E. Morris, *J. Am. Chem. Soc.* **2007**, *129*, 1203-1209.
- (21) S. Hermes, T. Witte, T. Hikov, D. Zacher, S. Bahn Müller, G. Langstein, K. Huber, R. A. Fischer, *J. Am. Chem. Soc.* **2007**, *129*, 5324-5325.
- (22) E. Biemmi, C. Scherb, T. Bein, *J. Am. Chem. Soc.* **2007**, *129*, 8054-8055.

- (23) B. D. Chandler, G. Enright, D. S. Pawsey, K. Udachin, J. A. Ripmeester, D. T. Cramb, G. K. H. Shimizu, *Nature Mater.* **2008**, *7*, 229-235.
- (24) J. C. MacDonald, P. C. Dorrestein, M. M. Pilley, M. M. Foote, J. L. Lundburg, R. W. Henning, A. J. Schultz, J. L. Manson, *J. Am. Chem. Soc.* **2000**, *122*, 11692-11702.
- (25) J. C. Noveron, M. S. Lah, R. E. Del Sesto, A. M. Arif, J. S. Miller, P. J. Stang, *J. Am. Chem. Soc.* **2002**, *124*, 6613-6625.
- (26) S. Ferlay, W. Hosseini, *Chem. Commun.* **2004**, 788-789.
- (27) E. F. Brès, S. Ferlay, P. Dechambenoit, H. Leroux, W. Hosseini, S. Reybtjens, *J. Mater. Chem.* **2007**, *17*, 1559-1562.
- (28) K. Seki, W. Mori, *J. Phys. Chem. B* **2002**, *106*, 1380-1385.
- (29) D. N. Dybtsev, H. Chun, K. Kim, *Angew. Chem. Int. Ed.* **2004**, *43*, 5033-5036.
- (30) R. Kitaura, F. Iwahori, R. Matsuda, S. Kitagawa, Y. Kubota, M. Takata, T. C. Kobayashi, *Inorg. Chem.* **2004**, *43*, 6522-6524.
- (31) H. Chun, D. N. Dybtsev, H. Kim, K. Kim, *Chem. –Eur. J.* **2005**, *11*, 3521-3529.
- (32) B. –Q. Ma, K. L. Mulfort, J. T. Hupp, *Inorg. Chem.* **2005**, *44*, 4912-4914.
- (33) B. Chen, C. Liang, J. Yang, D. S. Contreras, Y. L. Clancy, E. B. Lobkovsky, O. M. Yaghi, S. Dai, *Angew. Chem. Int. Ed.* **2006**, *45*, 1390-1393.
- (34) D. Tanaka, S. Horike, S. Kitagawa, M. Ohba, M. Hasegawa, Y. Ozawa, K. Toriumi, *Chem. Commun.* **2007**, 3142-3144.
- (35) T. Uemura, Y. Ono, K. Kitagawa, S. Kitagawa, *Macromolecules* **2008**, *41*, 87-94.
- (36) D. Tanaka, M. Higuchi, S. Horike, R. Matsuda, Y. Kinoshita, N. Yanai, S. Kitagawa, *Chem. Asian J.* **2008**, *3*, 1343-1349.
- (37) M. Bukowska-Strzyżewska, J. Skoweranda, E. Heyduk, J. Mroziński, *Inorg. Chem. Acta* **1983**, *73*, 207-213.
- (38) W. Clegg, I. R. Little, B. P. Straughan, *J. Chem. Soc. Dalton Trans.* **1986**, 1283-1288.
- (39) K. H. Michaelian, S. M. Ziegler, *Appl. Spectrosc.* **1973**, *27*, 13-21.
- (40) L. Pérez-García, D. B. Amabilino, *Chem. Soc. Rev.* **2002**, *31*, 342-356.
- (41) S. De Feyter, F. C. De Schryver, *Chem. Soc. Rev.* **2003**, *32*, 139-150
- (42) E. Nishibori, M. Takata, K. Kato, M. Sakata, Y. Kubota, S. Aoyagi, Y. Kuroiwa, M. Yamakata, N. Ikeda, *J. Phys. Chem. Solid* **2001**, *62*, 2095.
- (43) A. Boultif, D. Louer, *Journal of Applied Crystallography* **1991**, *24*, 987.
- (44) B. LeBail, H. Duroy, J. L. Fourquet, *Mat. Res. Bull.* **1988**, *23*, 447
- (45) H. M. Rietveld, *Journal of Applied Crystallography* **1969**, *2*, 65.
- (46) F. Izumi, T. Ikeda, *Mater. Sci. Forum* **2000**, *198*, 321.



## Chapter 2

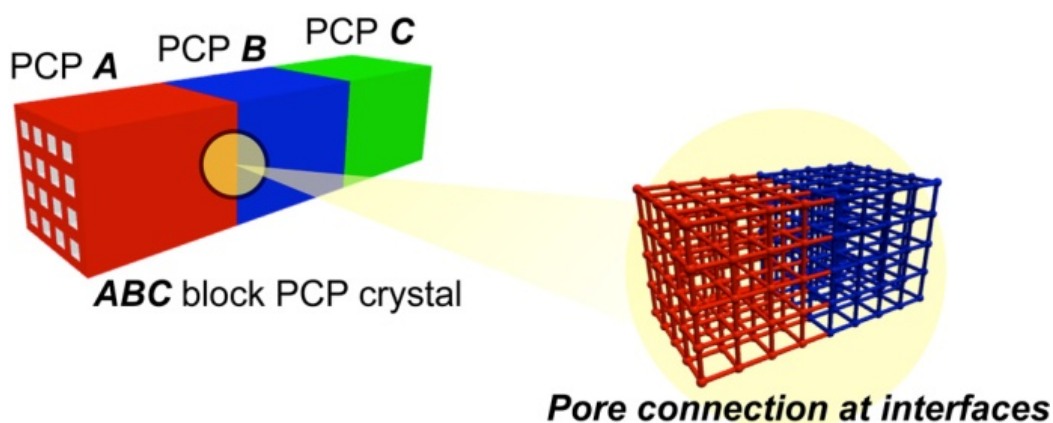
### A Block PCP Crystal: Anisotropic Hybridization of Porous Coordination Polymers by Face-Selective Epitaxial Growth

#### Abstract

Porous coordination polymers (PCPs) or metal organic frameworks (MOFs) have many attracting functions such as gas adsorption, separation, and catalytic activity. One way to develop such porous materials is to integrate several functions into one crystal, thus to create a core/shell type PCP crystal. Here we demonstrate a fabrication of the fabrication of sandwich type crystal;  $[\text{Zn}_2(\text{ndc})_2(\text{dabco})]_n$  (**1**) as the core crystal and  $[\text{Zn}_2(\text{ndc})_2(\text{dpndi})]_n$  (**3**) as the second crystal, (ndc = 1,4-naphthalenedicarboxylate, dabco = 1,4-diazabicyclo[2,2,2]octane, dpndi = *N,N'*-di(4-pyridyl)-1,4,5,8-naphthalenetetracarboxydiimide). This is because that the secondary crystal growth at the {100} surfaces of the core crystal that consist of ndc and dabco was prohibited because of the mismatch of molecular lengths between dabco and dpndi. The second crystal **3** could be only grown at the {001} surfaces that only consists of the common component, ndc.

## Introduction

The assembly of well-designed organic ligands with metal ions offers crystalline framework solids, so-called porous coordination polymers (PCPs) or metal–organic frameworks (MOFs), wherein the geometry and directional coordination interaction dominate the topology of the resulting infinite framework architectures.<sup>1–3</sup> In addition to such a molecular component system, higher order organization of materials can be achieved by using the crystal itself as another assembly component.<sup>4</sup> Thus, as in block copolymers, each individual crystal acts as a chemically distinct component to fabricate “block PCPs”, in which different framework structures are hybridized at the single crystal level (Scheme 1).<sup>5</sup> Because the intrinsic void space in the framework system makes PCPs an intriguing class of porous materials,<sup>6–11</sup> the connection of distinct PCP crystals with characteristic pore surface functionalities promises to improve the porous properties and create multifunctional PCPs.



**Scheme 1.** The schematic illustration of a block PCP concept.

Recently, we illustrated a “PCP-on-PCP” (or “MOF-on-MOF”) concept and succeeded in the fabrication of hybridized heterometallic core–shell PCP crystals by epitaxial growth.<sup>5</sup> The molecular assembly of components to grow the shell crystal was successfully performed on the surfaces of core crystals.<sup>12–18</sup> Here, we show that face-selective hybridization of single PCP crystals leads to the fabrication of sandwich-type block PCPs, where only two surfaces of a rectangular prism crystal were used selectively as substrates for epitaxial growth of the second PCP crystal. Surface X-ray diffraction proved the epitaxy of the second crystal grown on the core crystal, which implies connection of one-dimensional channels with different pore functionalities. A series of tetragonal porous frameworks,  $[M_2(\text{dicarboxylate})_2(\text{N ligand})]_n$  (Fig. 1a),<sup>19–27</sup>

wherein the dicarboxylate layer ligands link the dimetal clusters into 2-D square lattices which are further connected through the nitrogen pillar ligands at the lattice points, is a good scaffold with which to investigate anisotropic hybridization of PCPs. Their single crystal morphology is a rectangular prism, reflecting the tetragonal crystal system. Whereas four crystal surfaces denoted as  $\{100\}$  have rectangular lattices comprising one layer ligand and one pillar ligand,  $\{001\}$  surfaces with square lattices based only on layer ligands appear on the remaining two surfaces. Here, we targeted the  $\{001\}$  surface for growth of the second crystal because choosing the same layer ligand both in the core PCP and the second PCP does not require the lattice distances in the  $[001]$  direction to match, thus allowing free usage of the pillar ligand. To differentiate between the pore surface functionalities of the core PCP and the second PCP, aliphatic 1,4-diazabicyclo[2.2.2]octane (dabco) and aromatic *N,N'*-di(4-pyridyl)-1,4,5,8-naphthalenetetracarboxydiimide (dpndi) were used as the pillar ligands, respectively (Fig. 1b):  $[\text{Zn}_2(\text{ndc})_2(\text{dabco})]_n^{21}$  (**1**) as the core crystal and  $[\text{Zn}_2(\text{ndc})_2(\text{dpndi})]_n$  (**2**) as the second crystal (ndc = 1,4-naphthalene dicarboxylate).

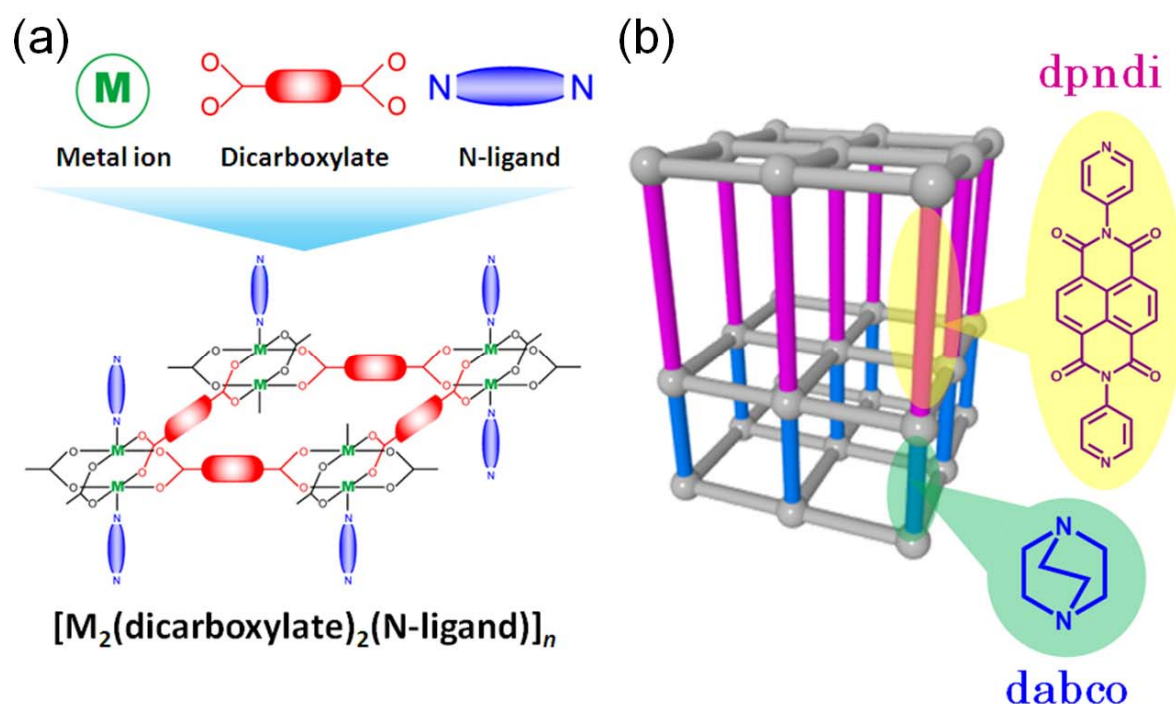


**Figure 1.** (a) Schematic illustration of the series of frameworks  $[\text{M}_2(\text{dicarboxylate})_2(\text{N-ligand})]_n$ . (b) Schematic illustration of anisotropic epitaxial growth of the second framework, **2**, on the core framework, **1**.

## Results and Discussion

The anisotropic hybridization of two frameworks into a single crystal was successfully achieved by a simple solvothermal synthesis; pieces of single crystals of **1** were put into a solution of  $\text{Zn}(\text{NO}_3)_2 \cdot 6\text{H}_2\text{O}$ , 1,4-naphthalene dicarboxylic acid, and dpndi in DMF, and the solution was heated to 353 K for two days. The hybridized crystals (**1/2**) were harvested after cooling at room temperature. The optical microscopic image (Fig. 2a) of **1/2** clearly demonstrated that the orange crystal of **2** grew on only two surfaces of the colorless crystal of **1**, leading to the formation of *BAB*-type block PCPs with the core crystal *A* between second crystals *B*. Each part of the hybridized crystal was identified as the respective framework structure by microscopic attenuated total reflectance (ATR) infrared spectroscopy (Fig. 2b–e). The characteristic sharp peaks of the core crystal *A* correspond to those of **1**. On the other hand, the broad features of the second crystal *B* resemble those of **2**. The broadness of the peaks most likely arises because of the presence of two species (ndc and dpndi) whose naphthalene and carbonyl peaks overlap. The spectral similarity of the second crystal to **2** suggests that the second framework of **2** successfully grew on the core framework of **1**.

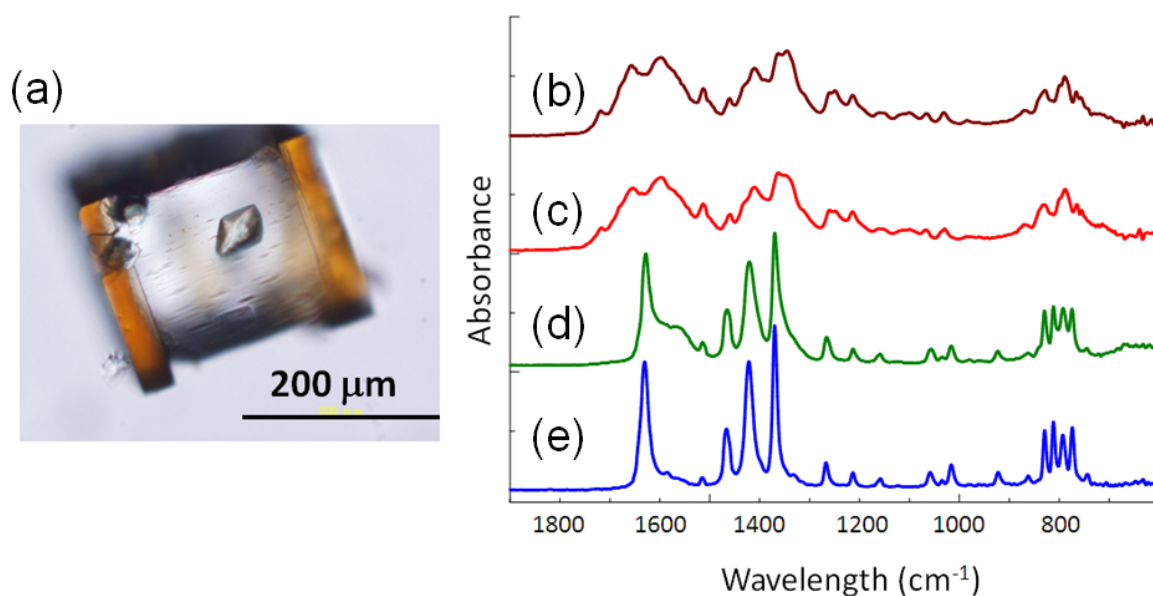


**Figure 2.** (a) The optical microscopic image of the hybridized crystal, **1/2**. (b) The infrared spectrum by microscopic attenuated total reflection (ATR) measurement of the orange part of **1/2**, crystal B, (c) the single crystal sample of **2**, (d) the colorless part of **1/2**, crystal A, (e) the single crystal sample of **1**.

Both crystals have the same tetragonal space group,  $P4/mmm$ , and very similar unit cell parameters in the  $a$  axes ( $a = 10.921(1)$  for **1** and  $10.906(2)$  for **2**). However, the  $c$  axes of the unit cell parameters are significantly different ( $c = 9.611(1)$  for **1** and  $22.456(4)$  for **2**), which enables determination of the structural parameters between the core crystal  $A$  and the second crystal  $B$ . Synchrotron X-ray diffraction measurements for film structural analysis were, therefore, performed using a four-circle diffractometer at beamline BL13XU for surface and interface structures, SPring-8. A block PCP crystal of **1/2** with a size larger than  $200\ \mu\text{m}$  and a second crystal with thickness larger than  $50\ \mu\text{m}$  was fixed on a glass surface with the configuration illustrated in Fig. 3a, and diffraction data were recorded using an X-ray beam with a size of  $1 \times 1\ \mu\text{m}^2$ . The  $\theta$ - $2\theta$  scan of **1/2** from the initial position ( $\chi = 90^\circ$ ) provided two sharp 00l peaks from both crystal  $A$  and  $B$ : the 002 Bragg peak for crystal  $B$  at  $2\theta = 5.1261$  and the 001 Bragg peak for crystal  $A$  at  $2\theta = 5.9461$ . The observation of 00l Bragg peaks simultaneously from both crystal  $A$  and  $B$  directly suggests that the epitaxial growth of crystal  $B$  only occurs at the  $\{001\}$  surfaces of the core crystal  $A$  and the growth of crystal  $B$  occurs in the direction of the  $c$  axis with the Zn–N ligand coordination mode. Since pillar ligands with different lengths (dabco for **1** and dpndi for **2**) were used for the crystal hybridization, the secondary growth at the  $\{100\}$  surfaces of the core crystal  $A$  that consist of one layer ligand and one pillar ligand was significantly prohibited because of the lattice mismatch. The lattice constants of the  $c$  axes ( $c = 9.611(1)$  for **1** and  $22.456(4)$  for **2**) are different enough to obtain diffraction positions of each crystal in the hybridized crystal, which enables us to investigate the structural relationship between them.

The scan of rotational angle around  $[001]$  (the  $\phi$  scan) at the 101 Bragg position of the core crystal  $A$ , **1**, gave two peaks at  $\phi = 0.0001 \pm 0.0391$  from the 101 position and at  $\phi = 89.9931 \pm 0.0081$  from the 011 position (Figure 4a). Two diffraction peaks with a  $90^\circ$  difference implies the square lattice structure ( $a = b$ ) of  $\{001\}$  surfaces of **1**. Similar to the  $\phi$  scan of **1**, two peaks at the same  $\phi$  angles ( $\phi = 0.0131 \pm 0.0451$  and  $90.0041 \pm 0.1311$ ) were observed in the  $\phi$  scan at the 101 and 011 Bragg position of the second crystal  $B$ , **2** (Figure 4b), respectively. The identical  $\phi$  angles between crystals  $A$  and  $B$ , as illustrated in the reciprocal lattice space (Figure 4c), indicate that the second crystal was grown epitaxially on the core crystal with a perfect lattice match at the  $\{001\}$  surfaces of both crystals ( $a = 10.921(1)$  for **1** and  $10.906(2)$  for **2**). Unlike the reported core–shell crystal with a heterometallic system,<sup>5</sup>  $[\text{Cu}_2(\text{ndc})_2(\text{dabco})]_n$  on  $[\text{Zn}_2(\text{ndc})_2(\text{dabco})]_n$  (**1**), where in-plane rotational epitaxial growth compensates for the difference (ca.  $0.1\ \text{\AA}$ ) in lattice constants at the  $\{001\}$  surface, the negligible difference in lattice constants here (ca.  $0.015\ \text{\AA}$ ) promises the pore connection as shown in Scheme 1.

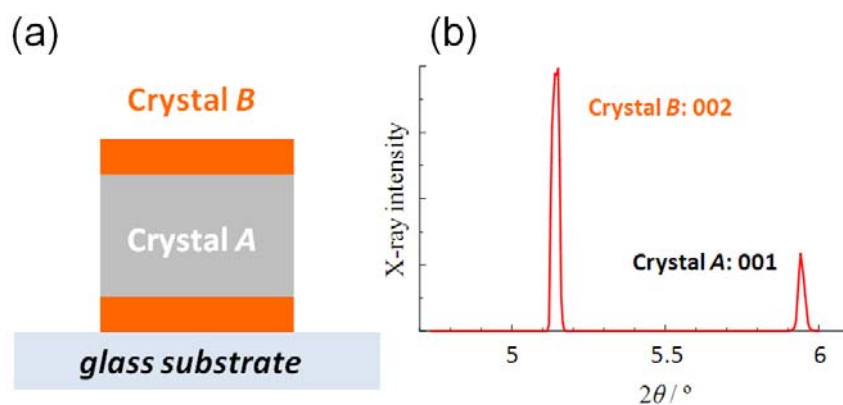


**Figure 3.** (a) The schematic illustration of configuration of a block PCP crystal, **1/2**, on a glass substrate for synchrotron X-ray diffraction measurements. (b) The  $\theta$ - $2\theta$  scan of the block PCP crystal immobilized as illustrated in Fig. 3a at the initial position ( $\chi = 90^\circ$ ). Two peaks assigned to the 002 Bragg peak for crystal *B*, **2**, ( $2\theta = 5.126^\circ$ ) and the 001 Bragg peak for crystal *A*, **1**, ( $2\theta = 5.946^\circ$ ) were obtained simultaneously in the same scan.

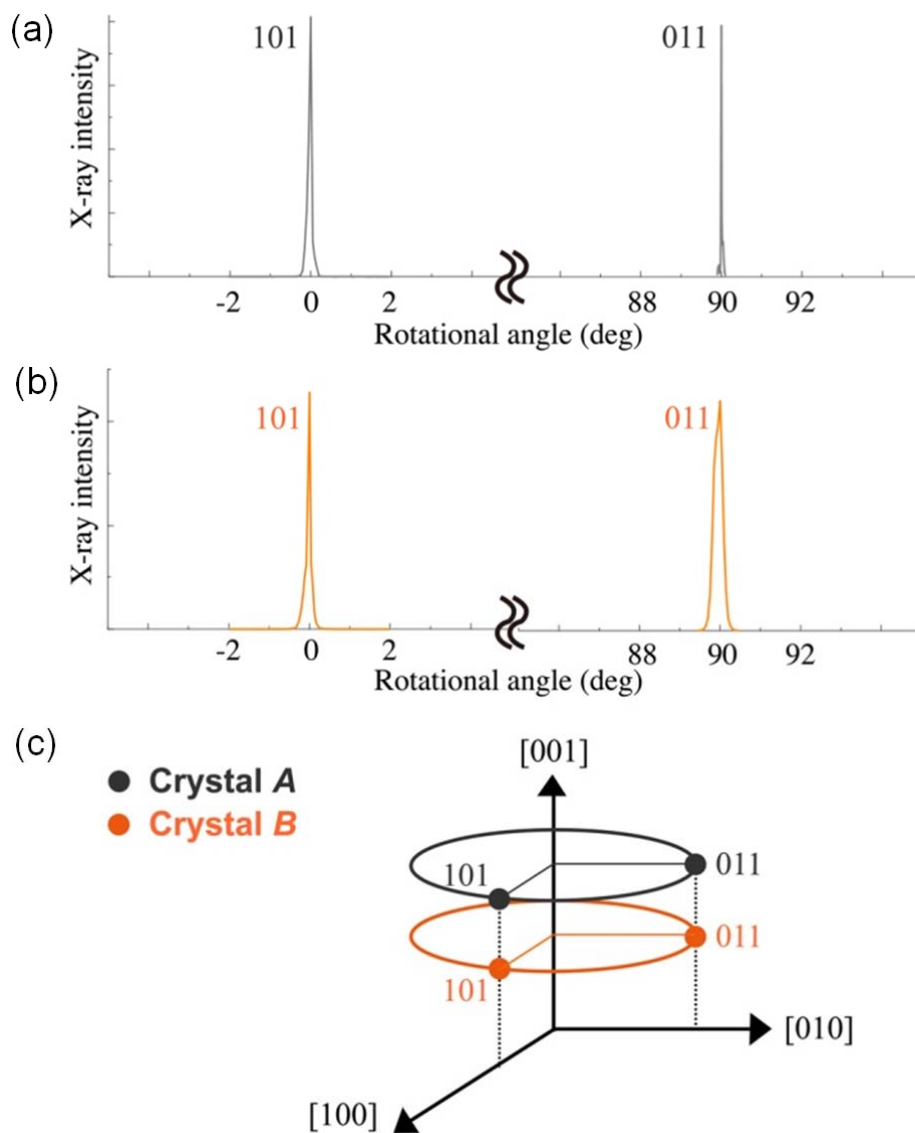


**Figure 4.** (a) The scan of rotational angle around the [001] direction (the  $\phi$  scan) of the core crystal *A*, **1** and (b) of the second crystal *B*, **2**. (c) The reciprocal lattice space corresponding to the  $\phi$  scan.

## Conclusion

In conclusion, we have demonstrated that face-selective epitaxial growth of a second PCP crystal on a core PCP crystal with a tetragonal system, leading to a block PCP crystal, can be achieved by using matching lattices on the specific surfaces. By using the same layer ligand for crystal hybridization, epitaxial growth on two {001} surfaces of the core crystal no longer requires the use of a pillar ligand with the same lattice constant, thus a variety of pillar ligands is available for use, with the possibility of a pore connection at the interface. This methodology will open the way for fabrication of a multifunctional PCP where several porous properties are integrated into a single crystal. For instance, the crystal array illustrated in Scheme 1 can be recognized as “a crystal factory” when sorption, separation, and reaction properties are integrated in *A*, *B*, and *C* crystals, respectively.

## Experimental Section

### Materials

Dehydrated DMF, 1,4-naphthalene dicarboxylic acid (ndc), and  $\text{Zn}(\text{NO}_3)_2 \cdot 6\text{H}_2\text{O}$  were purchased from Wako Pure Chemical Industries. 1,4-diazabicyclo[2,2,2]octane (dabco) was purchased from TCI. All chemicals were used without further purification. The syntheses of *N,N'*-di(4-pyridyl)-1,4,5,8-naphthalenetetracarboxydiimide (dpndi),<sup>28</sup> and  $[\text{Zn}_2(\text{ndc})_2(\text{dabco})]_n$  (**1**),<sup>21</sup> were prepared according to literature procedures. Synthesis of **2**  $\supset$  Solvents. The solution of  $\text{Zn}(\text{NO}_3)_2 \cdot 6\text{H}_2\text{O}$  (6.1 mg, 0.020 mmol), ndc (4.4 mg, 0.020 mmol), and dpndi (4.2 mg, 0.010 mmol) in 4 mL DMF were heated up to 373 K for 2 days. After cooling, the reaction solution was left at room temperature for a few days. The orange crystals were harvested. Elemental analysis calcd. for  $\text{C}_{73.5}\text{H}_{83.5}\text{N}_{12.5}\text{O}_{20.5}\text{Zn}_2 \{[\text{Zn}_2(\text{ndc})_2(\text{dpndi})] \cdot 8.5\text{DMF}\}_n$ : C, 55.15; H, 5.26; N, 10.99, Found: C, 54.95; H, 5.25; N, 11.15.

### Synthesis of hybridized crystal, **1/2**.

Dozens of the core crystals (the size about  $200 \times 300 \times 300 \text{ mm}^3$ ) of **1**, were put into 4 mL of the reaction solution for **2** as  $\text{Zn}(\text{NO}_3)_2 \cdot 6\text{H}_2\text{O}$  (6.1 mg, 0.020 mmol), ndc (4.4 mg, 0.020 mmol), and ndi (4.2 mg, 0.010 mmol) in 4 mL DMF, then, the reaction mixture was heated up to 353 K for 2 days. After cooling, the reaction solution was left at room temperature. The two-color (colorless and orange) hybridized crystals (**1/2**) were obtained.

### Microscopic IR measurement

Infrared spectra were measured by a FT/IR 6100 with a infrared microscope IRT-5000 (JASCO). The attenuated total reflection attachment (ATR) was used for the measurement. Elemental analysis was carried out with a Thermo Finnigan EA1112.

### Single crystal X-ray crystallographic analysis

The single crystal of **2**  $\supset$  DMF was mounted in glass capillary. X-ray data collection ( $6.4 < 2\theta < 55^\circ$ ) was conducted at 223K on Rigaku AFC10 diffractometer Mo-K $\alpha$  radiation ( $\lambda = 0.7105 \text{ \AA}$ ) with Rigaku Saturn CCD system. The structures were solved by a direct method (SHELXL) and expanded using Fourier techniques. All calculations were performed using the crystal clear crystallographic software package 3.8 of Rigaku. The crystallizing solvents (DMF molecules) were severely disorderd and could not be satisfactorily localized. All non-hydrogen atoms except for those of

disordered solvent molecules were refined anisotropically. Hydrogen atoms of **ndc** severely disordered and could not be satisfactorily localized. Hydrogen atoms except for those of **ndc**, were added at their geometrically ideal positions and refined isotropically. Crystal data for **2**·8.5DMF: C<sub>48</sub>H<sub>24</sub>N<sub>4</sub>O<sub>12</sub>Zn<sub>2</sub>, tetragonal, space group *P4/mmm*, (no. 123),  $a = 10.906$  (2) Å,  $c = 22.456$  (4) Å,  $V = 2670.8$  (9) Å<sup>3</sup>,  $Z = 1$ ,  $T = 223$  K.  $\rho_{\text{calcd}} = 0.609$  gcm<sup>-3</sup>,  $\mu(\text{MoK}\alpha) = 0.478$ cm<sup>-1</sup>, 1839 reflections measured, 1325 observed ( $I > 2.00\sigma(I)$ ) 99 parameters;  $R_1 = 0.0916$ ,  $wR_2 = 0.0748$ , GOF = 0.912.

### Synchrotron X-ray measurement for film-structural analysis

The measurements were performed with a four-circle diffractometer having  $\phi$ ,  $\chi$ ,  $\theta$ , and  $2\theta$  circles at beamline BL13XU for surface and interface structures, SPring-8. The hybridized crystal, **1/2**, was picked up just before the measurement, and then fixed on the glass substrate with the orientation where orange part of **1/2** was parallel to the glass substrate by double-faced adhesive. The measurement was carried out under Helium gas condition. In this condition, guest DMF molecules were most likely accommodated in pores of the PCP crystal. The  $\theta$ - $2\theta$  scan at the initial position ( $\chi = 90^\circ$ ) was carried out to determine the orientation of hybridized crystals. Only  $00l$  Bragg peaks of from both **1** and **2** were observed. The  $00l$  Bragg peaks simultaneously observed from **1** and **2** in the same scan suggest that the epitaxial growth of **2** occurs at (001) surfaces of **1**. The angles of  $\phi$ ,  $\chi$ ,  $\theta$  and  $2\theta$  were moved to a desired Bragg position where diffractions were recorded. A scan of the rotation angle around the [001] direction (the  $\phi$  scan) at the 101 and 011 Bragg position from **1** gave two sharp peaks assigned to the 110 and 110 Bragg peaks. In the same way, two peaks at the same  $\phi$  angles as **1** were observed, and assigned to the 101 and 110 Bragg position of **2**. This result indicates that the (001) surface of **2** perfectly matches to the (001) surfaces of **1** at the crystal-crystal interfaces.

## References

- (1) S. Batten and R. Robson, *Angew. Chem., Int. Ed.*, **1998**, *37*, 1460-1494.
- (2) B. Moulton and M. Zaworotko, *Chem. Rev.*, **2001**, *101*, 1629-1658.
- (3) M. O’Keeffe, M. A. Peskov, S. J. Ramsden and O. M. Yaghi, *Acc. Chem. Res.*, **2008**, *41*, 1782-1789.
- (4) Z. Popovic, M. Otter, G. Calzaferri and L. De Cola, *Angew. Chem., Int. Ed.*, **2007**, *46*, 6188-6191.
- (5) S. Furukawa, K. Hirai, K. Nakagawa, Y. Takashima, R. Matsuda, T. Tsuruoka, M. Kondo, R. Haruki, D. Tanaka, H. Sakamoto, S. Shimomura, O. Sakata and S. Kitagawa, *Angew. Chem., Int. Ed.*, **2009**, *48*, 1766-1770.
- (6) M. Yaghi, M. O’Keeffe, N. W. Ockwig, H. K. Chae, M. Eddaoudi and J. Kim, *Nature*, **2003**, *423*, 705-714.
- (7) S. Kitagawa, R. Kitaura and S. i. Noro, *Angew. Chem., Int. Ed.*, **2004**, *43*, 2334-2375.
- (8) G. Férey, C. Mellot-Draznieks, C. Serre and F. Millange, *Acc. Chem. Res.*, **2005**, *38*, 217-225.
- (9) U. Mueller, M. Schubert, F. Teich, H. Puetter, K. Schierle-Arndt and J. Pastre , *J. Mater. Chem.*, **2006**, *16*, 626-636.
- (10) R. E. Morris and P. S. Wheatley, *Angew. Chem., Int. Ed.*, **2008**, *47*, 4966-4981.
- (11) M. Dincă and J. R. Long, *Angew. Chem., Int. Ed.*, **2008**, *47*, 6766-6779.
- (12) J. C. MacDonald, P. C. Dorrestein, M. M. Pilley, M. M. Foote, J. L. Lundburg, R. W. Henning, A. J. Schultz and J. L. Manson, *J. Am. Chem. Soc.*, **2000**, *122*, 11692-11701.
- (13) J. C. Noveron, M. S. Lah, R. E. Del Sesto, A. M. Arif, J. S. Miller and P. J. Stang, *J. Am. Chem. Soc.*, **2002**, *124*, 6613-6625.
- (14) S. Ferlay and W. Hosseini, *Chem. Commun.*, **2004**, 788-789.
- (15) T.-J. M. Luo, J. C. MacDonald and G. T. R. Palmore, *Chem. Mater.*, **2004**, *16*, 4916-4927.
- (16) P. Dechambenoit, S. Ferlay and M. W. Hosseini, *Cryst. Growth Des.*, **2005**, *5*, 2310-2312.
- (17) J. W. Steed, A. E. Goeta, J. Lipkowski, D. Swierczynski, V. Panteleon and S. Handa, *Chem. Commun.*, **2007**, 813-815.
- (18) E. F. Bre` s, S. Ferlay, P. Dechambenoit, H. Leroux, W. Hosseini and S. Reybtjens, *J. Mater. Chem.*, **2007**, *17*, 1559-1562.
- (19) K. Seki and W. Mori, *J. Phys. Chem. B*, **2002**, *106*, 1380-1385.

- (20) D. N. Dybtsev, H. Chun and K. Kim, *Angew. Chem., Int. Ed.*, **2004**, *43*, 5033-5036.
- (21) R. Kitaura, F. Iwahori, R. Matsuda, S. Kitagawa, Y. Kubota, M. Takata and T. C. Kobayashi, *Inorg. Chem.*, **2004**, *43*, 6522-6524.
- (22) H. Chun, D. N. Dybtsev, H. Kim and K. Kim, *Chem. Eur. J.*, **2005**, *11*, 3521-3529.
- (23) B. Q. Ma, K. L. Mulfort and J. T. Hupp, *Inorg. Chem.*, **2005**, *44*, 4912-4914.
- (24) B. Chen, C. Liang, J. Yang, D. S. Contreras, Y. L. Clancy, E. B. Labkovsky, O. M. Yaghi and S. Dai, *Angew. Chem., Int. Ed.*, **2006**, *45*, 1390-1393.
- (25) D. Tanaka, S. Horike, S. Kitagawa, M. Ohba, M. Hasegawa, Y. Ozawa and K. Toriumi, *Chem. Commun.*, **2007**, 3142-3144.
- (26) T. Uemura, Y. Ono, K. Kitagawa and S. Kitagawa, *Macromolecules*, **2008**, *41*, 87-94.
- (27) D. Tanaka, M. Higuchi, S. Horike, R. Matsuda, Y. Kinoshita, N. Yanai and S. Kitagawa, *Chem. Asian J.*, **2008**, *3*, 1343-1349.
- (28) P. H. Dinolfo, M. E. Williams, C. L. Stern, J. T. Hupp, *J. Am. Chem. Soc.*, **2004**, *126*, 12989-13001.

## Chapter 3

# Sequential Functionalization of Porous Coordination Polymer Crystals

### Abstract

A wide variety of potential organic linkers in porous coordination polymers (PCPs) allows these materials to exhibit versatile porous properties such as adsorption, separation, catalysis and sensing. The integration of several organic molecules can yield multifunctional porous materials in which various components sequentially fulfill their respective porous functions. However, the general synthetic protocol of PCPs, in which several types of ligands are simply assembled by metal ions, leads to a single-phase material that is unable to perform the sequential tasks. Here, we show that heterostructured PCP crystal fabricated using epitaxial growth simultaneously process two contradictory porous functions, size selectivity and high storage. The framework is grown using small pores as a shell around the isoreticular core framework, which has large pores on the micrometre scale for a single crystal. The core/shell crystal not only perfectly extracted the linear petroleum molecule of hexadecane (cetane) from a mixture with its branched isomer isocetane, even when the cetane was present at a very low concentration (1 wt %), but also showed improved accumulation of the molecules in its pores.

## Introduction

Chemists fabricate multifunctional materials by integrating two or more distinct chemical functionalities into a single platform. This structural complexity allows the design of materials that possess contradictory properties. These materials have integrated properties that conventional singlephase materials can never achieve.<sup>1</sup> The key to this integration is arranging the chemical functionalities at the desired positions within the material. Organic polymer chemistry has shown that the spatial arrangement of functionalities determines the resulting properties, with a homogeneous distribution resulting in a mixed and a heterogeneous distribution leading to the formation of a separated phase. Whereas random copolymers with several chemical functionalities display functions that are different from their original ones, block copolymers that partition the chemically distinct phases lead to the coexistence of individual properties.<sup>2</sup> Herein, we introduce heterogeneity into hybridization systems of coordination polymers to fabricate multifunctional porous materials that synergistically exhibit two contradictory porous properties.

Porous coordination polymers (PCPs), or metal–organic frameworks (MOFs), form three-dimensional molecular skeletons consisting of organic spokes and inorganic nodes.<sup>3–6</sup> PCPs are an intriguing class of porous crystalline materials in which the properties can be modulated simply by altering the chemical functionalities on the organic spokes.<sup>7–19</sup> The porous properties can be controlled by introducing appropriate substituents. Pore size is affected by ligand bulkiness,<sup>20</sup> specific chemical affinity is affected by hydrogen bonding,<sup>21</sup> and reactivity is affected by the isolation or exposure of the reactive site.<sup>22</sup> The porous functions of PCPs can be broadly divided into two classes based on different length scales. Spatial function, such as storage or size selectivity, originate from the space surrounded by the framework scaffold, where the arrangement of chemical functionalities dominates the function. In contrast, local functions, such as reactivity or catalytic activity, arise from the chemical structure of components, such as open metal sites<sup>23</sup> or reactive organic sites.<sup>24</sup>

Although local functions can be integrated into a mixed homogeneous phase of PCPs using several organic linkers, homogeneous integration alters spatial functions owing to the random arrangement of organic linkers.<sup>25, 26</sup> One way to overcome this issue is to prepare heterogeneous structures containing bimodal pore networks. The simple but sequentially arranged hybridization of single PCP crystals affords control over the sequence of individual spatial functions. Such heterogeneous structured PCPs enable multifunctionality even when two contradictory properties are combined (Figure 1), such

as small and large pore sizes providing a simultaneous size selectivity and storage. Large cavities are essential to achieve a high storage capacity but accept any guest molecule, thus sacrificing size selectivity. To overcome this limitation, a platform could be designed containing both crystal A (small aperture) and B (large cavity) for separation and storage, respectively.

One of the most promising applications of PCPs is gas and liquid separation using column packing materials<sup>27-29</sup> or separation membranes.<sup>30</sup> Although these separation systems exhibit excellent performance with dynamically flowing mixtures, there is also a need to separate one substrate from a mixture under static conditions, such as for biological systems or in a fuel tank. The extraction of byproducts, impurities, or toxic substances in these sorts of system requires a single material that can be used for the sequential separation and accumulation of the extracted product.

Herein, the fabrication of a single-crystal extractor based on PCPs with core-shell heterostructures is presented in which the storage container is the core crystal and the size separation filter is the shell crystal. The design of isoreticular frameworks with organic ligands of different sizes allows the connection of pores at the interfaces between the two PCP crystals by epitaxial growth. We demonstrate the crystal extractor using the extraction of cetane (*n*-hexadecane) from its branched isomer, isocetane (2,2,4,4,6,8,8-heptamethylnonane), both of which are important molecules in diesel fuels.<sup>31-32</sup> Even at a low concentration of cetane (<1%), the sequentially hybridized PCP crystals only extract cetane from the mixture, which allows it to accumulate in the large pores of the core container.

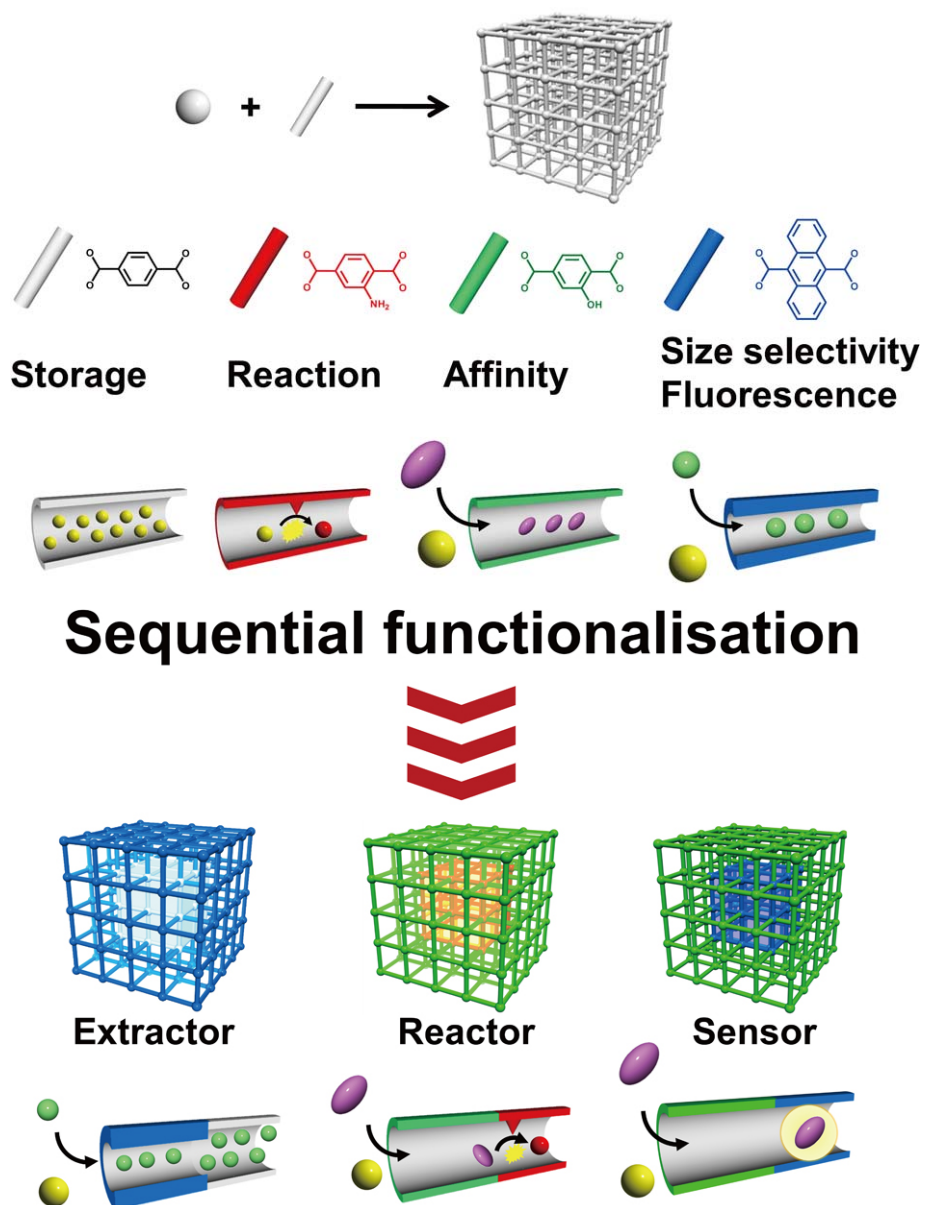


**Figure 1.** Porous coordination polymer crystal hybridization for sequential functionalization systems.

## Results and Discussion

A series of three-dimensional PCPs,  $\{\text{Zn}_2(\text{dicarboxylate})_2(\text{dabco})\}_n$ ,<sup>33-36</sup> gives a single micrometer-scale crystal with a well-defined cuboid morphology in which the dicarboxylate layer ligands link to the zinc paddlewheel clusters to form two-dimensional square lattices connected by dabco pillar ligands at the lattice points (dabco=1,4-diazabicyclo-[2.2.2]octane). The single-crystalline nature is essential for achieving sequential growth of the second crystal on the crystal surface. As the significant differences in pore sizes and surface areas between the core and shell crystals leads to the fabrication of the crystal extractor, we selected  $\{\text{Zn}_2(\text{bdc})_2(\text{dabco})\}_n$ <sup>34</sup> (**1**) as the core framework (bdc=1,4-benzene dicarboxylate; pore sizes  $7.5 \times 7.5 \text{ \AA}^2$  along the *c* axis,  $5.3 \times 3.2 \text{ \AA}^2$  along the *a* and *b* axes; micropore volume  $0.75 \text{ cm}^3 \text{ g}^{-1}$ ) and  $\{\text{Zn}_2(\text{adc})_2(\text{dabco})\}_n$ <sup>36</sup> (**2**) as the shell framework (adc = 9,10-anthracene dicarboxylate; pore sizes  $1.7 \times 1.7 \text{ \AA}^2$  along the *c* axis,  $4.5 \times 2.7 \text{ \AA}^2$  along the *a* and *b* axes; micropore volume  $0.31 \text{ cm}^3 \text{ g}^{-1}$ ). This system is shown in Figure 2.

Two frameworks were successfully hybridized into one crystal by a simple solvothermal synthesis.<sup>37</sup> Pieces of single crystals of **1** were placed into a solution of  $\text{Zn}(\text{NO}_3)_2 \cdot 6\text{H}_2\text{O}$ , 9,10-anthracene dicarboxylic acid, and dabco in *N,N*-dimethylformamide (DMF), and the solution was heated to 393 K for three days. The core-shell crystals (**1/2**) were harvested after cooling to room temperature.

Because both crystalline phases are colorless, it is inherently difficult to distinguish between the two phases using an optical microscope; therefore, we used a confocal laser scanning microscope (CLSM) with anthracene fluorescent emission as a probe to determine the three-dimensional configuration of the core-shell crystals. Horizontally sliced CLSM images at two different focal points are shown in the Figure 3 Whereas the image slice from the focal point at the bottom of the crystal showed fluorescence across the whole surface, the image slice from the focal point at the middle of the crystal gave an image with fluorescence on only four sides of the crystal (Figure 4 a). The CLSM images at different focal points indicated that the shell crystals of **2** covered all the surfaces of the core crystal **1**.

We also used microscopic laser Raman spectroscopy (MLRS) to examine core-shell crystals mechanically sliced at the middle of the crystal. As shown in Figure 3c-f, mapping according to characteristic Raman signals corresponding to the core and shell framework (colored red and green, respectively, in Figure 4b) supported the formation of a core-shell crystal with microscopically abrupt interfaces. The Raman mapping measurement indicated that the shell crystals was several tenths of a micrometer

in thickness. The molar ratio of the core framework to the shell framework was determined to be 8:2 by  $^1\text{H-NMR}$  spectroscopy of core-shell crystals that had been decomposed with hydrochloric acid (Figure 5). Furthermore, synchrotron X-ray diffraction measurements for film structural analysis revealed that the hybridization of two frameworks into one crystal with pore connections at the crystal interfaces had been achieved (Figures 6).

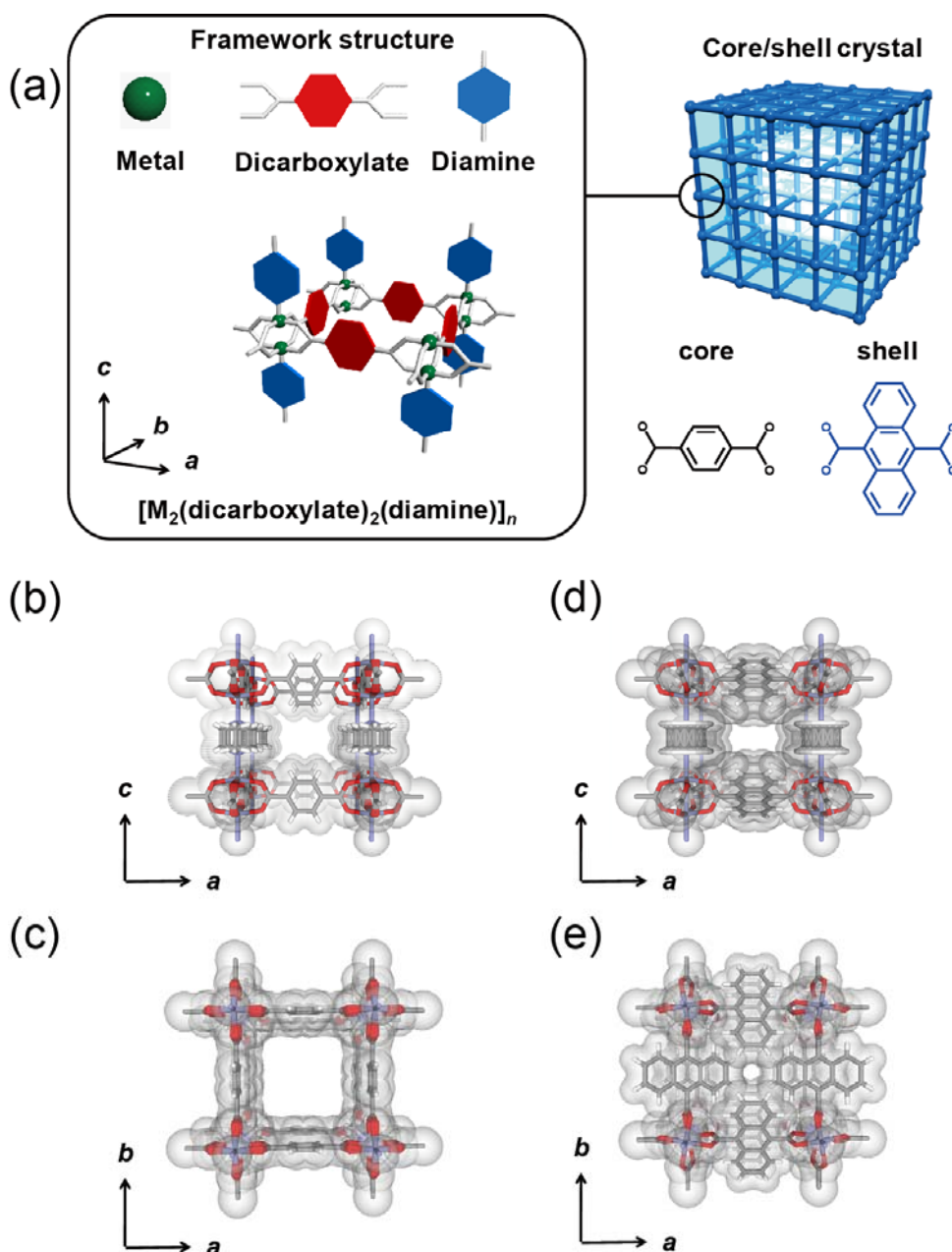


**Figure 2.** (a) A series of frameworks,  $[\text{M}_2(\text{dicarboxylate})_2(\text{diamine})]_n$ , The crystal structure of (1) viewed along (b) the  $b$  axis and (c) the  $c$  axis. The structure of (2) viewed along (d) the  $b$  axis and (e) the  $c$  axis.

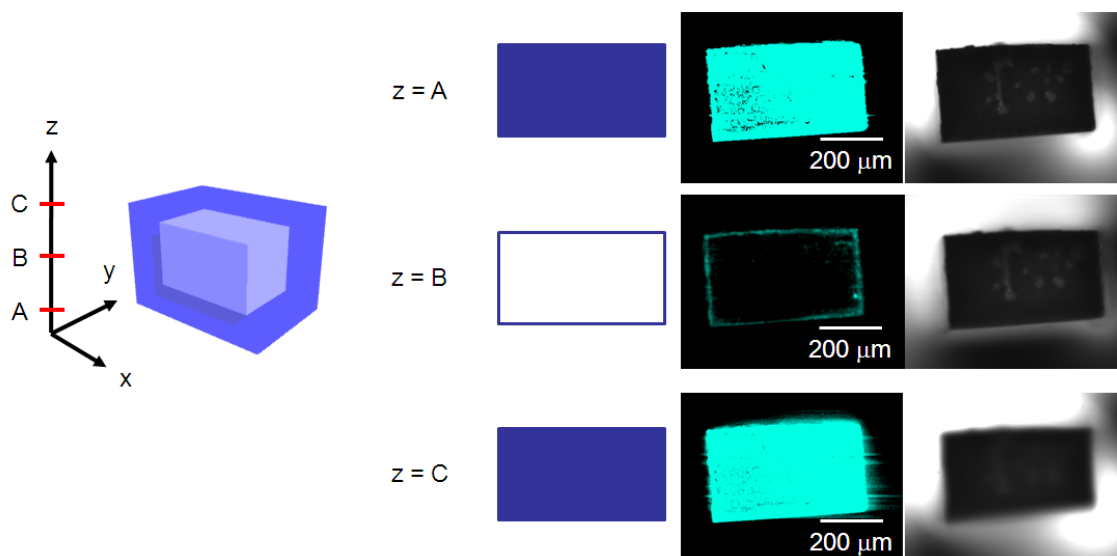


**Figure 3.** Schematic representations of the core/shell crystal and the CLSM and transmission images at  $z = A$ ,  $z = B$  and  $z = C$ .

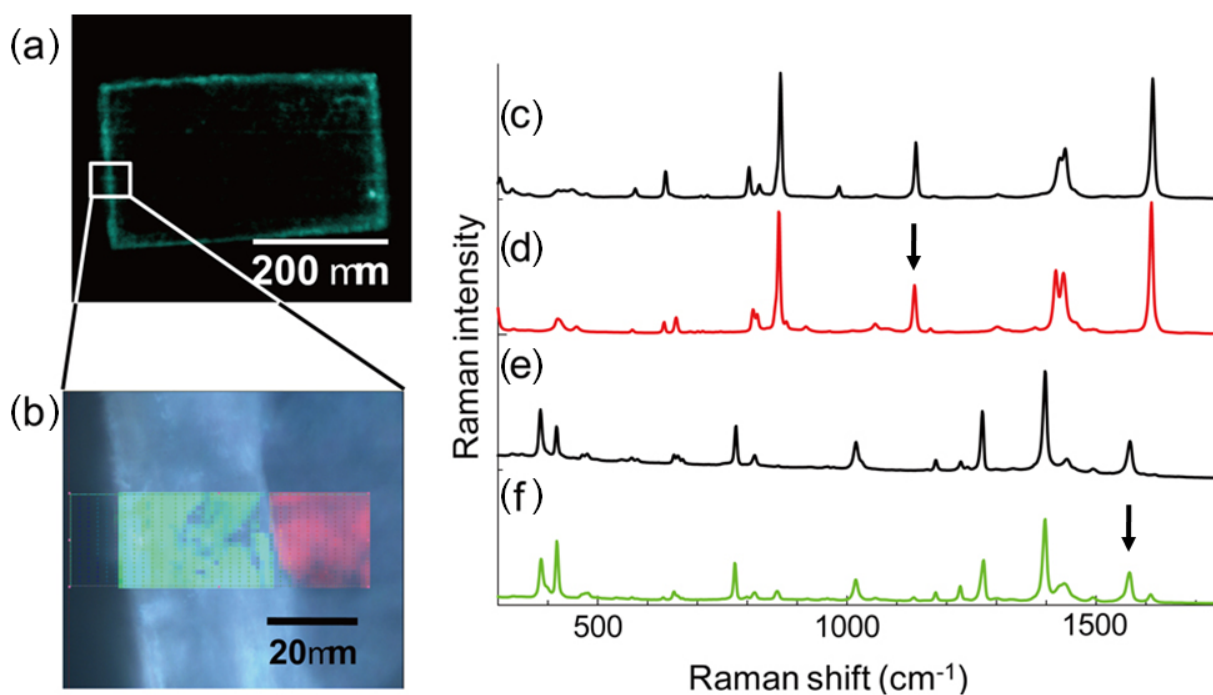


**Figure 4.** (a) The horizontally sliced CLSM image at the focal point at the middle of the crystal (b) The Raman mapping for the mechanically sliced core/shell crystal at the middle of the crystal. The Raman spectra obtained (c) from a single crystal of **(1)**, (d) the core part of **(1/2)**, (e) a single crystal of **(2)** and (f) the shell part of **(1/2)**. The arrows indicate the characteristic Raman signal corresponding to **(1)** and **(2)** that were used for the mapping in (b)

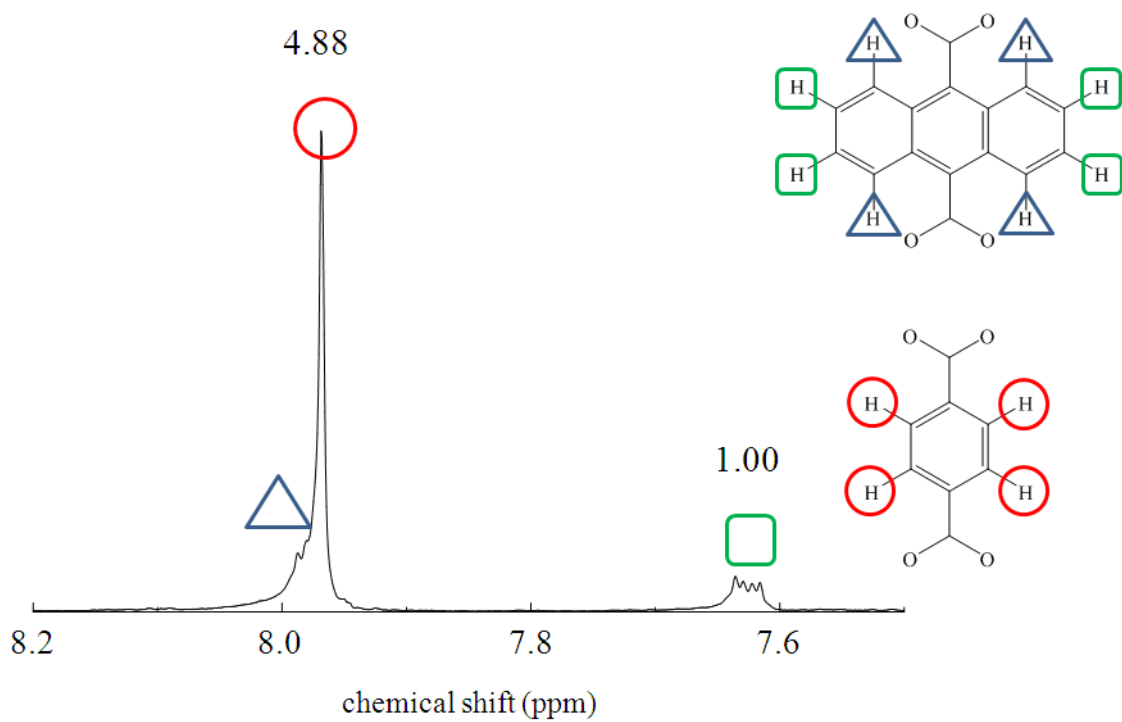


**Figure 5.**  $^1\text{H-NMR}$  spectrum of degassed core/shell crystal (1/2).

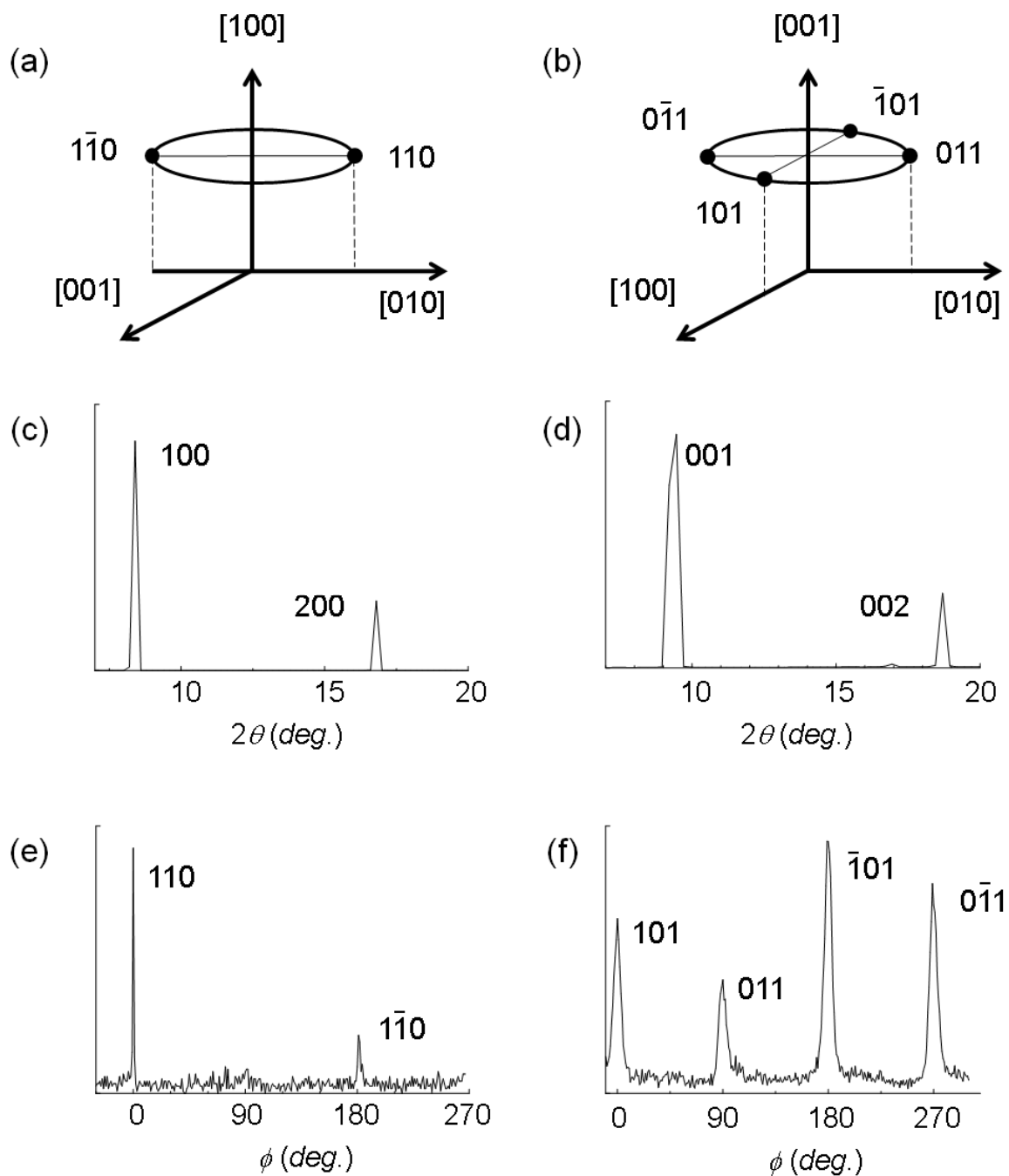


**Figure 6.** The reciprocal lattice space corresponding to the rotational scan, (a) around the [100] direction, and (b) around the [001] direction. The  $\theta$ - $2\theta$  scan of the core/shell crystal (**1/2**) on the glass substrate at the initial position ( $\chi = 90^\circ$ ), (c) with the  $a$  axis orientation, and (d) with the  $c$  axis orientation. The scan of the rotation angle, (e) around the [100] direction (the  $\phi$  scan), and (f) around the [001] direction.

We tested the accessibility of the guest petroleum molecules to the core crystal though the shell crystal. The guest-free core-shell crystals of **1/2** were separately immersed into either cetane or isocetane for a week. After filtration and drying, the MLRS technique was used to detect the characteristic signals of petroleum molecules inside the core crystal in the range 2600–3100  $\text{cm}^{-1}$  <sup>38</sup> (Figure 7). The Raman signal of cetane was observed when the excitation laser was focused at the core crystal, which suggested the successful travel of cetane through the pores of the shell framework and the crystal interfaces (Figure 7e, g). In contrast, no Raman signal indicative of isocetane was detected in either the core or shell crystals (Figure 7 f, h). This result indicates that the shell crystal restricts the adsorption of isocetane. When a single crystal of **2** was immersed into isocetane, no Raman signal was observed either (Figure 7d). Therefore, the bulkier branched isocetane was blocked by the steric effect of the small aperture of **2**. Note that this blocking indicated that there was no cracks or defects in the shell crystal that isocetane can pass through.

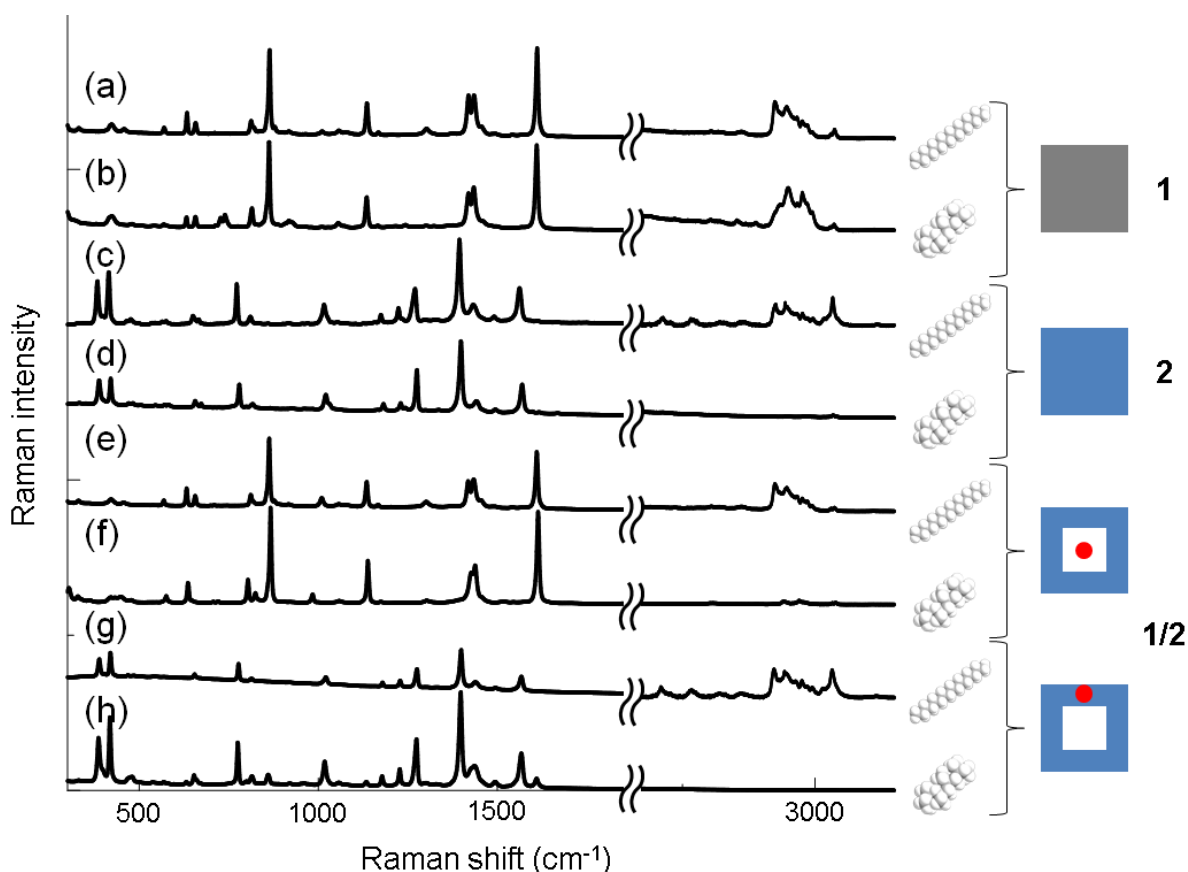


**Figure 7.** The Raman spectra obtained from the single crystal of **1** immersed in (a) cetane and (b) isocetane, from the single crystal of (**2**) immersed in (c) cetane and (d) isocetane, from the core portion of (**1/2**) immersed in (e) cetane and (f) isocetane, and from the shell portion of (**1/2**) immersed in (g) cetane and (h) isocetane. The red points in the core/shell crystal of (**1/2**) indicates the point at which the Raman laser is focused.

The preference for adsorbing cetane over isocetane was demonstrated by immersing single crystals of **1** and **2** and a core-shell crystal of **1/2** into a mixture of cetane/isocetane (1:1). After filtration and drying, these crystals were decomposed by hydrochloric acid and the adsorption ratio was determined by gas chromatography-mass spectrometry (GCMS; Figure 8). Branched isocetane (with a retention time of 2.72 min) was eluted from the GC column before its linear isomer cetane (with a retention time of 3.98 min). Whereas the large pores of **1** barely discriminated between these isomers, the small pores of **2** accumulated only the linear cetane molecules. The core-shell crystal also selectively adsorbed cetane owing to the small aperture of the shell crystal. When the cetane/isocetane ratio was decreased to 1:10 and 1:100 (Figure 9, and Figure 11a, respectively), the adsorption of isocetane in **1** increased. In contrast, the crystal of **2** and the core-shell crystal **1/2** maintained their selective adsorption of cetane.

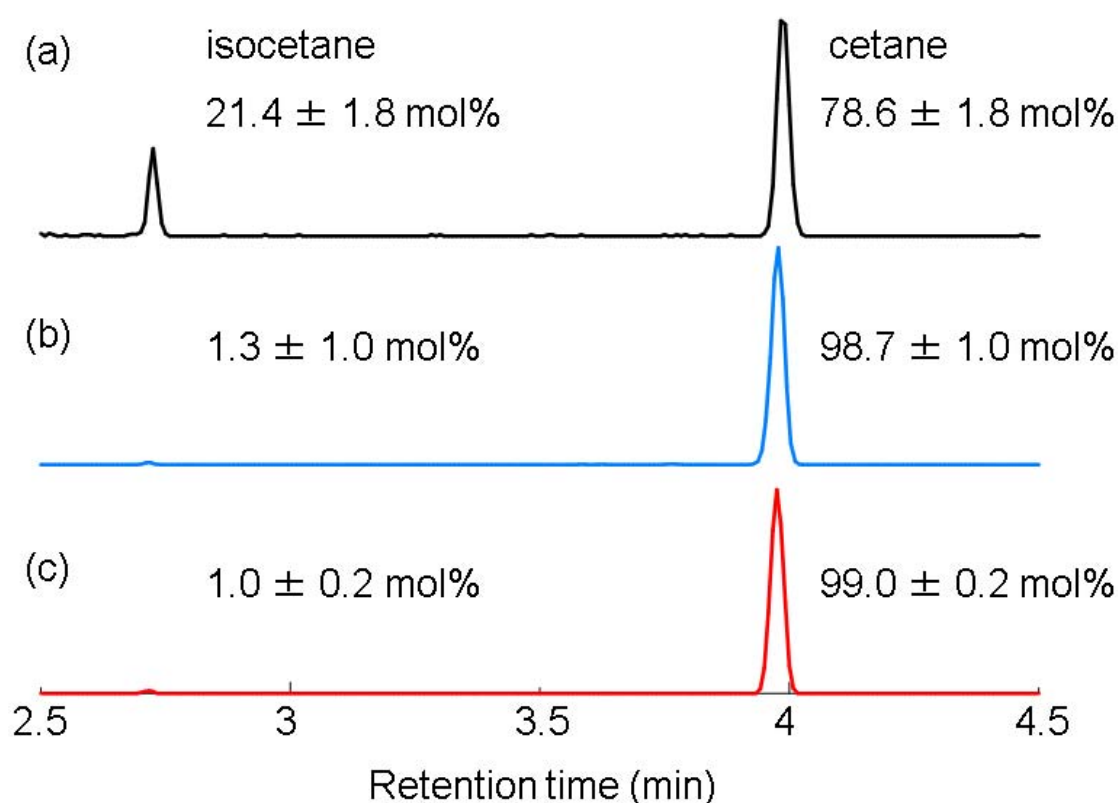


**Figure 8.** GC-MS spectra showed the ratio of cetane and isocetane adsorbed by **1**, **2**, and **1/2** at cetane/isocetane mixture ratios (1:1).

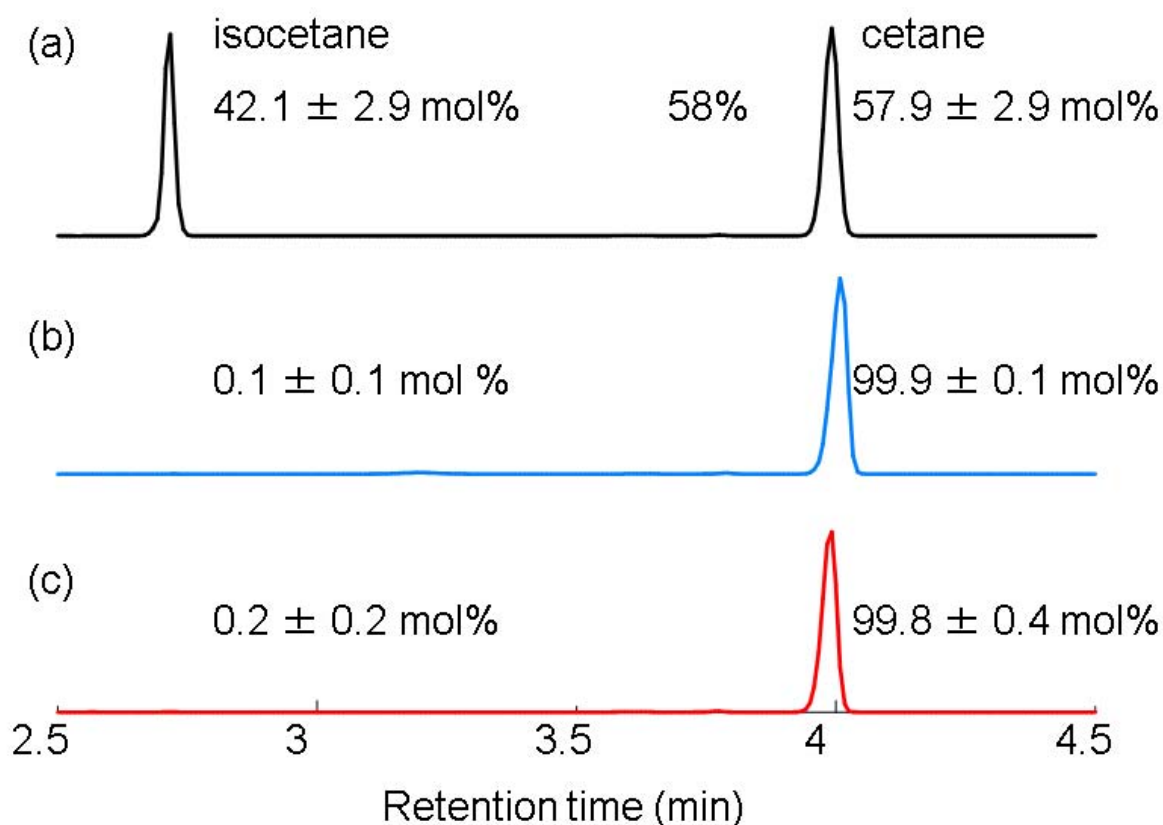


**Figure 9.** GC-MS spectra showed the ratio of cetane and isocetane adsorbed by **1**, **2**, and **1/2** at cetane/isocetane mixture ratios (1:10).

The storage capacity of cetane in the core–shell crystal of **1/2** was elucidated by thermogravimetric (TG) analysis. Because the weight loss of both the guest petroleum molecules and dabco<sup>39</sup> from the framework occurred from 250–330 °C, the weight loss from the guest molecules was calculated by subtracting the contribution of dabco from the total weight loss (Figure 10 and Table 1). For the 1:100 mixture of cetane/isocetane, the amount of cetane adsorbed in the core–shell crystal was estimated to be 26.9 wt%, which was twice that in the shell crystal of **2** (10.0 wt%; Figure 11b). This significant improvement in the cetane storage capacity arose from the large pore volume of the core framework of **1**. In contrast, the single crystal of **1** alone showed no selective adsorption, and both cetane (6.9 wt%) and isocetane (24.5 wt%) accumulated in its pores. Thus, covering the core crystal with the thin shell crystal is the key to the combination of selectivity for cetane and high storage capacity.

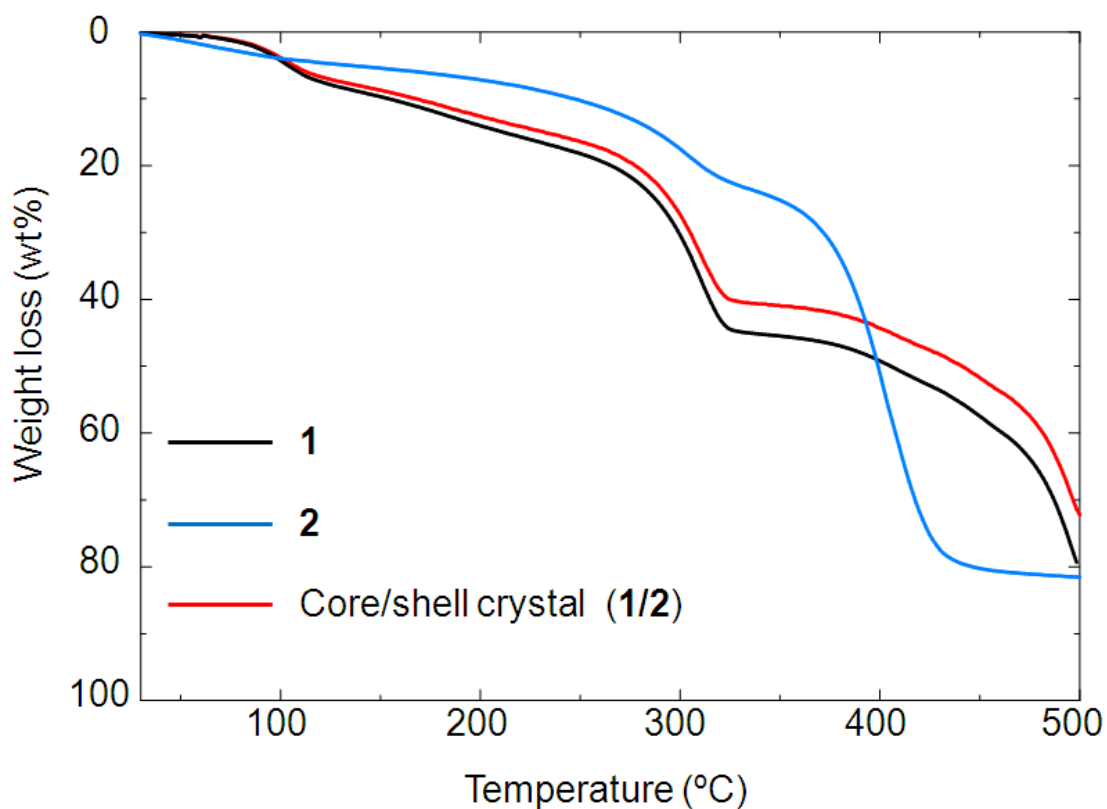


**Figure 10.** TG analysis showing the weight loss of alkane and dabco, from room temperature to 330 °C, followed by framework combustion

**Table S1.** The cetane storage amount of **1**, **2** and **1/2** at the cetane/isocetane mixture ratio (1:100)

	Host (g/mol)	a (wt%)	y (wt%)
<b>1</b>	571.15	44.9	31.4
<b>2</b>	771.39	23.1	10.0
<b>1/2</b>	612.20	40.3	26.9

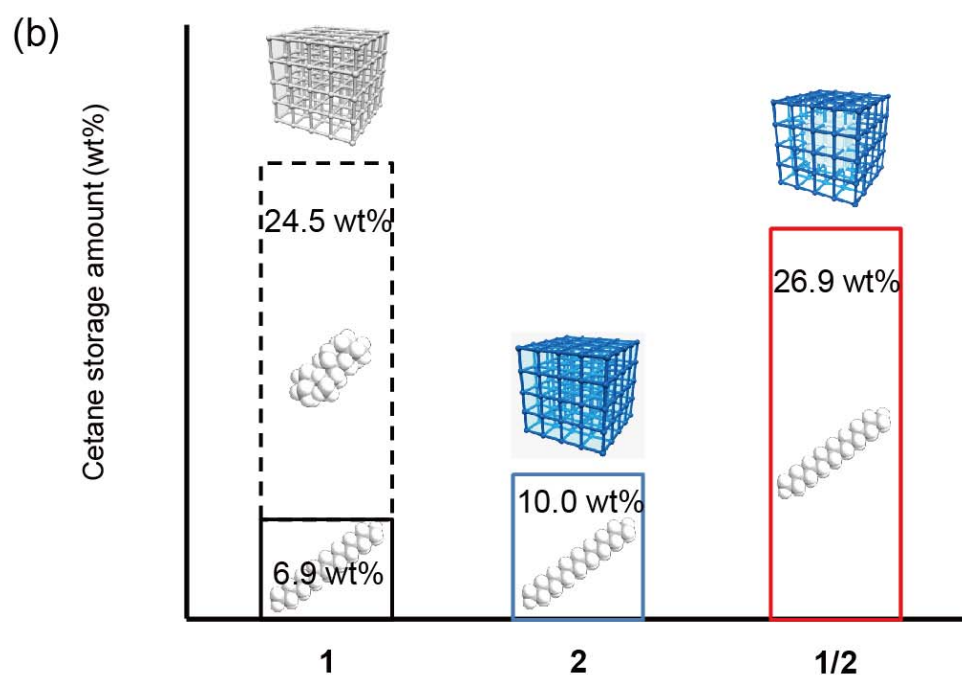
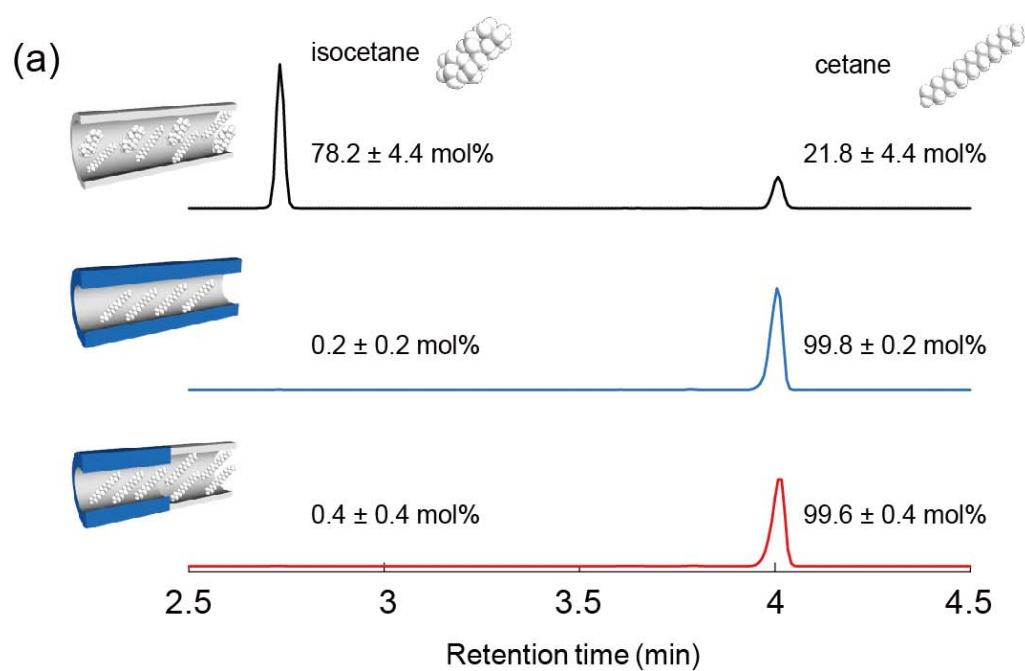


**Figure 11.** (a) The selective adsorption of cetane over isocetane from mixtures with a cetane :isocetane ratio of 1:100 was determined by GC-MS. The core/shell crystal only accumulated cetane (bottom) due to the small pores of the shell crystal of (2) (middle), which was in contrast to the preferential adsorption of isocetane by crystals of (1) (top). (b) The amount of cetane stored in (1), (2) and (1/2) when using a (1:100) mixture of cetane/isocetane.

## **Conclusion**

In conclusion, we have succeeded in sequential functionalization of PCP crystals by fabricating core–shell type heterostructures that exhibited size selectivity owing to the small aperture of the shell framework and high storage capacity owing to the large pore volume of the core framework. This successful integration of two contradictory spatial functions into one crystal was enabled by the heterogeneous arrangement of chemical functionalities on one basic framework skeleton. This first example of a multifunctional PCP crystal will enable further integration of other porous properties.

## Experimental Section

### Materials

Anhydrous DMF,  $\text{Zn}(\text{NO}_3)_2 \cdot 6\text{H}_2\text{O}$ , dabco, *n*-hexadecane, 2,4,4,6,8,8-heptametylnonane, *n*-hexane, and aqueous hydrochloric acid were purchased from Wako Pure Chemical Industries. 9,10-anthracenedicarboxylic acid ( $\text{H}_2\text{adc}$ ) was prepared according to a previously published procedure.<sup>40</sup>

### Synthesis

Compound **1** was prepared according to previously published procedures.<sup>34</sup> The reaction solution for **2** was prepared from  $\text{Zn}(\text{NO}_3)_2 \cdot 6\text{H}_2\text{O}$  (0.100 mg, 0.336 mmol), adc (0.089 mg, 0.336 mmol), and dabco (0.019 mg, 0.167 mmol) in DMF (4 mL). Dozens of single crystals of **1** were added to a 4 mL reaction solution. The reaction mixture was then heated to 393 K and maintained at that temperature for 3 days. After cooling, the coreless hybridized crystals of **1/2** were harvested.

### Cnfocal Laser Scanning Microscopy

The core-shell crystals (**1/2**) were immersed into DMF solvent and placed on a glass substrate. The fluorescence images at different depths were obtained by a FV1000 microscope (Olympus) with a semiconductor laser at 370 nm, and fluorescent emission was collected in the 400–430 nm range

### Microscopic Laser Raman Spectroscopy

The Raman spectra were measured by a LabRAM HR-800 spectrometer (Horiba Jobin Yvon Ltd.) with a semiconductor laser at 785 nm. The single crystal samples of **1**, **2**, or **1/2** were placed on the glass substrate.

### Gas chromatography mass spectrometry

Gas chromatography mass spectrometry (GC-MS) was performed using a SHIMADZU QP2010 with a DB-5MS capillary column (length 30 m, film thickness 0.25 mm, Agilent Technologies). The following conditions were employed: electron energy 70 eV, scan range from  $m/z$  50 to 276 in 0.5 s, ion source temperature 200 °C, transfer line temperature 200 °C, injector temperature 300 °C, column temperature 200 °C for 5 min, and He carrier gas flow rate 0.51 mL min<sup>-1</sup>. The crystals, which were immersed in the cetane/isocetane mixture, were decomposed by aqueous hydrochloric acid and all alkane molecules were extracted by *n*-hexane solvent. After the extraction, the adsorption ratio

of cetane/isocetane was analyzed by GC-MS.

### **Thermogravimetric Analysis**

Thermogravimetric (TG) analyses were performed using a Rigaku Thermo plus TG 8120 apparatus in the temperature range between 303 K and 773 K in a N<sup>2</sup> atmosphere and at a heating rate of 10 K min<sup>-1</sup>

### **Synchrotron X-ray Diffraction**

Synchrotron X-ray measurements were performed with a four-circle diffractometer having  $\phi$ ,  $\chi$ ,  $\theta$ , and  $2\theta$  circles at beamline BL13XU for surface and interface structures, SPring-8. An X-ray beam ( $50 \times 50 \mu\text{m}^2$ ) was incident on the sample. Si-PIN photo-diode and Oxford scintillation detectors were used for the measurement. The core-shell crystal (1/2) with a size over 300  $\mu\text{m}$  was fixed on the glass substrate with double-faced adhesive. The measurement was carried out under Helium gas condition. For each sample, the  $\theta$ - $2\theta$  scan at the initial position ( $\chi = 90^\circ$ ) was carried out to determine the orientation of the crystal, either the a axis orientation or the c axis orientation, and then the angles of  $\phi$ ,  $\chi$ ,  $\theta$ , and  $2\theta$  were moved to a desired Bragg position where diffractions were recorded.

## References

- (1) E. Katz, I. Willner, *Angew. Chem. Int. Ed.* **2004**, *43*, 6042-6108.
- (2) D. E. Discher, A. Eisenberg, *Science* **2002**, *297*, 967-973.
- (3) S. R. Batten, R. Robson, *Angew. Chem. Int. Ed.* **1998**, *37*, 1460-1494.
- (4) O. M. Yaghi, M. O'Keeffe, N. W. Ockwig, H. K. Chae, M. Eddaoudi, J. Kim, *Nature* **2003**, *423*, 705-714.
- (5) S. Kitagawa, R. Kitaura, S. Noro, *Angew. Chem. Int. Ed.* **2004**, *43*, 2334-2375.
- (6) G. Férey, C. Serre, *Chem. Soc. Rev.* **2009**, *38*, 1380-1399.
- (7) J. S. Seo, D. Whang, H. Lee, S. I. Jun, J. Oh, Y. J. Jeon, K. Kim, *Nature* **2000**, *404*, 982-986.
- (8) X. Zhao, B. Xiao, A. J. Fletcher, K. M. Thomas, D. Bradshaw, M. J. Rosseinsky, *Science* **2004**, *306*, 1012-1015.
- (9) S. Bureekaew, S. Horike, M. Higuchi, M. Mizuno, T. Kawamura, D. Tanaka, N. Yanai, S. Kitagawa, *Nat. Mater.* **2009**, *8*, 831-836.
- (10) J. A. Hurd, R. Vaidhyanathan, V. Thangadurai, C. I. Ratcliffe, I. L. Moudrakovski, G. K. H. Shimizu, *Nat. Chem.* **2009**, *1*, 705-710.
- (11) O. Shekhah, H. Wang, M. Paradinas, C. Ocal, B. Schöppach, A. Terfort, D. Zacher, R. A. Fischer, C. Wöll, *Nat. Mater.* **2009**, *8*, 481-484.
- (12) Y. Inokuma, T. Arai, M. Fujita, *Nat. Chem.* **2010**, *2*, 780-783.
- (13) D. Maspoch, D. Ruiz-Molina, K. Wurst, N. Domingo, M. Cavallini, F. Biscarini, J. Tejada, C. Rovira, J. Veciana, *Nat. Mater.* **2003**, *2*, 190-195.
- (14) B. Xiao, P. J. Byrne, P. S. Wheatley, D. S. Wragg, X. Zhao, A. J. Fletcher, K. M. Thomas, L. Peters, J. S. O. Evans, J. E. Warren, W. Zhou, R. E. Morris, *Nat. Chem.* **2009**, *1*, 289-294.
- (15) J. R. Li, H. C. Zhou, *Nat. Chem.* **2010**, *2*, 893-898.
- (16) O. K. Farha, O. Yazaydin, I. Eryazici, C. Malliakas, B. Hauser, M. G. Kanatzidis, S. T. Nguyen, R. Q. Snurr, J. T. Hupp, *Nat. Chem.* **2010**, *2*, 944-948.
- (17) S. Yang, X. Lin, A. J. Blake, G. S. Walker, P. Hubberstey, N. R. Champness, M. Schröder, *Nat. Chem.* **2009**, *1*, 487-493.
- (18) Z. Wang, S. M. Cohen, *Chem. Soc. Rev.* **2009**, *38*, 1315-1329.
- (19) T. Devic, P. Horcajada, C. Serre, F. Salles, G. Maurin, B. Moulin, D. Heurtaux, G. Clet, A. Vimont, J.-M. Grenèche, B. Le Ouay, F. Moreau, E. Magnier, Y. Filinchuk, J. Marrot, J.-C. Lavalley, M. Daturi, G. Férey, *J. Am. Chem. Soc.* **2010**, *132*, 1127-1136.
- (20) R. Banerjee, H. Furukawa, D. Britt, C. Knobler, M. O'Keeffe, O. M. Yaghi, *J. Am.*

*Chem. Soc.* **2009**, *131*, 3875-3877.

- (21) R. Matsuda, R. Kitaura, S. Kitagawa, Y. Kubota, R. V. Belosludov, T. C. Kobayashi, H. Sakamoto, T. Chiba, M. Takata, Y. Kawazoe, Y. Mita, *Nature* **2005**, *436*, 238-241.
- (22) H. Sato, R. Matsuda, K. Sugimoto, M. Takata, S. Kitagawa, *Nat. Mater.* **2010**, *9*, 661-666.
- (23) M. Dincă, A. Dailly, Y. Liu, C. M. Brown, D. A. Neumann, J. R. Long, *J. Am. Chem. Soc.* **2006**, *128*, 16876-16883.
- (24) S. Hasegawa, S. Horike, R. Matsuda, S. Furukawa, K. Mochizuki, Y. Kinoshita, S. Kitagawa, *J. Am. Chem. Soc.* **2007**, *129*, 2607-2614.
- (25) H. Deng, C. J. Doonan, H. Furukawa, R. B. Ferreira, J. Towne, C. B. Knobler, B. Wang, O. M. Yaghi, *Science* **2010**, *327*, 846-850.
- (26) T. Fukushima, S. Horike, Y. Inubushi, K. Nakagawa, Y. Kubota, M. Takata, S. Kitagawa, *Angew. Chem. Int. Ed.* **2010**, *49*, 4820-4824.
- (27) B. Chen, C. Liang, J. Yang, D. S. Contreras, Y. L. Clancy, E. B. Lobkovsky, O. M. Yaghi, S. Dai, *Angew. Chem. Int. Ed.* **2006**, *45*, 1390-1393.
- (28) B. Wang, A. P. Côté, H. Furukawa, M. O’Keeffe, O. M. Yaghi, *Nature* **2008**, *453*, 207-212.
- (29) L. Alaerts, C. E. A. Kirschhock, M. Maes M. A. van der Veen, V. Finsy, A. Depla, J. A. Martens, G. V. Baron, P. A. Jacobs, J. F. M. Denayer, D. E. De Vos, *Angew. Chem. Int. Ed.* **2007**, *46*, 4293-4297.
- (30) H. Bux, F. Liang, Y. Li, J. Cravillon, M. Wiebcke, J. Caro, *J. Am. Chem. Soc.* **2009**, *131*, 16000-16001.
- (31) G. Knothe, A. C. Matheaus, T.W. Ryan III, *Fuel* **2003**, *82*, 971-975.
- (32) L. Xing-cai, Y. Jian-guang, Z. Wu-gao, H. Zhen, *Fuel* **2004**, *83*, 2013-2020.
- (33) K. Seki, W. Mori, *J. Phys. Chem. B* **2002**, *106*, 1380-1385.
- (34) D. N. Dybtsev, H. Chun, K. Kim, *Angew. Chem. Int. Ed.* **2004**, *43*, 5033-5036.
- (35) B. Q. Ma, K. L. Mulfort, J. T. Hupp, *Inorg. Chem.* **2005**, *44*, 4912-4914.
- (36) D. Tanaka, S. Horike, S. Kitagawa, M. Ohba, M. Hasegawa, Y. Ozawa, K. Toriumi, *Chem. Commun.* **2007**, 3142-3144.
- (37) S. Furukawa, K. Hirai, K. Nakagawa, Y. Takashima, R. Matsuda, T. Tsuruoka, M. Kondo, R. Haruki, D. Tanaka, H. Sakamoto, S. Shimomura, O. Sakata, S. Kitagawa, *Angew. Chem. Int. Ed.* **2009**, *48*, 1766-1770.
- (38) R. G. Snyder, H. L. Strauss, C. A. Elllger, *J. Phys. Chem.* **1982**, *86*, 5145-5150.
- (39) Z. Chen, S. Xiang, D. Zhao, B. Chen, *Cryst. Growth Des.* **2009**, *9*, 5293-5296.
- (40) S. Jones, C. J. Atherton, R. J. M. Elsegood, W. Clegg, *Acta Crystallogr. Sect. C*

**2000**, 56, 881-883.

## Chapter 4

# Targeted Functionalisation of a Hierarchically-Structured Porous Coordination Polymer Crystal Enhances its Entire Function

### Abstract

A core-shell type porous coordination polymer (PCP) crystal has been synthesized:  $[\text{Zn}_2(\text{adc})_2(\text{dabco})]_n$  (**1**) as the core crystal and  $[\text{Zn}_2(\text{abdc})_2(\text{dabco})]_n$  (**2**) as the shell crystal (adc = 9,10-anthracene dicarboxylate, dabco = diazabicyclo[2.2.2]octane, abdc = 2-amino-1,4-benzene dicarboxylate). After the formation of the core-shell structure, a free carboxyl group was embedded in the shell crystal via heterogeneous acylation of amino groups with succinic anhydride to enhance the selectivity for *N,N*-dimethylaniline (DMA). The shell crystal allowed the core crystal to selectively accommodate DMA, thus leading to turning on intense exciplex emission by the formation of excited state between anthracene moiety and DMA.

## Introduction

As being particularly implemented in the field of biochemistry such as enzymes, antibodies and biological membranes, chemical modification to a distinct component in complex system impacts on the rest and even sophisticates the function of entire system.<sup>1-2</sup> This is because the overall function is dictated by synergistic collaboration of all the components. In that context, we applied this prominent feature to hybrid porous materials to stimulate the emergence of new applications.

Porous coordination polymers (PCPs) or metal-organic frameworks (MOFs)<sup>3-9</sup> have been intensively studied due to a wide variety of the applications such as adsorption,<sup>10-12</sup> separation,<sup>13-14</sup> catalysis<sup>15-16</sup> and chemical sensing.<sup>17-19</sup> Most recently, we demonstrated that the synergistic collaboration between distinct parts in a core-shell PCP determine its entire property: selectivity at the shell crystal and high storage capacity at the core crystal.<sup>20</sup> Considering the features of such complex systems, the functionalization on specific targeted part in the core-shell PCPs will improve the performance of entire system.

Because guest species are obliged to pass through the shell crystal before accessing the core crystal, the targeted functionalization on the shell crystal definitely affects the overall porous property of the hybrid crystal system. Here, we introduce amino group only into the shell crystal that can react with carboxyl group by PSM.<sup>21-24</sup> Such modification allows for the conversion of pore-surface property and totally changes the propensity of guest affinity. The introduction of the fluorescent unit into the core crystal for detection of the quantity of guest molecules in the pores allows us to visualize the molecular selectivity induced by PSM (Figure 1).

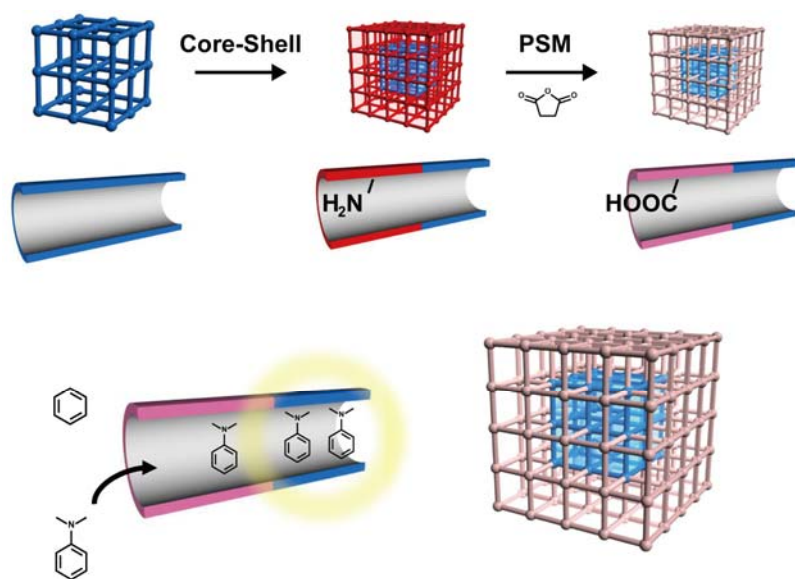


**Figure 1.** Schematic illustration of targeted functionalization.

## Results and Discussion

A series of three-dimensional PCPs,  $[\text{Zn}_2(\text{dicarboxylate})_2(\text{dabco})]_n$ ,<sup>25-28</sup> gives single crystals with a well-defined morphology, in which the dicarboxylate layer ligands link to the zinc paddlewheel clusters to form two-dimensional square lattices connected by dabco pillar ligands at the lattice points (dabco = 1,4-diazabicyclo[2.2.2]octane), as shown in Figure 2a-b. We selected  $[\text{Zn}_2(\text{adc})_2(\text{dabco})]_n$ <sup>28</sup> (**1**) as the core framework (adc = 9,10-anthracene dicarboxylate) and  $[\text{Zn}_2(\text{NH}_2\text{-bdc})_2(\text{dabco})]_n$  (**2**) as the shell framework (NH<sub>2</sub>-bdc = 2-amino-1,4-benzenedicarboxylate). For a successful hybridization by epitaxial growth two frameworks should have same coordination geometry.<sup>29-30</sup> However, the crystal structure of **2** has not yet been reported. Prior to the synthesis of the core-shell crystal, we successfully grew a single crystal of **2** and determined that the crystal structure would suit to hybridization. Two frameworks were then hybridized into one crystal. Single crystals of **1** were put into a reaction solution of  $\text{Zn}(\text{NO}_3)_2 \cdot 6\text{H}_2\text{O}$ , 2-amino-1,4-benzenedicarboxylic acid and dabco in *N,N*-dimethylformamide (DMF), and the solution was heated at 60 °C. The shell crystal of **2** was grown on the core crystal. The core-shell crystals were harvested after cooling to room temperature.

Prior to the PSM reaction in the core-shell PCP (**1/2**), the single crystal of **2** was modified using a heterogeneous acylation of its pendant amino groups with succinic anhydride, giving rise to a single crystal of **p2** (PSM modified **2** is denoted as **p2**).<sup>22</sup> We used <sup>1</sup>H-NMR technique to determine the conversion ratio of the amino group as 52% (Figure 2). Although each pore of **2** contains two reactive amino groups, succinic anhydride reacted with one out of two amino groups. This is because the pore size of **2** limits to the accommodation for one succinic acid and the second reaction is sterically restricted. In the same manner, the PSM reaction in the core-shell crystal (**1/2**) was carried out, giving rise to a PSM modified core-shell PCP (**1/p2**).

The optical microscopic image (Figure 3c) of **1/p2** clearly showed that the core crystal of **1** surrounded the colorless shell crystal of **p2** and the PSM reaction did not significantly damage the core-shell crystal. Each part of the hybridized crystal was identified as the respective framework structure by microscopic laser Raman spectroscopy (MLRS) (Figure 3d–h). The Raman signals of the core and shell crystal correspond to those of **1** and **p2**. The spectral correspondence suggests the formation of core-shell crystals of **1/p2**.

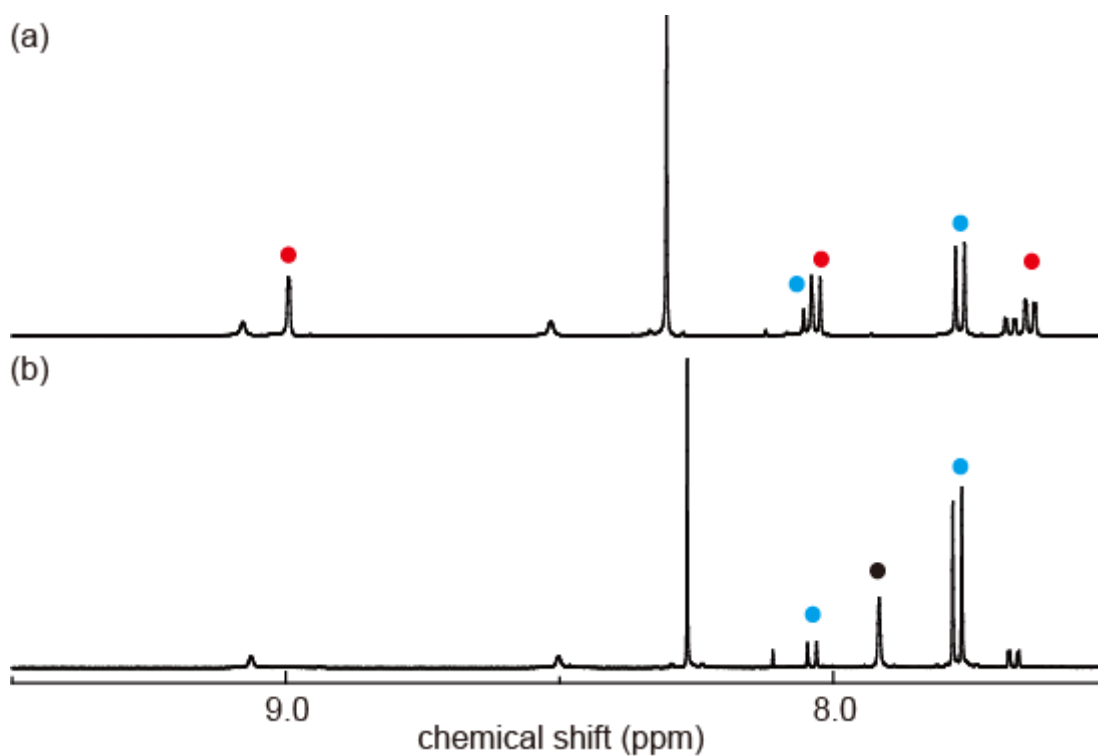


**Figure 2.**  $^1\text{H-NMR}$  spectra of a) **2** and b) **p2**. Red, blue and black circles are assigned to **p2**, **2** and DMF, respectively. The results suggest 52 % of  $\text{NH}_2$ -groups was reacted with succinic anhydride.

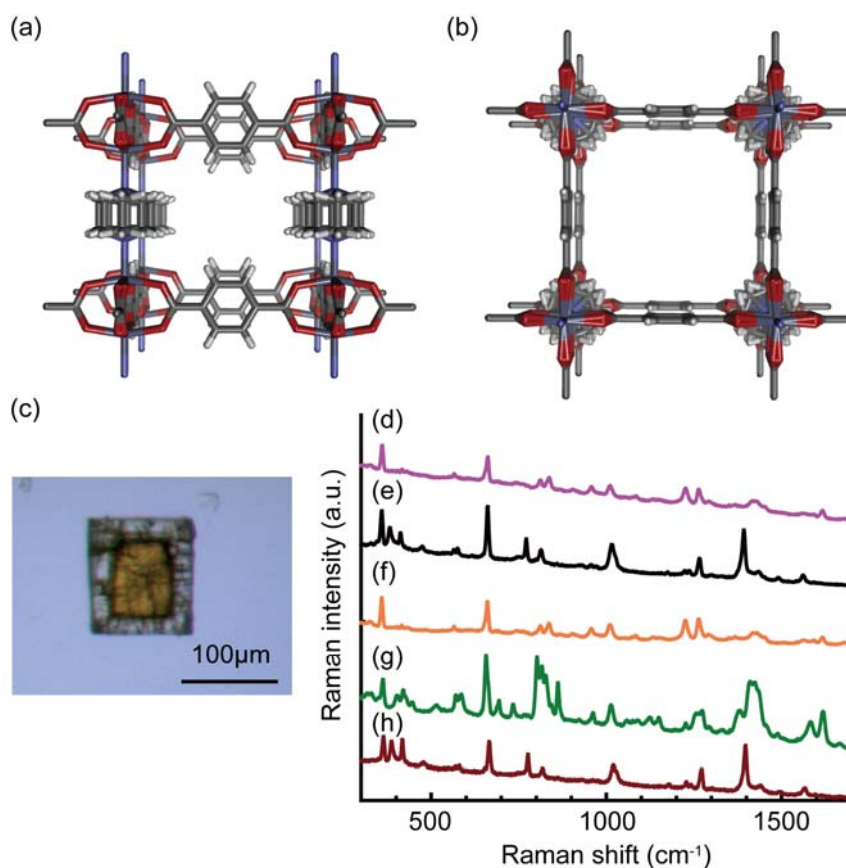


**Figure 3.** (a) The crystal structure of  $[\text{M}_2(\text{dicarboxylate})_2(\text{diamine})]_n$ , viewed along the  $a$  axis, (b)  $c$  axis. (c) The optical microscope image of the core-shell crystal **1/p2**. (d) The

microscopic laser Raman spectroscopic measurement of the core crystal of **1/p2**, (e) the shell crystal of **1/p2**, (f) the single crystal of **p2**, (g) the single crystal of **2**, (h) the single crystal of **1**.

The elucidation of the structural relationship between the core and shell frameworks was accomplished by synchrotron X-ray diffraction measurements using a four-circle diffractometer at beamline BL13XU for surface and interfacial structures, SPring-8. As we observed the sharp and single diffraction peaks at the 110 and 1-10 Bragg positions with 180° periodicity and at the 101, 011, -101, and 0-11 Bragg positions with 90° periodicity, the shell crystal of **2** grew epitaxially on both the {100} and {001} surfaces (Figure 4) and the single crystallinity of the shell crystal was maintained even after the PSM reaction. These results suggest the pore connection at the crystal interface between two frameworks.

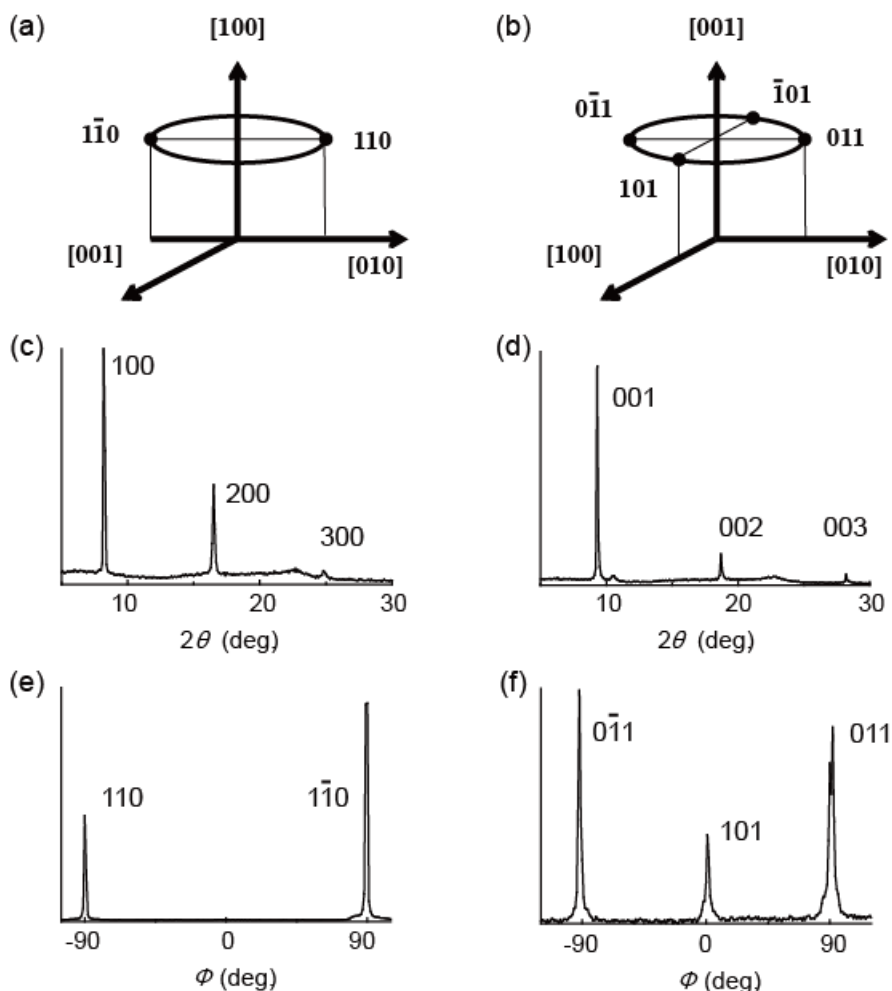


**Figure 4.** (a) The crystal structure of  $[M_2(\text{dicarboxylate})_2(\text{diamine})]_n$ , viewed along the  $a$  axis, (b)  $c$  axis. (c) The optical microscope image of the core-shell crystal **1/p2**. (d) The microscopic laser Raman spectroscopic measurement of the core crystal of **1/p2**, (e) the shell crystal of **1/p2**, (f) the single crystal of **p2**, (g) the single crystal of **2**, (h) the single crystal of **1**.

To examine the effect of PSM on the guest preference, *N,N*-dimethylaniline (DMA) and benzene were chosen as guest molecules for the following two reasons: (a) both are aromatic molecules but possess different chemical functionalities, which are suited to investigation of the selectivity based on chemical affinity; (b) the core crystal detects the accommodation of DMA by fluorescence based on the exciplex formation between anthracene unit (electron acceptor) and DMA (electron donor).<sup>31-32</sup> The preference for adsorbing DMA over benzene was demonstrated by immersing single crystals of **1**, **2**, **p2** and the core-shell crystals of **1/2**, **1/p2** into a mixture of DMA/benzene (1:1). After filtration and drying, these crystals were decomposed by hydrochloric acid and the adsorption ratio was determined by gas chromatography-mass spectrometry (GC-MS) (Table1). Whereas **1** and **2** barely discriminated between these aromatic molecules, **p2** preferentially adsorbed DMA molecules most likely due to the interaction between free carboxyl group being hung on the pore wall and adsorbed DMA (Figure 5). The red shift of carbonyl stretching vibration (from 1704 cm<sup>-1</sup> to 1682 cm<sup>-1</sup>) implied the interaction between free carboxyl group and DMA.<sup>33</sup> Unfortunately, peak shift of DMA was not clear in IR spectra, because the most characteristic peaks of DMA overlapped with the peaks of **p2**. However, the results of IR and GC-MS suggested that the embedded carboxyl group contributed to the selective adsorption of DMA most likely through the interaction between carboxyl group from the pore surface and tertiary amine from DMA. Although the core-shell crystal (**1/2**) did not show selectivity for these molecules, the PSM-modified core-shell crystal (**1/p2**) selectively adsorbed DMA. Furthermore, the strong Raman signal of DMA was detected in the core part of **1/p2**, which indicated the selective accommodation of DMA in the core part (Figure 6).<sup>34</sup> These results suggested that the functionalization of the shell crystal induced the selective accommodation of DMA even in the core crystal.

**Table 1.** Adsorption ratio of the single crystals of **1**, **2**, **p2** and the core/shell crystals of **1/2**, **1/p2** soaked in mixtures (DMA/benzene).

ratio \ compound	1:1
<b>1</b>	53:47
<b>2</b>	42:58
<b>p2</b>	82:18
<b>1/2</b>	39:61
<b>1/p2</b>	80:20

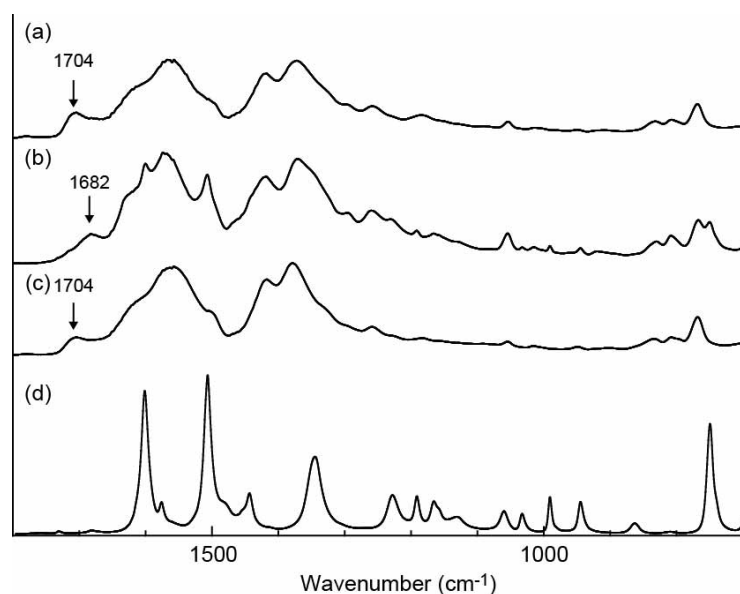


**Figure 5.** (a) Attenuated total reflection IR spectra of **p2** with benzene, (b) with DMA, (c) degassed **p2**, (d) DMA. Blue shift of CO vibration in free COOH group was observed in **p2** with DMA.

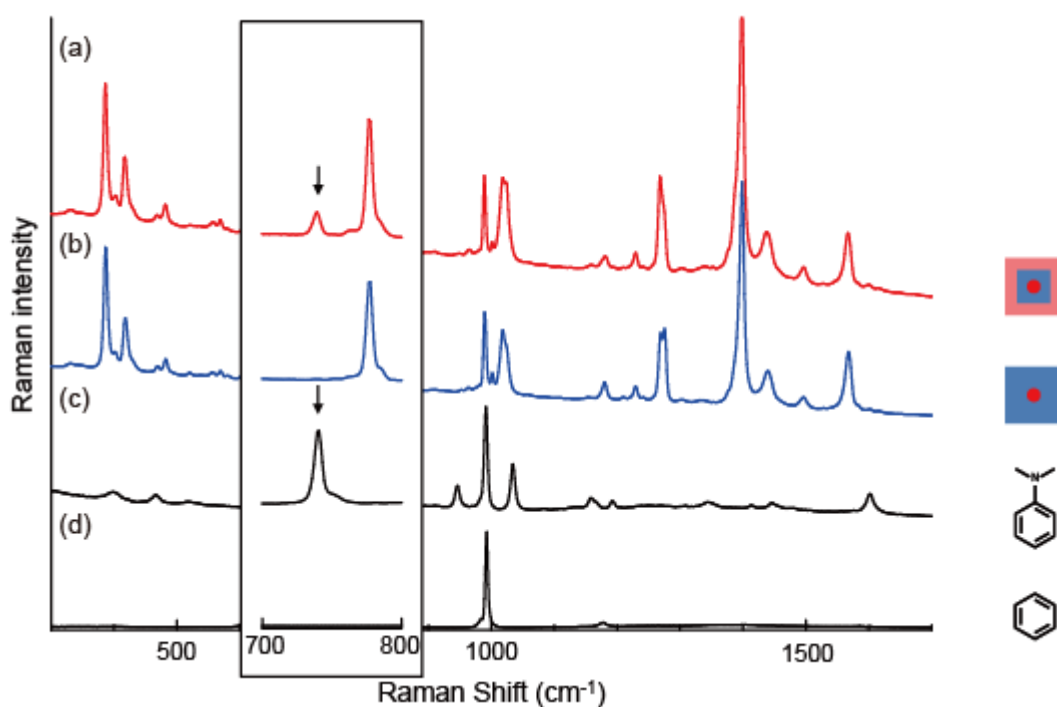


**Figure 6** The Raman spectra obtained from (a) the core part of **1/p2**, (b) **1** immersed in the mixture, (c) DMA and (d) benzene. The red points in the core-shell crystal of indicates the point at which the Raman laser is focused. The arrows indicate the characteristic Raman signal of DMA.

The fluorescent property of the core-shell crystal of **1/p2** was elucidated by confocal laser scanning microscopy (CLSM) technique (Figure 7a). Prior to the analysis of the core-shell crystal of **1/p2**, each fluorescent spectra of **1** with DMA and benzene were obtained using CLSM, green and blue dot lines, respectively, as shown in Figure 7b. Whereas **1** with benzene showed the fluorescence of anthracene unit, **1** with DMA showed highly efficient quenching in the fluorescence of monomeric anthracene and a new broad emission band in the range from 400 to 700 nm. The emission with large Stokes shift represents a photoinduced CT complex, an exciplex between the host anthracene unit and the guest DMA molecules.<sup>28</sup> The single crystals of **1** immersed in the mixture simultaneously showed broad exciplex emission (from 400 to 700 nm) and monomeric anthracene fluorescence (420 nm). In contrast, the fluorescent spectra from the core-shell crystal (**1/p2**) that was immersed in the mixture mainly showed exciplex fluorescence. The maximum intensity of the exciplex emission in the core crystal is  $1.9 \pm 0.3$  times stronger than the single crystal of **1** itself (Figure 7b). The stronger fluorescent intensity can be interpreted as the higher population of DMA in the core crystal as the consequence of selective filtering at the shell crystal. Thus, enhancement of guest selectivity of the shell crystal improves the intensity of the guest-responsive fluorescence of the core-shell crystal.

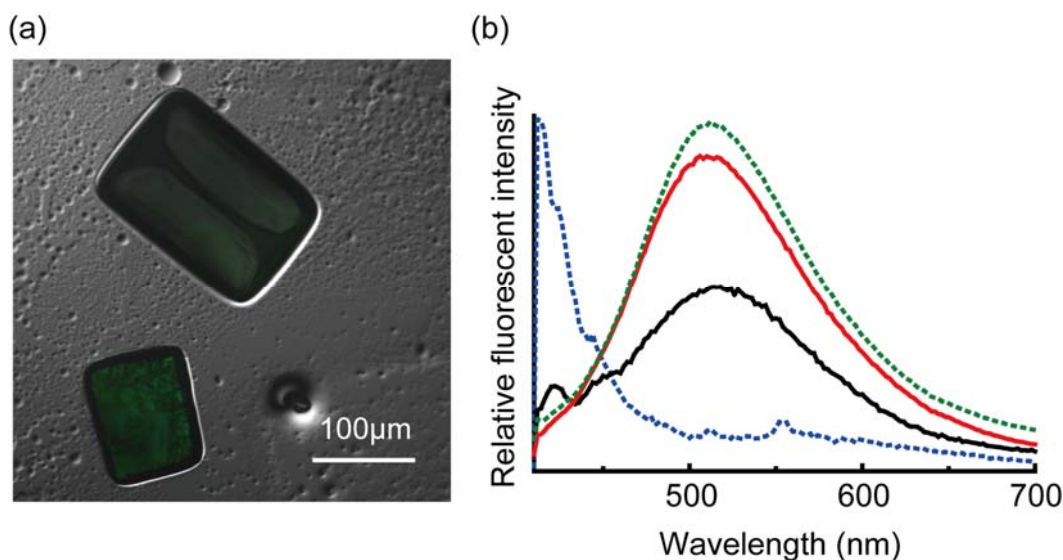


**Figure 7.** (a) The horizontally sliced CLSM image at the focal point at the middle of the core-shell crystal **1/p2** (lower) and single crystal of **1** (upper) immersed in the mixture for two days. (b) fluorescent spectra obtained using CLSM of **1** in DMA (green dot), **1** in benzene (blue dot), **1/p2** in the mixture (red) and **1** in the mixture (black). The excitation wavelengths is 405 nm.

## Conclusion

In conclusion, we demonstrated that functionalization only of the shell crystal sophisticated the function of the core-shell PCP crystal. The PSM-modified core-shell PCP crystal accumulated large amount of DMA over benzene and exhibited intense exciplex fluorescence. This example of further functionalization of hierarchically-structured PCP crystal will enable us to create a wide variety of multifunctional PCPs.

## Experimental Section

### Materials

Zn(NO<sub>3</sub>)<sub>2</sub>•6H<sub>2</sub>O, 2-amino-1,4-benzenedicarboxylic acid (H<sub>2</sub>abdc), 1,4-diaza[2.2.2]bicyclooctane (dabco), succinic anhydride, *N,N*-dimethylformamide (DMF), methanol (MeOH), *N,N*-dimethylaniline and benzene were purchased from Wako Pure Chemical Industries. 9,10-anthracene dicarboxylic acid (adc) was prepared according to the literature procedures.<sup>35</sup>

### Synthesis of 1

The solution of Zn(NO<sub>3</sub>)<sub>2</sub>•6H<sub>2</sub>O (125 mg, 0.420 mmol), H<sub>2</sub>adc (110 mg, 0.414 mmol), and dabco (23.8 mg, 0.213 mmol) in 25 mL DMF/MeOH (DMF : MeOH = 1 : 1) was stirred for several hours. After the white tiny crystals were removed by filtration, the transparent solution was diluted four times with DMF/MeOH. The solution was heated up to 333 K for 2 days. After cooling, the crystals were harvested.

### Synthesis of 1/2

The solution of Zn(NO<sub>3</sub>)<sub>2</sub>•6H<sub>2</sub>O (104 mg, 0.35 mmol), H<sub>2</sub>abdc (73 mg, 0.40 mmol), and dabco (72 mg, 0.64 mmol) in 10 mL DMF was stirred for several hours. After the white precipitates were removed by filtration, the dozens of well-dispersed single crystals of **1** were put into the solution. The solution was heated up to 333 K for 4 days. After cooling, the crystals were harvested.

### Post-synthetic modification of 1/2

Post-synthetic modification was performed according to the literature procedures.<sup>36</sup> Dozens of the core/shell crystal (**1/2**) was put in a container with succinic anhydride dissolved in CHCl<sub>3</sub>. After the sample was allowed to stand for two days, the crystals were washed with CHCl<sub>3</sub> then soaked in pure CHCl<sub>3</sub> for 3 days, with fresh CHCl<sub>3</sub> added every day. After the soaking, the crystals were stored in the last CHCl<sub>3</sub> solution until being analyzed.

### Synthesis of single crystal of 2

The solution of dabco (0.56 mg, 0.005 mmol) dissolved in 2 mL toluene was slowly layered on the solution of Zn(NO<sub>3</sub>)<sub>2</sub>•6H<sub>2</sub>O (2.98 mg, 0.01 mmol) and H<sub>2</sub>abdc (1.82 mg, 0.01 mmol) dissolved in 2 mL DMF, where a mixture of DMF/toluene (1:1) was placed between two layered solutions. The brown cuboid crystals suitable for

single crystal X-ray analysis were obtained after three month. Elemental analysis calcd. for  $C_{31}H_{47}N_7O_{11}Zn \{[Zn(abdc)(dabco)] \cdot (DMF)_3\}_n$ : C, 45.16; H, 5.746; N, 11.89, Found: C, 44.86; H, 5.47; N, 11.97.

### Characterization methods

The compounds were characterized with X-ray diffraction (XRD), microscopic laser Raman spectroscopy, synchrotron XRD, thermogravimetry (TG) and elemental analysis. Powder X-Ray diffraction (XRD) studies were performed using a Rigaku diffractometer with Cu  $K\alpha$  radiation ( $\lambda = 1.5418 \text{ \AA}$ ). The Raman spectra were measured by a LabRAM HR-800 spectrometer (Horiba Jobin Yvon Ltd.) with a semiconductor laser at 785 nm. TG measurements were carried out by Thermo plus EVO II. Elemental analysis was carried out on a Flash EA 1112 series, Thermo Finnigan instrument. Single crystal X-ray diffraction measurements were made on a Rigaku AFC10 diffractometer with Rigaku Saturn CCD system equipped with a rotating-anode X-ray generator producing multi-layer mirror monochromated  $MoK\alpha$  radiation.

### Physical measurement

The fluorescence images and spectra were obtained by a FV1000 microscope (Olympus). The fluorescent images were obtained by a FV1000 microscope (Olympus) with a semiconductor laser at 405 nm and fluorescent emission was collected in the 500-550 nm range. Gas chromatography-mass spectrometry (GC-MS) was performed using a SHIMADZU QP2010. IR measurement was performed by Thermo Scientific Nicolet iS5 FT-IR.

### Structure Determination

X-ray data collection ( $5^\circ < 2\theta < 55^\circ$ ) was conducted at 223K on Rigaku AFC10 diffractometer  $Mo-K\alpha$  radiation ( $\lambda = 0.7105 \text{ \AA}$ ) with Rigaku Mercury CCD system. The structures were solved by a direct method (SIR92) and expanded using Fourier techniques. All calculations were performed using the CrystalStructure crystallographic software package 4.0 of Rigaku. The crystallizing solvents (DMF molecules) were severely disordered and could not be satisfactorily localized. All non-hydrogen atoms except for those of disordered solvent molecules were refined anisotropically. Hydrogen atoms severely disordered and could not be satisfactorily localized. Crystal data for  $2\Delta$ solvent:  $C_{31}H_{47}N_7O_{11}Zn$ , tetragonal, space group  $P4/mmm$ , (no. 123),  $a = 10.9681(9) \text{ \AA}$ ,  $c = 9.7190(10) \text{ \AA}$ ,  $V = 1169.19(19) \text{ \AA}^3$ ,  $Z = 1$ ,  $T = 223 \text{ K}$ .  $\rho_{\text{calcd}} = 0.854 \text{ gcm}^{-3}$ ,  $\mu(MoK\alpha) = 1.054 \text{ cm}^{-1}$ , 1147 reflections measured, 923 observed ( $I > 2.00\sigma(I)$ ) 42

parameters;  $R_1 = 0.0815$ ,  $wR_2 = 0.3022$ , GOF = 1.177. These data can be obtained free of charge from The Cambridge Crystallographic Data Centre via [www.ccdc.cam.ac.uk/data\\_request/cif](http://www.ccdc.cam.ac.uk/data_request/cif). (CCDC number: 867374)

### **Synchrotron X-ray measurement for film-structural analysis**

The measurements were performed with a four-circle diffractometer having  $\phi$ ,  $\chi$ ,  $\theta$  and  $2\theta$  circles at beamline BL13XU for surface and interface structures, SPring-8. The hybridized crystal, **1/p2**, was picked up just before the measurement, and then fixed on the glass substrate with the orientation where orange part of **1/p2** was parallel to the glass substrate by double-faced adhesive. The measurement was carried out under Helium gas condition.

## References

- (1) E. Z. Eisenmesser, O. Millet, W. Labeikovsky, D. M. Korzhnev, M. Wolf-Watz, D. A. Bosco, J. J. Skalicky, L. E. Kay, D. Kern, *Nature*, **2005**, *438*, 117-121.
- (2) P. G. Schultz and R. A. Lerner, *Science*, **1995**, *269*, 1835-1842.
- (3) O. M. Yaghi, M. O’Keeffe, N. W. Ockwing, H. K. Chae, M. Eddaoudi and J. Kim, *Nature*, **2003**, *423*, 705-714.
- (4) S. Kitagawa, R. Kitaura and S. Noro, *Angew. Chem., Int. Ed.*, **2004**, *43*, 2334-2375.
- (5) G. Férey and C. Serre, *Chem. Soc. Rev.*, **2009**, *38*, 1380-1399.
- (6) S. Batten and R. Robson, *Angew. Chem., Int. Ed.*, **1998**, *37*, 1460-1494.
- (7) U. Mueller, M. Schubert, F. Teich, H. Puetter, K. Schierle-Arndt and J. Pastré, *J. Mater. Chem.*, **2006**, *16*, 626-636.
- (8) H. L. Jiang and Q. Xu, *Chem. Commun.*, **2011**, *47*, 3351-3370.
- (9) C. P. Li and M. Du, *Chem. Commun.*, **2011**, *47*, 5958-5972.
- (10) M. Dincă, A. Dailly, Y. Liu, C. M. Brown, D. A. Neumann and J. R. Long, *J. Am. Chem. Soc.*, **2006**, *128*, 16876-16883.
- (11) S. Ma, D. Sun, J. M. Simmons, C. D. Collier, D. Yuan and H. C. Zhou, *J. Am. Chem. Soc.*, **2008**, *130*, 1012-1016.
- (12) S. Ma and H. C. Zhou, *Chem. Commun.*, **2010**, *46*, 44-53.
- (13) L. Alaerts, C. E. A. Kirschhock, M. Maes, M. A. van der Veen, V. Finsky, A. Depla, J. A. Martens, G. V. Baron, P. A. Jacobs, J. F. M. Denayer and D. E. De Vos, *Angew. Chem., Int. Ed.*, **2007**, *46*, 4293-4297.
- (14) B. Chen, C. Liang, J. Yang, D. S. Contreras, Y. L. Clancy, E. B. Lobkovsky, O. M. Yaghi and S. Dai, *Angew. Chem., Int. Ed.*, **2006**, *45*, 1390-1393.
- (15) J. S. Seo, D. Whang, H. Lee, S. I. Jun, J. Oh, Y. J. Jeon and K. Kim, *Nature*, **2000**, *404*, 982-986.
- (16) C. D. Wu, A. Hu, L. Zhang and W. Lin, *J. Am. Chem. Soc.*, **2005**, *127*, 8940-8941.
- (17) M. D. Allendorf, C. A. Bauer, R. K. Bhakta and R. J. T. Houk, *Chem. Soc. Rev.*, **2009**, *38*, 1330-1352.
- (18) Y. Takashima, V. M. Martinez, S. Furukawa, M. Kondo, S. Shimomura, H. Uehara, M. Nakahama, K. Sugimoto and S. Kitagawa, *Nat. Commun.*, **2011**, *2*, 168-176.
- (19) L. E. Kreno, K. Leong, O. K. Farha, M. Allendorf, R. P. Van Duyne and J. T. Hupp, *Chem. Rev.*, **2012**, *112*, 1105-1125.
- (20) K. Hirai, S. Furukawa, M. Kondo, H. Uehara, O. Sakata and S. Kitagawa, *Angew. Chem., Int. Ed.*, **2011**, *50*, 8057-8061.
- (21) Z. Wang and S. Cohen, *Angew. Chem., Int. Ed.*, **2008**, *47*, 4699-4702.

- (22) S. J. Garibay, Z. Wang, K. K. Tanabe and S. Cohen, *Inorg. Chem.*, **2009**, *48*, 7341-7349.
- (23) T. Gadzikwa, O. K. Farha, K. L. Mulfort, J. T. Hupp and S. T. Nguyen, *Chem. Commun.*, **2009**, 3720-3722.
- (24) S. M. Cohen, *Chem. Rev.*, **2012**, *112*, 970-1000.
- (25) K. Seki, *Chem. Commun.*, **2001**, 1496-1497.
- (26) D. N. Dybtsev, H. Chun and K. Kim, *Angew. Chem., Int. Ed.*, **2004**, *43*, 5033-5036.
- (27) B. Q. Ma, K. L. Mulfort and J. T. Hupp, *Inorg. Chem.*, **2005**, *44*, 4912-4914.
- (28) D. Tanaka, S. Horike, S. Kitagawa, M. Ohba, M. Hasegawa, Y. Ozawa and K. Toriumi, *Chem. Commun.*, **2007**, 3142-3144.
- (29) S. Furukawa, K. Hirai, K. Nakagawa, Y. Takashima, R. Matsuda, T. Tsuruoka, M. Kondo, R. Haruki, D. Tanaka, H. Sakamoto, S. Shimomura, O. Sakata and S. Kitagawa, *Angew. Chem., Int. Ed.*, **2009**, *48*, 1766-1770.
- (30) S. Furukawa, K. Hirai, Y. Takashima, K. Nakagawa, M. Kondo, T. Tsuruoka, Sakata and S. Kitagawa, *Chem. Commun.*, **2009**, 5077-5079.
- (31) A. Tramer, V. Brenner, P. Millié and F. Piuzzi, *J. Phys. Chem. A*, **1998**, *102*, 2798-2807.
- (32) R. K. Guo, *J. Lumin.*, **1992**, *50*, 361-371.
- (33) M. Wierzejewska-Hnat, Z. Mielke and H. Ratajczak, *J. Chem. Soc., Faraday Trans. II*, **1980**, *76*, 834-843.
- (34) O. Poizat, V. Guichard and G. Buntinx, *J. Chem. Phys.*, **1989**, *90*, 4697-4703.
- (35) S. Jones, C. J. Atherton, R. J. M. Elsegood and W. Clegg, *Acta Crystallogr. Sect. C: Cryst. Struct. Commun.*, **2000**, *56*, 881-883.
- (36) J. Garibay, Z. Wang, K. K. Tanabe and S. M. Cohen, *Inorg. Chem.*, **2009**, *48*, 7341-7349.

## Chapter 5

# Programmed Crystallization via Epitaxial Growth and Ligand Replacement towards a Hybridized Porous Coordination Polymer

### Abstract

Two-dimensional (2D) porous coordination polymer (PCP) crystals have been hybridized through epitaxial growth or ligand replacement:  $[\text{Zn}_2(\text{NO}_2\text{-ip})_2(\text{dpndi})]_n$  (**1**) as the core crystal and  $[\text{Zn}_2(\text{NO}_2\text{-ip})_2(\text{bpy})]_n$  (**2**) as the shell crystal (NO<sub>2</sub>-ip = 5-nitroisophthalate, dpndi = *N,N'*-di(4-pyridyl)-1,4,5,8-naphthalenetetracarboxydiimide, bpy = 4,4'-bipyridyl). Whereas the epitaxial growth on the core crystal leads to a sandwich type PCP, the ligand replacement nearby surface of the core crystal results in a core-shell type PCP.

## Introduction

Porous coordination polymers (PCPs) or metal-organic frameworks (MOFs) are an intriguing class of crystalline materials due to a wide variety of porous properties such as gas storage,<sup>1-3</sup> separation,<sup>4-5</sup> catalysis<sup>6-7</sup> and polymerization.<sup>8</sup> These porous properties are basically dominated by the framework structures, pore structure, chemical affinity and reactive site. In contrast, the creation of hierarchical structures of PCPs, such as membrane, macroporous architectures and hybrid PCPs, further sophisticate the porous properties and provide new applications.

In that context, the methods to fabricate well-designed architectures have been developed by spatial control of the crystallization process. The control of the crystallization process is traditionally performed by heterogeneous nucleation on templates. This basic approach was employed to fabricate two-dimensional membrane,<sup>9-11</sup> three-dimensional architectures<sup>12-13</sup> and heterogeneously hybridized particles.<sup>14-15</sup> PCPs also offer an opportunity of being utilized as crystalline templates for the crystallization of another PCP on their surfaces. This characteristic feature enable to fabricate hybridized PCP crystals through epitaxial growth.<sup>16-17</sup>

The crystal surface of PCPs is rather dynamic in solutions due to the coordination equilibrium, where the organic ligands and solvent molecules compete to terminate the surfaces.<sup>18-19</sup> Thus, the organic ligands nearby the crystal surfaces can be replaced by other ligands with the same chemical functionality. The ligand exchange around the crystal surfaces will also result in the formation of another PCP on the original PCP, thus leading to heterogeneously hybridized PCP. In both approaches, epitaxial growth and ligand replacement, the crystallization of second PCP was spatially programmed by the surface of the template PCP.

Herein, we demonstrate the synthesis of hybridized PCP through epitaxial growth and ligand replacement. As we demonstrated in previous studies, a sandwich type hybrid PCP (**S-1/2**) was synthesized by epitaxial growth.<sup>20</sup> In contrast, a core-shell type hybrid PCP (**C-1/2**), in which all the surfaces are surrounded by the second PCP, was obtained by ligand replacement (Figure 1). We usually employed two-steps solvothermal reaction in order to hybridize different PCPs by epitaxial growth. The second solvothermal reaction often gives the pure-phased compound. The ligand replacement approach would generate a hybrid PCP with restricting the formation of pure-phased compounds.

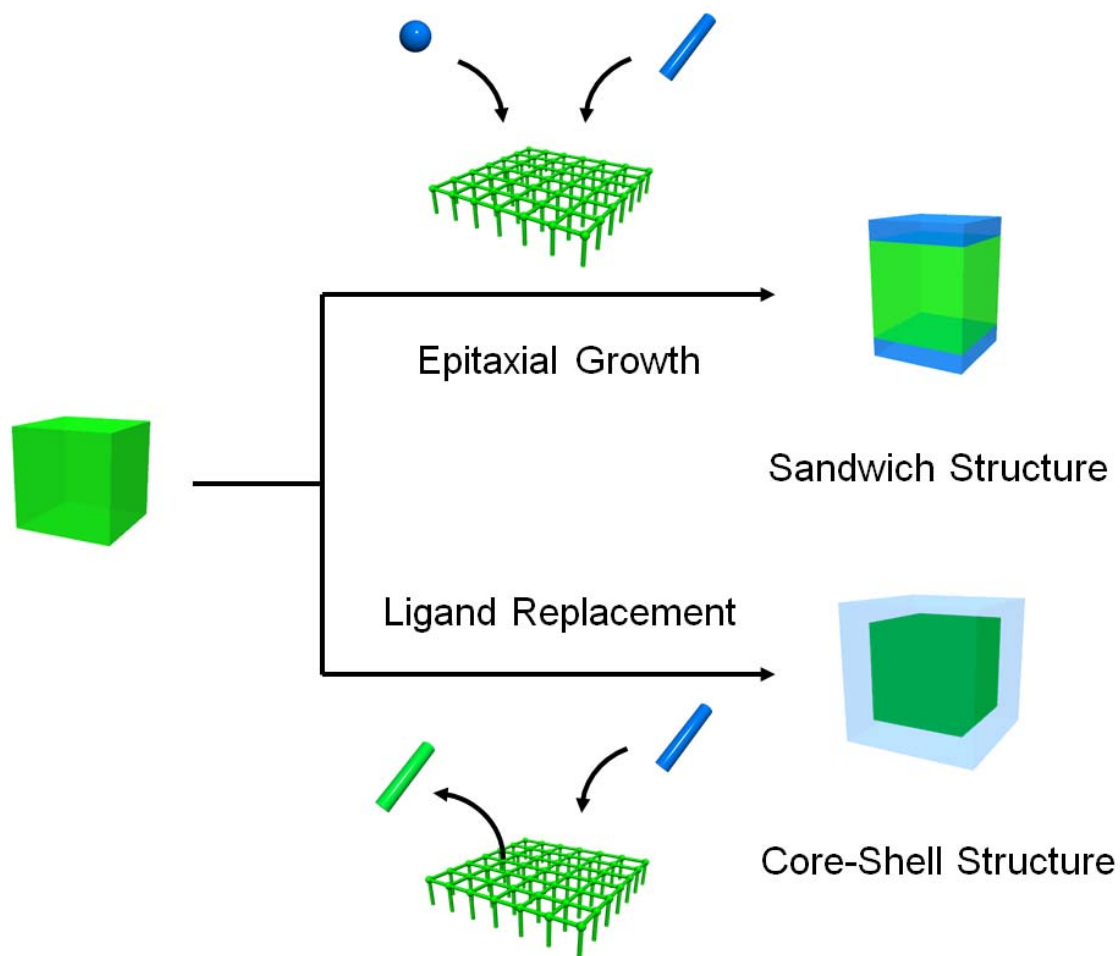


**Figure 1.** Two approaches, epitaxial growth and ligand replacement, towards hybridized PCPs.

## Results and Discussion

A series of two-dimensional frameworks,  $[M(\text{isophthalate})(\text{diamine})]_n$ , is an excellent candidate, wherein three components, namely the metal ions, V-shaped layer ligands, and diamine pillar ligands, can be varied without changing the original framework topology.<sup>21-23</sup> Coordination frameworks of  $\{[\text{Zn}(\text{NO}_2\text{-ip})(\text{dpndi})] \cdot (\text{DMF})_{0.5}(\text{MeOH})_{0.5}\}_n$  (**1**  $\supset$  solvents) and  $\{[\text{Zn}(\text{NO}_2\text{-ip})(\text{bpy})] \cdot (\text{DMF})_{0.5}(\text{MeOH})_{0.5}\}_n$  (**2**  $\supset$  solvents) were synthesized via the solvothermal reaction of  $\text{Zn}(\text{NO}_3)_2 \cdot 6\text{H}_2\text{O}$ ,  $\text{NO}_2\text{-ip}$  and bpy or dpndi in a DMF/MeOH solution ( $\text{NO}_2\text{-ip}$  = 5-nitroisophthalate, dpndi =  $N,N'$ -di(4-pyridyl)-1,4,5,8-naphthalenetetracarboxydiimide, bpy = 4,4'-bipyridyl). As shown in Figure 2a, the Zn ion have a distorted octahedral  $\text{N}_2\text{O}_4$  geometry, being coordinated by two diamine molecules at the axial positions, one chelating carboxylate of  $\text{NO}_2\text{-ip}$  and two other monodentate carboxylate of  $\text{NO}_2\text{-ip}$  in the equatorial plane. The coordination of  $\text{NO}_2\text{-ip}$  ligands to the Zn ions constructed one-dimensional (1D) chain structure, followed by the linkage of the adjacent chains through diamine in the axial positions, leading to the formation of two-dimensional (2D) sheets. The 2D sheets are alternatively interdigitated, forming **1** and **2**, as shown in Figure 2b-c.

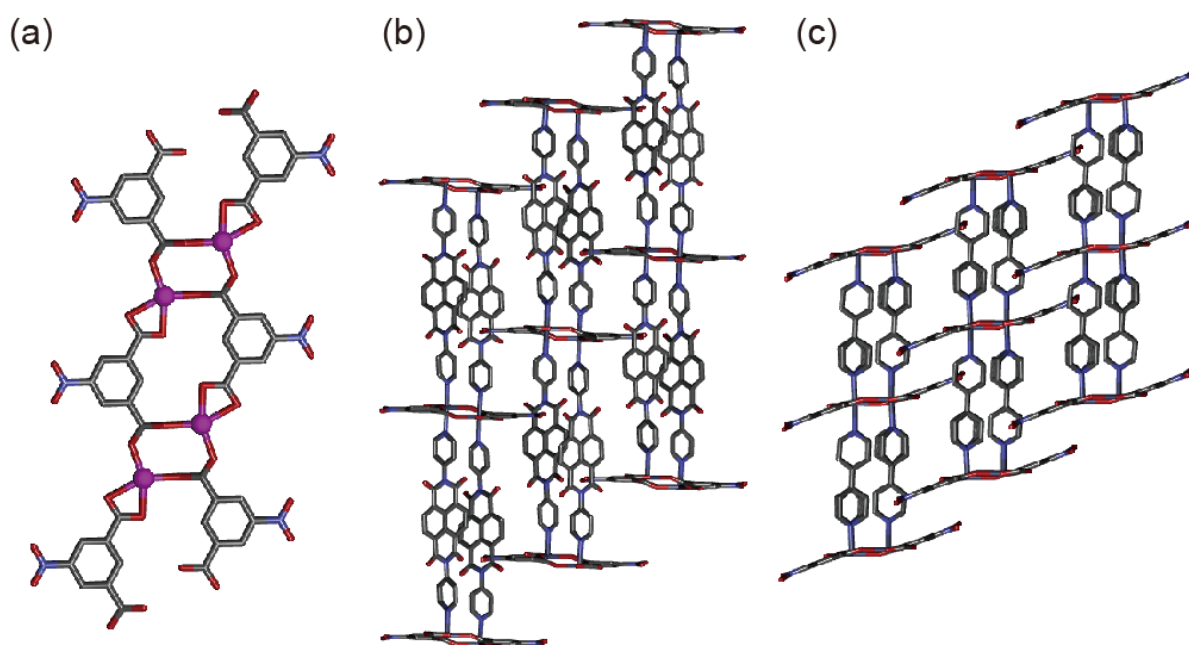


**Figure 2.** Crystal structures of (a) the 1D chain structure composed of Zn ions and  $\text{NO}_2\text{-ip}$ , and the sheet structure of (b) **1** and (c) **2**. Gray, blue, red, and purple are C, N, O and Zn, respectively. The hydrogen atoms and guest molecules are omitted for clarity.

As we demonstrated before, the hybridization of these two frameworks into one single crystal has been successfully achieved by a simple solvothermal synthesis; pieces of the single crystal of **1** (50  $\mu\text{m}$ ) were put into a DMF solution of  $\text{Zn}(\text{NO}_3)_2 \cdot 6\text{H}_2\text{O}$ , 5-nitroisophthalic acid and bpy, and the solution was heated to 393 K. The hybrid crystals (**S-1/2**) were harvested after cooling to room temperature. The optical microscopic image (Figure 3a) of **S-1/2** clearly demonstrated that the shell crystal of **2** grew on only two surfaces of the core crystal of **1**, leading to the formation of a sandwich type hybrid PCP. Each part of the hybridized crystal was identified as the respective framework structure by microscopic laser Raman spectroscopy (Figure 3b–e). The characteristic peaks of the core and shell crystals correspond to those of **2** and **1**. The result suggests that the second framework of **2** successfully grew on the core framework of **1**.

Both crystals have the same 1D chain structures comprising of Zn ions and  $\text{NO}_2$ -ip. However, the distances between 1D chains are significantly different due to the difference in the length of dpndi and bpy, which enables easy determination of the structural parameters between the core and shell crystal. Synchrotron X-ray measurements for film-structural analysis were, therefore, performed using a four-circle diffractometer at beamline BL13XU for surface and interface structures, SPring-8. The hybridized core-shell crystal of **S-1/2** with a size over 50  $\mu\text{m}$  and a shell crystal thickness over 5  $\mu\text{m}$  was fixed on a glass substrate with the configuration illustrated in Figure 3f, and diffractions were recorded at a desired Bragg position using an X-ray beam with the size of  $1 \times 1 \mu\text{m}^2$ . The  $\theta$ - $2\theta$  scan of **S-1/2** at the top of the crystal provided only one sharp peak assigned to 01-1 Bragg peak of the shell (**2**), which is parallel to the direction of bpy pillar ligands. In contrast, the  $\theta$ - $2\theta$  scan of **S-1/2** at the middle of the crystal gave one strong peak assigned to 40-2 Bragg peak of the core (**1**) and two weak peaks assigned to 60-2 Bragg peak of the shell (**1**) and 01-1 Bragg peak of the core (**2**), respectively (Figure 3g-j). All the observed peaks are nearly parallel to the pillar ligands, bpy and dpndi. This result suggested that the shell crystal of **2** was epitaxially grown on the core crystal of **1** along pillar direction.

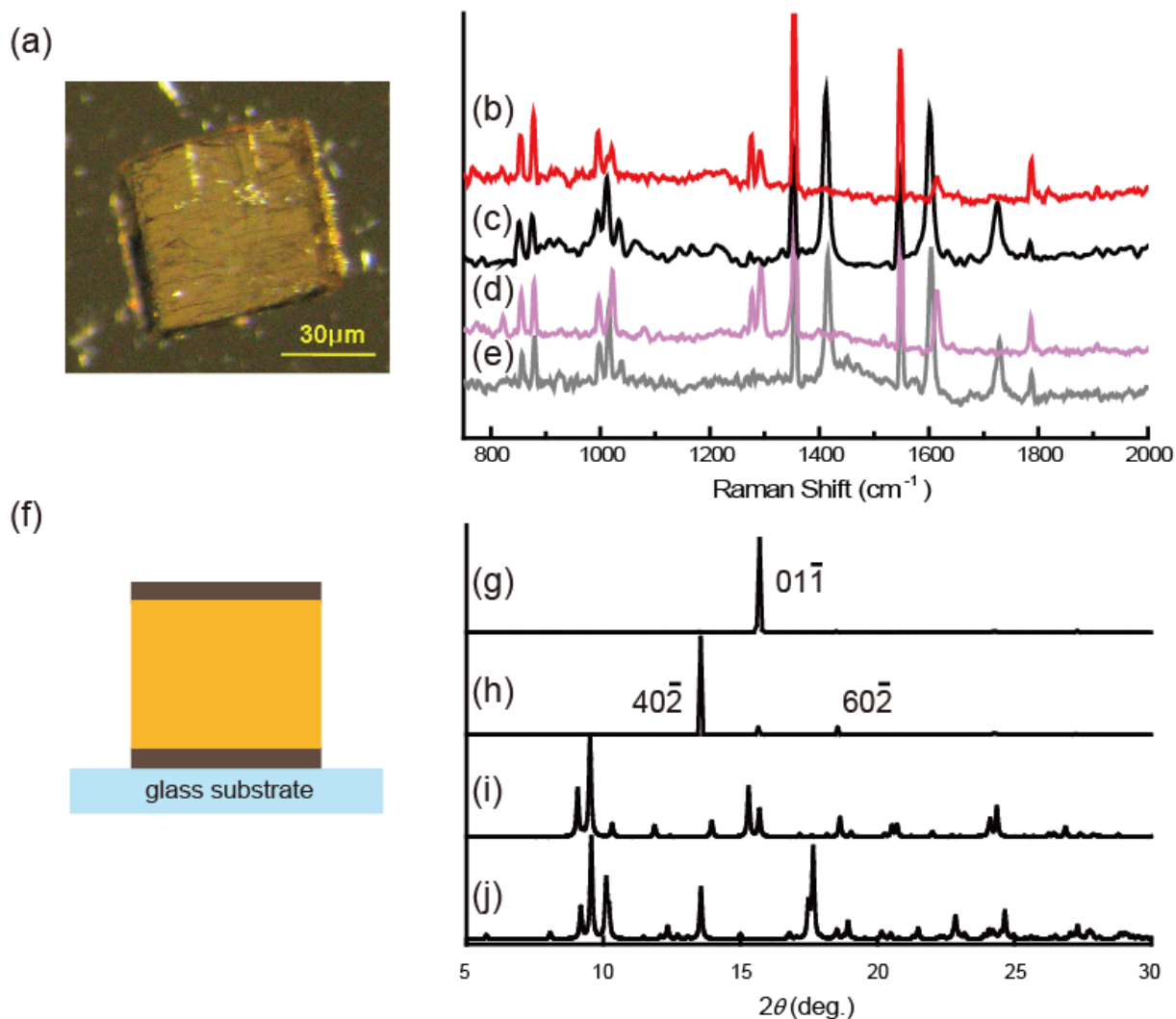


**Figure 3.** (a) The hybrid crystal (**C-1/2**) (b) The Raman spectra of shell part, (c) core part, (d) **2**, and (e) **1**. (f) The schematic illustration of configuration of the hybrid crystal (**C-1/2**) on a glass substrate for synchrotron X-ray diffraction measurements. (g) The  $\theta$ - $2\theta$  scan of shell part, and (h) core part. The simulation XRD patterns of (i) **2**, and (j) **1**.

The core-shell type hybrid PCP (**C-1/2**), where all the surfaces are covered by second PCP, was synthesized via ligand replacement from dpndi to bpy. The powder crystals of few micrometers (**1**) were immersed in the stoked solution of bpy and stirred for 12 hours at room temperature. The X-ray diffraction measurements on the hybrid PCP (**C-1/2**) suggested the existence of both of **1** and **2** in the powder samples (Figure 4a-e). The molar ratio of dpndi to bpy was determined to be 7:3 by  $^1\text{H-NMR}$  measurement of the hybrid crystals (**C-1/2**) that had been decomposed with hydrochloric acid.

Whereas **2** can adsorb iodopropane, the small pores of **1** does not accommodate iodopropane. The hybrid crystals (**C-1/2**) were soaked in iodopropane to detect the location of **2** by scanning electron microscopy with energy dispersive X-ray spectroscopy

(SEM-EDX). After soaking and drying, the spatial distribution of iodine in the crystals were mapped by SEM-EDX. As shown in Figure 4f-g, iodine are localized at the edges of a crystal, suggesting that the edge of core crystal of **1** is converted to **2** via ligand exchange from dpndi to bpy. This method does not achieve the anisotropic growth of **2** as well as epitaxial growth does. Although the distances between 1D chains are different due to the difference in the length of dpndi and bpy, all the crystal surfaces of **1** was surrounded by **2**, forming a core-shell type structure.

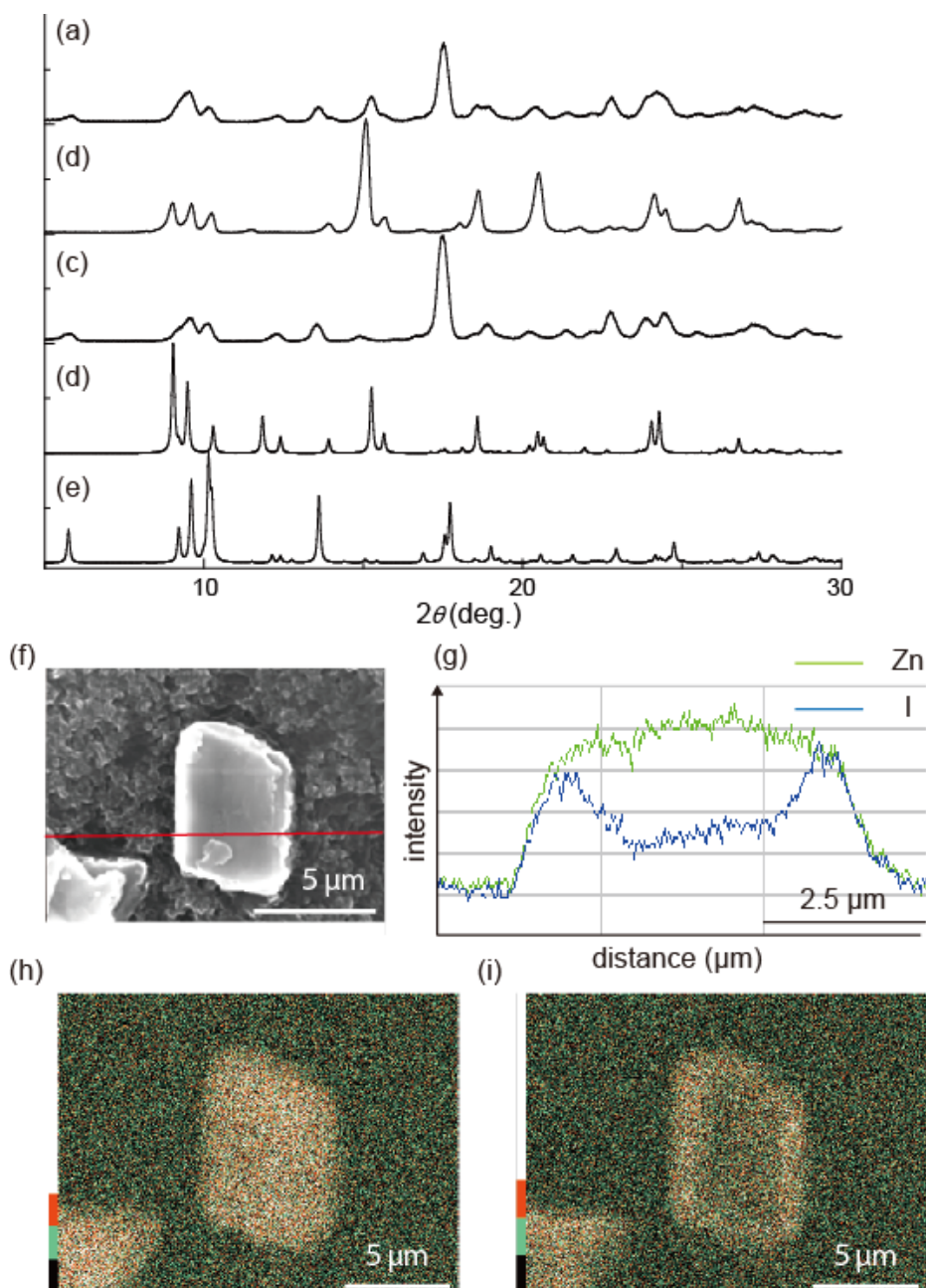


**Figure 4.** (a) PXRD of hybrid crystal (C-1/2), (b) **2**, (c) **1**, (d) simulation of as-synthesized **2**, and (e) **1**. (f) SEM image of hybrid crystal (C-1/2). The red line indicates the measurement line of EDX, (g) Line profile for intensity of Zn and I, (h) mapped intensity of Zn, and (i) I.

Since the hybrid crystals (**C-1/2**) suitable for adsorption measurements were harvested, the adsorption experiments on **1**, **2** and hybrid crystals (**C-1/2**) were performed for CO<sub>2</sub>, N<sub>2</sub>, and O<sub>2</sub>, as shown in Figure 5. **1** and **2**, does not adsorb O<sub>2</sub> and N<sub>2</sub> at 77 K, but adsorbs CO<sub>2</sub> at 195 K with gate-opening process. As previously reported, the gate-opening adsorption of **2** is due to the structural transformation from closed phase to open phase. **1** also shows step-wise adsorption of CO<sub>2</sub> probably because of the structural transformation. The sorption profile of hybrid PCP (**C-1/2**) for CO<sub>2</sub> is sum of those of **1** and **2**. The uptake amount of **C-1/2** is nearly same as physical mixtures of **1** and **2**. This result suggested that both of **1** and **2** in hybrid PCP (**C-1/2**) maintained permanent porosity and the guest molecules reached to core of **1** through the shell of **2**.

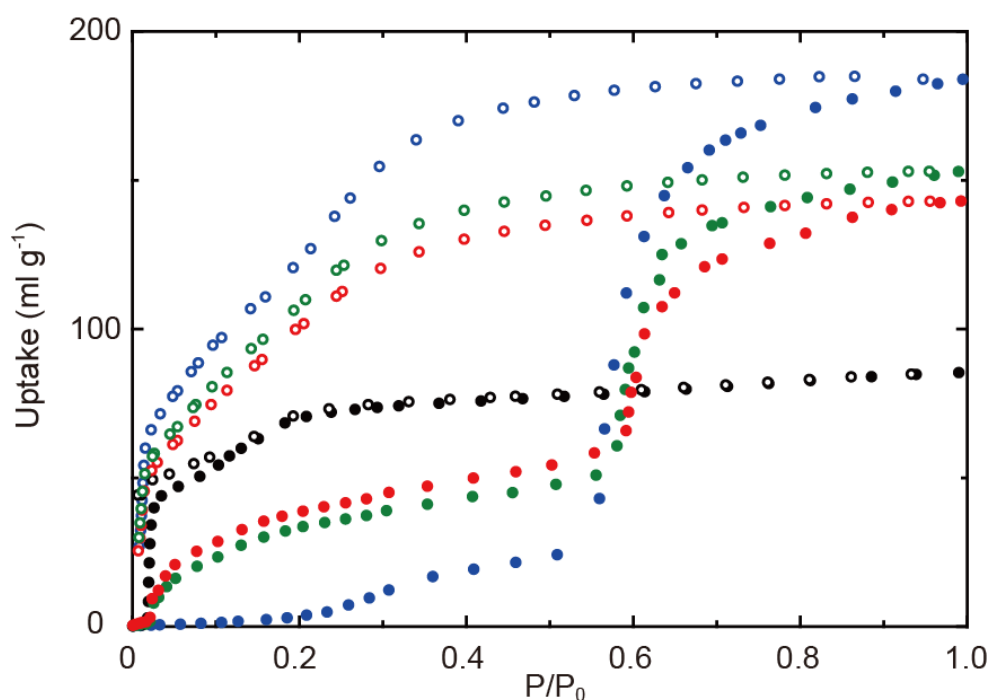


**Figure 5.** Adsorption isotherms of CO<sub>2</sub> for **1** (blue), **2** (black), **C-1/2** (red) and physical mixture of **1** and **2**. Closed and open symbols show adsorption and desorption, respectively.

## Conclusion

In summary, we have demonstrated the crystal hybridization of two-dimensional PCPs by epitaxial growth and ligand exchange. The sandwich type hybrid PCP was synthesized by epitaxial growth. In contrast, the core-shell type hybrid PCP, in which all the surfaces are covered by the second PCP, was obtained by ligand replacement. These results suggested that ligand replacement as well as epitaxial growth are one of good methods to fabricate hybridized PCPs.

## Experimental Section

### Materials

Zn(NO<sub>3</sub>)<sub>2</sub>•6H<sub>2</sub>O, *N,N*-dimethylformamide (DMF), methanol (MeOH) and idopropane were purchased from Wako Pure Chemical Industries. 5-nitroisophthalic acid (NO<sub>2</sub>-ipH<sub>2</sub>) were purchased from acid Sigma-Aldrich, Inc. 4,4'-bipyridyl (bpy) were purchased from Tokyo Chemical Industry. *N,N'*-di(4-pyridyl)-1,4,5,8-naphthalenetetracarboxydiimide (dpndi) was prepared according to the literature procedures.

### Synthesis of single crystals of **1**

The suspension of dpndi (42.0 mg, 0.10 mmol) in MeOH (2 mL) was slowly layered on the top of the solution of Zn(NO<sub>3</sub>)<sub>2</sub>•6H<sub>2</sub>O (29.7 mg, 0.10 mmol), NO<sub>2</sub>-ipH<sub>2</sub> (21.1 mg, 0.10 mmol) in DMF (2mL). The solution was heated at 70 °C for 1 day. After cooling, yellow crystals were harvested. Elemental analysis calcd. for C<sub>34</sub>H<sub>20.5</sub>N<sub>5.5</sub>O<sub>11</sub>Zn {[Zn(NO<sub>2</sub>-ip)(dpndi)]•(DMF)<sub>0.5</sub>(MeOH)<sub>0.5</sub>}<sub>n</sub>: C, 54.63; H, 2.76; N, 10.31, Found: C, 53.86; H, 3.09; N, 10.98.

### Synthesis of powder crystals of **1**

The solution of Zn(NO<sub>3</sub>)<sub>2</sub>•6H<sub>2</sub>O (118.8 mg, 0.4 mmol), NO<sub>2</sub>-ipH<sub>2</sub> (84.4 mg, 0.4 mmol) and bpy (168 mg, 0.4 mmol) in 20 mL DMF was stirred for several hours. The dozens of well-dispersed single crystals of **1** were put into the solution. The solution was heated up to 393 K for 3 hours by microwave (Initiator, Biotage). After cooling, the powder crystals were harvested.

### Synthesis of hybrid single crystal, **1/2**

The solution of Zn(NO<sub>3</sub>)<sub>2</sub>•6H<sub>2</sub>O (59.4 mg, 0.2 mmol), NO<sub>2</sub>-ipH<sub>2</sub> (42.2 mg, 0.2 mmol) and bpy (31.2 mg, 0.2 mmol) in 10 mL DMF was stirred for several hours. The dozens of well-dispersed single crystals of **1** were put into the solution. The solution was heated up to 353 K for several days. After cooling, the crystals were harvested.

### Synthesis of hybrid powder crystals, **1/2**

The solution of bpy (15.6 mg, 0.1 mmol) in 100 mL DMF was stirred for several hours. The powder crystals of **1** (7.47 mg, 0.01 mmol) were put into the solution and the solution was stirred for 12 hours.

## Characterization methods

The compounds were characterized with X-ray diffraction (XRD), microscopic laser Raman spectroscopy, synchrotron XRD, thermogravimetry (TG), <sup>1</sup>H-NMR and elemental analysis. Powder X-Ray diffraction (XRD) studies were performed using a Rigaku diffractometer with Cu K<sub>α</sub> radiation ( $\lambda = 1.5418 \text{ \AA}$ ). The Raman spectra were measured by a LabRAM HR-800 spectrometer (Horiba Jobin Yvon Ltd.) with a semiconductor laser at 785 nm. TG measurements were carried out by Thermo plus EVO II. Elemental analysis was carried out on a Flash EA 1112 series, Thermo Finnigan instrument. Single crystal X-ray diffraction measurements were made on a Rigaku AFC10 diffractometer with Rigaku Saturn CCD system equipped with a rotating-anode X-ray generator producing multi-layer mirror monochromated MoK<sub>α</sub> radiation.

## Structural determination of as-synthesized and degassed **1**

X-ray data collection ( $5^\circ < 2\theta < 55^\circ$ ) was conducted at 223K on Rigaku AFC10 diffractometer Mo-K<sub>α</sub> radiation ( $\lambda = 0.7105 \text{ \AA}$ ) with Rigaku Mercury CCD system. The structures were solved by a direct method (SIR92) and expanded using Fourier techniques. All calculations were performed using the CrystalStructure crystallographic software package 4.0 of Rigaku. The crystallizing solvents (DMF and MeOH molecules) were severely disordered and could not be satisfactorily localized. All non-hydrogen atoms except for those of disordered solvent molecules were refined anisotropically. Hydrogen atoms severely disordered and could not be satisfactorily localized.

Crystal data for **1**⊃solvent: C<sub>64</sub>H<sub>30</sub>N<sub>10</sub>O<sub>20</sub>Zn<sub>2</sub>, *monoclinic*, space group *C2/c*, (no. 15),  $a = 31.110(9) \text{ \AA}$ ,  $b = 10.192(3) \text{ \AA}$ ,  $c = 22.095(6) \text{ \AA}$ ,  $\beta = 93.938(4)$ ,  $V = 6990(4) \text{ \AA}^3$ ,  $Z = 4$ ,  $T = 223 \text{ K}$ .  $\rho_{\text{calcd}} = 1.391 \text{ gcm}^{-3}$ ,  $\mu(\text{MoK}\alpha) = 0.769 \text{ cm}^{-1}$ , 8009 reflections measured, 6499 observed ( $I > 2.00\sigma(I)$ ) 433 parameters;  $R_1 = 0.0603$ ,  $wR_2 = 0.1868$ , GOF = 1.101.

## References

- (1) O. M. Yaghi, M. O'Keeffe, N. W. Ockwing, H. K. Chae, M. Eddaoudi and J. Kim, *Nature*, **2003**, *423*, 705-714.
- (2) M. Dincă , A. Dailly, Y. Liu, C. M. Brown, D. A. Neumann and J. R. Long, *J. Am. Chem. Soc.*, **2006**, *128*, 16876-16883.
- (3) S. Ma, D. Sun, J. M. Simmons, C. D. Collier, D. Yuan, and H. C. Zhou, *J. Am. Chem. Soc.*, **2008**, *130*, 1012-1016.
- (4) L. Alaerts, C. E. A. Kirschhock, M. Maes, M. A. van der Veen, V. Finsky, A. Depla, J. A. Martens, G. V. Baron, P. A. Jacobs, J. F. M. Denayer, and D. E. De Vos, *Angew. Chem. Int. Ed.* **2007**, *46*, 4293-4297.
- (5) B. Chen, C. Liang, J. Yang, D S. Contreras, Y. L. Clancy, E. B. Lobkovsky, O. M. Yaghi, and S. Dai, *Angew. Chem. Int. Ed.* **2006**, *45*, 1390-1393.
- (6) J. S. Seo, D. Whang, H. Lee, S. I. Jun, J. Oh, Y. J. Jeon, K. Kim, *Nature* **2000**, *404*, 982-986.
- (7) C.-D. Wu, A. Hu, L. Zhang, W. Lin, *J. Am. Chem. Soc.* **2005**, *127*, 8940-8941.
- (8) T. Uemura, S. Horike, S. Kitagawa, *Chem. Asian. J.* **2006**, *1*, 36-44.
- (9) S. Hermes, F. Schröder, R. Chelmoski, C. Wöll, R. A. Fischer, *J. Am. Chem. Soc.* **2005**, *127*, 13744-13745.
- (10) E. Biemmi, C. Scherb, T. Bein, *J. Am. Chem. Soc.* **2007**, *129*, 8054-8055.
- (11) Y. S. Li, F. Y. Liang, H. Bux, A. Feldhoff, W. S. Yang, J. Caro, *Angew. Chem. Int. Ed.* **2010**, *49*, 548-551.
- (12) J. Reboul, S. Furukawa, N. Horike, M. Tsotsalas, K. Hirai, H. Uehara, M. Kondo, N. Louvain, O. Sakata, S. Kitagawa, *Nature Mater.* **2012**, *11*, 717-723.
- (13) Y. Wu, F. Li, W. Zhu, J. Cui, C. Tao, C. Lin, P. M. Hannam, G. Li, *Angew. Chem. Int. Ed.* **2011**, *50*, 12518-12522
- (14) M. R. Lohe, K. Gedrich, T. Freudenberg, E. Kockrick, T. Dellmann, S. Kaskel, *Chem. Commun.*, **2011**, *47*, 3075-3077
- (15) M. E. Silvestre, M. Franzreb, P. G. Weidler, O. Shekhah, C. Wöll, *Adv. Funct. Mater.*, **2012**, *in press*
- (16) S. Furukawa, K. Hirai, K. Nakagawa, Y. Takashima, R. Matsuda, T. Tsuruoka, M. Kondo, R. Haruki, D. Tanaka, H. Sakamoto, S. Shimomura, O. Sakata and S. Kitagawa, *Angew. Chem., Int. Ed.* **2009**, *48*, 1766-1770.
- (17) K. Koh, A. J. Wong-Foy, A. J. Matzger, *Chem. Comm.* **2009**, 6162-6164.
- (18) M. Kim, J. F. Cahill, Y. Su, K. A. Prather and S. M. Cohen, *Chem. Sci.* **2012**, *3*, 126-130.

- (19) M. Kondo, S. Furukawa, K. Hirai, S. Kitagawa, *Angew. Chem. Int. Ed.* **2010**, *49*, 5327-5330.
- (20) S. Furukawa, K. Hirai, Y. Takashima, K. Nakagawa, M. Kondo, T. Tsuruoka, O. Sakata, S. Kitagawa, *Chem. Commun.* **2009**, 5097-5099.
- (21) J. Tao, X. M. Chen, R. B. Huang, L. S. Zheng, *J. Solid State Chem.* **2003**, *170*, 130-134.
- (22) S. Horike, D. Tanaka, K. Nakagawa and S. Kitagawa, *Chem. Commun.* **2007**, 3395-3397.
- (23) T. Fukushima, S. Horike, Y. Inubushi, K. Nakagawa, Y. Kubota, M. Takata, S. Kitagawa, *Angew. Chem. Int. Ed.* **2010**, *49*, 4820-4824.



## Chapter 6

# Multilength-Scales Structuralization Emerged from One Reaction

### Abstract

The fabrication of macroscale structures with controlling the formation of porous coordination polymers (PCPs) is a critical challenge for developing separation systems, heterogeneous catalysts or ion/electron transport. Here, we discover a new phenomenon, in which the macropore is formed inside the cuboid crystal synchronized with the generation of solid-solution type PCPs. As a result, a box-shaped architecture consisting of solid-solution type PCP is synthesized. The chemical alteration of organic ligands converts framework topology from not-interpenetrated to interpenetrated structures with maintaining the coordination geometry. The interpenetration stabilizes the degassed phase of framework and improve the uptake amount of CO<sub>2</sub>. Furthermore, the hollow structure enhances the diffusion kinetics of CO<sub>2</sub>. This structuralization across chemical and macroscale structures is derived from the differences in the diffusion rates of two organic ligands during dissolution of pre-existing PCP and crystallization of solid-solution PCP.

## Introduction

A central challenge in material chemistry is to fabricate exquisite macroscale architectures comprising of desired compounds. This is because the properties of solid-state materials are determined by two structures across different length scales: chemical and macroscale structures.<sup>1-2</sup> The chemical structure determines the inherent properties of materials, while the macroscale structure is a crucial factor for their applications. As often seen in metallurgical phenomena such as topotactic transformation<sup>3-4</sup> or nanoscale Kirkendall Effect,<sup>5-7</sup> the macroscale architectures can be fabricated accompanied with the formation of target compounds. These phenomena are promising methods for fabricating well-designed architectures with desired metallic compounds; however, such phenomena have not been discovered in molecular materials composed of weak chemical bonds.

Porous coordination polymers (PCPs) or metal-organic frameworks (MOFs) are an intriguing class of crystalline materials due to a wide variety of porous properties such as gas storage,<sup>8-9</sup> separation,<sup>10-11</sup> catalysis<sup>12-13</sup> and conductivity.<sup>14-15</sup> These inherent porous properties are basically dominated by the chemical structures: pore size, pore surface functionality and framework topology. Therefore, considerable effort has been devoted to synthesize new compounds and evaluate these molecular-based properties at the early stage of this research field. In contrast, the macroscale structure is also one of crucial factors to sophisticate the properties, especially for separation efficiency, catalytic activity, and adsorption kinetics.<sup>16-18</sup> The fabrication of well-designed architectures of PCPs is traditionally achieved by controlling the crystallization process on templates; dispersed particles,<sup>19-20</sup> substrates<sup>21-24</sup> and three-dimensional (3D) superstructures.<sup>25</sup> These templates give fascinating opportunities to design the macroscale structures; however, such templating methods often lead to undesired chemical structures of PCPs.

The lessons from metallurgy suggest that a key to fabricate macroscale structures with controlling the chemical structures is employing molecular-based materials as the templates. The molecular-based templates can transcribe their chemical and macroscale structures to the obtained compounds, thus resulting in the macroscale architectures comprising of target compounds. Herein, we discover a new phenomenon in which the macroscale architectures are fabricated coupled with the formation of solid-solution type PCP (Figure 1). The pre-existing cuboid crystals are transformed into the box-shaped architecture via the void formation inside the original crystals. Concurrently with the formation of a box architecture, not-interpenetrated PCP is converted to solid-solution

type interpenetrated PCP with maintaining the original coordination geometry. The framework stability was improved due to the interpenetration, enhancing the uptake amount of CO<sub>2</sub>. Furthermore, the characteristic box-shaped structure shortened the diffusion path of guest species and accelerated the sorption kinetics. This templating method across framework structures and macroscale morphology will be a promising way to fabricate well-defined architectures with solid-solution type PCPs.

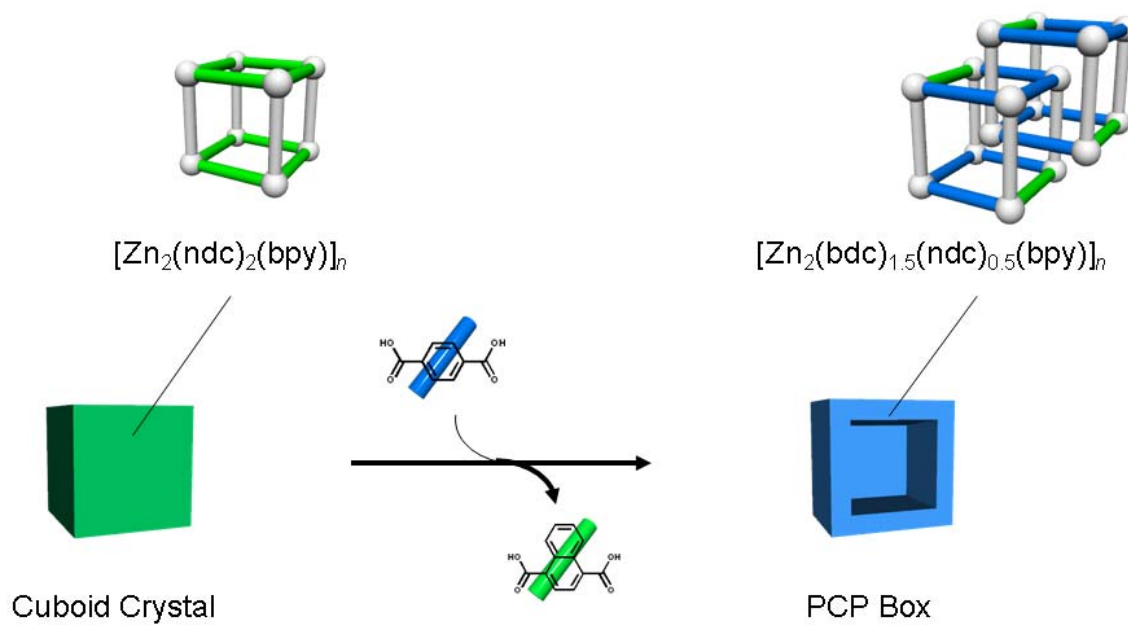


**Figure 1.** The schematic illustrations of multiscale structuralization of PCPs.

## Results and Discussion

PCPs with a three-dimensional structure,  $[\text{Zn}_2(\text{ndc})_2(\text{bpy})]_n$ <sup>26-29</sup> (**1**), in which ndc layer ligands link to the zinc paddlewheel clusters to form two-dimensional square lattices connected by bpy pillar ligands at the lattice points, was utilized as a starting materials (ndc = 1,4-naphthalenedicarboxylate, bpy = 4,4'-bipyridyl) (Figure 2a-b). Micrometer-sized cuboid crystals of **1** were put into a solution of H<sub>2</sub>bdc in DMF (bdc = 1,4-benzenedicarboxylate, DMF = *N,N*-dimethylformamide), and the temperature was rapidly elevated and kept at 353 K for 30 min by a microwave reactor. After cooling and drying, the obtained compounds were observed by scanning electron microscope (SEM). The SEM image showed that the assembly of meso-sized crystals (200 nm ~) formed a cuboid architecture, whose size and morphology are nearly same as the original cuboid crystal of **1** ( $5 \times 5 \times 10 \mu\text{m}^3$ ) (Figure 3a-b). The ultrasonication irradiation partially broke a side wall of the cuboid architecture and the inner vacant space appeared, suggesting that a micrometer-sized box (*micro-box*) was obtained (Figure 3c-e). The transmission electron microscope (TEM) observation of a sliced sample also supported the results of SEM observations. The *micro-box* was embedded in epoxy resin and then sliced using the microtome. The TEM image of a sliced *micro-box* also showed the vacant space inside the cuboid architecture (Figure 3f).

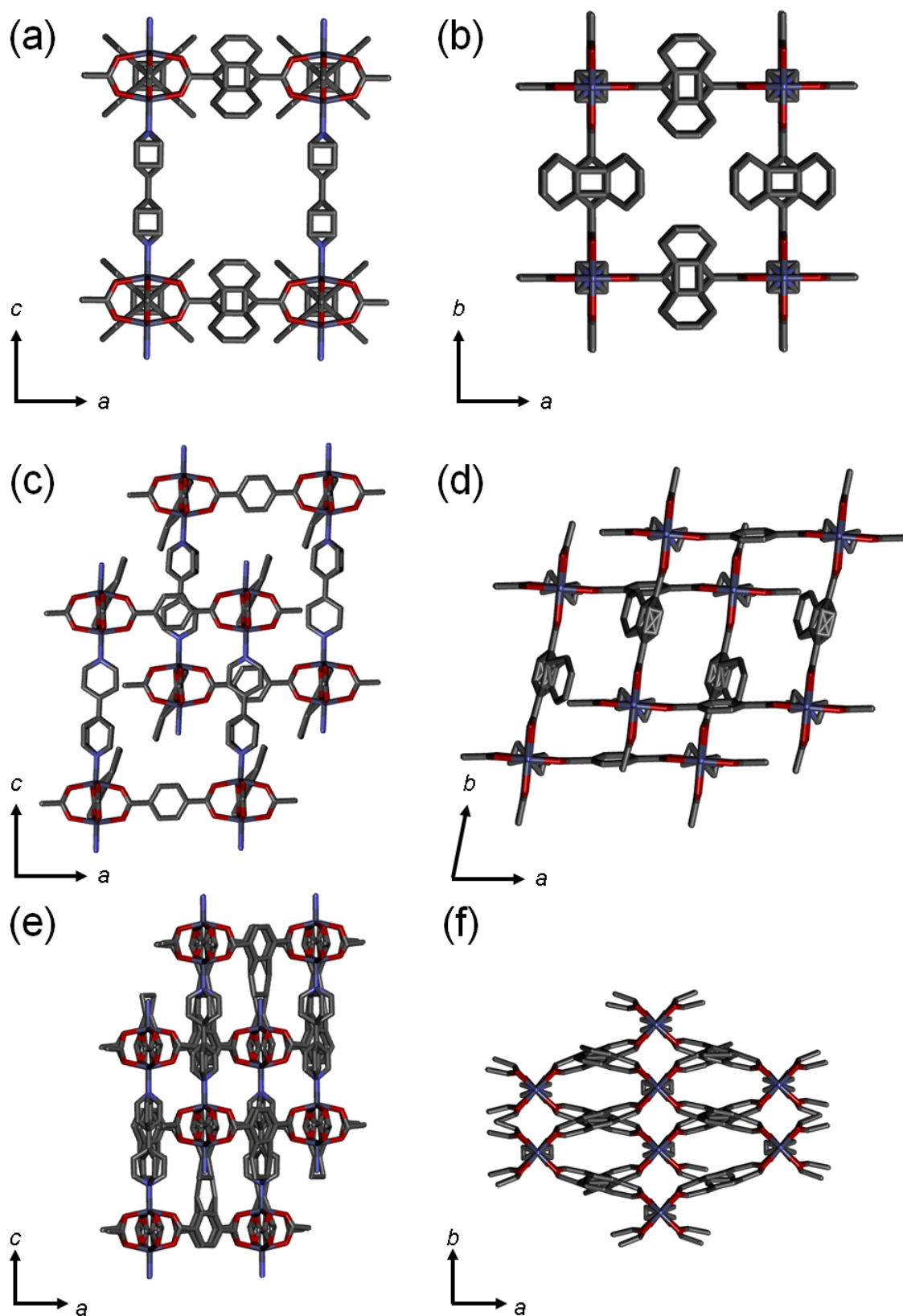


**Figure 2.** The crystal structure of **1**; (a) the view from *b* axis, and (b) the view from *c* axis. The crystal structure of **S1**; (c) the view from *b* axis, and (d) the view from *c* axis. The crystal structure of degassed **S1**; (e) the view from *b* axis, and (f) the view from *c* axis. The naphthalene moieties are disordered due to the symmetry.

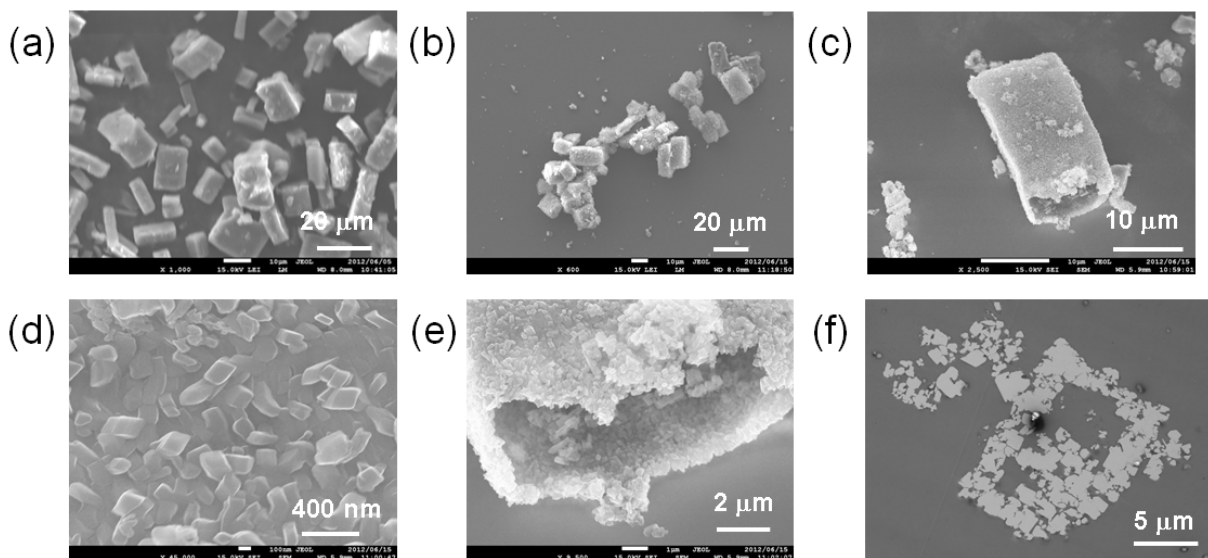


**Figure 3.** Electron microscopic observations: (a) **1**, (b) *micro-box*; (c) *micro-box* after ultrasonication, (d) side wall of a *micro-box*, (e) inner vacant space of a *micro-box*, (f) a *micro-box* sliced with microtome.

X-ray diffraction measurement (XRD) on *micro-box* revealed that the compound maintained the framework geometry of starting material (**1**) (Figure 4). The organic components of *micro-box* decomposed with hydrochloric acid were analyzed by  $^1\text{H-NMR}$ . The ratio of dicarboxylates (bdc and ndc) to bpy was 2:1, corresponding to the chemical composition of the framework structures,  $[\text{Zn}_2(\text{dicarboxylate})_2(\text{bpy})]_n$ . Both dicarboxylates, bdc and ndc, were detected by  $^1\text{H-NMR}$  and the ratio of bdc and ndc was 75:25, which suggested that the original compound of **1** was converted to the solid-solution type PCP,  $[\text{Zn}_2(\text{bdc})_{1.5}(\text{ndc})_{0.5}(\text{bpy})]_n$  (**S1**), by ligand exchange (Figure 5). We successfully determined the single crystal structure of **S1** at as-synthesized and evacuated states (Figure 2c-f). Although the coordination geometry of **S1** is totally same as that of starting material of **1**, the not-interpenetrated structure of **1** was converted into the interpenetrated structure of **S1**. The ligand replacement from bulky ndc to simple bdc makes enough space for the interpenetration, resulting in the topological transformation from **1** to **S1** during the formation of macroscale architecture of *micro-box*. The crystal structures of **S1** was changed with respond to removal of guest molecules (Figure 2e-f). This structural transformation of **S1** corresponded to the structural transformation of *micro-box* (Figure 4), which also implied that the *micro-box* consists of solid-solution type interpenetrated PCP (**S1**). Noted that this structural conversion from not-interpenetrated structure (**1**) to interpenetrated structures (**S1**) improves the framework stability. Although the compound **1** becomes amorphous against guest

removal due to the large porosity, *micro-box* consisting of interpenetrated **S1** maintains the crystallinity against guest evacuation (Figure 4). This is because the interpenetration induced by ligand alternation from ndc to bdc, stabilizes the framework structure. The poor crystallinity of degassed **1** significantly decreased the uptake amount of CO<sub>2</sub> (40 ml/g); however, the stabilization of the framework structures of **S1** improves the uptake amount of CO<sub>2</sub> (120 ml/g), in spite of smaller pore volume (Figure 6). The step-wise uptake at lower pressure probably due to the structural transformation of **S1** was observed.

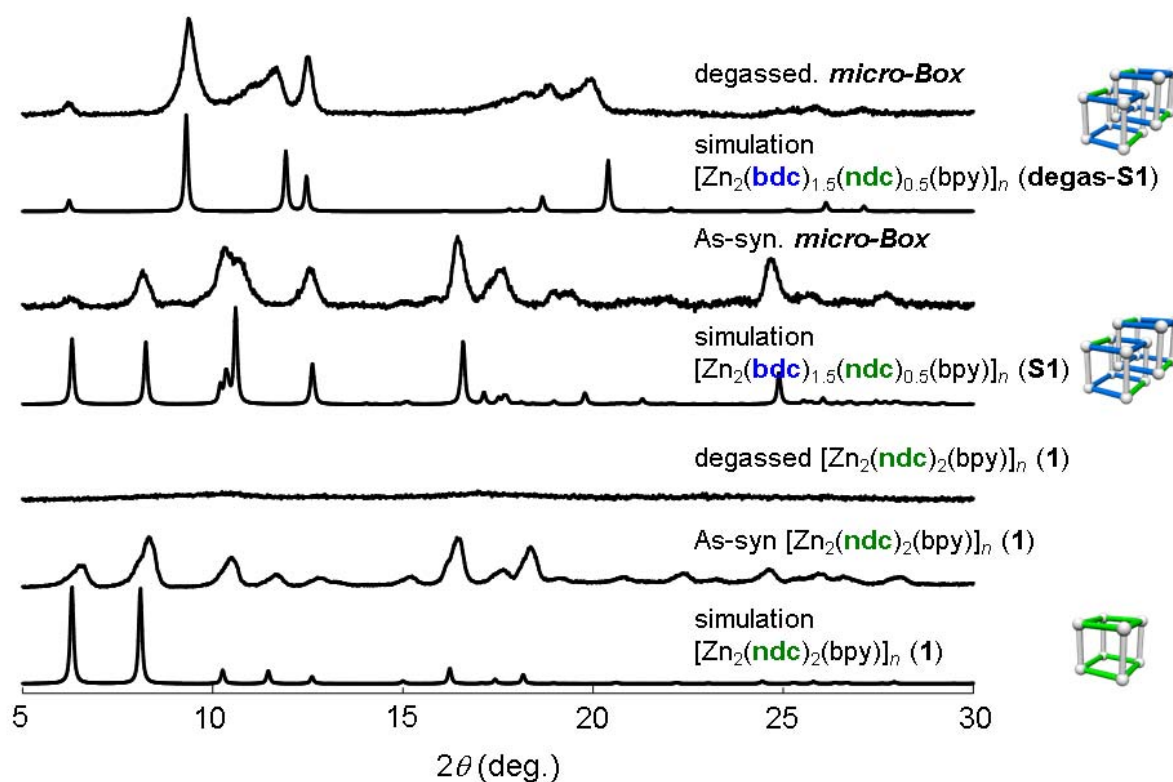


**Figure 4.** Simulated XRD patterns of **1**, **S1** and degassed **S1**. XRD patterns of **1**, degassed **1** and *micro-box* and degassed *micro-box*

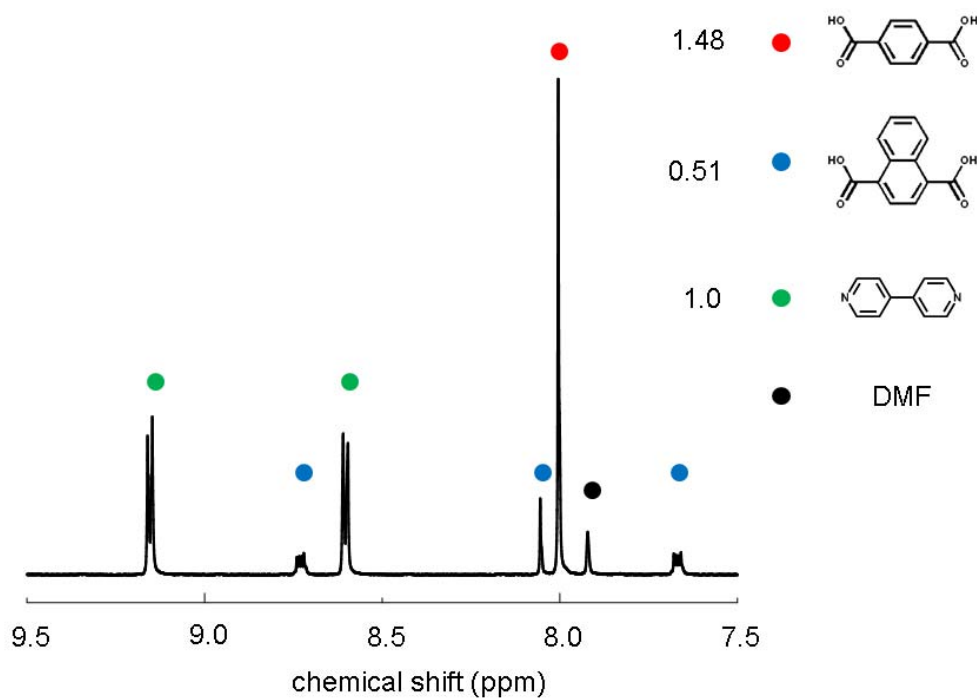


**Figure 5.**  $^1\text{H-NMR}$  spectrum of digested *micro-box*

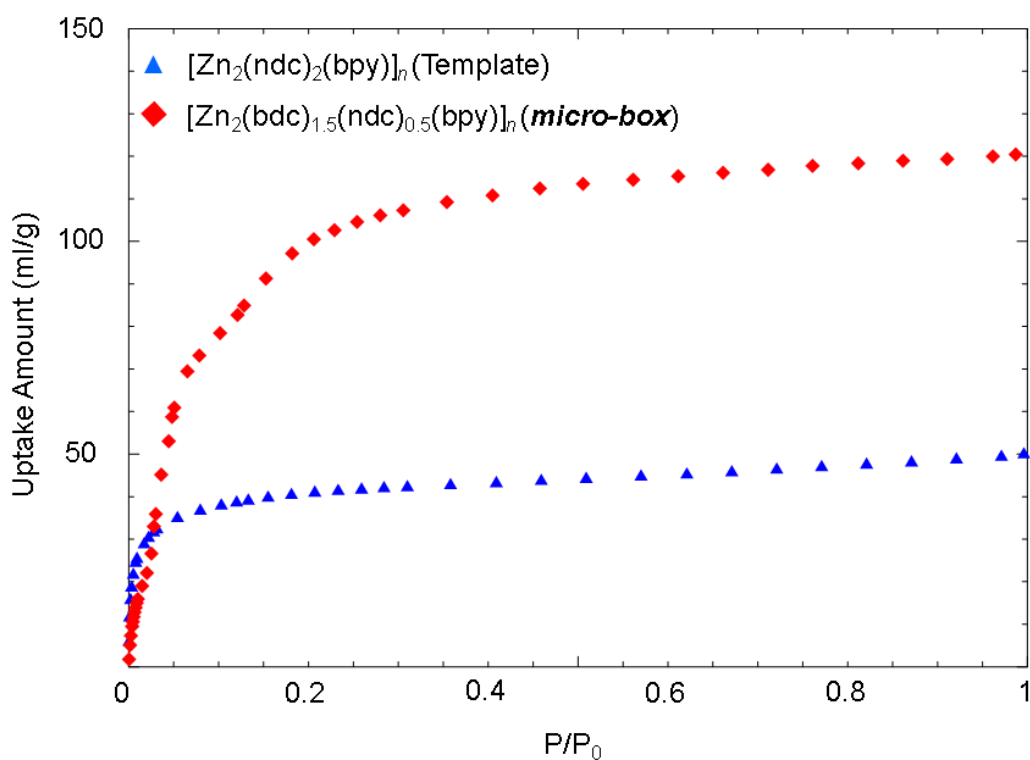


**Figure 6.** Adsorption isotherm of **1** and *micro-box* for  $\text{CO}_2$

Furthermore, the adsorption kinetics for  $\text{CO}_2$  were investigated by real-time monitoring of the pressure change after the introduction of  $\text{CO}_2$  at  $P/P_0 = 0.78$  into the sample tube. The time dependent uptake ( $P_t/P_e$ :  $P_t$  is the uptake at time  $t$  and  $P_e$  is the

equilibrium uptake) for CO<sub>2</sub> on the *microbox* and micrometer-sized crystals of **S1** is illustrated in Figure 7. The result shows the effect of the macroscale structures on the kinetics of CO<sub>2</sub> uptake; the rate of CO<sub>2</sub> sorption for *microbox* is much faster than that for the micrometer-sized crystals of **S1**. In order to elucidate the sorption kinetics for CO<sub>2</sub> depending on the macroscale structures, we here introduce the double-exponential (DE) model for the analyses as described in equation (eq1),<sup>30</sup>

$$P_t/P_e = A_1 \{1 - \exp(-k_1 t)\} - A_2 \{1 - \exp(-k_2 t)\} \quad (\text{eq1})$$

where  $k_1$  and  $k_2$  are kinetic rate constants, with  $A_1 + A_2 = 1$ . This is because there can be two kinetic processes each with different diffusion barriers; one is faster diffusion at the gas/crystal interface and the other is slower diffusion inside the pores. Since the diffusions inside the pores are determined by the framework structures, respectively, we attempted the global fitting analysis for CO<sub>2</sub> sorption kinetics by treating the  $k_2$  value as lateral fitting parameters. Kinetic parameters obtained by DE model are summarized in Table 1. The  $A_2$  contribution (pore diffusion inside crystals) of micrometer-sized crystals of **S1** for CO<sub>2</sub> sorption kinetics significantly increases ( $A_2 = 0.583$ ), compared with that for the *microbox* ( $A_2 = 0.315$ ). It is quite reasonable to consider that the latter contribution decreases in case of the *micro-box*, because the diffusion path should be shorter. The morphological difference between micrometer-sized crystals of **S1** and the *micro-box* influences the CO<sub>2</sub> sorption kinetics. Although we also demonstrated the single-exponential model that only includes one kinetic rate constant for the analyses, the model does not give a satisfactory fit for the normalized experimental data.

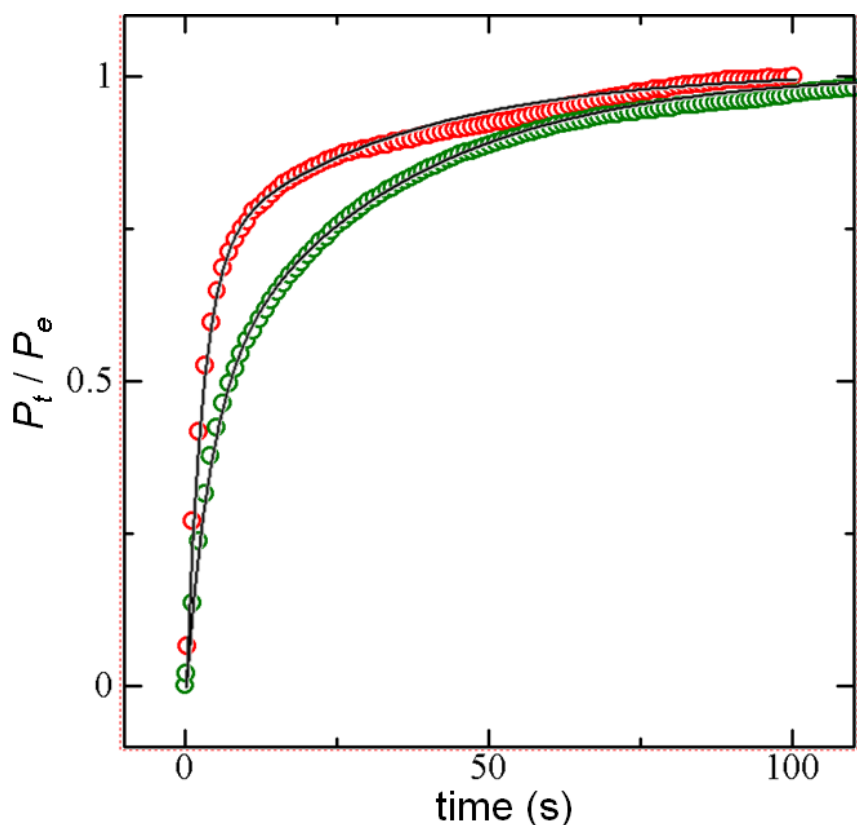


**Figure 7.** Adsorption kinetics profiles for CO<sub>2</sub> ( $P/P_0 = 0.78$ , 195 K). Sampling rate = 1 s. Green: micrometer-sized crystals of **S1**, red: *micro-box* (**S1**), respectively. Corresponding fits for the DE model are also shown.

**Table 1.** DE model fitting parameter for micrometer-sized crystals of **S1**, *micro-box*.

	$A_1$	$k_1 / 10^{-1} \text{ s}^{-1}$	$A_2$	$k_2 / 10^{-2} \text{ s}^{-2}$	$R^2$
<i>micro-box</i>	0.700	3.75	0.300	3.06	0.998
$\mu\text{m}$ -sized crystal ( <b>S1</b> )	0.465	2.51	0.545		0.999

To unveil the detailed reaction mechanism of this phenomenon, we carried out sets of experiments where the reaction time was systematically varied. The time-course experiments on <sup>1</sup>H-NMR of digested *micro-box* suggested that the ndc was quickly replaced with bdc and the molar ratio of bdc to ndc reached 75:25 in 4 minutes. The ratio (75:25) was maintained till 30 minutes, which suggests that the chemical composition of **S1** is most stable phase in this replacement condition (Figure 8). The time-course experiments on XRD supported that the framework geometry of [Zn<sub>2</sub>(dicarboxylate)<sub>2</sub>(bpy)]<sub>n</sub> was maintained during this reaction. The organic components in residual solution was also analyzed by <sup>1</sup>H-NMR. The molar amount of bdc and ndc was calculated by comparing the integration area of methanol (0.1 mmol),

bdc and ndc. The transported amount of bdc (from liquid to solid) and ndc (from solid to liquid) can be estimated from the calculated molar amount of bdc and ndc. The time-course experiments on  $^1\text{H-NMR}$  of the residual solution showed that the transported amount of ndc is always larger than that of bdc (Figure 9). The starting material of **1** was dissolved and ndc was eluted to the solution. In the meantime, the crystals of **S1** was formed on the surface of the original cuboid crystals by employing Zn, ndc and bpy from starting materials and bdc from solution. A certain amount of bdc was consumed to form the solid solution type PCP of **S1**. The larger amount of ndc was transported (from solid to liquid) than that of bdc during this chemical alternation, leading to the void formation inside the material.

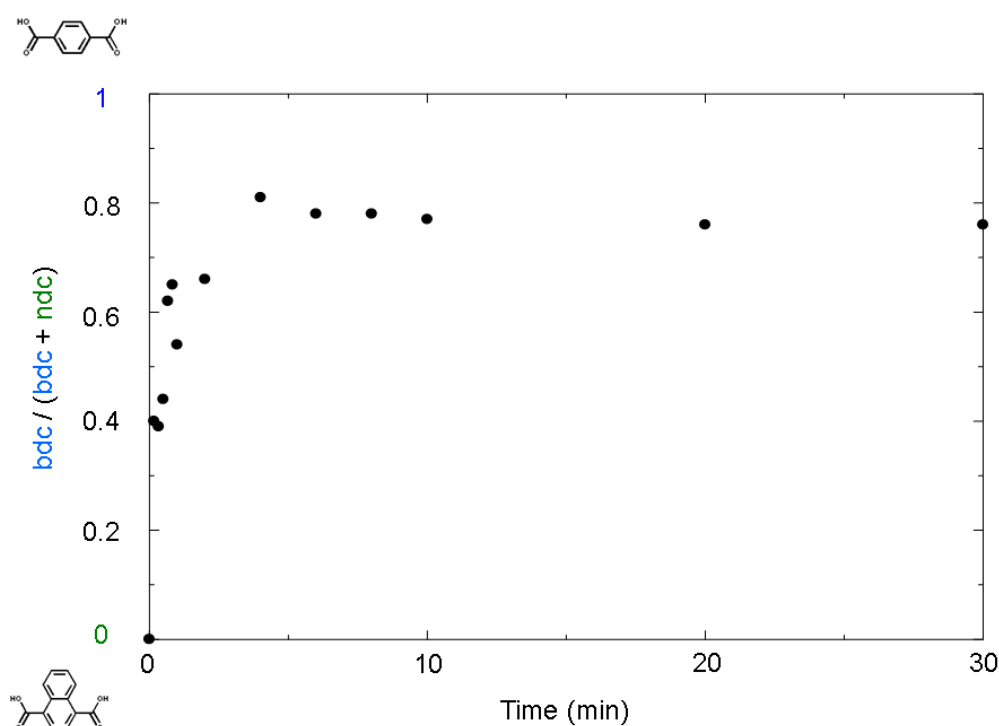


**Figure 8.** The chronological change in the ratio of bdc and ndc in the solid-state compounds

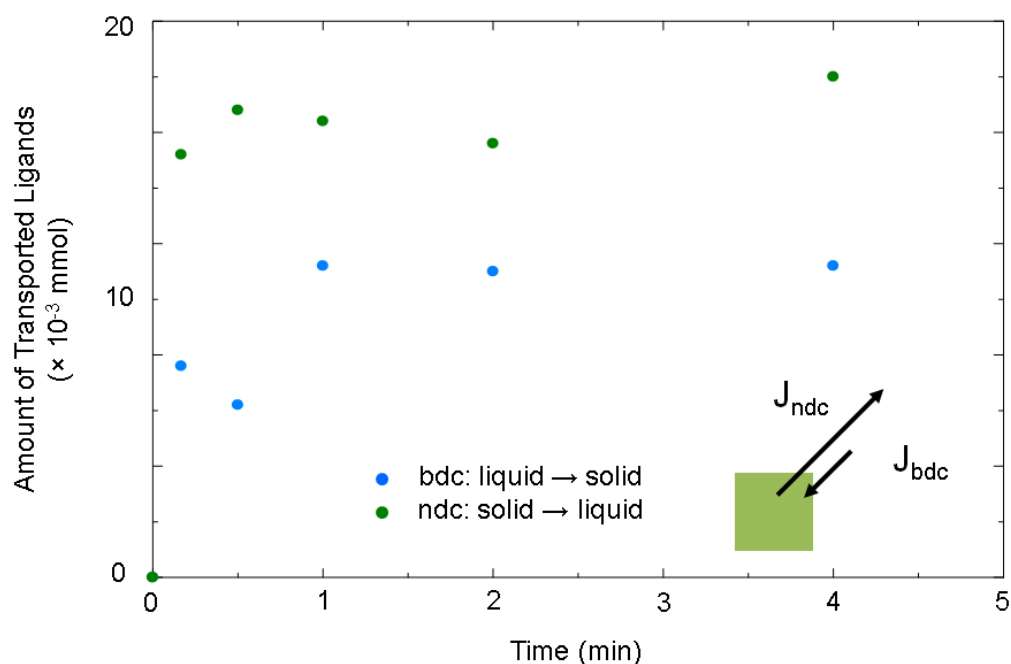


**Figure 9.** The chronological change of transported amount of bdc and ndc.

This kind of phenomenon also occurred in a millimeter-sized crystal of **1**. A huge single crystal of **1** ( $2 \times 2 \times 1 \text{ mm}^3$ ) was placed in a solution of  $\text{Zn}_2(\text{NO}_3)_2 \cdot 6\text{H}_2\text{O}$ ,  $\text{H}_2\text{bdc}$ , bpy in DMF, and the solution was kept at 393 K for two days. The upper surface of obtained compound (cubic architecture) was manually sliced with a microscopic knife. The optical microscopic observation of the sliced sample clearly showed that the millimeter-sized cubic crystal was converted to a millimeter-sized box (*mil-box*) (Figure 10). To unveil the conversion process from a cubic crystal to a box architecture, the reaction was stopped at 1 day and the upper surface of cubic object was sliced. A portion of original crystal (**1**) was still remained inside the box (Figure 10d). Furthermore,  $^1\text{H-NMR}$  measurement on digested *mil-box* was same as **S1**,  $[\text{Zn}_2(\text{bdc})_{1.5}(\text{ndc})_{0.5}(\text{bpy})]_n$ . Since the obtained architecture (*mil-box*) was enough large to investigate the growth direction, surface XRD measurements on *mil-box* was performed. Interestingly, the crystal orientation of *mil-box* (**S1**) was totally same as single crystals of **1**. New crystals of **S1** was grown on the template of **1** with maintaining the original crystal orientation of **1** (Figure 11). Although we attempted to synthesize the mil-box without  $\text{Zn}_2(\text{NO}_3)_2 \cdot 6\text{H}_2\text{O}$  and bpy, the box architecture was not maintained and tiny crystals were obtained. This is probably because the dissolution of template is faster than the new crystallization of **S1** in the reaction of an oil heater.

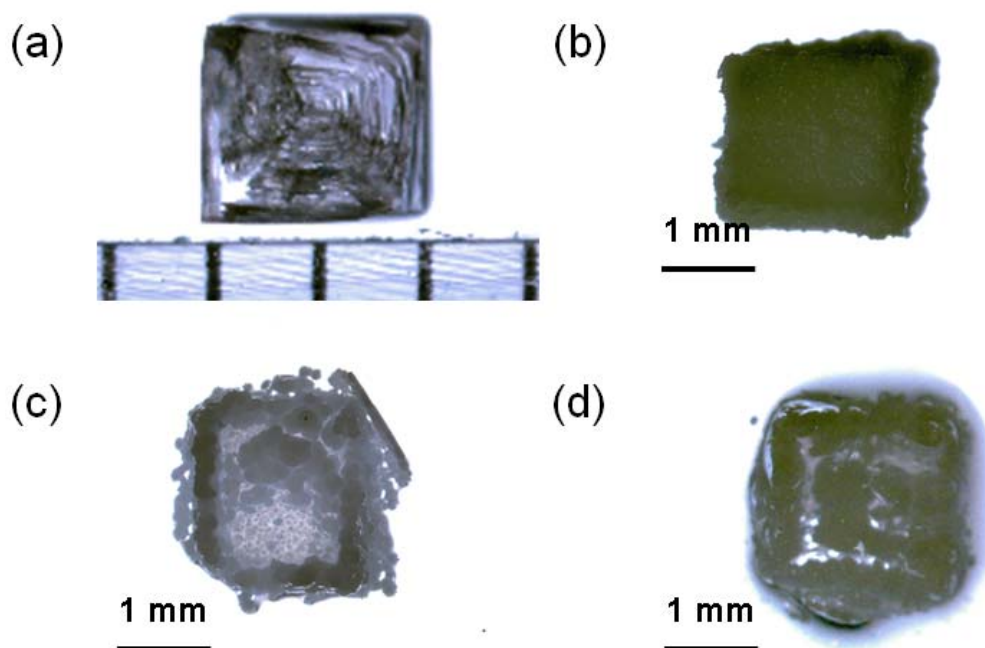


**Figure 10.** Optical microscopic observations: (a) **1**, (b) *mil-box*; (c) *mil-box* sliced with a microscopic knife, (d) intermediate state of a *mil-box*.

Based on the series of experiments, we can propose the reaction process of this phenomenon. (a) The cuboid crystals of **1** are dissolved and the components ( $\text{Zn}^{2+}$ , ndc and bpy) are eluted to the solution. (b) **S1** was crystallized on the surface of **1** by employing  $\text{Zn}^{2+}$ , ndc and bpy from starting materials and bdc from solution. The original coordination geometry and orientation were maintained during this process. (c) More amount of ndc was transported from solid to solution and less amount of bdc was consumed to form **S1**. As a result, the voids were formed inside the cuboid crystals. (d) Finally, the cuboid crystals of **1** was converted to box architectures of **S1** (Figure 12).

These results demonstrate a new method for designing macroscale architecture with controlling the chemical structures of PCPs. The ligand replacements allows for the formation of solid-solution type PCP and the differences in transported amount of organic ligands creates the box architecture. We applied this phenomenon to another framework structure, IR-MOF.<sup>31-32</sup> The box architecture of IR-MOF was successfully obtained by this phenomenon (Figure 13). We hope that this discovery will give a new insight to fabricate the well-designed architectures of PCPs.

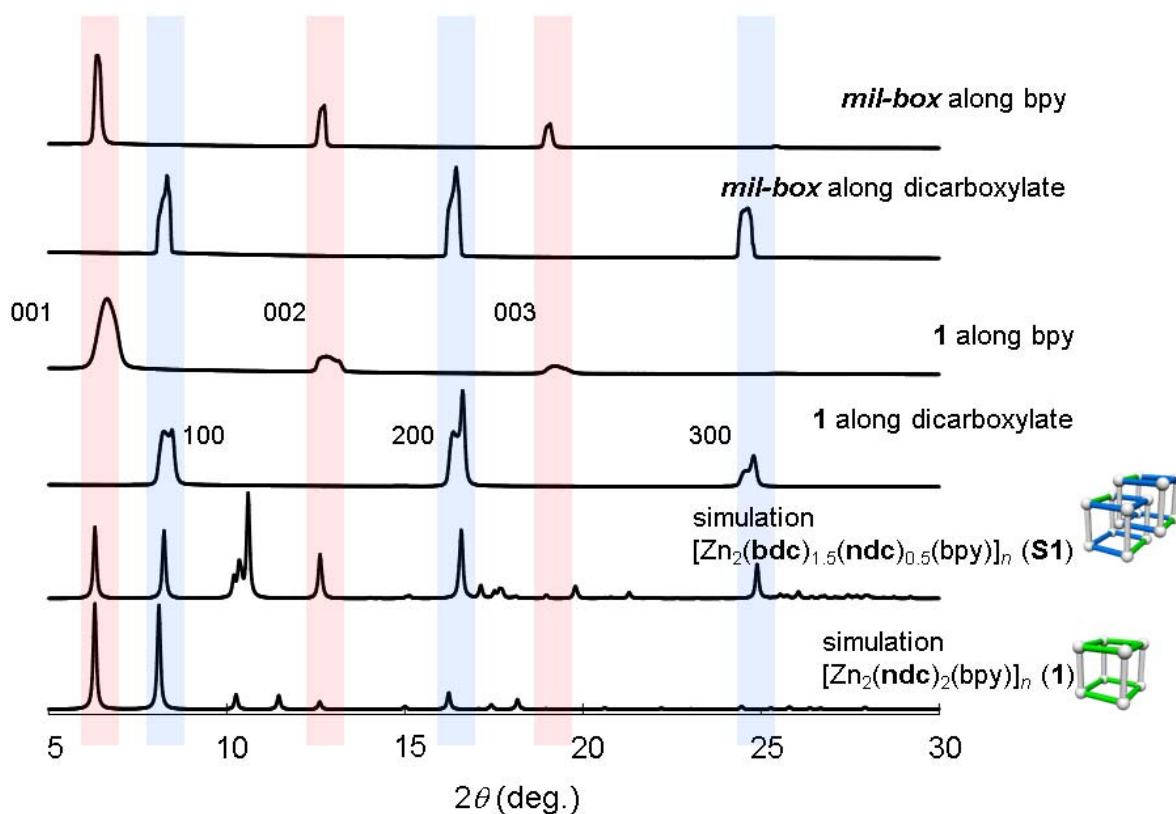


**Figure 11.** Simulated XRD patterns of and **S1**. XRD patterns of **1** and **S1**, along dicarboxylate and bpy directions.

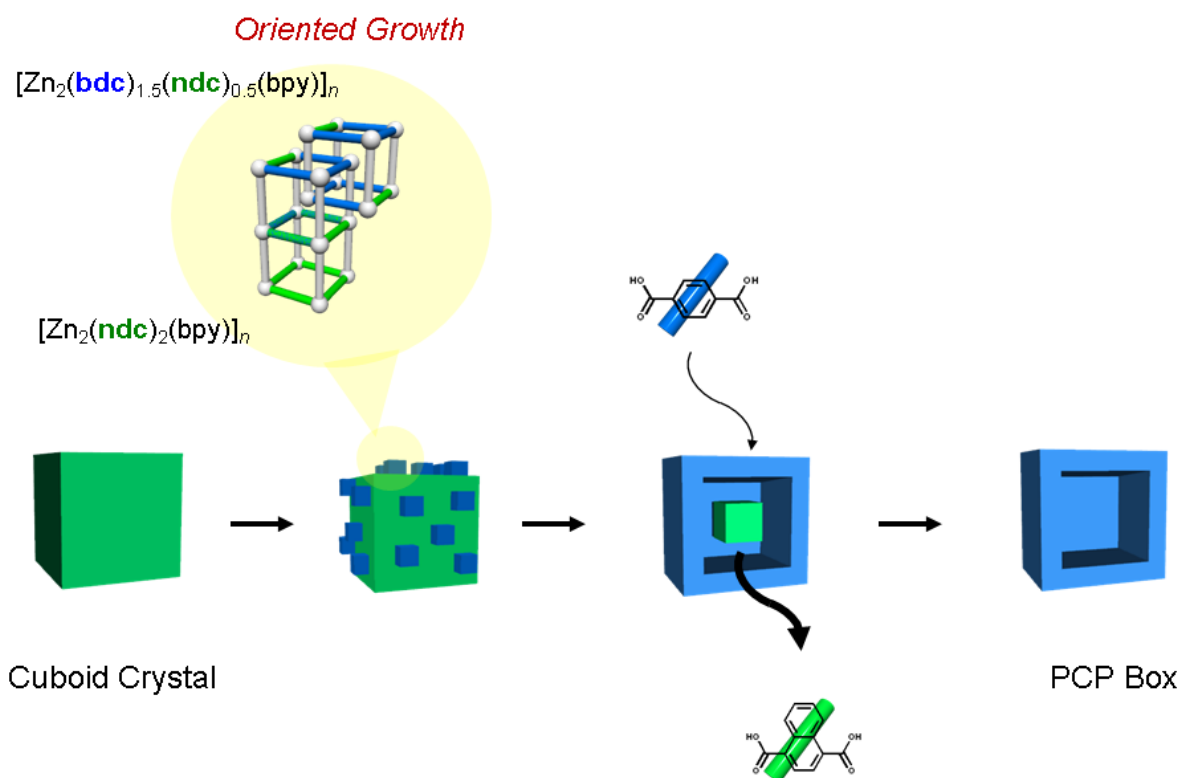


**Figure 12.** Schematic illustration of the structural transformation from the cuboid crystal to the box architecture.

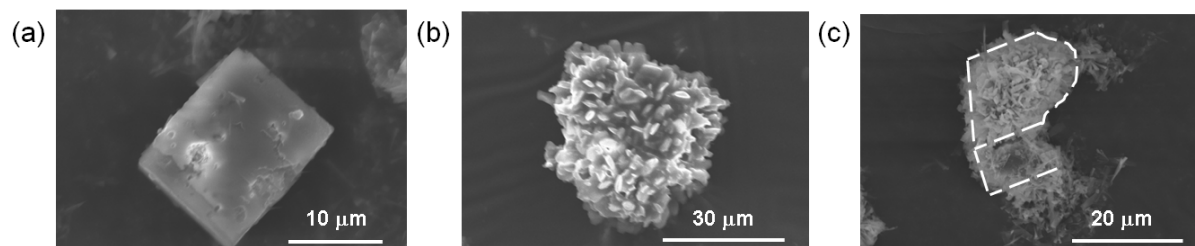


**Figure 13.** SEM images of *micro-box* of IR-MOF. (a) template (MOF-5), (b) *micro-box* before ultrasonication, (c) *micro-box* after ultrasonication. The dot lines indicates the edges of the broken *micro-box*.

## Conclusion

In summary, this work demonstrate that a new phenomenon of PCPs and suggest a new method for designing macroscale architecture with solid-solution type PCP. The kinetics and spatial coupling between the dissolution of parent PCP and the crystallization of solid-solution type PCPs enables the production of box-shaped architectures. We believe that the precise control of parent PCPs should permit the design of PCP hollow architectures with a great variety of useful geometries.

## Experimental Section

### Synthesis of the single crystals, **1**

Zn(NO<sub>3</sub>)<sub>2</sub>•6H<sub>2</sub>O (72.3 mg, 2.5 × 10<sup>-1</sup> mmol), 1,4-naphthalenedicarboxylic acid (54.0 mg, 2.5 × 10<sup>-1</sup> mmol) and 4,4'-bipyridyl (21.0 mg, 1.25 × 10<sup>-1</sup> mmol) were dissolved in 5 mL of *N,N*-dimethylformamide (DMF). The temperature was kept at 80 °C for two days. After cooling, two-millimeter sized single crystals were harvested.

### Synthesis of the powder crystals, **1**

Zn(NO<sub>3</sub>)<sub>2</sub>•6H<sub>2</sub>O (148.5 mg, 5.0 × 10<sup>-1</sup> mmol), 1,4-naphthalenedicarboxylic acid (108.0 mg, 5.0 × 10<sup>-1</sup> mmol) and 4,4'-bipyridyl (42.0 mg, 2.5 × 10<sup>-1</sup> mmol) were dissolved in 10 mL of DMF. The temperature was kept at 120 °C for three hours by microwave instrument (Biotage, Initiator).

### Synthesis of *micro-box*

1,4-benzenedicarboxylic acid (16.6 mg, 1.0 × 10<sup>-1</sup> mmol) was dissolved in 2 mL of DMF. The powder crystals of **1** (8.0 mg, 2.0 × 10<sup>-2</sup> mmol) were put into the solution and the temperature was kept at 80 °C by microwave instrument (Biotage, Initiator).

### Synthesis of *mil-box*

Zn(NO<sub>3</sub>)<sub>2</sub>•6H<sub>2</sub>O (5.94 mg, 2.0 × 10<sup>-2</sup> mmol), 1,4-benzenedicarboxylic acid (3.32 mg, 2.0 × 10<sup>-2</sup> mmol) and 4,4'-bipyridyl (1.68 mg, 1.0 × 10<sup>-2</sup> mmol) were dissolved in 1 mL of DMF. A single crystal of **1** was placed in the stocked solution and the temperature was kept at 120 °C for two days. After cooling, a two-millimeter sized PCP-Box was obtained.

### Synthesis of **S1**

Zn(NO<sub>3</sub>)<sub>2</sub>•6H<sub>2</sub>O (11.9 mg, 4.0 × 10<sup>-2</sup> mmol), H<sub>2</sub>bdc (5.3 mg, 3.2 × 10<sup>-2</sup> mmol), and H<sub>2</sub>ndc (1.7 mg, 0.8 × 10<sup>-2</sup> mmol) were dissolved in 2 mL of DMF. 4,4'-bipyridyl (1.6 mg, 1.0 × 10<sup>-2</sup> mmol) was dissolved in 1 mL of MeOH. 2 mL of DMF solution was put in a narrow glass tube. 0.5 mL of the mixture of DMF and MeOH (DMF : MeOH = 1:1) was layered on top of the DMF solution, and then 1 mL of MeOH solution of bpy was layered on top of the mixture. The stocked solution was kept at 90 °C for two days.

### **<sup>1</sup>H-NMR on digested *mil-box* and *micro-box***

The dozens of crystals are decomposed in dimethyl sulfoxide-d<sub>6</sub> with hydrochloric acid. The obtained solution was analyzed by 500MHz <sup>1</sup>H-NMR (JNM-A500).

### **<sup>1</sup>H-NMR on residual solution**

The mixture of 0.3 ml of the residual solution, 0.3 ml of dimethyl sulfoxide-d<sub>6</sub> and 40.6 μl of methanol was analyzed by 500MHz <sup>1</sup>H-NMR (JNM-A500). The peaks of H<sub>2</sub>bdc, H<sub>2</sub>ndc and methanol were fitted by Lorentz function to compare the exact integration areas of peaks.

### **Field-emission scanning electron microscopy (FE-SEM)**

SEM observations were performed with a JEOL Model JSM-7001F4 SEM system operating at 15.0 kV. The samples were deposited on carbon tape and coated with osmium prior to measurement.

### **X-ray diffraction measurement (XRD) and surface X-ray diffraction measurement (SXRD)**

The samples were deposited on glass substrates. XRD and SXRD patterns were recorded by RINT-2000 (Rigaku) and Smart Lab (Rigaku), respectively.

### **Sorption experiments**

The sorption isotherms of **1** and *mil-box* (**S1**) for N<sub>2</sub>, O<sub>2</sub> and CO<sub>2</sub> were recorded on a BELSORP-mini adsorption instrument from BEL Japan, Inc. Before adsorption measurements, the samples were degassed under vacuum at 323 K for 6 h.

### **Diffusion kinetics**

The sorption kinetics of micrometer-sized **S1** and *micro-box* for N<sub>2</sub>, O<sub>2</sub> and CO<sub>2</sub> were recorded on a BELSORP-18 adsorption instrument from BEL Japan, Inc. The pressure value of the sample tube was recorded every 1 second. Before adsorption measurements, the samples were degassed under vacuum at 323 K for 6 h.

### **Structure Determination**

X-ray data collection ( $5^\circ < 2\theta < 55^\circ$ ) was conducted at 223K on Rigaku AFC10 diffractometer Mo-K $\alpha$  radiation ( $\lambda = 0.7105 \text{ \AA}$ ) with Rigaku Mercury CCD system. The structures were solved by a direct method (SIR2002) and expanded using Fourier

techniques. All calculations were performed using the CrystalStructure crystallographic software package 4.0 of Rigaku.

Crystal data for **1**⊃solvent: C<sub>34</sub>H<sub>20</sub>N<sub>2</sub>O<sub>8</sub>Zn<sub>2</sub>, *tetragonal*, space group *P4/mmm*, (no. 123),  $a = 10.9396(6)$  Å,  $c = 14.0640(11)$  Å,  $V = 1683.11(19)$  Å<sup>3</sup>,  $Z = 1$ ,  $T = 223$  K.  $\rho_{\text{calcd}} = 1.148$  gcm<sup>-3</sup>,  $\mu(\text{MoK}\alpha) = 0.776$  cm<sup>-1</sup>, 1185 reflections measured, 985 observed ( $I > 2.00\sigma(I)$ ) 63 parameters;  $R_1 = 0.0692$ ,  $wR_2 = 0.2315$ , GOF = 1.158.

Crystal data for **S1**⊃solvent: C<sub>31</sub>H<sub>21</sub>N<sub>3</sub>O<sub>9</sub>Zn<sub>2</sub>, *triclinic*, space group *P-1*, (no. 2),  $a = 10.887(3)$  Å,  $b = 10.923(3)$  Å,  $c = 14.068(4)$  Å,  $V = 1645.1(7)$  Å<sup>3</sup>,  $Z = 2$ ,  $T = 93$  K.  $\rho_{\text{calcd}} = 1.434$  gcm<sup>-3</sup>,  $\mu(\text{MoK}\alpha) = 1.513$  cm<sup>-1</sup>, 13134 reflections measured, 7178 observed ( $I > 2.00\sigma(I)$ ) 446 parameters;  $R_1 = 0.0512$ ,  $wR_2 = 0.1835$ , GOF = 1.098.

Crystal data for **S1**: C<sub>31</sub>H<sub>21</sub>N<sub>3</sub>O<sub>9</sub>Zn<sub>2</sub>, *triclinic*, space group *P-1*, (no. 2),  $a = 10.887(3)$  Å,  $b = 10.923(3)$  Å,  $c = 14.068(4)$  Å,  $V = 1645.1(7)$  Å<sup>3</sup>,  $Z = 2$ ,  $T = 93$  K.  $\rho_{\text{calcd}} = 1.434$  gcm<sup>-3</sup>,  $\mu(\text{MoK}\alpha) = 1.513$  cm<sup>-1</sup>, 13134 reflections measured, 7178 observed ( $I > 2.00\sigma(I)$ ) 446 parameters;  $R_1 = 0.0512$ ,  $wR_2 = 0.1835$ , GOF = 1.098.

## References

- (1) P. A. Alivisatos, *Science* **1996**, *271*, 933-937.
- (2) H. Matsubara, S. Yoshimoto, H. Saito, Y. Jianglin, Y. Tanaka, S. Noda, *Science* **2008**, *319*, 445-447.
- (3) J. W. Johnson, D. C. Johnston, A. J. Jacobson, J. F. Brody, *J. Am. Chem. Soc.* **1984**, *106*, 8123-8128.
- (4) Z. Wang, B. Huang, Y. Dai, X. Zhang, X. Qin, Z. Li, Z. Zheng, H. Chenga, L. Guo, *CrystEngComm* **2012**, *14*, 4578-4581.
- (5) Y. Yin, R. M. Rioux, C. K. Erdonmez, S. Hughes, G. A. Somorjai, A. P. Alivisatos, *Science* **2004**, *304*, 711-714.
- (6) H. J. Fan, U. Gösele, M. Zachariask, *Small* **2007**, *10*, 1660-1671.
- (7) E. González, J. Arbio, V. F. Puentes, *Science* **2011**, *334*, 1377-1380.
- (8) M. Dincă, A. Dailly, Y. Liu, C. M. Brown, D. A. Neumann and J. R. Long, *J. Am. Chem. Soc.*, **2006**, *128*, 16876-16883.
- (9) S. Ma, D. Sun, J. M. Simmons, C. D. Collier, D. Yuan, and H. C. Zhou, *J. Am. Chem. Soc.*, **2008**, *130*, 1012-1016.
- (10) L. Alaerts, C. E. A. Kirschhock, M. Maes, M. A. van der Veen, V. Finsy, A. Depla, J. A. Martens, G. V. Baron, P. A. Jacobs, J. F. M. Denayer, and D. E. De Vos, *Angew. Chem. Int. Ed.* **2007**, *46*, 4293-4297.
- (11) B. Wang, A. P. Côté, H. Furukawa, M. O’Keeffe, O. M. Yaghi, *Nature* **2008**, *453*, 207-212.
- (12) J. S. Seo, D. Whang, H. Lee, S. I. Jun, J. Oh, Y. J. Jeon, K. Kim, *Nature* **2000**, *404*, 982-986.
- (13) C.-D. Wu, A. Hu, L. Zhang, W. Lin, *J. Am. Chem. Soc.* **2005**, *127*, 8940-8941.
- (14) S. Bureekaew, S. Horike, M. Higuchi, M. Mizuno, T. Kawamura, D. Tanaka, N. Yanai, S. Kitagawa, *Nature Mater.* **2009**, *8*, 831-836.
- (15) J. A. Hurd, R. Vaidhyanathan, V. Thangadurai, C. I. Ratcliffe, I. L. Moudrakovski, G. K. H. Shimizu, *Nature Chem.* **2009**, *1*, 705-710.
- (16) J. Reboul, S. Furukawa, N. Horike, M. Tsotsalas, K. Hirai, H. Uehara, M. Kondo, N. Louvain, O. Sakata, S. Kitagawa, *Nature Mater.* **2012**, *11*, 717-723.
- (17) A. Dhakshinamoorthy, M. Alvaro, Y. K. Hwang, Y. K. Seo, A. Corma, H. Garcia, *Dalton Trans.* **2011**, *40*, 10719-10724.
- (18) S. H. Jung, J. H. Lee, J. W. Yoon, C. Serre, G. Férey, J. S. Chang, *Adv. Mater.* **2007**, *19*, 121-124.
- (19) S. Jung, W. Cho, H. J. Lee, M. Oh, *Angew. Chem. Int. Ed.* **2009**, *48*, 1459-1462.

- (20) Hee Jung Lee, Won Cho and Moonhyun Oh, *Chem. Commun.* **2012**, 48, 221-223.
- (21) S. Hermes, F. Schröder, R. Chelmowski, C. Wöll, R. A. Fischer, *J. Am. Chem. Soc.* **2005**, 127, 13744-13745.
- (22) O. Shekhah, H. Wang, S. Kowarik, F. Schreiber, M. Paulus, M. Tolan, C. Sternemann, F. Evers, D. Zacher, R. A. Fischer, C. Wöll, *J. Am. Chem. Soc.* **2007**, 129, 15118-15119.
- (23) E. Biemmi, C. Scherb, T. Bein, *J. Am. Chem. Soc.* **2007**, 129, 8054-8055.
- (24) H. Bux, F. Liang, Y. Li, J. Cravillon, M. Wiebcke, J. Caro, *J. Am. Chem. Soc.* **2009**, 131, 16000-16001.
- (25) Y. Wu, F. Li, W. Zhu, J. Cui, C. Tao, C. Lin, P. M. Hannam, G. Li, *Angew. Chem. Int. Ed.* **2011**, 50, 12518-12522.
- (26) D. N. Dybtsev, H. Chun, K. Kim, *Angew. Chem. Int. Ed.* **2004**, 43, 5033-5036.
- (27) H. Chun, D. N. Dybtsev, H. Kim, K. Kim, *Chem. –Eur. J.* **2005**, 11, 3521-3529.
- (28) B. Chen, C. Liang, J. Yang, D. S. Contreras, Y. L. Clancy, E. B. Lobkovsky, O. M. Yaghi, S. Dai, *Angew. Chem. Int. Ed.* **2006**, 45, 1390-1393.
- (29) B. –Q. Ma, K. L. Mulfort, J. T. Hupp, *Inorg. Chem.* **2005**, 44, 4912-4914.
- (30) M. B. Rao, R. G. Jenkins, W. A. Steele, *Langmuir* **1985**, 1, 137-141.
- (31) M. Eddaoudi, J. Kim, N. Rosi, D. Vodak, J. Wachter, M. O’Keeffe, O. M. Yaghi, *Science* **2002**, 295, 469-472.
- (32) O. M. Yaghi, M. O’Keeffe, N. W. Ockwig, H. K. Chae, M. Eddaoudi, J. Kim, *Nature* **2003**, 423, 705-714.



## **Chapter 7**

### **Redox Reaction in Two-Dimensional Porous Coordination Polymers Based on Ferrocenedicarboxylates**

#### **Abstract**

A series of 1,1'-ferrocenedicarboxylate-based twodimensional porous coordination polymers were synthesized by incorporating different diamine coligands. These compounds immobilized on electrodes, exhibited reversible redox reactions, arising from ferrocenyl moiety.

## Introduction

Porous coordination polymers (PCPs), assembled from metal ions and organic ligands, are an interesting class of crystalline materials.<sup>1-5</sup> They have been extensively studied for applications in gas storage,<sup>6-8</sup> separation<sup>9-11</sup> and chemical sensing.<sup>12-15</sup> Compared with these porous properties, only a few studies on the electronic properties of the frameworks have been reported.<sup>16-18</sup> The synergetic collaboration between the electronic properties of the framework and the intrinsic porous properties has led to new applications of PCPs in a wide range of important fields. In particular, a redox active PCP may be useful material for electrochemical applications such as ion storage<sup>19</sup> or electrocatalysis.<sup>20</sup> The key to successful implementation is not only to construct the redoxactive framework itself, but also to hybridize the framework with an electrode, which allows the investigation of redox process in the pores.

Although the judicious choice of metal ion and organic linker provides the redox activity within PCP frameworks,<sup>21-23</sup> the redox reaction often changes the coordination environment of metal ions, thus leading to destruction of the framework. One way to overcome the issues is to construct the framework with stable ligands for the redox reaction. In this context, 1,1'-ferrocenedicarboxylate (Fc<sub>2</sub>dc) is an excellent candidate because it contains the stable ferrocene moiety and two carboxylate coordination sites.<sup>24-26</sup> Some research groups have reported on the syntheses of ferrocene-based coordination polymers,<sup>27-29</sup> but there are only a few reports of the solid-state electrochemical properties of coordination polymers containing the Fc<sub>2</sub>dc ligand.<sup>30-31</sup> Recently we reported on a series of two-dimensional (2D) PCPs, so-called coordination polymers with an interdigitated structure (CID), of which the three components, namely the metal ions, V-shaped dicarboxylate ligands, and diamine pillar ligands, participate in the construction.<sup>32-35</sup> Their porous properties and chemical functionalities can be easily modulated by varying the components. Although there is a limit to the angle of two carboxylates in the V-shaped ligand in the range 118°-152°, the rotational freedom of the ferrocenyl moiety enables the ligand to mimic the V-shape, thus providing CID frameworks with stable redox properties.

Here we report the rational synthesis of ferrocene-based CID frameworks by incorporating different diamine pillar ligands. The length of the pillar ligand determines the configuration of the 2D sheets, resulting in different thermal stabilities. The electrochemical properties were elucidated by the immobilization of these crystals on gold electrodes. A coordination framework of  $\{[\text{Zn}(\text{Fc}_2\text{dc})(\text{bpy})]\cdot(\text{DMF})_{0.5}(\text{MeOH})_{0.5}\}_n$  (**1** ⊃ solvents) was synthesized via the reaction of  $\text{Zn}(\text{NO}_3)_2\cdot 6\text{H}_2\text{O}$ ,  $\text{H}_2\text{Fc}_2\text{dc}$  and bpy in a

DMF/MeOH solution at 353 K (bpy = 4,4'-bipyridyl). As shown in Fig. 1a and b, the Zn ion has a distorted octahedral  $N_2O_4$  geometry; it is coordinated by two bpy molecules at the axial positions, one chelating carboxylate of Fcdc and two other monodentate carboxylates of Fcdc in the equatorial plane. The coordination of Fcdc ligands to the Zn ions constructed a onedimensional (1D) chain structure as shown in Figure 1a, followed by the linkage of the adjacent chains through bpy in the axial positions, leading to the formation of a 2D sheet. Alternatively assembled are two types of sheet structures, sheets A and B, which are mirror images of each other. It should be noted that the length of bpy (7.1 Å) is too short to form the interdigitation because of the bulkiness of the ferrocenyl moiety (the distance between cyclopentadienyl rings is 6.8 Å), compared with the phenyl ring, seen in the reported CID structure. Therefore, the noninterdigitation between the sheets provided 1D channels with a window size of  $4.4 \times 6.0 \text{ \AA}^2$  (Figure 2a-b).

Elongation of the pillar ligands from bpy to dpb or dpndi created a space between the 1D chains and allowed them to form the interdigitation (dpb = 1,4-di(pyridin-4-yl)benzene, dpndi = *N,N'*-di(4-pyridyl)-1,4,5,8-naphthalenetetracarboxydiimide). These analogous frameworks were synthesized by the solvothermal reaction of  $Zn(NO_3)_2 \cdot 6H_2O$  with  $H_2Fcdc$  and dpb or dpndi in a DMF/MeOH solution:  $\{[Zn(Fcdc)(dpb)] \cdot (DMF)_{0.5}(MeOH)_{0.5}\}_n$  (**2**  $\supset$  solvents) or  $\{[Zn(Fcdc)(dpndi)] \cdot (DMF)_{0.5}(MeOH)_{0.5}\}_n$  (**3**  $\supset$  solvents), respectively. Although the compound **2** formed the alternative assembly of sheet structures as seen in **1**, only one type of 2D sheet (sheet A) was found in the compound **3**. The expansion of the interchain distance in **2** and **3** resulting from the incorporation of the longer pillar ligands (dpb (11.4 Å) or dpndi (15.5 Å)) enables the 2D sheets to form the interdigitation. Whereas the 1D channels with a window size of  $4.4 \times 4.9 \text{ \AA}^2$  extend along the *c* axis in compound **2**, the 1D channels with a window size of  $4.8 \times 4.5 \text{ \AA}^2$  runs along the *a* axis in compound **3**(Figure 2c-e).

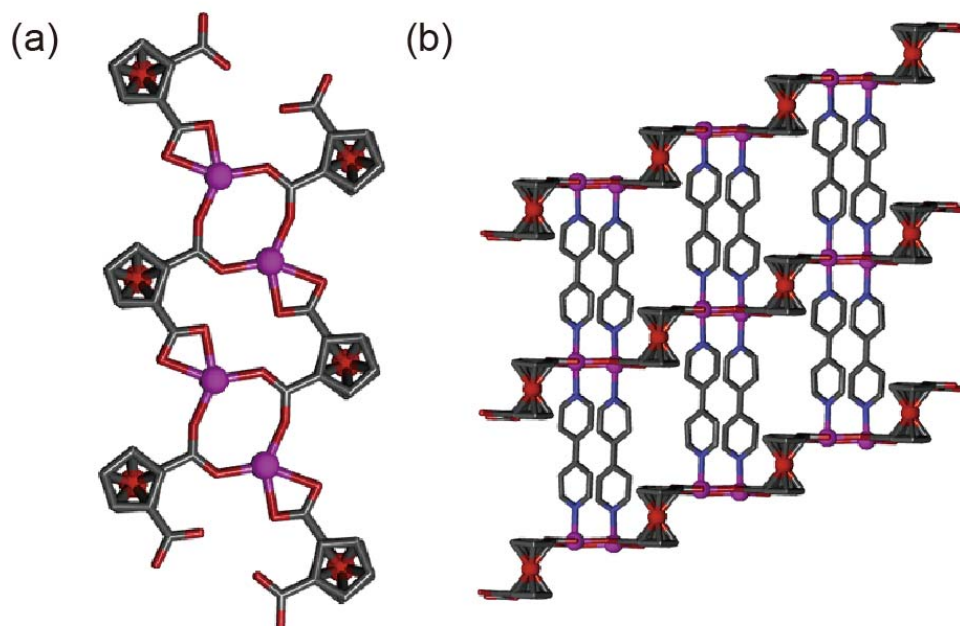


**Figure 1.** Crystal structures of (a) the 1D chain structure composed of Zn ions and Fcdc, and (b) the sheet structure of **1**. Gray, blue, red, orange, and purple are C, N, O, Fe and Zn, respectively. The hydrogen atoms and guest molecules are omitted for clarity.

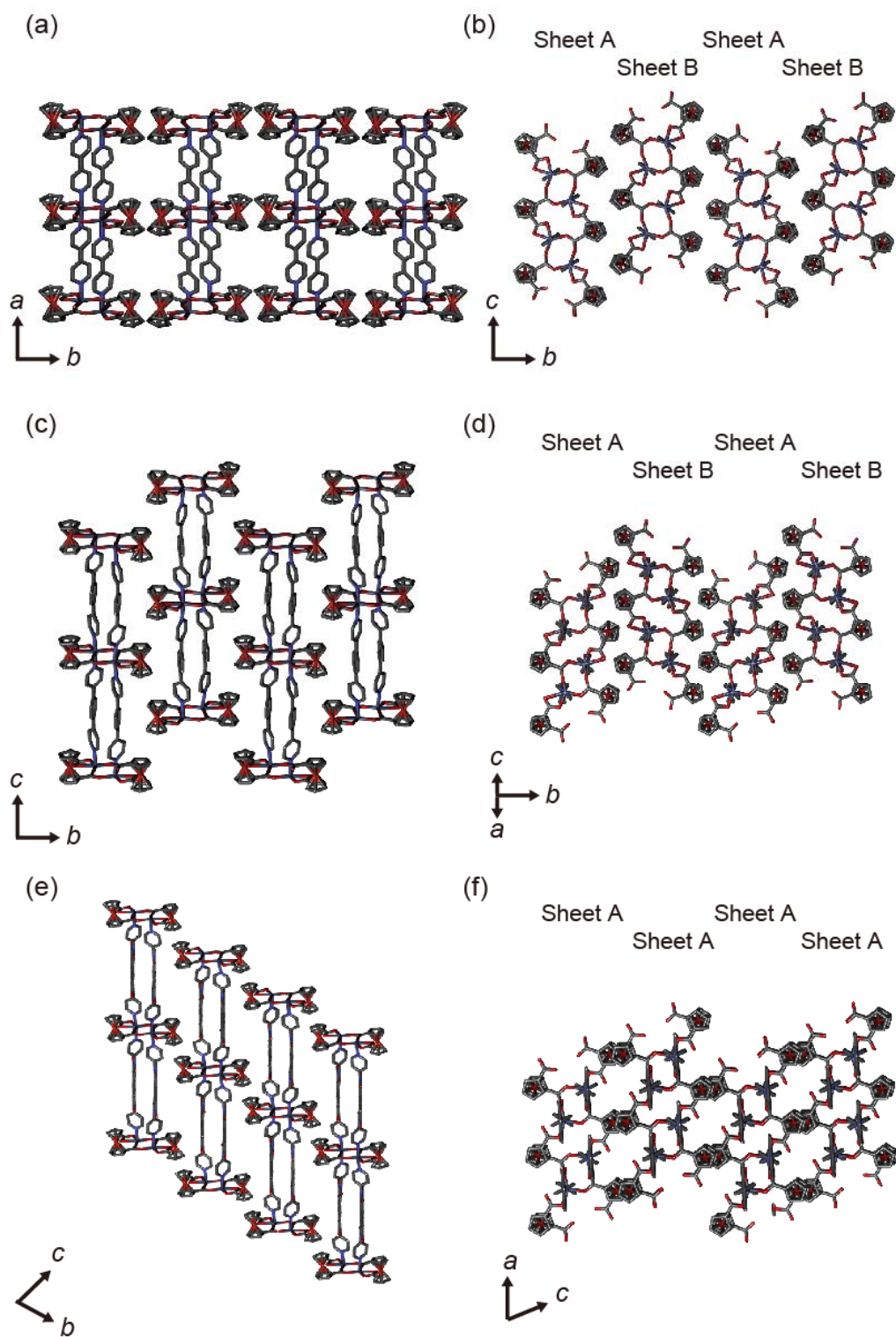


**Figure 2.** Crystal structures showing (a) the side view, (b) the top view of assembled structure of 1D solvents, (c) the side view, (d) the top view of assembled structure of 2D solvents, (e) the side view, (f) the top view of assembled structure of 3D solvents.

Thermogravimetric analysis indicated that **1**, **2** and **3** released the guest molecules up to 200 °C (Figure 3). Although **1** started to decompose around 250 °C, **2** and **3** were stable up to 350 °C. The difference in the collapse temperature between **1**, **2** and **3** is probably because of the interdigitation of the 2D sheets in **2** and **3**, which lends further thermal stability to the frameworks.

X-ray powder diffraction (XRD) analysis of the evacuated frameworks was carried out to confirm the stability of the open structures in the absence of guest molecules. All the compounds retained their crystallinity, as shown in Figure 4. Adsorption measurements of ferrocene-based PCPs were performed for CO<sub>2</sub>, N<sub>2</sub>, and O<sub>2</sub>, as shown in Figure 5. The adsorption isotherms of all compounds showed a Type I step uptake for CO<sub>2</sub> at the low pressure region, indicating the preservation of the ordered porous structure, but no eventual uptake for N<sub>2</sub> and O<sub>2</sub>. Generally, PCPs preferentially adsorb CO<sub>2</sub> over other small gases because of its small kinetic diameter.<sup>36</sup>

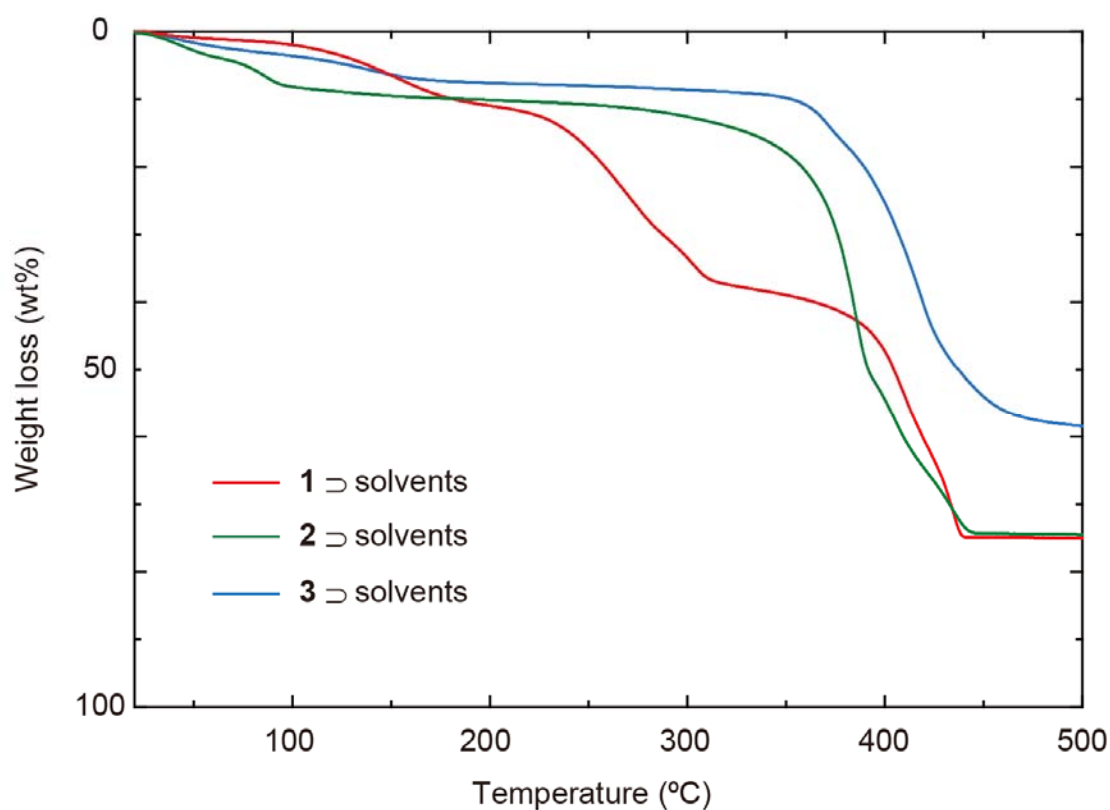


**Figure 3.** TG analysis showing the weight loss in **1**, **2** and **3** ⊃ solvents. The observed weight loss corresponds to the weight of solvent molecules.

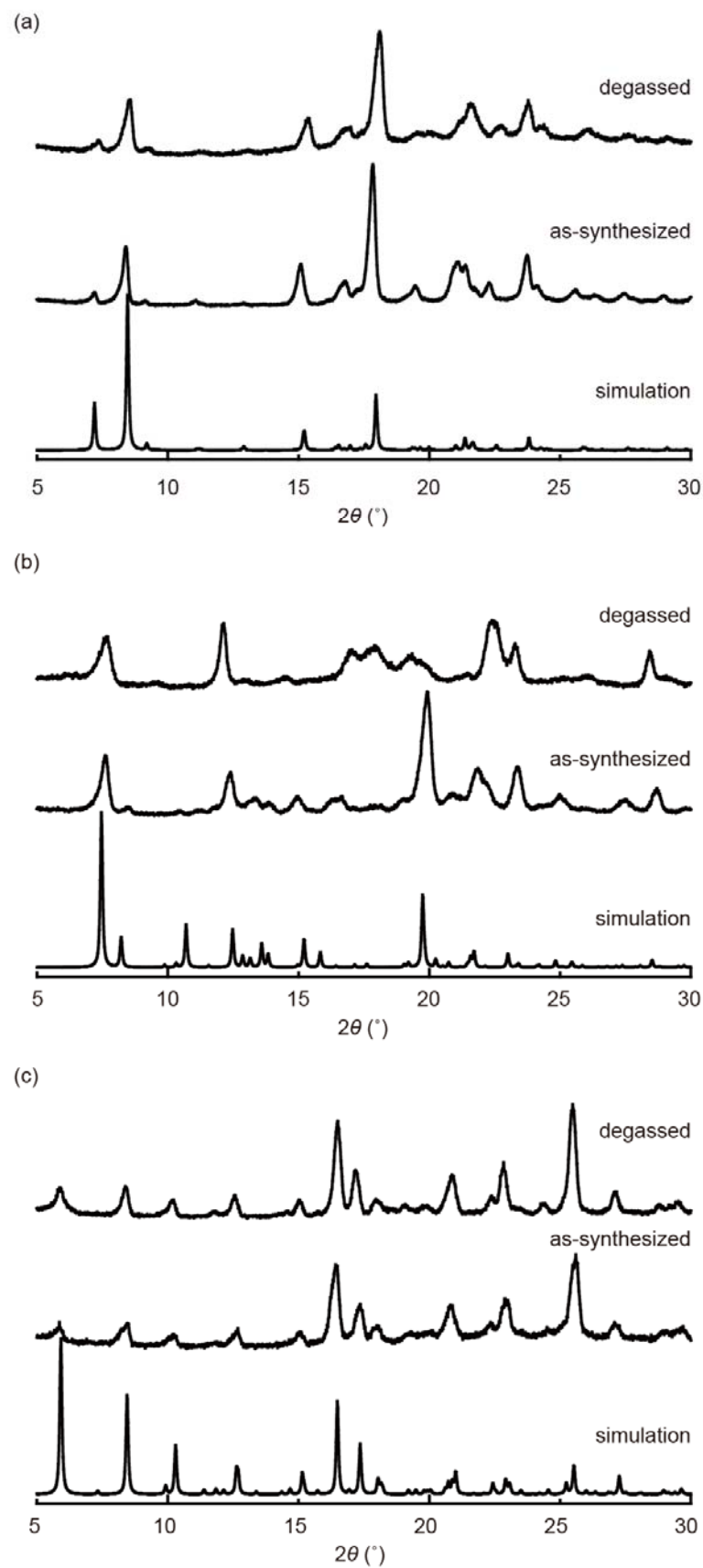


**Figure 4.** Powder X-ray diffraction patterns of as-synthesized, degassed, and simulated (a) **1**, (b) **2**, (c) **3**.

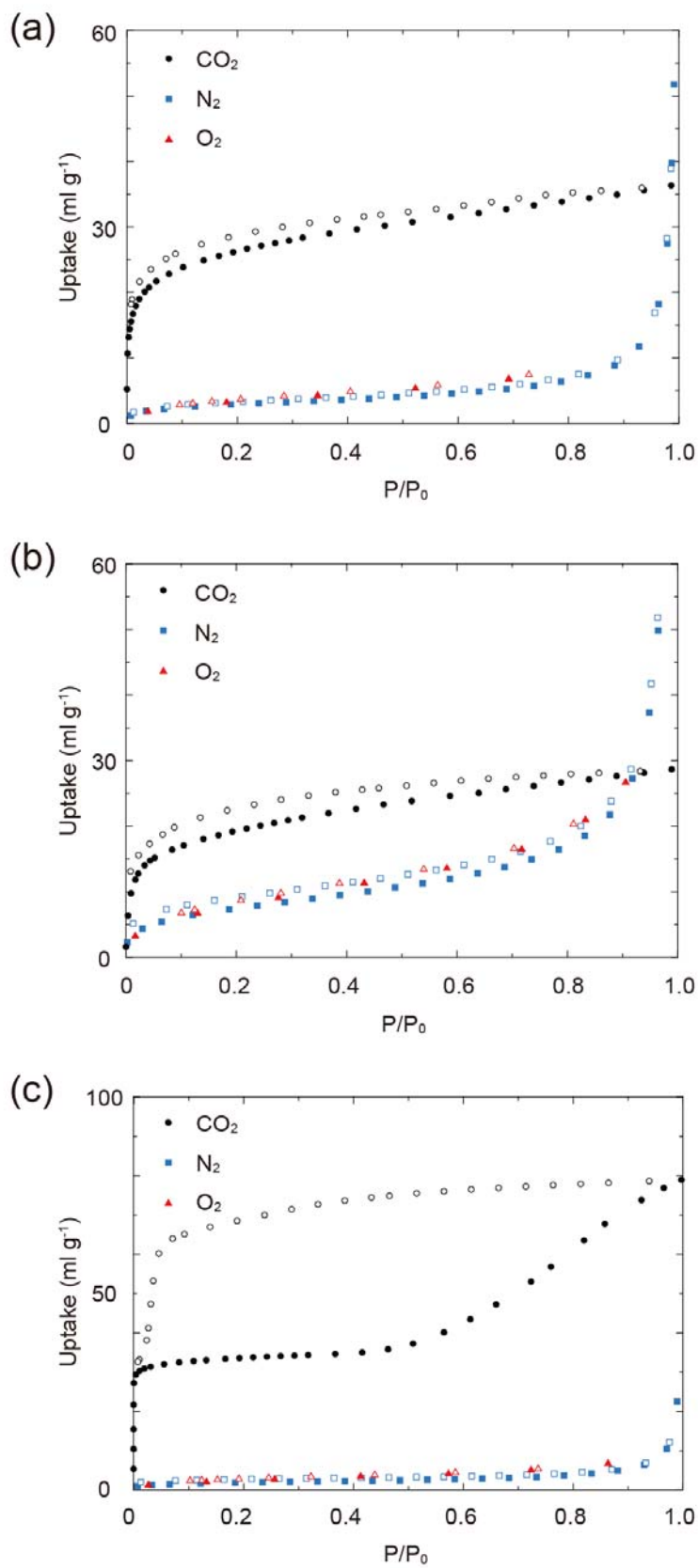


**Figure 5.** Adsorption isotherms of gas molecules for (a) **1**, (b) **2**, (c) **3**. Closed and open symbols show adsorption and desorption, respectively.

To date, the redox properties of coordination polymers containing ferrocenes have been reported after either dissolving the crystals in solvent or by depositing the crystals on a working electrode. In both cases, however, it is very difficult to elucidate the redox property of the framework itself. These methods most likely led to the determination of the electrochemical activity of the solute species (soluble oligomers or metal complexes).<sup>37-38</sup> To overcome this issue and to determine the redox properties of the PCPs themselves, we immobilized the crystals of ferrocene-based PCPs on gold electrodes. A gold substrate was placed in the reaction solution for four days to grow the PCP crystals directly on the surface, in a perpendicular fashion to avoid coating by sedimentation.<sup>39-41</sup> The substrates were rinsed with DMF and dried in air. The plate-like crystals of **1** were densely grown on the electrode surface, whereas the crystals of **2** and **3** partially covered the substrates (Figure 6). The low solubility of the diamine ligands, dpb and dpndi, most likely prevented the dense growth of **2** and **3**.

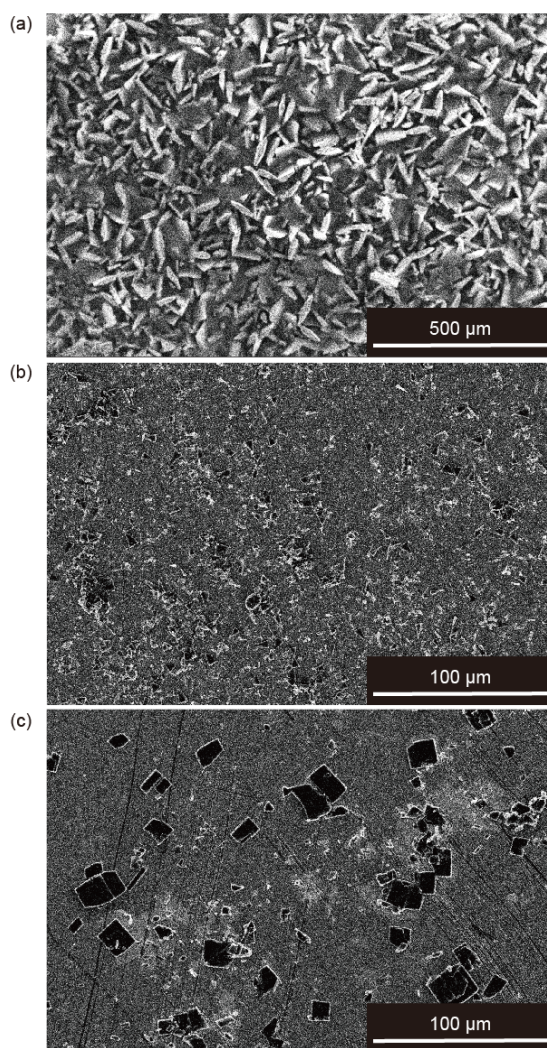


**Figure 6.** SEM images of a) **1**/Au b) **2**/Au, c) **3**/Au.

XRD results of the substrate samples revealed that crystals were preferentially oriented on the substrates (Figure 7). The out-of-plane XRD scans of **1** and **3** on the gold electrodes (denoted as **1**/Au and **3**/Au) demonstrated the presence of a preferentially oriented crystalline material perpendicular to 020 and 011 respectively. The oriented crystal growth of **1** and **3** on the substrates can be explained by the coordination bond of carboxylates to the gold atoms. Together with the in-plane data, the PCP crystals of **1** and **3** were successfully immobilized on the gold electrodes. Compound **2** on the gold electrode (denoted as **2**/Au) showed rather weak diffraction because of the low crystallinity on the substrate.

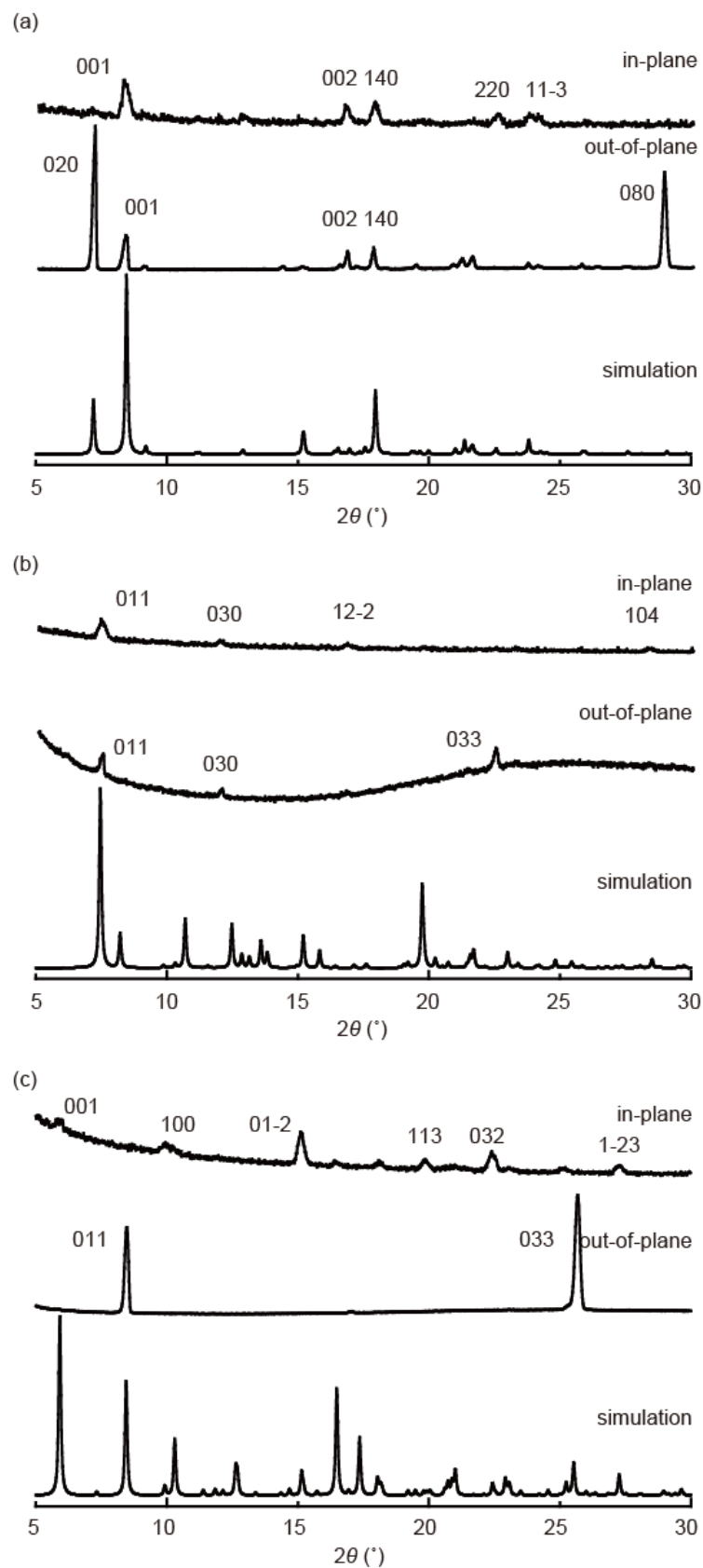


**Figure 7.** XRD patterns of in-plane diffraction, out-of-plane diffraction, simulation of (a) 1/Au, (b) 2/Au, (c) 3/Au.

The electrochemical behavior of **1**/Au was investigated by cyclic voltammetry (CV) in CH<sub>2</sub>Cl<sub>2</sub> solution with 0.1 mol L<sup>-1</sup> *n*-Bu<sub>4</sub>NBF<sub>4</sub> as electrolyte. A reversible redox wave was observed at 0.95 V. It was assigned to a Ferrocene/Ferrocenium cation in the PCP crystals (Figure 8). Compared with the redox potential of H<sub>2</sub>Fcdc in *n*-Bu<sub>4</sub>NBF<sub>4</sub> solution (0.88 V), that of **1**/Au (0.95 V) is shifted to a more positive potential (Fig. 8a and Table 1). The reason for this is the electron-withdrawing property of the carboxylates from the cyclopentadienyl rings and the coordination bond between carboxylate and Zn ions.<sup>42</sup> Unfortunately, **2**/Au and **3**/Au did not show clear CV profiles, probably because of the low density of crystals on the electrodes.

A negative shift of the redox potential was observed (0.78 V) when changing the electrolyte from *n*-Bu<sub>4</sub>NBF<sub>4</sub> to *n*-Bu<sub>4</sub>NNO<sub>3</sub>, which suggests that NO<sub>3</sub> forms the stronger ion pair with the positively charged oxidized compounds of ferrocenium (Table 1). This can be explained by the smaller ionization energy of NO<sub>3</sub> resulting in a higher degree of ion-pair formation.<sup>43-44</sup>

It is interesting that the peak currents show a linear dependence on the square roots of the scan rate, as shown in Figure 8b. The linearity in the plots indicates that the charge transfer in the redox process is controlled by the diffusion of charges in the PCPs as described by the empirical Randles-Sevcik equation.<sup>45</sup> Since the PCP crystals are immobilized on the electrode surface, the current is most likely limited by the diffusion of counteranions in the pores.<sup>46</sup> of counteranions in the pores. The present PCP system, possessing the accessible porosity, is certainly different from the case of ferrocene-incorporated [Cu<sub>3</sub>(btc)<sub>2</sub>], in which the electrohopping through the ferrocene molecules was dominating its electrochemical reaction.<sup>47</sup> The contribution of the solute species to the redox reaction could be ignored because there was no dissolution of the Fcdc ligands from the framework under the conditions used, as confirmed by the CV measurement of the residual solution. Therefore, the redox reaction observed here was subsequently attributed to the ferrocene moiety embedded into the framework.

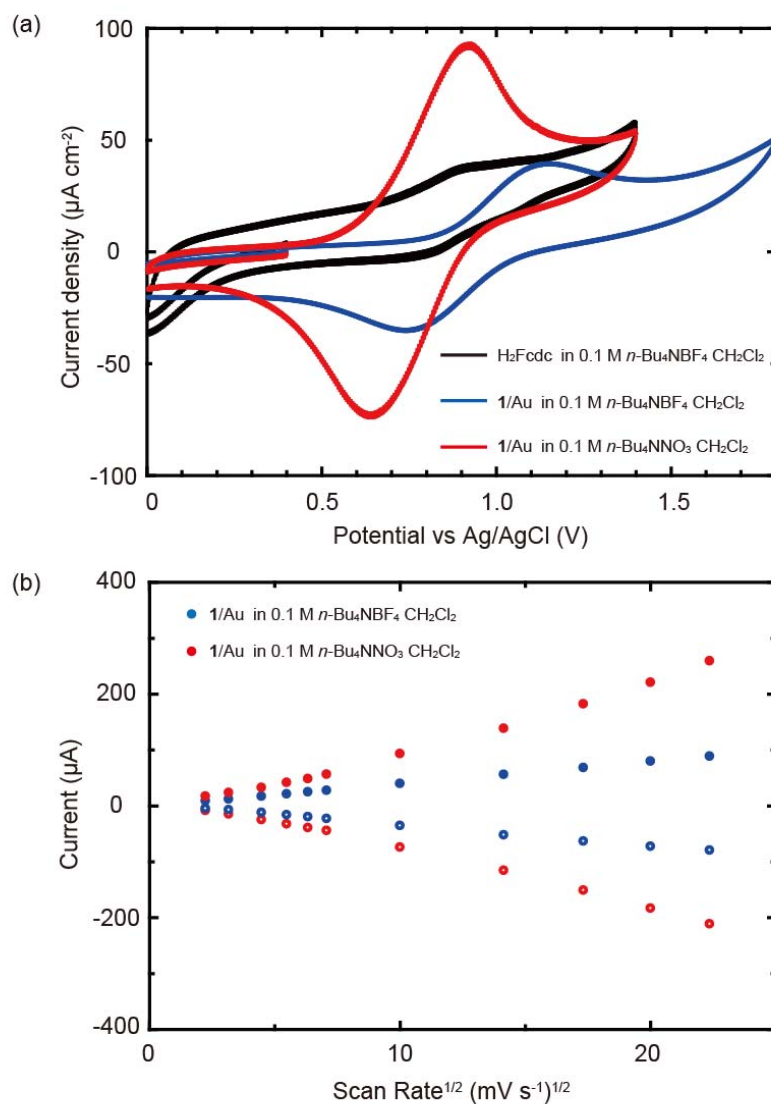


**Figure 8.** (a) Cyclic voltammograms of H<sub>2</sub>Fcdc and **1** at 100mV/s scan rates. The dispersed H<sub>2</sub>Fcdc in CH<sub>2</sub>Cl<sub>2</sub> was deposited onto the gold electrode. The current intensity of H<sub>2</sub>Fcdc is magnified twice for clarify. (b) Dependence of peak currents on scan rates. Closed and open circles show oxidation and reduction, respectively.

**Table. 1** Electrochemical data of **1** and Fcdc on an Au substrate at 100mV/s scan rates

compounds	$E_{1/2}$ <sup>[a]</sup> (V)	$\Delta E$ <sup>[b]</sup> (V)	$\Gamma$ <sup>[c]</sup> (mol cm <sup>-2</sup> )	electrolytes
H <sub>2</sub> Fcdc	0.88	0.099	–	<i>n</i> -Bu <sub>4</sub> NBF <sub>4</sub>
<b>1</b> /Au	0.95	0.412	$6.82 \times 10^{-10}$	<i>n</i> -Bu <sub>4</sub> NBF <sub>4</sub>
<b>1</b> /Au	0.78	0.301	$2.09 \times 10^{-9}$	<i>n</i> -Bu <sub>4</sub> NNO <sub>3</sub>

[a] The half wave potential,  $E_{1/2} = (E_{ox} + E_{red})/2$ . [b] The difference of the oxidation potential and reduction potential,  $\Delta E = E_{ox} - E_{red}$ . [c] Surface concentration of redox active species.

## Conclusion

In summary, we have demonstrated the redox reaction of ferrocene-based PCPs achieved by creating crystals on gold substrates. Although the crystals are immobilized on the substrate, the redox process is controlled by the diffusion of charges. The CV results were interpreted as the diffusion of counteranions into the channels. This results indicates that Fcdc ligand allows for the incorporation of the redox activity into PCP frameworks and opens the way for their use in a wide range of electronic applications.

## Experimental Section

### Materials

Zn(NO<sub>3</sub>)<sub>2</sub>•6H<sub>2</sub>O, 1,1'-ferrocenedicarboxylic acid (H<sub>2</sub>Fcdc), 1,4-diaza[2.2.2]bicyclooctane (dabco), 4,4'-bipyridyl (bpy), *N,N*-dimethylformamide (DMF) and methanol (MeOH) were purchased from Wako Pure Chemical Industries. The syntheses of 1,4-di(pyridin-4-yl)benzene (dpb) and *N,N'*-di(4-pyridyl)-1,4,5,8-naphthalenetetracarboxydiimide (dpndi), were prepared according to literature procedures.<sup>48-49</sup>

### Synthesis of 1

The solution of Zn(NO<sub>3</sub>)<sub>2</sub>•6H<sub>2</sub>O (84.8 mg, 0.286 mmol), H<sub>2</sub>Fcdc (78.3 mg, 0.286 mmol), and bpy (44.8 mg, 0.286 mmol) in 10 mL DMF/MeOH (DMF : MeOH = 2 : 1) were heated up to 353 K for 2 days. After cooling, the crystals were harvested. Elemental analysis calcd. for C<sub>24</sub>H<sub>21.5</sub>N<sub>2.5</sub>O<sub>5</sub>ZnFe {[Zn(Fcdc)(bpy)] • (DMF)<sub>0.5</sub>(MeOH)<sub>0.5</sub>}<sub>n</sub>: C, 52.78; H, 3.97; N, 6.41, Found: C, 49.58; H, 3.73; N, 6.28.

### Synthesis of 2

The solution of Zn(NO<sub>3</sub>)<sub>2</sub>•6H<sub>2</sub>O (74.3 mg, 0.25 mmol), H<sub>2</sub>Fcdc (68.5 mg, 0.25 mmol), and dpb (58.0 mg, 0.25 mmol) in 10 mL DMF/MeOH (DMF : MeOH = 1 : 2) were heated up to 373 K for 2 days. After cooling, the crystals were harvested. Elemental analysis calcd. for C<sub>30</sub>H<sub>25.5</sub>N<sub>2.5</sub>O<sub>5</sub>ZnFe {[Zn(Fcdc)(dpb)] • (DMF)<sub>0.5</sub>(MeOH)<sub>0.5</sub>}<sub>n</sub>: C, 57.91; H, 4.13; N, 5.63, Found: C, 53.22; H, 3.77; N, 5.09.

### Synthesis of 3

The solution of Zn(NO<sub>3</sub>)<sub>2</sub>•6H<sub>2</sub>O (74.3 mg, 0.25 mmol), H<sub>2</sub>Fcdc (68.5 mg, 0.25 mmol), and dpndi (105 mg, 0.25 mmol) in 10 mL DMF/MeOH (DMF : MeOH = 2 : 1) were heated up to 353 K for 2 days. After cooling, the crystals were harvested. Elemental analysis calcd. for C<sub>38</sub>H<sub>37.5</sub>N<sub>4.5</sub>O<sub>9</sub>ZnFe {[Zn(Fcdc)(dpndi)] • (DMF)<sub>0.5</sub>(MeOH)<sub>0.5</sub>}<sub>n</sub>: C, 55.49; H, 4.60; N, 7.66, Found: C, 54.56; H, 3.30; N, 7.89.

### Fabrication of 1 on Au substrates

The stocked reaction solution of **1** was prepared as Zn(NO<sub>3</sub>)<sub>2</sub>•6H<sub>2</sub>O (84.8 mg, 0.286 mmol), H<sub>2</sub>Fcdc (78.3 mg, 0.286 mmol), and bpy (44.8 mg, 0.286 mmol) in the mixed solvent (6.7 mL of DMF and 3.3 mL of MeOH). A gold substrate was placed in the solution and the reaction mixture was heated up to 353 K for 4 days. After cooling, the wafers were rinsed with DMF.

### **Fabrication of 2 on Au substrates**

The stocked reaction solution of **2** was prepared as Zn(NO<sub>3</sub>)<sub>2</sub>•6H<sub>2</sub>O (14.9 mg, 0.05 mmol), H<sub>2</sub>Fcdc (13.7 mg, 0.05 mmol), and dpb (11.6 mg, 0.05 mmol) in the mixed solvent (3.3 mL of DMF and 6.7 mL of MeOH). A gold substrate was placed in the solution and the reaction mixture was heated up to 373 K for 4 days. After cooling, the wafers were rinsed with DMF.

### **Fabrication of 3 on Au substrates**

The stocked reaction solution of **3** was prepared as Zn(NO<sub>3</sub>)<sub>2</sub>•6H<sub>2</sub>O (74.3 mg, 0.25 mmol), H<sub>2</sub>Fcdc (68.5 mg, 0.25 mmol), and dpndi (105 mg, 0.25 mmol) in the mixed solvent (6.7 mL of DMF and 3.3 mL of MeOH). A gold substrate was placed in the solution and the reaction mixture was heated up to 353 K for 4 days. After cooling, the wafers were rinsed with DMF.

### **Characterization methods**

The PCP crystals were characterized with X-ray diffraction (XRD), thermogravimetry (TG), elemental analysis and IR-RAS. Powder X-Ray diffraction (XRD) studies were measured using a Rigaku diffractometer with Cu K $\alpha$  radiation ( $\lambda = 1.5418 \text{ \AA}$ ). Surface XRD diffraction (SXR) studies were measured using Rigaku SmartLab ( $\lambda = 1.5418 \text{ \AA}$ ). TG measurements were carried out by Thermo plus EVO II. Elemental analysis was carried out on a Flash EA 1112 series, Thermo Finnigan instrument. Single crystal X-ray diffraction measurements were made on a Rigaku AFC10 diffractometer with Rigaku Saturn CCD system equipped with a rotating-anode X-ray generator producing multi-layer mirror monochromated MoK $\alpha$  radiation. IR-RAS measurement was performed by JASCO FT-IR6100.

### **Physical measurements**

Gas sorption isotherms of N<sub>2</sub>, O<sub>2</sub> and CO<sub>2</sub> were recorded on a BELSORP-mini volumetric-adsorption instrument from BEL Japan. Cyclic voltammetry (CV) studies were carried out with an ALS400B electrochemical analyzer utilizing the three-electrode configuration of an Au substrate electrode, a Pt auxiliary electrode and a Ag/AgCl reference electrode. The measurements were performed in CH<sub>2</sub>Cl<sub>2</sub> solution containing tetrabutylammonium tetrafluoroborate or tetrabutylammonium nitrate (0.1 mol L<sup>-1</sup>) as supporting electrolyte. CV curves were recorded at various scan rates.

### **Structural determinationPhysical measurements**

X-ray data collection ( $5^\circ < 2\theta < 55^\circ$ ) was conducted at 223K on Rigaku AFC10 diffractometer Mo-K $\alpha$  radiation ( $\lambda = 0.7105 \text{ \AA}$ ) with Rigaku Saturn CCD system. The structures were solved by a direct method (SIR92) and expanded using Fourier techniques. All calculations were performed using the CrystalStructure crystallographic software package 4.0 of Rigaku. These data can be obtained free of charge from The Cambridge Crystallographic Data Centre via [www.ccdc.cam.ac.uk/data\\_request/cif](http://www.ccdc.cam.ac.uk/data_request/cif).

## References

- (1) O. M. Yaghi, M. O’Keeffe, N. W. Ockwing, H. K. Chae, M. Eddaoudi and J. Kim, *Nature*, **2003**, *423*, 705-714.
- (2) S. Kitagawa, R. Kitaura and S. Noro, *Angew. Chem. Int. Ed.*, **2004**, *43*, 2334-2375.
- (3) G. Férey, C. Mellot-Dranznies, C. Serre and F. Millange, *Acc. Chem. Res.*, **2005**, *38*, 217-225.
- (4) S. Batten and R. Robson, *Angew. Chem. Int. Ed.*, **1998**, *37*, 1460-1494.
- (5) U. Mueller, M. Schubert, F. Teich, H. Puetter, K. Schierle-Arndt and J. Pastré, *J. Mater. Chem.*, **2006**, *16*, 626-636.
- (6) M. Dincă, A. Dailly, Y. Liu, C. M. Brown, D. A. Neumann and J. R. Long, *J. Am. Chem. Soc.*, **2006**, *128*, 16876-16883.
- (7) S. Ma, D. Sun, J. M. Simmons, C. D. Collier, D. Yuan, and H. C. Zhou, *J. Am. Chem. Soc.*, **2008**, *130*, 1012-1016.
- (8) R. Matsuda, R. Kitaura, S. Kitagawa, Y. Kubota, R. V. Belosludov, T. C. Kobayashi, H. Sakamoto, T. Chiba, M. Takata, Y. Kawazoe, Y. Mita, *Nature*, **2005**, *436*, 238-241.
- (9) B. Wang, A. P. Côté, H. Furukawa, M. O’Keeffe and O. M. Yaghi, *Nature*, **2008**, *453*, 207-211.
- (10) L. Alaerts, C. E. A. Kirschhock, M. Maes, M. A. van der Veen, V. Finsy, A. Depla, J. A. Martens, G. V. Baron, P. A. Jacobs, J. F. M. Denayer, and D. E. De Vos, *Angew. Chem. Int. Ed.*, **2007**, *46*, 4293-4297.
- (11) B. Chen, C. Liang, J. Yang, D. S. Contreras, Y. L. Clancy, E. B. Lobkovsky, O. M. Yaghi, and S. Dai, *Angew. Chem. Int. Ed.* **2006**, *45*, 1390-1393.
- (12) M. D. Allendorf, C. A. Bauer, R. K. Bhakta and R. J. T. Houk, *Chem. Soc. Rev.*, **2009**, *38*, 1330-1352.
- (13) G. J. McManus, J. J. Perry IV, M. Perry, B. D. Wagner, and M. J. Zaworotko, *J. Am. Chem. Soc.*, **2007**, *129*, 9094-9101.
- (14) K. C. Stylianou, R. Heck, S. Y. Chong, J. Bacsá, J. T. A. Jones, Y. Z. Khimiyak, D. Bradshaw and M. J. Rosseinsky, *J. Am. Chem. Soc.*, **2010**, *132*, 4119-4130.
- (15) Y. Takashima, V. M. Martinez, S. Furukawa, M. Kondo, S. Shimomura, H. Uehara, M. Nakahama, K. Sugimoto, S. Kitagawa, *Nature Commun.*, **2011**, *2*, 168.
- (16) S. Takaishi, M. Hosoda, T. Kajiwará, H. Miyasaka, M. Yamashita, Y. Nakanishi, Y. Kitagawa, K. Yamaguchi, A. Kobayashi, and H. Kitagawa, *Inorg. Chem.*, **2009**, *48*, 9048-9050.
- (17) M. H. Zeng, Q. X. Wang, Y. X. Tan, S. Hu, H. X. Zhao, L. S. Long and M. Kurmoo,

- J. Am. Chem. Soc.*, **2010**, *132*, 2561-2563.
- (18) S. Shimomura, M. Higuchi, R. Matsuda, K. Yoneda, Y. Hijikata, Y. Kubota, Y. Mita, J. Kim, M. Takata and S. Kitagawa, *Nature Chem.*, **2010**, *2*, 633-637.
- (19) G. Férey, F. Millange, M. Morcrette, C. Serre, M. L. Doublet, J. M. Grenéche and J. M. Tarascon, *Angew. Chem. Int. Ed.*, **2007**, *46*, 3259-3263.
- (20) L. Yang, S. Kinoshita, T. Yamada, S. Kanda, H. Kitagawa, M. Tokunaga, T. Ishimoto, T. Ogura, R. Nagumo, A. Miyamoto and M. Koyama, *Angew. Chem. Int. Ed.*, **2010**, *49*, 5348-5351.
- (21) H. R. Moon, J. H. Kim and M. P. Suh, *Angew. Chem. Int. Ed.*, **2005**, *44*, 1261-1265.
- (22) L. M. Rodriguez-Albelo, A. R. Ruiz-Salvador, A. Sampieri, D. W. Lewis, A. Gómez, B. Nohra, P. Mialane, J. Marrot, F. Sécheresse, C. Mellot-Draznieks, R. N. Biboum, B. Keita, L. Nadjo and A. Dolbecq, *J. Am. Chem. Soc.*, **2009**, *131*, 16078-16087.
- (23) Y. Kobayashi, B. Jacobs, M. D. Allendorf and J. R. Long, *Chem. Mater.*, **2010**, *22*, 4120-4122.
- (24) R. Horikoshi and T. Mochida, *Eur. J. Inorg. Chem.*, **2010**, *49*, 5355-5357.
- (25) V. Chandrasekhar and R. Thirumoorthi, *Dalton Trans.*, **2010**, *39*, 2684-2691.
- (26) L. Wang, X. Meng, E. Zhang, H. Hou, Y. Fan, *J. Organomet. Chem.*, **2007**, *692*, 4367-4376.
- (27) M. Meilikhov, K. Yusenko and R. A. Fischer, *J. Am. Chem. Soc.*, **2009**, *131*, 9644-9645.
- (28) J. E. Halls, A. Hernán-Gómez, A. D. Burrows and F. Marken, *Dalton Trans.*, **2012**, *41*, 1475-1480.
- (29) K. J. Wei, J. Ni and Y. Liu, *Inorg. Chem.*, **2010**, *49*, 1834-1848.
- (30) J. Yang, J. F. Ma, Y. Y. Liu, S. L. Li and G. L. Zheng, *Eur. J. Inorg. Chem.*, **2005**, 2174-2180.
- (31) Y. Xu, C. Ran, L. Zhu and Y. Fan, *J. Coord. Chem.*, **2009**, *62*, 410-416.
- (32) S. Horike, D. Tanaka, K. Nakagawa and S. Kitagawa, *Chem. Commun.*, **2007**, 3395-3397.
- (33) D. Tanaka, K. Nakagawa, M. Higuchi, S. Horike, Y. Kubota, T. C. Kobayashi, M. Takata and S. Kitagawa, *Angew. Chem. Int. Ed.*, **2008**, *47*, 3914-3918.
- (34) K. Nakagawa, D. Tanaka, S. Horike, S. Shimomura, M. Higuchi and S. Kitagawa, *Chem. Commun.*, **2010**, *46*, 4258-4260.
- (35) Y. Takashima, S. Furukawa and S. Kitagawa, *CrystEngComm*, **2011**, *13*, 3360-3363.
- (36) D. N. Dybtsev, H. Chun, S. H. Yoon, D. Kim and Kimoon Kim, *J. Am. Chem. Soc.*, **2004**, *126*, 32-33.
- (37) B. Q. Liu, P. F. Yan, J. Zhang, P. Chen, G. M. Li, *J. Organomet. Chem.*, **2010**, *695*,

2441-2446.

- (38) J. Kühnert, T. Ruffer, P. Ecorchard, B. Bräuer, Y. Lan, A. K. Powell and H. Lang, *Dalton Trans.*, **2009**, 4499-4508.
- (39) S. Hermes, F. Schröder, R. Chelmowski, C. Wöll and R. A. Fischer, *J. Am. Chem. Soc.*, **2005**, *127*, 13744-13745.
- (40) O. Shekhah, H. Wang, S. Kowarik, F. Schreiber, M. Paulus, M. Tolan, C. Sternemann, F. Evers, D. Zacher, R. A. Fischer and C. Wöll, *J. Am. Chem. Soc.*, **2007**, *129*, 15118-15119.
- (41) E. Biemmi, C. Scherb and T. Bein, *J. Am. Chem. Soc.*, **2007**, *129*, 8054-8055.
- (42) D. Warren, H. Charles, D. Russell, *J. Am. Chem. Soc.*, **1967**, *89*, 2316-2322.
- (43) K. Uosaki, Y. Sato, H. Kita, *Langmuir*, **1991**, *7*, 1510-1514.
- (44) M. Péter, R. G. H. Lammertink, M. A. Hempenius and G. J. Vancsoion, *Langmuir*, **2005**, *21*, 5115-5123.
- (45) K. Itaya, I. Uchida and V. D. Neff, *Acc. Chem. Res.*, **1986**, *19*, 162-168.
- (46) M. Strømme, G. A. Niklasson and C. G. Granqvist, *Solid State Commun.*, **1995**, *96*, 151-154.
- (47) A. Dragässer, O. Shekhah, O. Zybaylo, C. Shen, M. Buck, C. Wöll and D. Schelettwein, *Chem. Commun.*, **2012**, *48*, 663-665.
- (48) P. H. Dinolfo, M. E. Williams, C. L. Stern, J. T. Hupp, *J. Am. Chem. Soc.*, **2004**, *126*, 12989-13001.
- (49) K. Biradha and M. Fujita, *Dalton Trans.*, **2000**, 3805-3810.



## Chapter 8

# Crystal Orientation Controls Analyte Detection Kinetics of Porous Coordination Polymer Hybrid Sensor with Quartz Oscillator

### Abstract

The hybridization of porous coordination polymers (PCPs) with an electronic device promises for a great enhancement of chemical sensing. In particular, quartz crystal microbalance (QCM) is a good candidate for a delicate electronic sensor into which PCP crystals can be integrated. Herein, we successfully immobilize flexible PCPs,  $[\text{Zn}(\text{NO}_2\text{-ip})(\text{bpy})]_n$  ( $\text{NO}_2\text{-ip}$  = 5-nitroisophthalate,  $\text{bpy}$  = 4,4'-bipyridyl), on QCM substrates and establish a PCP/QCM hybrid sensor. The crystal orientation was controlled by introducing chemical functionality into the surface of QCM substrates. Besides the chemical functionality, coordination modulation method was also employed to control the crystal orientation. Although the rapid crystal growth by microwave heating led to not-oriented crystals, microwave heating with coordination modulator gave oriented crystals on a QCM substrate. The effect of crystal orientation on detection kinetics of organic vapor (methanol) was analyzed by the environmentally-controlled QCM measurements. In case that the one dimensional channel of PCPs was running parallel to the direction of gas flow, the diffusion of organic vapor was clearly enhanced, thus leading to quick response of QCM sensors to the organic vapor. Prior to evaluating detection kinetics, we confirmed that the PCP crystals over 1  $\mu\text{m}$  maintain the characteristic gate-effect, which enables to distinguish guest molecules. These results open a way for the fabrication of the PCP/QCM hybrid sensor device and will clarify a way to improve its sensor performance without spoiling original adsorption properties.

## Introduction

Detection and quantification of chemical species is a critical and challenging task for biotechnology,<sup>1</sup> environmental monitoring<sup>2</sup> as well as molecular sensors.<sup>3</sup> Most chemical sensors have been developed by following the key principle: recognition to selectively trap specific molecules and transduction to convert the recognition event into a detectable signal.<sup>4-5</sup> Therefore, integration of well-developed host-guest systems, which selectively capture target molecules, into electronic sensor device is a promising way to establish a sophisticated chemical sensor.

Porous coordination polymers (PCPs) or metal-organic frameworks (MOFs)<sup>6-10</sup> are an intriguing class of materials in which porous properties can be designed by a judicious choice of metal ions and organic ligands.<sup>11-12</sup> Among a vast number of compounds, flexible PCPs have been identified as a unique type of porous material because of their structural transformations in response to guest accommodation.<sup>13-15</sup> In particular, a gate effect occurs when the framework structure changes during the adsorption process from a closed form to an open form at a specific vapor pressure, so-called gate-opening pressure.<sup>16-18</sup> Interestingly, the pressure value totally depends on the characteristics of guest molecules.<sup>19</sup> In other words, flexible PCPs seems to distinguish among molecules by the gate-opening pressure. Therefore, flexible PCPs are excellent candidates to be integrated as recognition moiety into electronic sensor devices that transduce the recognition event to corresponding readout.

Because the guest uptake leads to the weight gain of PCPs, the deposition of flexible PCPs onto quartz crystal microbalance (QCM),<sup>20</sup> in which the mass change is converted to a change of oscillation frequency, enables to quantitatively detect specific molecules.<sup>21-23</sup> One of the most important factors for the improvement of chemical sensors is the quickness of response to target molecules. Therefore, PCPs on QCM substrates should rapidly adsorb guest molecules. The most common approach to accelerate the guest uptake is to downsize the crystals.<sup>24</sup> However, reducing the crystal size of flexible PCPs often decreases the crystallinity and weakens the guest recognition abilities.

In case of porous membranes, channel orientations against the direction of gas flow is crucial to achieve high separation efficiency.<sup>25</sup> This fact suggests that the channel orientation influences on the diffusion kinetics in porous thin film. Bearing that in mind, one way to accelerate the diffusion kinetics of hybrid sensor with maintaining the recognition ability is to deposit a flexible PCP on a QCM substrate with appropriate crystal orientation.

Herein, we successfully immobilize micrometer-sized flexible PCPs and control the crystal orientation on QCM substrates. The proper orientation of PCP crystals accelerates analyte detection kinetics. Thus, controlling the crystal orientation of flexible PCPs on QCM will give an opportunity to sophisticate the hybrid sensor (Figure 1). We also confirmed that the micrometer-sized flexible PCPs maintain the characteristic gate-effect.

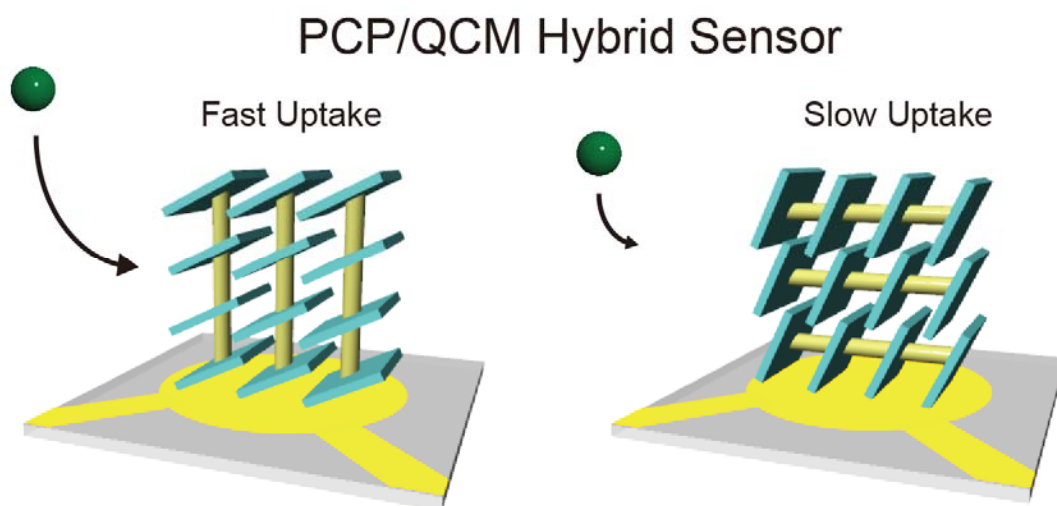


**Figure 1.** Orientation-controlled flexible PCPs on a QCM substrate.

## Results and Discussion

### The Effect of Crystal Size on Adsorption Properties

A series of two-dimensional coordination polymers,  $[M(\text{dicarboxylate})(\text{diamine})]_n$ , so-called coordination frameworks with interdigitated structure (CID),<sup>26-28</sup> is an excellent candidates for the flexible PCPs. In particular,  $[\text{Zn}(\text{NO}_2\text{-ip})(\text{bpy})]_n$ , (**Zn-CID-5**), exhibits extremely high guest selectivity due to the gate-opening property derived from structural transformation<sup>29</sup> ( $\text{NO}_2\text{-ip}$  = 5-nitroisophthalate, bpy = 4,4'-bipyridyl). As shown in Figure 2a and b, the Zn ion have a distorted octahedral  $\text{N}_2\text{O}_4$  geometry, being coordinated by two bpy molecules at the axial positions, one chelating carboxylate of  $\text{NO}_2\text{-ip}$  and two other monodentate carboxylate of  $\text{NO}_2\text{-ip}$  in the equatorial plane. The coordination of  $\text{NO}_2\text{-ip}$  to the Zn ions constructed one-dimensional (1D) chain structure as shown in Figure 2a, followed by the linkage of the adjacent chains through bpy in the axial positions, leading to the formation of two-dimensional (2D) sheet. The 2D sheets are alternatively interdigitated, forming **Zn-CID-5**. As previously reported, the crystal structure of **Zn-CID-5** changes from an open form to a closed form through the removal of guest molecule.<sup>15</sup> Since the accommodated guest molecules suppress the twisting of  $\text{NO}_2\text{-ip}$ , the guest removal induces a reorientation of the interdigitation (Figure 2b and c). The gate-opening adsorption is attributed to this structural transformation.

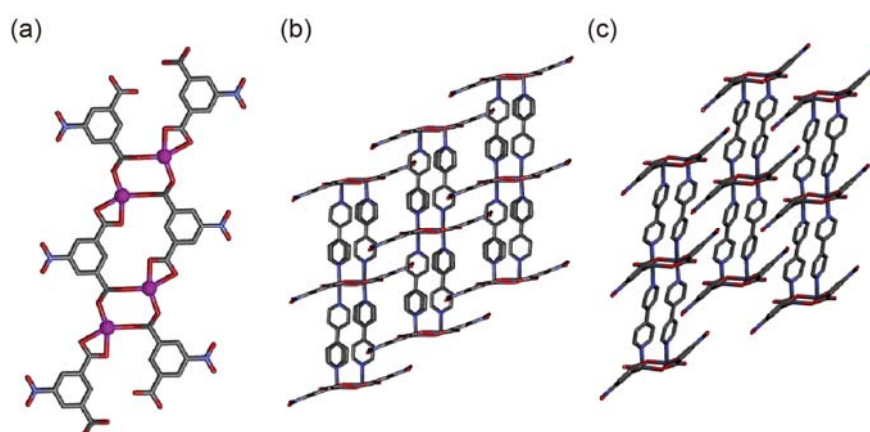


**Figure 2.** Crystal structures of (a) the 1D chain structure composed of Zn ions and  $\text{NO}_2\text{-ip}$ , and (b) the 2D sheet structure in open form, (c) in closed form. Gray, blue, red, and purple are C, N, O, and Zn, respectively. The hydrogen atoms and guest molecules are omitted for clarity.

**Zn-CID-5** was successfully synthesized via microwave reaction of  $\text{Zn}(\text{NO}_3)_2 \cdot 6\text{H}_2\text{O}$ ,  $\text{H}_2(\text{NO}_2\text{-ip})$  and bpy in a DMF solution. To optimize the synthesis condition of **Zn-CID-5**, we carried out sets of experiments where the temperature and reaction time was systematically varied. Firstly, the temperature was varied from 30 °C to 120 °C, keeping the reaction time as 5 min. Whereas unknown peaks ( $2\theta = 12.8$  and 16.5) were observed in the compounds prepared at 30 and 40 °C, pure-phase of **Zn-CID-5** was obtained over 50 °C, as shown in Figure 3. Although the yield of **Zn-CID-5** was nearly same in the range from 50 °C to 90 °C, higher temperature over 100 °C gave high yield of **Zn-CID-5**. Thus, 120 °C is the best condition to obtain large amount of pure phase of **Zn-CID-5** (Table 1). Secondly, the reaction time was varied from 5 to 30 min, keeping the temperature as 120 °C. In all the reaction conditions, pure-phase of **Zn-CID-5** was successfully synthesized (Figure 4). Although longer reaction time led to higher yield of **Zn-CID-5**, the crystals synthesized in 5 min is already larger than 2  $\mu\text{m}$  (Figure 5a). Such micrometer-sized crystals are not suitable to investigate the size effect on adsorption properties of **Zn-CID-5**.

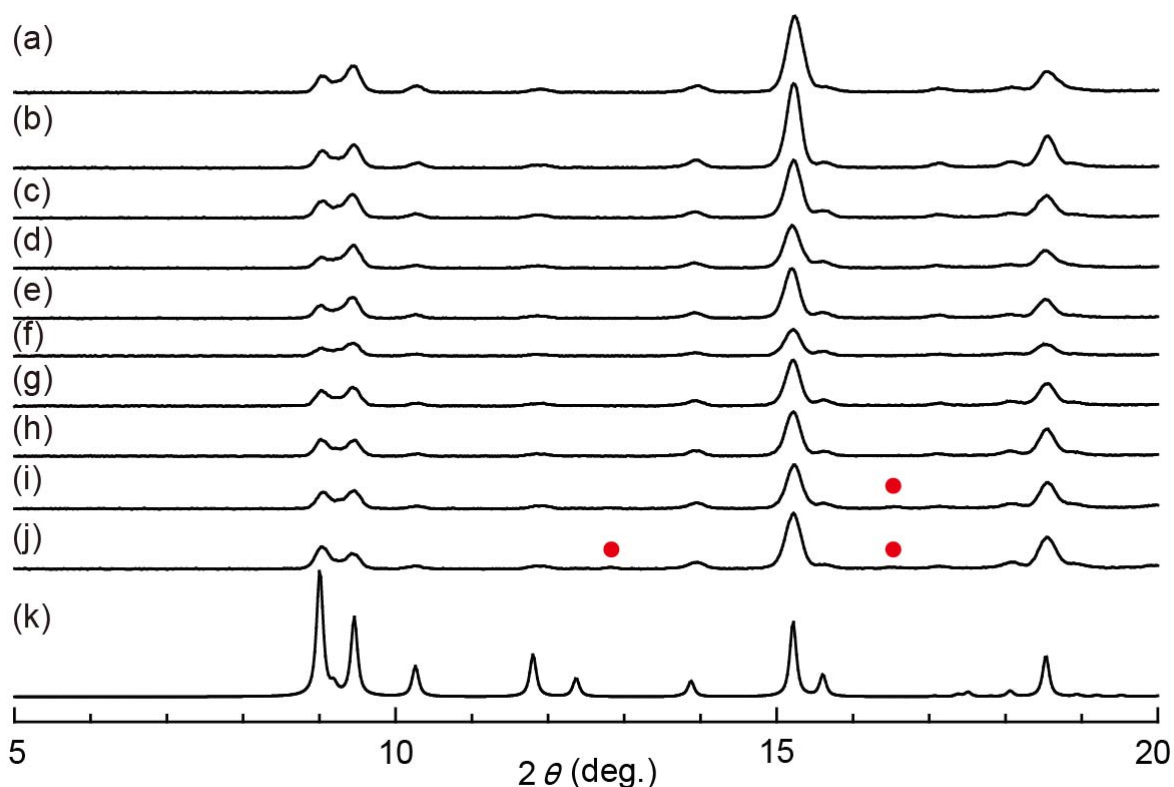


**Figure 3.** XRD patterns of compounds under various temperatures: (a) 120, (b) 110, (c) 100, (d) 90, (e) 80, (f) 70, (g) 60, (h) 50, (i) 40, (j) 30 °C and simulation of **Zn-CID-5** (open form). The red circles indicate the unknown peaks.

**Table 1** The yield of **Zn-CID-5** at various temperatures.

Temperature	Time	Yield		Product
		Yield (mg)	Yield (%)	
30 °C	5 min	9.81 mg	-	Zn-CID-5 + X
40 °C	5 min	17.7 mg	-	Zn-CID-5 + X
50 °C	5 min	12.0 mg	15.0 %	Zn-CID-5
60 °C	5 min	11.7 mg	14.6 %	Zn-CID-5
70 °C	5 min	10.4 mg	13.0 %	Zn-CID-5
80 °C	5 min	10.2 mg	12.7 %	Zn-CID-5
90 °C	5 min	10.4 mg	13.0 %	Zn-CID-5
100 °C	5 min	17.3 mg	21.2 %	Zn-CID-5
110 °C	5 min	18.4 mg	23.0 %	Zn-CID-5
120 °C	5 min	30.2 mg	37.6 %	Zn-CID-5

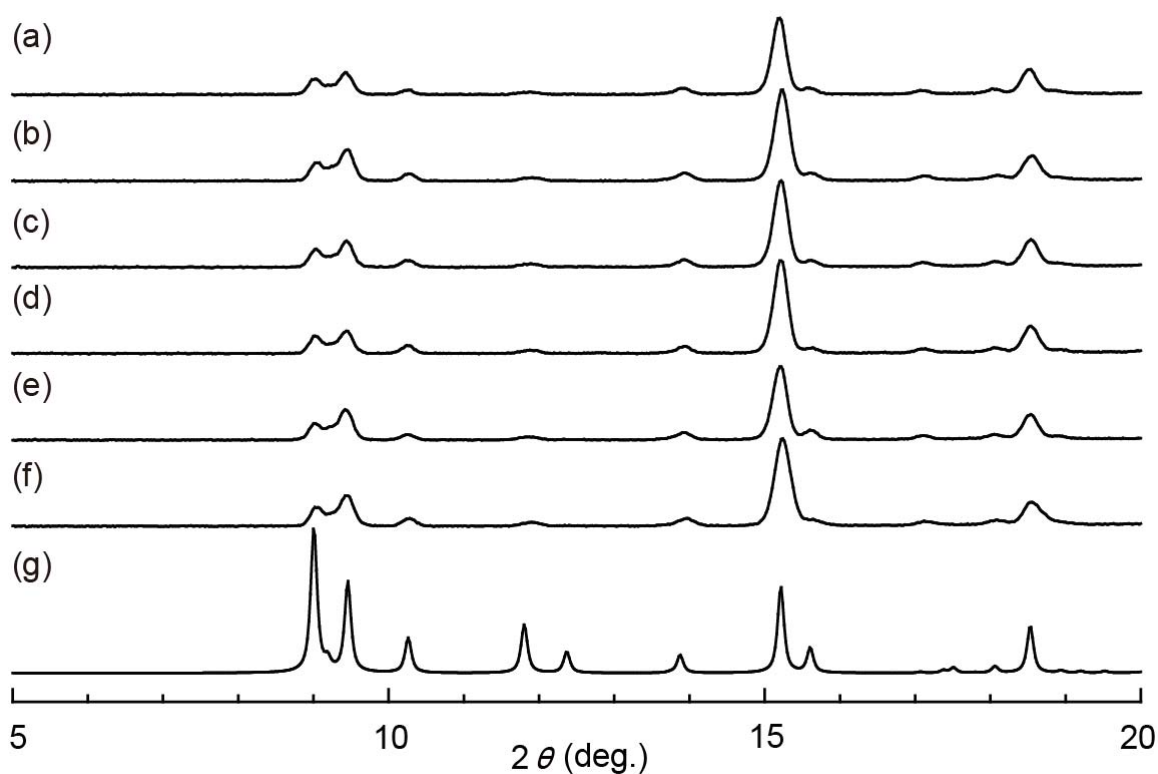


**Figure 4** XRD patterns of compounds under various reaction time: (a) 30, (b) 25, (c) 20, (d) 15, (e) 10, (f) 5 min, (g) and simulation of **Zn-CID-5** (open form).

Thus, we applied coordination modulation method to obtain nanometer-sized crystals of **Zn-CID-5**. We have recently demonstrated this method for the synthesis of PCP nanocrystals by altering the coordination equilibrium at the crystal surface during the growth process, through competitive interactions originating from a capping additive (modulator) with the same chemical functionality as the framework linker.<sup>30-32</sup> A monoamine molecule (4-phenylpyridine) was chosen as a modulator for **Zn-CID-5**. The addition of 4-phenylpyridine clearly influenced on the size of resulting crystals ( $r$  is varied from 1 to 15, where  $r$  is defined as the ratio of 4-phenylpyridine to bpy). While micrometer-sized crystals ( $2.0 \times 3.5 \mu\text{m}^2$ ) were obtained when  $r = 0$ , nanometer-sized crystals ( $370 \times 540 \text{ nm}^2$ ) were obtained when  $r = 15$ . As increasing the amount of 4-phenylpyridine, the crystal size decreased, as shown in Figure 5 and 6. This is probably because 4-phenylpyridine competed with bpy during the growth process and inhibited the further growth of **Zn-CID-5**. Although the pure-phase of **Zn-CID-5** was successfully obtained in all the reaction conditions, the crystal morphology became ill-defined as decreasing the crystal size. The XRD peaks of nanometer-sized **Zn-CID-5** ( $r = 15$ ) is broader than micrometer-sized **Zn-CID-5** ( $r = 0$ ) (Figure 7).

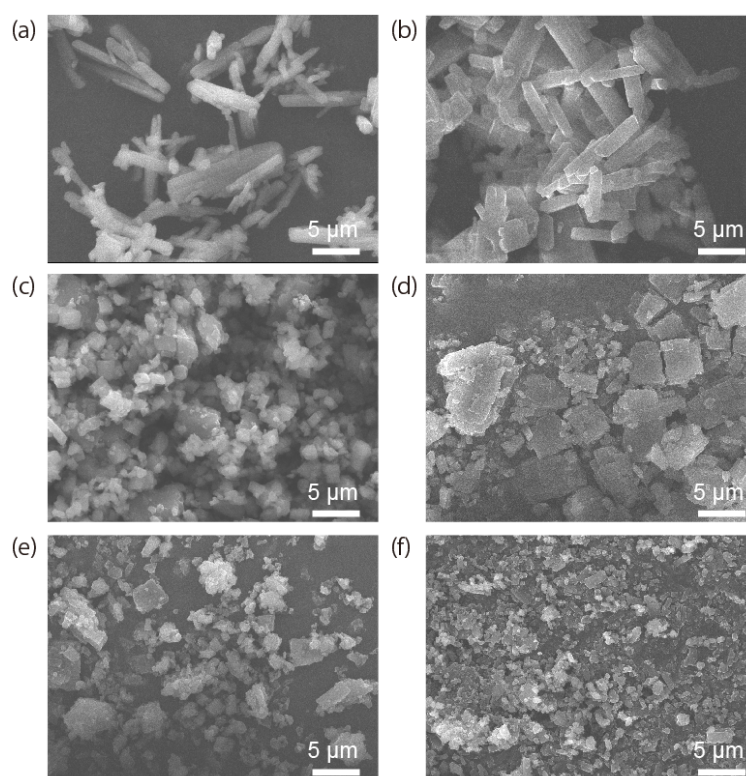


**Figure 5.** SEM images of **Zn-CID-5** obtained under various conditions;  $r$  represents the ratio between monoamine: (a)  $r = 0$ , (b)  $r = 1$ , (c)  $r = 5$ , (d)  $r = 7.5$ , (e)  $r = 10$ , (f)  $r = 15$ .

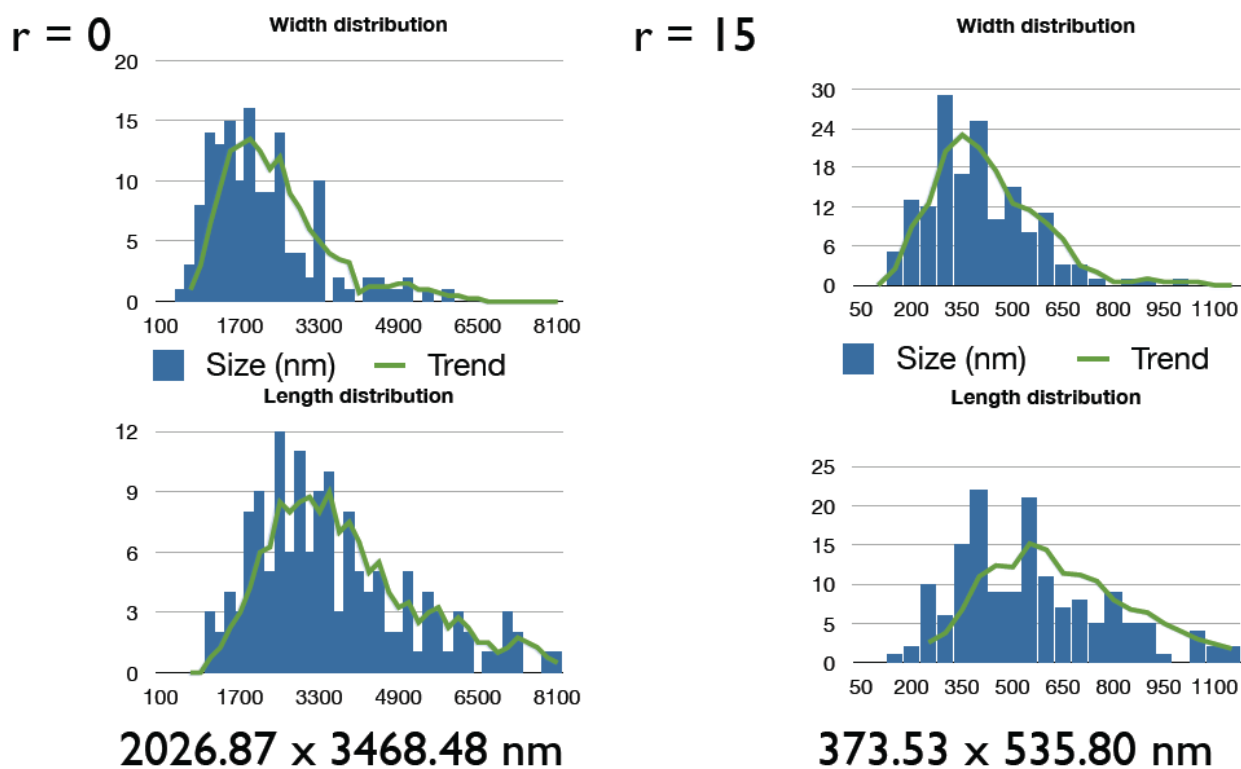


**Figure 6.** Size distribution of Zn-CID-5 obtained at  $r = 0$  and 15.

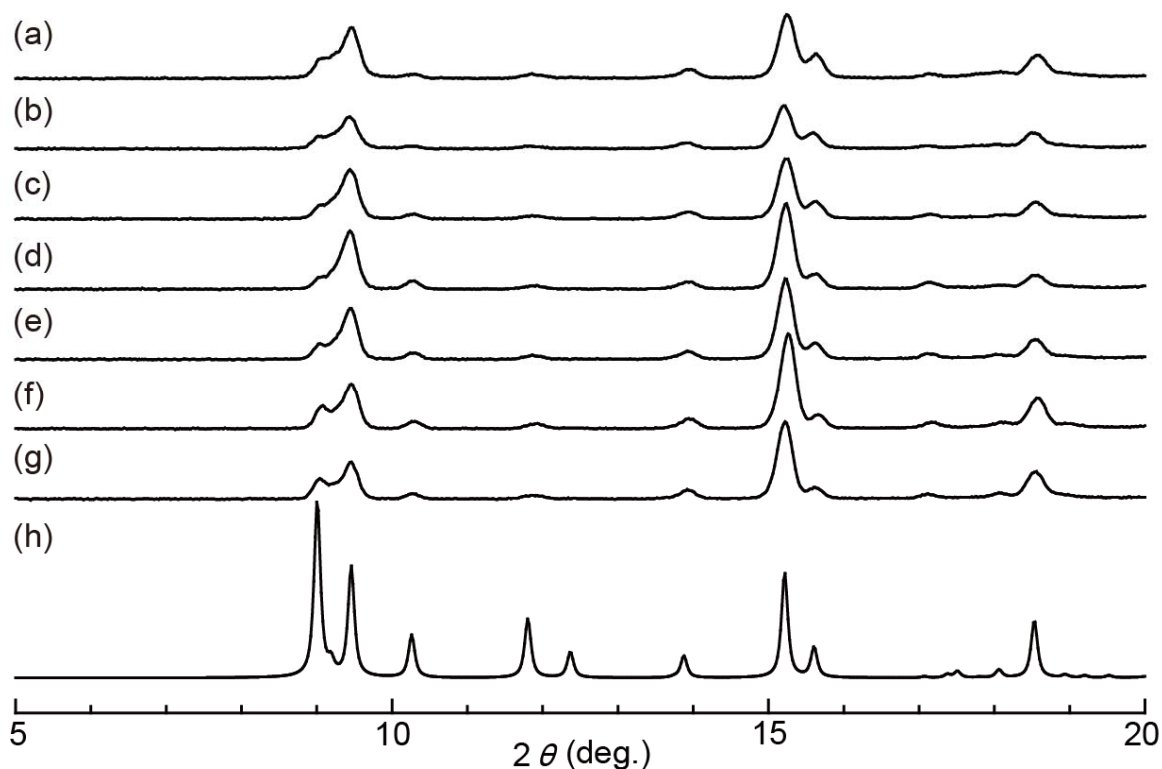


**Figure 7.** XRD patterns of compounds under various reaction conditions: (a)  $r = 15$ , (b)  $r = 12.5$ , (c)  $r = 10$ , (d)  $r = 7.5$ , (e)  $r = 5$ , (f)  $r = 1$ , (g)  $r = 0$ , (h) and simulation of Zn-CID-5 (open form).

The size-controlled crystals of **Zn-CID-5** allowed us to investigate the correlation between the crystal size and the sorption behaviors. The adsorption experiments for methanol and chloroform were carried out. The methanol adsorption isotherm of the conventional micrometer-sized crystals ( $r = 0$ ) was carried out at 25 °C, and the characteristic gate-opening adsorption was observed at  $P/P_0 = 0.20$  (Figure 10). Using an environmentally-controlled XRD system, we determined that this gate-opening adsorption is originating from the structural transformation from the non-porous closed form to the porous open form in response to methanol accommodation (Figure 8 and 9). The structural transformation from the closed form to open form occurred over  $P/P_0 = 0.2$  in the adsorption process and the transformation from open form to closed form occurred under  $P/P_0 = 0.05$  in the desorption process, which corresponds to the gate-opening adsorption and hysteresis in desorption process.

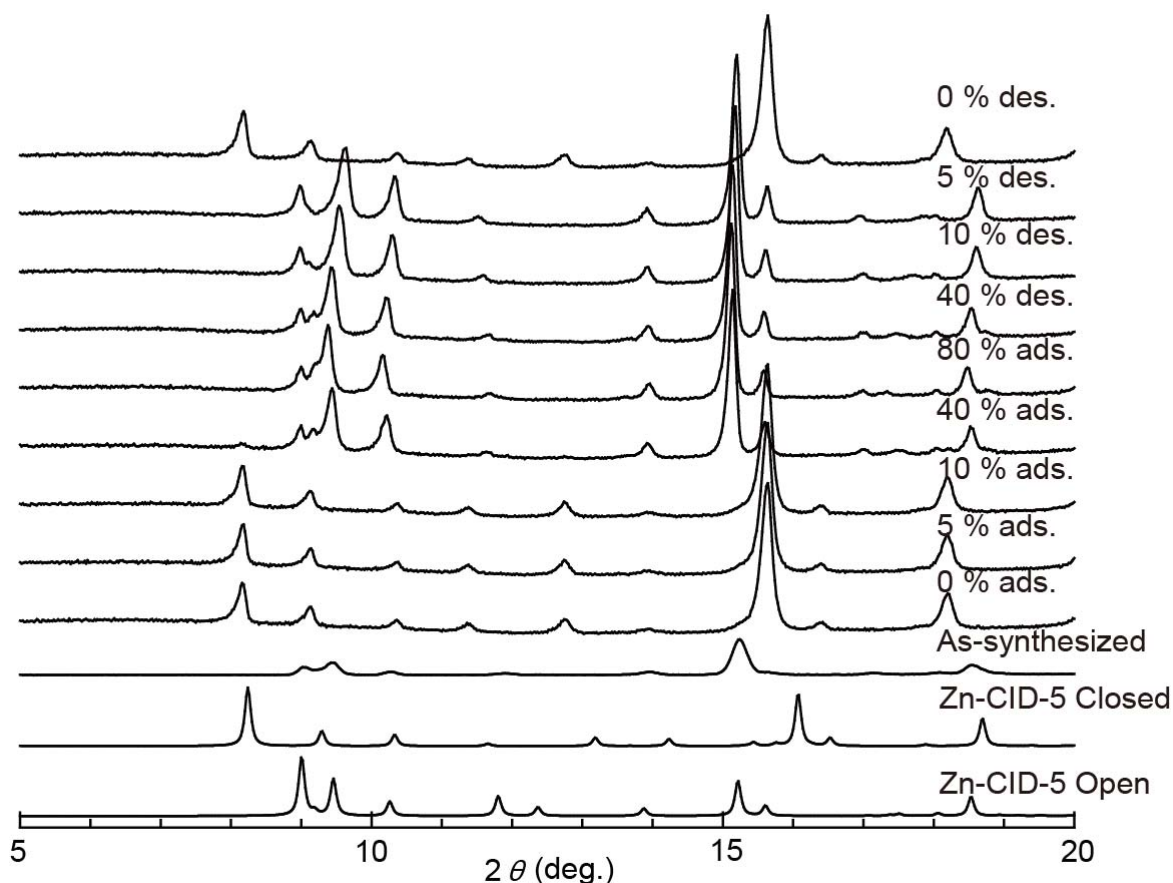


**Figure 8.** XRD patterns of **Zn-CID-5** ( $r = 0$ ) under various methanol humidity in adsorption and desorption process.

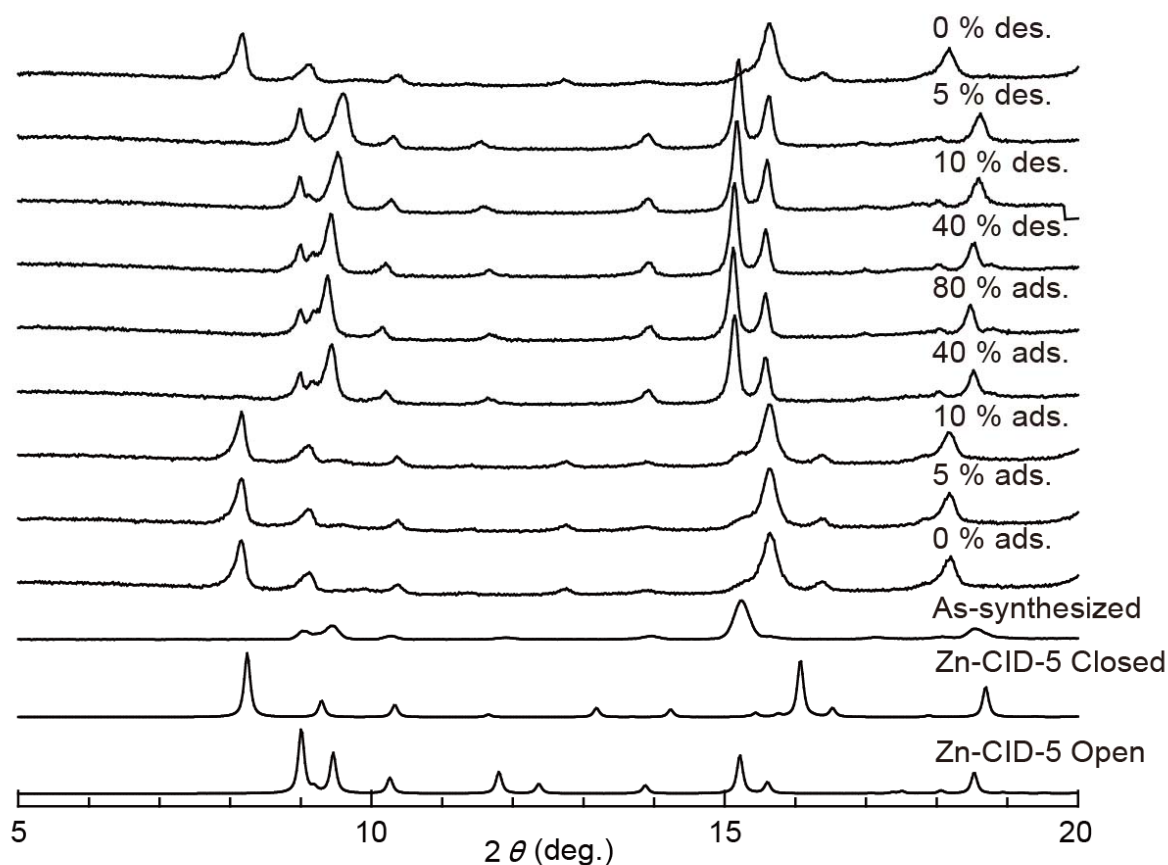


**Figure 9.** XRD patterns of **Zn-CID-5** ( $r = 15$ ) under various methanol humidity in adsorption and desorption process.

We then performed methanol adsorption measurements on the smaller sized **Zn-CID-5**,  $r = 7.5$ , 12.5 and 15. As the crystal size decreased, the gradual uptake of methanol at low pressure region was observed. While the conventional micrometer-sized **Zn-CID-5** ( $r = 0$ ) did not adsorb methanol under  $P/P_0 = 0.2$ , nanometer-sized **Zn-CID-5** ( $r = 15$ ) adsorbed certain amount of methanol ( $\sim 10$  mg/g). This tendency suggests that downsizing the crystals leads to the larger external surface area, which gives the gradual uptake at low pressure region, so-called surface adsorption.<sup>33-34</sup> The same tendency was observed in adsorption for chloroform (Figure 11). As previously reported, downsizing the crystals weakened the gate-opening property, reducing the recognition ability of flexible PCPs.

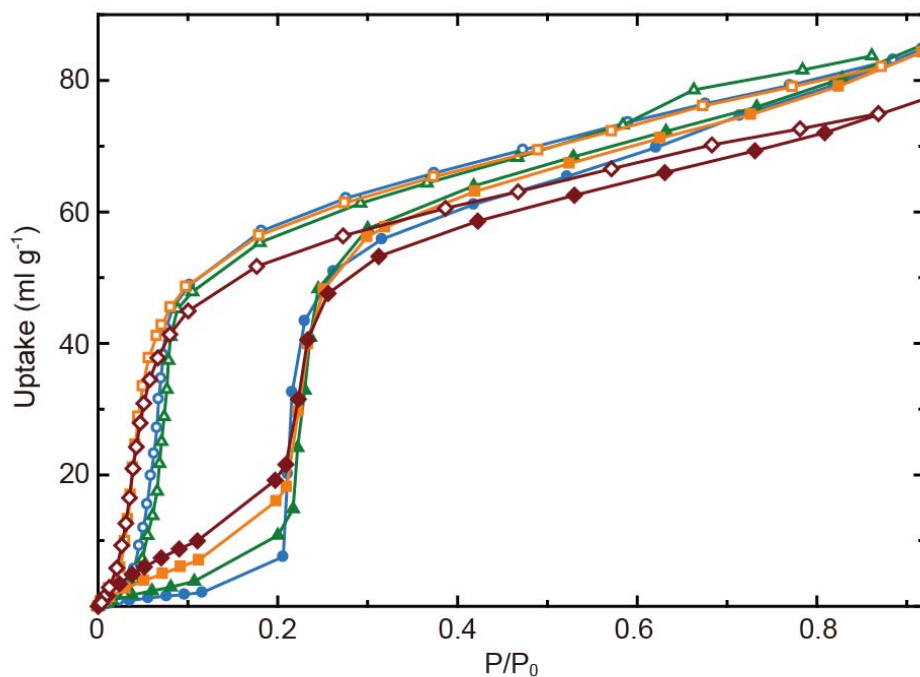


**Figure 10.** Adsorption isotherms of Zn-CID-5 obtained under various conditions for methanol:  $r = 0$  (blue),  $r = 7.5$  (green),  $r = 12.5$  (orange) and  $r = 15$  (brown). Closed and open symbols show adsorption and desorption, respectively.

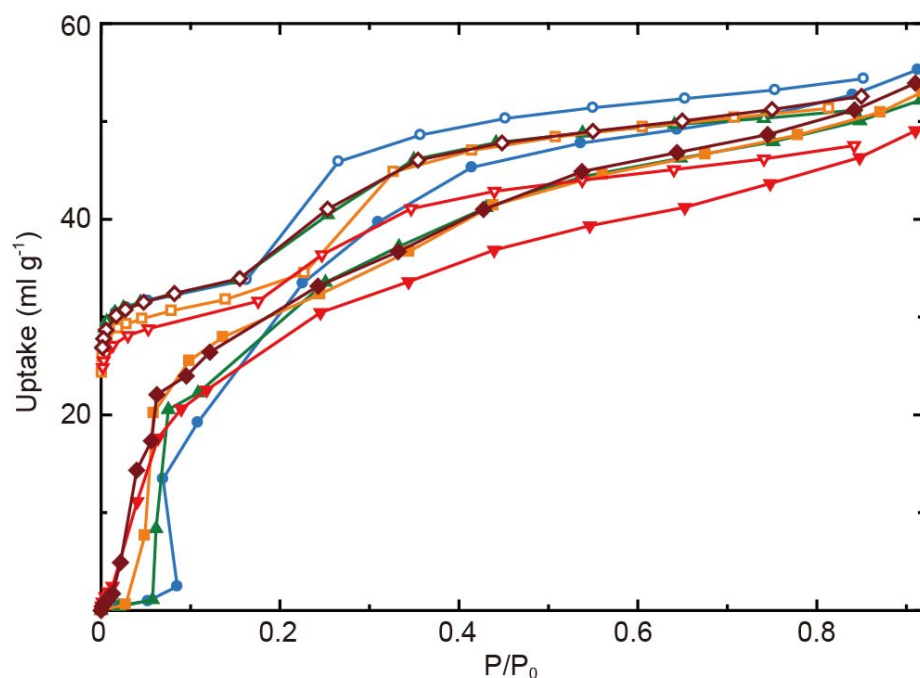


**Figure 11.** Adsorption isotherms of Zn-CID-5 obtained under various conditions for chloroform:  $r = 0$  (blue),  $r = 1$  (green),  $r = 5$  (orange),  $r = 12.5$  (brown) and  $r = 15$  (red). Closed and open symbols show adsorption and desorption, respectively.

## Flexible PCPs based Hybrid Sensor Device

Towards integration of **Zn-CID-5** into the QCM substrate, gold substrates were modified with monolayers of  $\text{HS}(\text{CH}_2)_{15}\text{COOH}$ .<sup>35-36</sup> We anticipated different orientations of the crystals, depending on a bare gold or COOH-functionalized SAMs.<sup>37-38</sup> The substrates were placed as vertical fashion (to avoid precipitation) in the solution of  $\text{Zn}(\text{NO}_3)_2 \cdot 6\text{H}_2\text{O}$  and  $\text{H}_2(\text{NO}_2\text{-ip})$  in DMF. The mixture of DMF and ethanol was layered on top of the DMF solution, and then solution of bpy in ethanol was layered on top of the mixture. The stocked solution was kept at 70 °C for 12 hours. The bundles of plate like crystals of **Zn-CID-5** (50-100  $\mu\text{m}$ ) were formed on the substrates as shown in Figure 12. The crystals grown on the COOH terminated SAMs were oriented along the [1-1-1] direction, while the bare gold substrate induced an orientation along the [100] direction (Figure 13). The tilted COOH-terminated SAMs (the tilted angle of SAMs: 30-40°) on substrate induces the tilted growth of 1D chain ([100] orientation). In contrast, the coordination bond between Au atom and carboxyl group of  $\text{NO}_2\text{-ip}$  leads to the growth of 1D chain perpendicular to the substrate ([1-1-1] orientation), as shown in Figure 13.

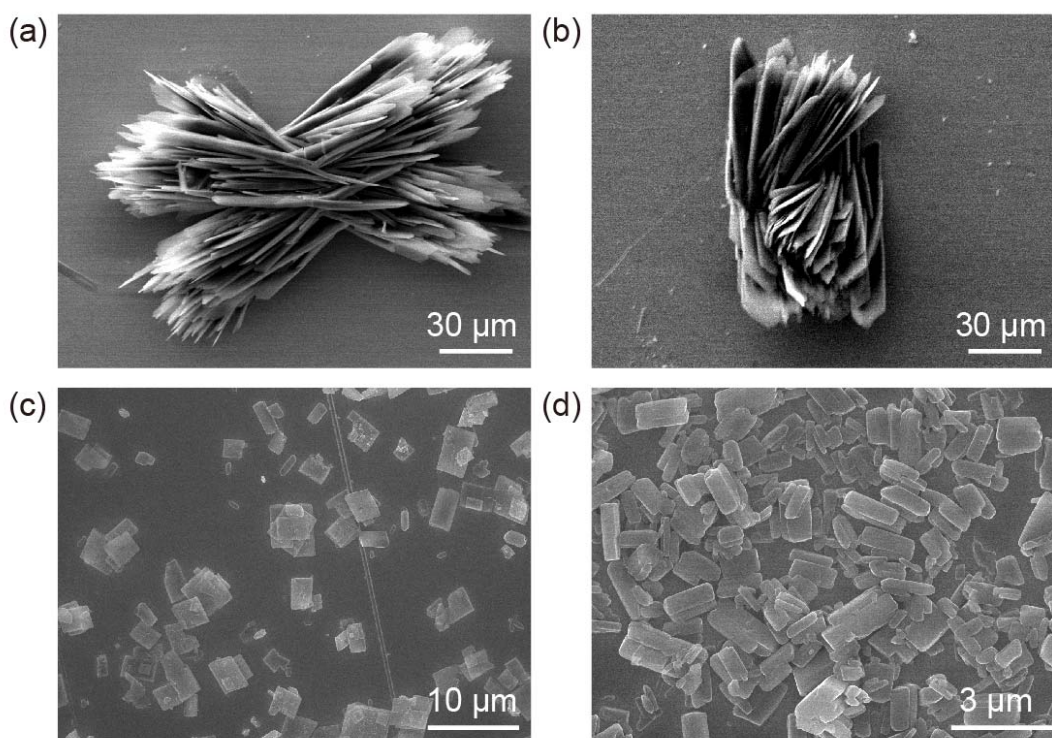


**Figure 12.** SEM images of **Zn-CID-5** on substrates obtained under various conditions: (a) solvothermal condition for bare Au, (b) solvothermal condition for SAMs, (c) microwave heating without modulator, (d) microwave heating with modulator.

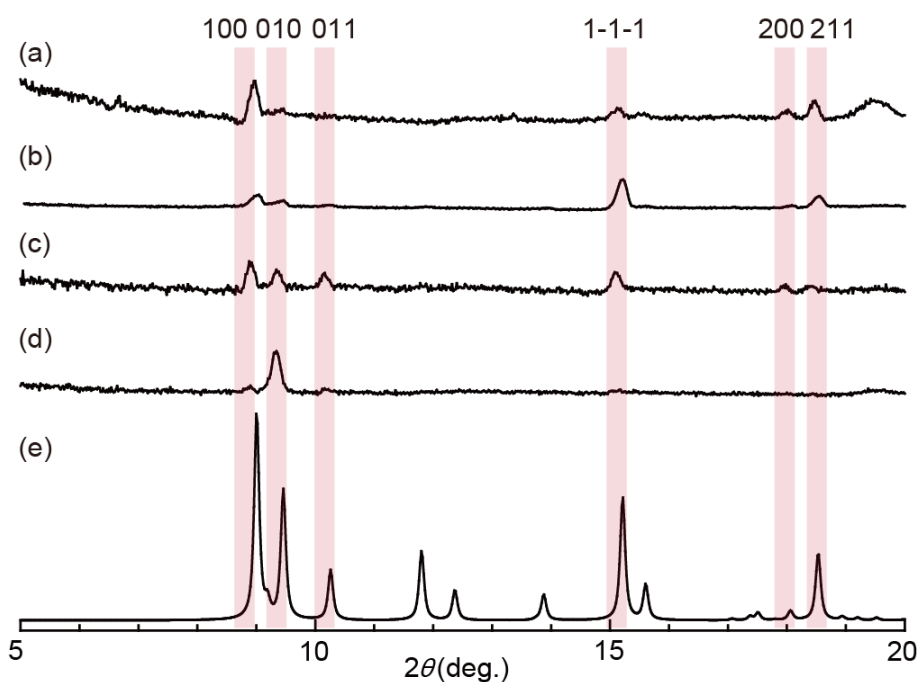


**Figure 13.** XRD patterns of **Zn-CID-5** on substrates obtained under various conditions: (a) solvothermal condition for SAMs ([100] orientation), (b) solvothermal condition for bare Au ([1-1-1] orientation), (c) microwave heating without modulator (no orientation), (d) microwave heating with modulator ([010] orientation), (e) simulation of **Zn-CID-5** (open form).

Although simple solvothermal reaction gave large plate like crystals (50-100  $\mu\text{m}$ ), rapid crystal growth by micro-wave heating gave smaller block crystals (5-10  $\mu\text{m}$ ), as shown in Figure 12. Noted that the rapid crystal growth gave not-oriented **Zn-CID-5** on the substrate. We applied coordination modulation method to slow down the crystal growth. Microwave heating with the modulator ( $r = 15$ ) led to the [010] orientation of **Zn-CID-5** (Figure 13). The nuclei is most likely terminated by monoamine molecules (4-phenylpyridine), according to the previous studies.<sup>30</sup> The terminating ligand of 4-phenylpyridine was replaced with bpy due to the same chemical functionality between 4-phenylpyridine and bpy. Thus, the crystals were grown preferentially along bpy direction (the [010] direction), as shown in Figure 13.

Prior to the evaluation of adsorption properties, the structural flexibility of deposited **Zn-CID-5** was confirmed by XRD under methanol atmosphere. All the as-synthesized crystals on substrates transformed from the open form to a closed form through guest removal. The Bragg peaks of 100 ( $2\theta = 9.0$ ) and 1-1-1 ( $2\theta = 15.2$ ) shifted to higher angles because the twisting of carboxylates and leaning of bpy shrank the interlayer and innerlayer distances. The Bragg peak of 010 ( $2\theta = 9.5$ ) disappeared and a new peak ( $2\theta = 8.2$ ) was appeared due to the bending of  $\text{NO}_2\text{-ip}$  (Figure 14). The

structural transformation from the closed form to an open form occurred over  $P/P_0 = 0.2$  in the adsorption process and under  $P/P_0 = 0.05$  in the desorption process, which corresponds to the gate-opening adsorption and hysteresis of desorption process of bulk samples. These results suggested that all the deposited micrometer-sized **Zn-CID-5** crystals maintain the original structural flexibility.

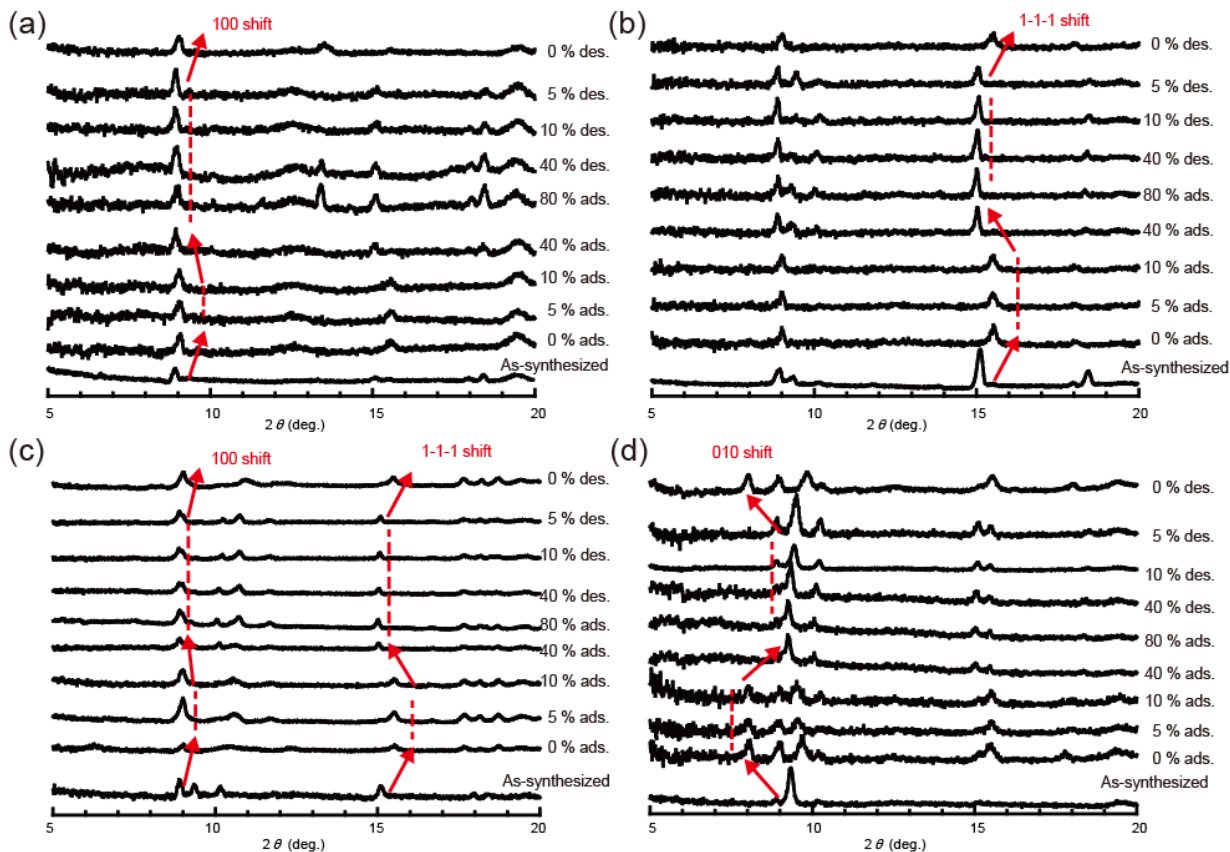


**Figure 14.** XRD patterns of (a) [100], (b) [1-1-1], (c) non-oriented and (d) [010] oriented samples under various methanol humidity in adsorption and desorption process.

In order to clarify the sorption properties of deposited **Zn-CID-5**, we implemented an environmentally-controlled QCM system that controlled the partial vapor pressure of volatile organic compounds (VOCs) in helium carrier gas.<sup>39</sup> The PCP modified QCM substrate (AT-cut, 9 MHz) was activated prior to the measurement according to the following protocol; the modified QCM oscillator was soaked into pure  $\text{CHCl}_3$  and then heated in QCM chamber under dry helium gas flow. The amount of **Zn-CID-5** crystals deposited on QCM substrate was estimated by the comparison of the fundamental frequency with the current frequency.

The vapor adsorption kinetics were investigated by real-time monitoring of the frequency change after the introduction of a vapor flow of MeOH at  $P/P_0 = 0.4$  into the QCM chamber. The time dependent mass uptake ( $M_t/M_e$ :  $M_t$  is the uptake at time  $t$  and  $M_e$  is the equilibrium uptake) for methanol vapors on the samples. Figure 15 shows the

effect of the crystal orientation on the kinetics of MeOH uptake. The rate of methanol sorption for the [100] and [010] oriented crystals was much faster than that of the [1-1-1] oriented or not-oriented samples. While the channel of the [1-1-1] oriented sample is perpendicular to the substrate, the channels of the [100] and [010] oriented samples run parallel to the substrate. Since the organic vapor was injected from the side of sample cell, the channels of the [100] and [010] oriented samples face in the direction of gas flow. Thus, the [100] and [010] oriented sample quickly adsorbed methanol. Noted that the guest uptake of [100] and [010] oriented samples have been completed less than 10 seconds.

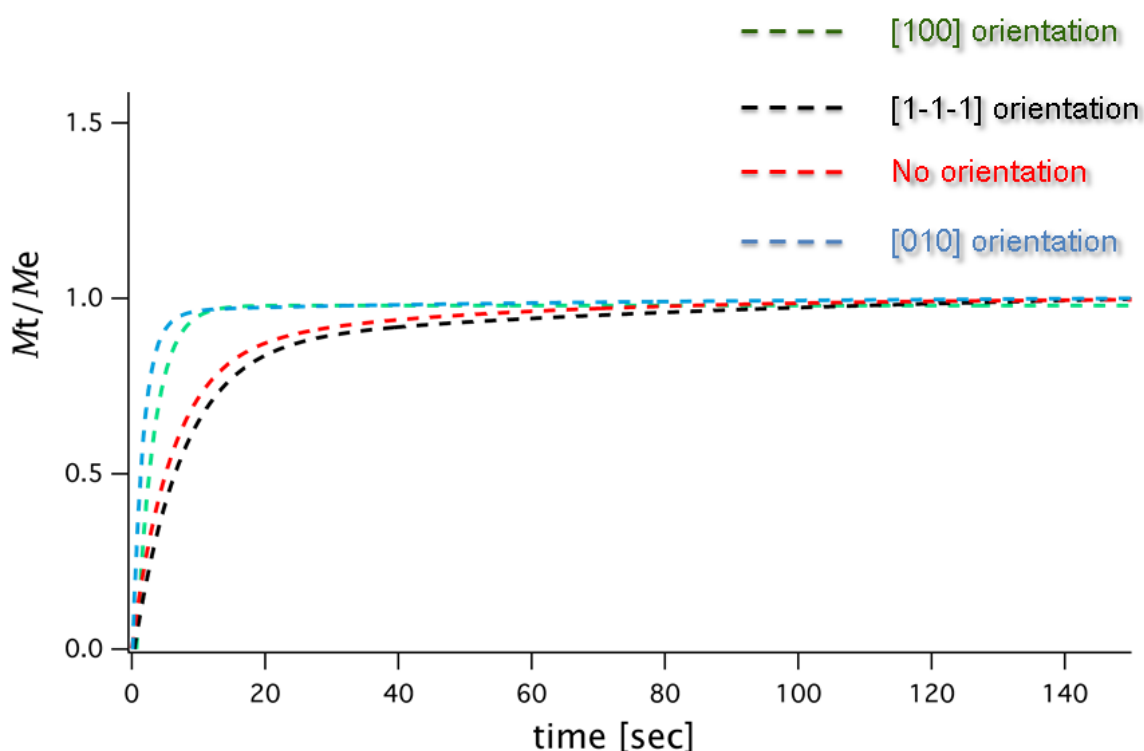


**Figure 15.** Time dependent MeOH mass uptakes of [1-1-1] orientation (black), [100] orientation (green), [010] orientation (blue) and no orientation (red) at  $P/P_0 = 0.4$ .

## Conclusion

In summary, we have successfully controlled the crystal size of  $[\text{Zn}(\text{NO}_2\text{-ip})(\text{bpy})]_n$  (**Zn-CID-5**) by coordination modulation method and investigated the effect of crystal size on sorption properties. The downsizing the crystals under 1  $\mu\text{m}$  spoiled the characteristic gate-opening properties. Moreover, the micrometer-sized **Zn-CID-5** crystals were fabricated on QCM substrate with controlling the crystal orientation. By the environmentally-controlled QCM system, we have quantitatively analyzed the sorption kinetics of **Zn-CID-5** on QCM substrates. In case that the channels are running parallel to the direction of gas flow, **Zn-CID-5** quickly adsorbed organic vapors. This result opens the way for the fabrication of the PCP sensor device and will clarify the way to improve its sensor performance.

## Experimental Section

### Materials

Reagents and solvents were purchased from commercial sources and used without further purification.

### Synthesis of bulk Zn-CID-5

Zn(NO<sub>3</sub>)<sub>2</sub>•6H<sub>2</sub>O (44.6 mg, 0.15 mmol), 5-nitroisophthalic acid (31.6 mg, 0.15 mmol) and 4,4'-bipyridyl (23.4 mg, 0.15 mmol) were dissolved in 20 mL of *N,N*-dimethylformamide (DMF). The solution was heated by use of microwave reactor (Initiator, Biotage).

### Coordination Modulation Method for Zn-CID-5

Zn(NO<sub>3</sub>)<sub>2</sub>•6H<sub>2</sub>O (89.6 mg, 0.30 mmol), 5-nitroisophthalic acid (63.3 mg, 0.30 mmol), 4,4'-bipyridyl (46.9 mg, 0.15 mmol) and 4-phenylpyridine were dissolved in 20 mL of *N,N*-dimethylformamide. The solution was heated up to 120 °C for 5 min by microwave reactor, Initiator from Biotage.

### Adsorption Measurements

Prior to the measurement, the sample has been soaked in dry methanol for 24 hours at room temperature, activated under vacuum at 393 K for 4 hours, and the degree of residual vacuum was checked to be lower than  $5 \times 10^{-2}$  Pa/min using the “leak check” option. The sorption isotherms of CID-5 for methanol, chloroform and hexane at 298 K were recorded on a BELSORP-max volumetric adsorption instrument from BEL Japan, Inc.

### In situ XRD during MeOH Sorption

The XRD patterns under MeOH were recorded using Smart Lab (Rigaku) equipped with a rotating anode Cu K $\alpha$  X-ray generator. The partial pressure of MeOH vapor was controlled by a BEL-Flow vapor control system (BEL Japan).

### Preparation of SAMs on Substrates

COOH-terminated SAMs was prepared by immersing the substrates in a solution of mercaptohexadecanoic acid for 1 day. The substrate was removed from the solution, thoroughly rinsed with 10 % acetic acid in ethanol.

### **Deposition of CID-5 on Substrates**

Zn(NO<sub>3</sub>)<sub>2</sub>•6H<sub>2</sub>O (5.95 mg, 0.02 mmol) and 5-nitroisophthalic acid (4.39 mg, 0.02 mmol) were dissolved in 2 mL of *N,N*-dimethylformamide in a glass vial. The substrate was immersed in the stocked solution. Then, 1 mL of DMF/EtOH (1:1) mixture was slowly layered on top of the DMF solution. Finally, 2mL of a EtOH solution of 4,4'-bipyridyl (3.12 mg, 0.02 mmol) was slowly layered on top of the DMF/EtOH mixture. The solution was heated up to 70 °C for 12 hours. bpy slowly diffused towards the bottom layer and CID-5 was crystallized on the substrate.

### **Microwave-assisted deposition of CID-5 on Substrates**

Zn(NO<sub>3</sub>)<sub>2</sub>•6H<sub>2</sub>O (0.30 g, 1 mmol) and 5-nitroisophthalic acid (0.21 g, 1 mmol) were dissolved in 20 mL of *N,N*-dimethylformamide at room temperature. Then, 10 mL of a methanolic solution of 4,4'-bipyridyl (0.16 g, 1 mmol) was added to the previous reaction vessel. After stirring to obtain an homogeneous mixture, a gold sub-strate was placed standing(to avoid aggregation from gravity) in the solution. The solution was heated up to 120 °C for 5 min by microwave reactor, Initiator from Biotage.

### **Field-Emission Scanning Electron Microscopy**

Scanning electron microscopy (SEM) observations were performed with a JEOL Model JSM-7001F4 SEM.

### **Quartz Crystal Microbalance**

The sorption properties of hybrid QCM sensors for volatile organic compounds (VOCs) were investigated by environment-controlled BEL-QCM system. The He carrier gas flow was controlled by mass flow controllers with a total mass flow of 100 cm<sup>3</sup> min<sup>-1</sup>. The mass of deposited PCP material was estimated by the comparison of the fundamental frequency with the current frequency.

## References

- (1) T. G. Drummond<sup>1</sup>, M. G. Hill, J. K. Barton<sup>1</sup>, *Nature Biotech.* **2003**, *21*, 1192-1199.
- (2) A. Kolmakov, Y. Zhang, G. Cheng, M. Moskovits, *Adv. Mater.* **2003**, *15*, 997-1000.
- (3) A. P. de Silva, H. Q. N. Gunaratne, T. Gunnlaugsson, A. J. M. Huxley, C. P. McCoy, J. T. Rademacher, T. E. Rice, *Chem. Rev.* **1997**, *97*, 1515-1566.
- (4) F. Patolsky, G. Zheng, C. M. Lieber, *Anal. Chem.* **2006**, *78*, 4260-4269.
- (5) Y. Takashima, V. M. Martinez, S. Furukawa, M. Kondo, S. Shimomura, H. Uehara, M. Nakahama, K. Sugimoto, S. Kitagawa, *Nature Commun.* **2011**, *2*, 168
- (6) O. M. Yaghi, M. O'Keeffe, N. W. Ockwig, H. K. Chae, M. Eddaoudi, J. Kim, *Nature* **2003**, *423*, 705-714.
- (7) S. Kitagawa, R. Kitaura, S. -i. Noro, *Angew. Chem. Int. Ed.* **2004**, *43*, 2334-2375.
- (8) G. Férey, C. Mellot-Draznieks, C. Serre, F. Millange, *Acc. Chem. Res.* **2005**, *38*, 217-225.
- (9) S. Batten, R. Robson, *Angew. Chem. Int. Ed.* **1998**, *37*, 1460-1494.
- (10) U. Mueller, M. Schubert, F. Teich, H. Puetter, K. Schierle-Arndt, J. Pastré, *J. Mater. Chem.* **2006**, *16*, 626-636.
- (11) M. Eddaoudi, J. Kim, N. L. Rosi, D. T. Vodak, J. Wachter, M. O'Keeffe, O. M. Yaghi, *Science* **2002**, *295*, 469-472.
- (12) T. Devic, P. Horcajada, C. Serre, F. Salles, G. Maurin, B. Mooulin, D. Heurtaux, G. Clet, A. Vimont, J. M. Grenèche, B. Le Ouay, F. Moreau, E. Magnier, Y. Filinchuk, J. Marrot, J. C. Lavalley, M. Daturi, G. Férey, *J. Am. Chem. Soc.* **2010**, *132*, 1127-1136.
- (13) S. Horike, S. Shimomura, S. Kitagawa, *Nature Chem.* **2009**, *1*, 695-704.
- (14) G. Férey, C. Serre, *Chem. Soc. Rev.* **2009**, *38*, 1380-1399.
- (15) B. Chen, C. Liang, J. Yang, D. S. Contreras, Y. L. Clancy, E. B. Lobkovsky, O. M. Yaghi, S. Dai, *Angew. Chem. Int. Ed.* **2006**, *45*, 1390-1393.
- (16) C. Serre, F. Millange, C. Thouvenot, M. Noguès, G. Marsolier, D. Louër, G. Férey, *J. Am. Chem. Soc.* **2002**, *124*, 13519-13526.
- (17) S. Aguado, G. Bergeret, M. P. Titus, V. Moizan, C. N. Draghi, N. Batsb, D. Farrusseng, *New J. Chem.* **2011**, *35*, 546-550.
- (18) R. Kitaura, K. Fujimoto, S. Noro, M. Kondo, S. Kitagawa, *Angew. Chem. Int. Ed.* **2002**, *41*, 133-135.
- (19) D. Tanaka, K. Nakagawa, M. Higuchi, S. Horike, Y. Kubota, T. C. Kobayashi, M. Takata, S. Kitagawa, *Angew. Chem. Int. Ed.* **2008**, *47*, 3914-3918.
- (20) C.K. O'Sullivan, G.G. Guilbault, *Biosen. Bioelect.* **1999**, *14*, 663-748.

- (21) H. Uehara, S. Diring, S. Furukawa, Z. Kalay, M. Tsotsalas, M. Nakahama, K. Hirai, M. Kondo, O. Sakata, S. Kitagawa, *J. Am. Chem. Soc.* **2011**, *133*, 11932-11935.
- (22) E. Biemmi, A. Darga, N. Stock, T. Bein, *Micropor. Mesopor. Mater.* **2008**, *114*, 380-386.
- (23) Y. Yant, T. Bein, *J. Am. Chem. Soc.* **1995**, *117*, 9900-9995.
- (24) S. H. Jung, J. H. Lee, J. W. Yoon, C. Serre, G. Férey, J. S. Chang, *Adv. Mater.* **2007**, *19*, 121-124.
- (25) Z. Lai, G. Bonilla, I. Diaz, J. G. Nery, K. Sujaoti, M. A. Amat, E. Kokkoli, O. Terasaki, R. W. Thompson, M. Tsapatsis, D. G. Vlachos, *Science* **2003**, *300*, 456-460.
- (26) J. Tao, X. M. Chen, R. B. Huang, L. S. Zheng, *J. Solid State Chem.* **2003**, *170*, 130-134.
- (27) S. Horike, D. Tanaka, K. Nakagawa and S. Kitagawa, *Chem. Commun.* **2007**, 3395-3397.
- (28) K. Nakagawa, D. Tanaka, S. Horike, S. Shimomura, M. Higuchi and S. Kitagawa, *Chem. Commun.* **2010**, *46*, 4258-4260.
- (29) T. Fukushima, S. Horike, Y. Inubushi, K. Nakagawa, Y. Kubota, M. Takata, S. Kitagawa, *Angew. Chem. Int. Ed.* **2010**, *49*, 4820-4824.
- (30) T. Tsuruoka, S. Furukawa, Y. Takashima, K. Yoshida, S. Isoda, S. Kitagawa, *Angew. Chem. Int. Ed.* **2009**, *48*, 4739-4743.
- (31) S. Diring, S. Furukawa, Y. Takashima, T. Tsuruoka, S. Kitagawa, *Chem. Mater.* **2010**, *22*, 4531-4538.
- (32) A. Schaate, P. Roy, A. Godt, J. Lippke, F. Waltz, M. Wiebcke, P. Behrens, *Chem. Eur. J.* **2011**, *17*, 6643-6651.
- (33) D. Tanaka, A. Henke, K. Albrecht, M. Moeller, K. Nakagawa, S. Kitagawa, J. Groll, *Nature Chem.* **2010**, *2*, 410-416.
- (34) A. Kondo, N. Kojima, H. Kajiro, H. Noguchi, Y. Hattori, F. Okino, K. Maeda, T. Ohba, K. Kaneko, H. Kanoh, *J. Phys. Chem. C* **2012**, *116*, 4157-4162.
- (35) J. C. Love, L. A. Estroff, J. K. Kriebel, R. G. Nuzzo, G. M. Whitesides, *Chem. Rev.* **2005**, *105*, 1103-1170.
- (36) S. Hermes, F. Schröder, R. Chelmowski, C. Wöll, R. A. Fischer, *J. Am. Chem. Soc.* **2005**, *127*, 13744-13745.
- (37) O. Shekhah, H. Wang, S. Kowarik, F. Schreiber, M. Paulus, M. Tolan, C. Sternemann, F. Evers, D. Zacher, R. A. Fischer, C. Wöll, *J. Am. Chem. Soc.* **2007**, *129*, 15118-15119.
- (38) E. Biemmi, C. Scherb, T. Bein, *J. Am. Chem. Soc.* **2007**, *129*, 8054-8055.

- (39) M. Meilikhov, S. Furukawa, K. Hirai, R. A. Fischer, S. Kitagawa, *Angew. Chem. Int. Ed.* 2012, *in press*.

# List of Publications

## Chapter 1.

Heterogeneously Hybridized Porous Coordination Polymer Crystals: Fabrication of Heterometallic Core–Shell Single Crystals with an In-Plane Rotational Epitaxial Relationship

Shuheï Furukawa, Kenji Hirai, Keiji Nakagawa, Yohei Takashima, Ryotaro Matsuda, Takaaki Tsuruoka, Mio Kondo, Rie Haruki, Daisuke Tanaka, Hirotoishi Sakamoto, Satoru Shimomura, Osami Sakata, Susumu Kitagawa  
*Angew. Chem. Int. Ed.* **2009**, *48*, 1766-1770.

## Chapter 2.

A block PCP crystal: anisotropic hybridization of porous coordination polymers by face-selective epitaxial growth

Shuheï Furukawa, Kenji Hirai, Yohei Takashima, Keiji Nakagawa, Mio Kondo, Takaaki Tsuruoka, Osami Sakata, Susumu Kitagawa  
*Chem. Commun.* **2009**, 5077-5079.

## Chapter 3.

Sequential Functionalization of Porous Coordination Polymer Crystals

Kenji Hirai, Shuheï Furukawa, Mio Kondo, Hiromitsu Uehara, Osami Sakata, Susumu Kitagawa  
*Angew. Chem. Int. Ed.* **2011**, *50*, 8057-8061.

## Chapter 4.

Targeted functionalisation of a hierarchically-structured porous coordination polymer crystal enhances its entire function

Kenji Hirai, Shuheï Furukawa, Mio Kondo, Mikhail Meilikhov, Yoko Sakata, Osami Sakata, Susumu Kitagawa  
*Chem. Commun.* **2012**, *48*, 6472-6474.

## Chapter 5.

Programmed crystallization via epitaxial growth and ligand replacement towards a hybridized porous coordination polymer

Kenji Hirai, Kebi Chen, Shuheï Furukawa, Tomohiro Fukushima, Satoshi Horike, Mikhail Meilikhov, Nicolas Louvain, Chiwon Kim, Yoko Sakata,

Susumu Kitagawa

*to be submitted*

#### **Chapter 6.**

Multilength-scales structuralization emerged from one reaction

Kenji Hirai, Shuhei Furukawa, Julien Reboul, Nobuhiro Morone, Susumu Kitagawa

*in preparation.*

#### **Chapter 7.**

Redox reaction in two-dimensional porous coordination polymers based on ferrocenedicarboxylate

Kenji Hirai, Hiromitsu Uehara, Susumu Kitagawa, Shuhei Furukawa

*Dalton Trans.* **2012**, *41*, 3924-3927.

#### **Chapter 8.**

Crystal Orientation Controls Analyte Detection Kinetics of Porous Coordination Polymer Hybrid Sensor with Quartz Oscillator

Kenji Hirai, Mikhail Meilikhov, Shuhei Furukawa, Nicolas Louvain, Masashi Nakahama, Hiromitsu Uehara, Susumu Kitagawa

*to be submitted*

#### **Other Publication**

Fabrication of Coordinatively Immobilized Monolayers on Porous Coordination Polymer Crystals

Mio Kondo, Shuhei Furukawa, Kenji Hirai, Susumu Kitagawa

*Angew. Chem. Int. Ed.*, **2010**, *49*, 5327-5330.

MOF-on-MOF Heteroepitaxy: Perfectly oriented  $[\text{Zn}_2(\text{ndc})_2(\text{dabco})]_n$  grown on  $[\text{Cu}_2(\text{ndc})_2(\text{dabco})]_n$  thin films

Osama Shekah, Kenji Hirai, Hui Wang, Hiromitsu Ueahara, Mio Kondo, Stephane Diring, Denise Zacher, Roland A. Fischer, Osami Sakata, Ssusumu Kitagawa, Shuhei Furukawa, Chrisof Wöll

*Dalton Trans.*, **2011**, *40*, 4954-4958.

Liquid phase separation of polyaromatics on [Cu<sub>2</sub>(BDC)<sub>2</sub>(dabco)]

Michael Maes, Stijn Schouteden, Kenji Hirai, Shuhei Furukawa, Susumu Kitagawa, Dirk E. De Vos

*Langmuir*, **2011**, *27*, 9083-9087.

Porous Coordination Polymer Hybrid Device with Quartz Oscillator: Effect of Crystal Size on Sorption Kinetics

Hiromitsu Uehara, Stephane Diring, Shuhei Furukawa, Ziya Kalay, Manuel Tsotsalas, Masashi Nakahama, Kenji Hirai, Mio Kondo, Osami Sakata, Susumu Kitagawa

*J. Am. Chem. Soc.*, **2011**, *133*, 11932-11935.

Mesoscopic architectures of porous coordination polymers fabricated by pseudomorphic replication

Julien Reboul, Shuhei Furukawa, Nao Horike, Manuel Tsotsalas, Kenji Hirai, Hiromitsu Uehara, Mio Kondo, Nicolas Louvain, Osami Sakata, Susumu Kitagawa

*Nature Mater.*, **2012**, *11*, 11932-11935.

Binary Janus Porous Coordination Polymer Coatings for Sensor Devices with Tunable Analyte Affinity

Mikhail Meilikhov, Shuhei Furukawa, Kenji Hirai, Roland A. Fischer and Susumu Kitagawa

*Angew. Chem. Int. Ed.*, **2013**, *52*, 341-345.

Shape Memory Nanopores Induced in Coordination Frameworks by Crystal Downsizing

Yoko Sakata, Shuhei Furukawa, Mio Kondo, Kenji Hirai, Nao Horike, Yohei Takashima, Hiromitsu Uehara, Nicolas Louvain, Mikhail Meilikhov, Takaaki Tsuruoka, Seiji Isoda, Wataru Kosaka, Osami Sakata, Susumu Kitagawa

*Science*, *in press*